Summaries of the Fifth Annual JPL Airborne Earth Science Workshop January 23–26, 1995
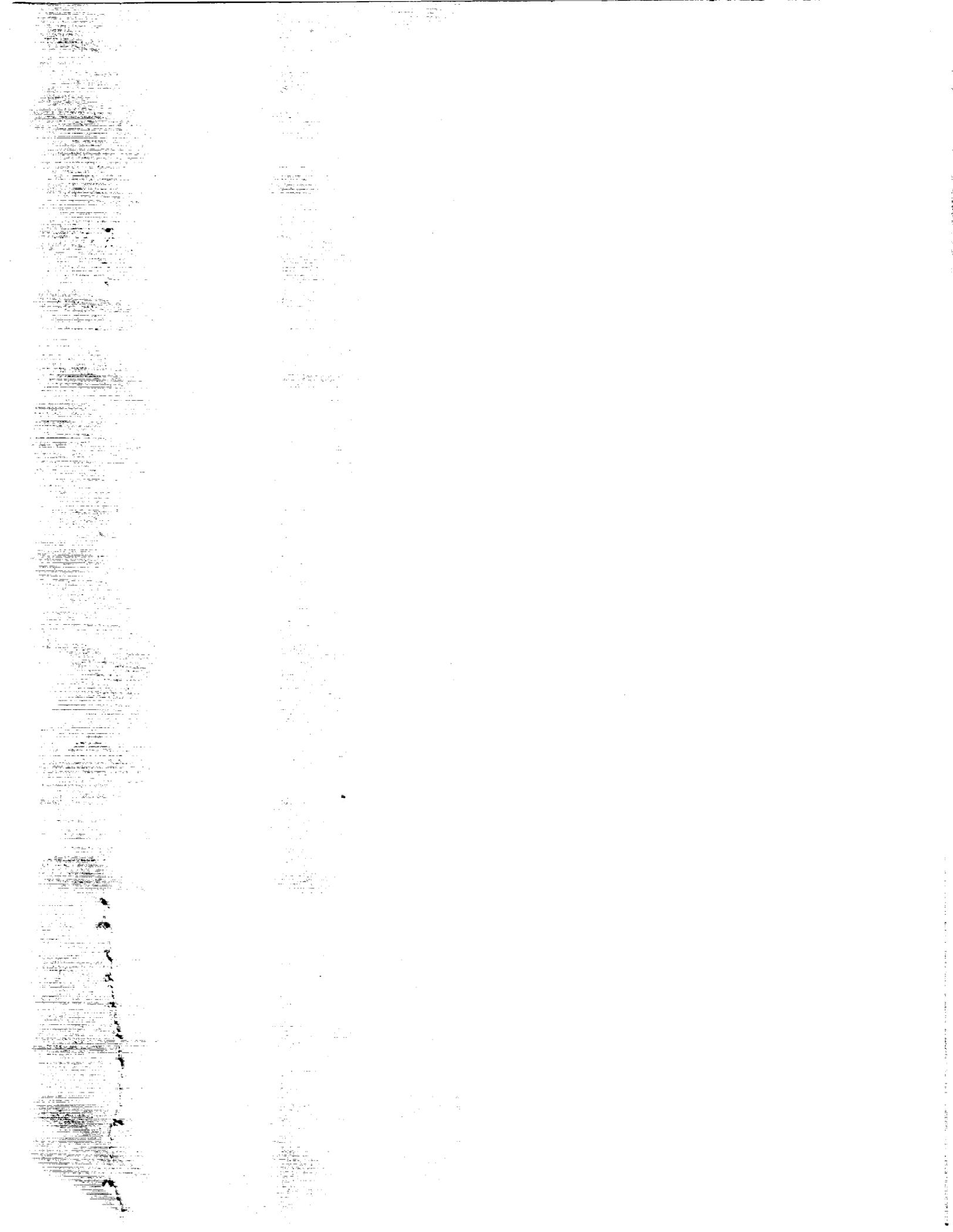
Volume 1. AVIRIS Workshop

Robert O. Green
Editor

January 23, 1995

NASA

National Aeronautics and
Space Administration

Jet Propulsion Laboratory
California Institute of Technology
Pasadena, California

Summaries of the Fifth Annual JPL Airborne Earth Science Workshop January 23–26, 1995

Volume 1. AVIRIS Workshop

Robert O. Green
Editor

January 23, 1995

ABSTRACT

This publication contains the summaries for the Fifth Annual JPL Airborne Earth Science Workshop, held in Pasadena, California, on January 23–26, 1995. The main workshop is divided into three smaller workshops as follows:

- The Airborne Visible/Infrared Imaging Spectrometer (AVIRIS) workshop, on January 23–24. The summaries for this workshop appear in Volume 1.

- The Airborne Synthetic Aperture Radar (AIRSAR) workshop, on January 25–26. The summaries for this workshop appear in Volume 3.

- The Thermal Infrared Multispectral Scanner (TIMS) workshop, on January 26. The summaries for this workshop appear in Volume 2.

FOREWORD

In some of the papers for the AVIRIS Workshop, reference is made to color slides. A packet containing these slides was supplied at the time of the initial distribution of this volume.

Volume 1: AVIRIS Workshop

Volume 2: TIMS Workshop

Volume 3: AIRSAR Workshop

HIGH SPECTRAL RESOLUTION REMOTE SENSING OF CANOPY CHEMISTRY

John D. Aber and Mary E. Martin

Complex Systems Research Center, Morse Hall, University of New Hampshire, Durham, NH USA 03824

1   INTRODUCTION

Near infrared laboratory spectra have been used for many years to determine nitrogen and lignin concentrations in plant materials (Norris *et al.* 1976; Wessman *et al.* 1988a). In recent years, similar high spectral resolution visible and infrared data have been available via airborne remote sensing instruments. Using data from NASA's Airborne Visible/Infrared Imaging Spectrometer (AVIRIS) we attempt to identify spectral regions correlated with foliar chemistry at the canopy level in temperate forests.

2   METHODS

Two well-studied research sites were used for this study. Harvard Forest is a 1200 hectare research site in central Massachusetts, USA (Latitude 42°32'N Longitude 72°11'W) containing a combination of hardwood and mixed hardwood/conifer stands as well as several plantations of pine, spruce and larch. Blackhawk Island in south-central Wisconsin, USA (Latitude 43°40'N Longitude 89°45'W), is a natural area containing a wide diversity of forest types including maple, oak, pine and hemlock.

Field data were collected for 20 plots at each site within 10 days of the acquisition of remote sensing data. Fresh leaf samples were collected from five trees of each overstory species in each plot. Nitrogen concentrations in all samples were determined by CHN analysis and lignin by a sequential extraction/sulfuric acid digestion procedure (McClaugherty and Berg 1987). Litterfall collections, sorted by species, were used to determine the relative canopy biomass of each species. Total canopy nitrogen and lignin concentrations were calculated as mean concentration per species weighted by foliar mass per species.

Remote sensing data were acquired using AVIRIS on 15 June 1992 at Harvard Forest and 21 June 1992 at Blackhawk Island. AVIRIS records data in 224 contiguous spectral bands covering the spectral range of 400 - 2500nm with a spectral resolution of 10nm and spatial resolution of 20m (Vane *et al.* 1988). Atmospheric corrections of the AVIRIS data were done by the ATREM program (Gao *et al.* 1992). This program uses information in each AVIRIS radiance spectra to parameterize a radiative transfer model that is then used to convert radiance data to ground reflectance by removing the effects of atmospheric gases, water vapor and aerosols. In addition to the ATREM correction, a secondary correction was made based on the difference between a ground calibrated Blackhawk Island scene and the same ATREM corrected scene (Clark *et al.* 1993)(personal communication, K. Heidebrecht).

Atmospherically corrected AVIRIS data were transformed to first difference spectra. The mean of the first difference spectra from a 2x2 array of pixels overlapping each of the 10 field locations was used in this analysis.

3 RESULTS

Data from both Harvard Forest and Blackhawk Island were combined for lignin and nitrogen calibrations. Validations of the calibration equations were assessed by an iterative cross-validation method in which each sample in turn was dropped from the calibration process and predicted from the resulting equation (Mark and Workman 1991). Canopy nitrogen concentrations were predicted from first difference AVIRIS spectra using equation 1:

$$\%Nitrogen = 0.486 + (0.001 * 783nm) + (0.003 * 1640nm) \tag{1}$$

The relationship between field measured and AVIRIS predicted nitrogen for the forty plots is shown in figure 1a. Absorption at 764nm corresponds with both a third overtone N-H absorption feature and a chlorophyll absorption feature (Gates et al. 1965). Chlorophyll content in foliage is highly correlated with total protein, and hence total nitrogen content. 1640nm is a first overtone of a C-H absorption band (Murray and Williams 1987).

Similarly, canopy lignin concentrations were predicted with equation 2 using four bands of the first difference absorption spectra:

$$\%Lignin = 33.36 - (0.048 * 822nm) + (0.106 * 627nm) + (0.005 * 756nm) + (0.052 * 1660nm) \tag{2}$$

Absorption at 1660nm is related to absorption overtones of unsaturated or phenolic C-C bonds which are abundant in lignin molecules (Murray and Williams 1987). The three shorter wavelengths used in this equation correspond to a region of high absorbance observed in the laboratory spectra of lignin. Figure 1b shows the relationship between field measured and AVIRIS predicted lignin concentrations. Figures 2a and 3a shows the AVIRIS predicted nitrogen and lignin concentrations for each pixel in the Harvard Forest and Blackhawk Island scenes, respectively.

Previous research at Blackhawk Island has demonstrated a very strong ($R^2 = .96, n = 7, p < .001$) relationship between canopy lignin concentration and annual net nitrogen mineralization, or nitrogen cycling (Wessman et al. 1988b). This relationship has been used with remote sensing data from a low-elevation airborne platform to produce a verified map of nitrogen mineralization for Blackhawk Island (Wessman et al. 1988b). A nearly identical map is generated from an image of estimated lignin concentrations from 1992 AVIRIS data (Figure 3b).

At the Harvard Forest, a simple model of monthly carbon balances driven largely by foliar nitrogen concentrations, has been validated against monthly carbon balance data obtained by eddy-correlation methods (Aber and Federer 1992). Applying this model to an image of foliar nitrogen concentrations at the Harvard Forest, yields an estimate of net ecosystem exchange of carbon for the entire research site (Figure 2b).

These results demonstrate the potential for high resolution remote sensing to increase both the accuracy of spatially averaged estimates of carbon and nitrogen cycling in temperate forest ecosystems, and to increase the spatial detail of those estimates.

4 REFERENCES

Aber, J. D. and Federer, C. A. (1992). A generalized, lumped-parameter model of photosynthesis, evapotranspiration and net primary production in temperate and boreal forest ecosystems. *Oecologia*, **92**, 463–474.

Clark, R. N., Swayze, G., Heidebrecht, K., Goetz, A. F. H., and Green, R. O. (1993). Comparison of methods for calibrating AVIRIS data to ground reflectance. In R. O. Green, editor, *Summaries of the Fourth Annual JPL Airborne Geoscience Workshop: AVIRIS*, volume 1, pages 35–36, Pasadena, California, USA. Jet Propulsion Laboratory.

Gao, B., Heidebrecht, K. B., and Goetz, A. F. H. (1992). *Atmosphere removal program (ATREM) user's guide*. Center for the Study of Earth from Space/CIRES, University of Colorado.

Gates, D. M., Keegan, H. J., Schleter, J. C., and Weidner, V. R. (1965). Spectral properties of plants. *Applied Optics*, **4**, 11–20.

Mark, H. and Workman, J. (1991). *Statistics in Spectroscopy*. Academic Press, San Diego.

McClaugherty, C. and Berg, B. (1987). Cellulose, lignin and nitrogen concentrations as rate regulating factors in late stages of forest litter decomposition. *Pedobiologia*, **30**, 101–112.

Murray, I. and Williams, P. C. (1987). Chemical principles of near-infrared technology. In P. Williams and K. Norris, editors, *Near-Infrared Technology in the Agricultural and Food Industries*. American Association of Cereal Chemists, Inc, St. Paul, Minnesota, USA.

Norris, K. H., Barnes, R. F., Moore, J. E., and Shenk, J. S. (1976). Predicting forage quality by infrared reflectance spectroscopy. *Journal of Animal Science*, **43**, 889–897.

Vane, G., Porter, W. M., Reimer, J. H., Chrien, T. G., and Green, R. O. (1988). AVIRIS performance during the 1987 flight season: An AVIRIS project assessment and summary of the NASA-sponsored performance evaluation. In G. Vane, editor, *Proceedings of the Airborne Visible/Infrared Imaging Spectrometer (AVIRIS) Performance Evaluation Workshop*, pages 1–20, Pasadena, California, USA. Jet Propulsion Lab.

Wessman, C. A., Aber, J. D., Peterson, D. L., and Melillo, J. M. (1988a). Foliar analysis using near infrared reflectance spectroscopy. *Canadian Journal of Forest Research*, **18**, 6–11.

Wessman, C. A., Aber, J. D., Peterson, D. L., and Melillo, J. M. (1988b). Remote sensing of canopy chemistry and nitrogen cycling in temperate forest ecosystems. *Nature*, **335**, 154–156.
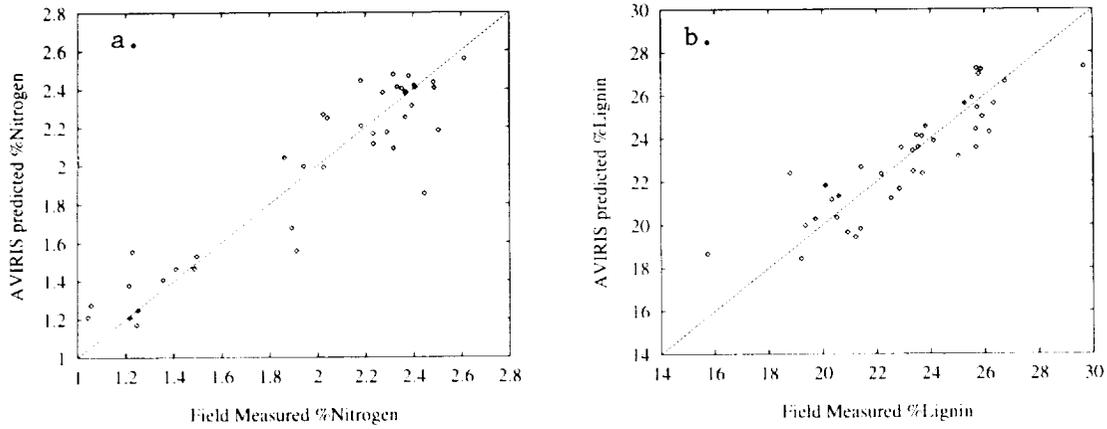
Figure 1: AVIRIS predicted vs field measured nitrogen (a) and lignin (b) - Blackhawk Island and Harvard Forest Sites combined.
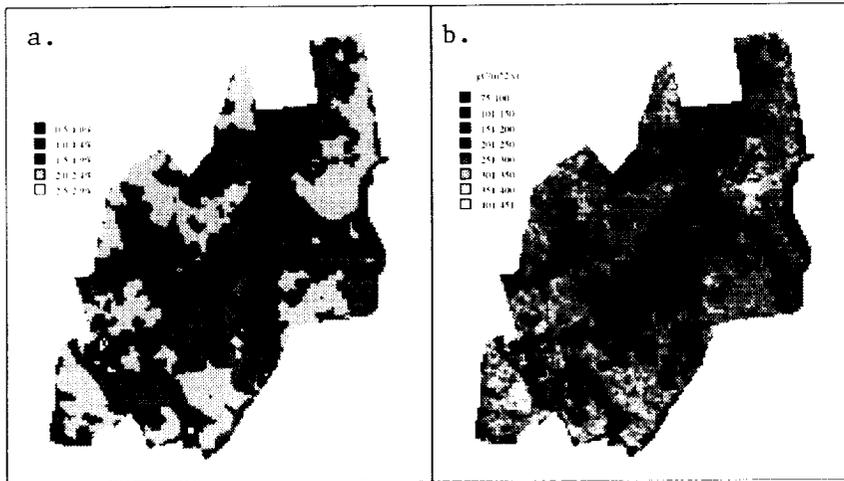
Figure 2: Harvard Forest - a. percent canopy nitrogen as calculated with AVIRIS data (equation 1). b. net ecosystem productivity predicted using AVIRIS derived nitrogen as a model input parameter.
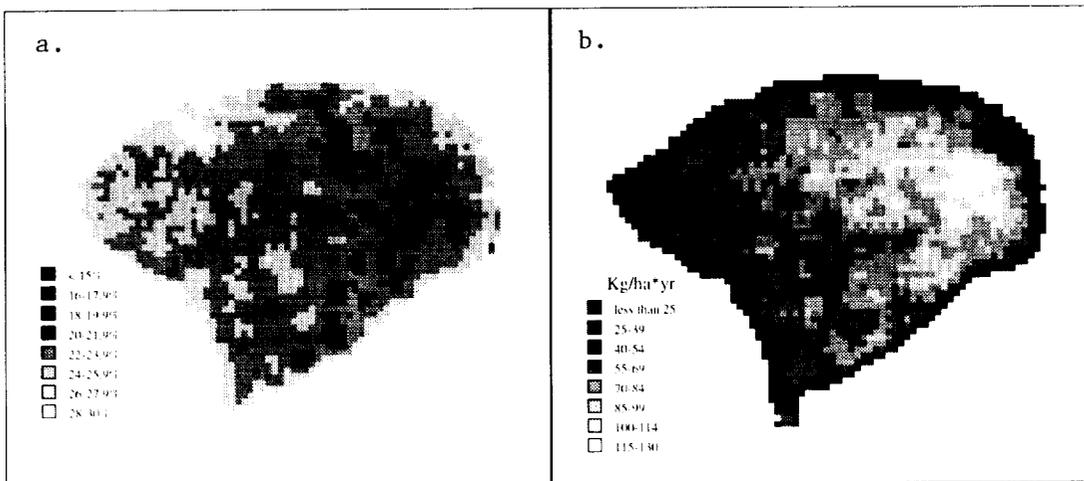
Figure 3: Blackhawk Island - a. percent canopy lignin as calculated with AVIRIS data (equation 2) b. nitrogen mineralization rate.

MODTRAN3: AN UPDATE AND RECENT VALIDATIONS AGAINST AIRBORNE HIGH RESOLUTION INTERFEROMETER MEASUREMENTS

Gail P. Anderson, Jinxue Wang, and James H. Chetwynd

Air Force Phillips Laboratory/GPOS, Hanscom AFB, MA 01731

1. Introduction

MODTRAN, the Moderate Resolution Atmospheric Radiance and Transmittance Model, encompasses all the capabilities of LOWTRAN 7 (*Kneizys et al.*, 1988), the widely used 20 cm^{-1} resolution radiance code, but incorporates a much more sensitive molecular band model with 2 cm^{-1} resolution. The band model is based directly on the HITRAN spectral line compilation, including both temperature and pressure (Voigt line shape) dependencies. The 2 cm^{-1} spectral resolution of the MODTRAN band model is based on the original development of Berk, Bernstein, and Robertson (*Berk et al.*, 1989). With the expected release of HITRAN94 data base at the end of 1994, MODTRAN will be immediately updated to accommodate new spectroscopy. MODTRAN contains many important elements that other band model based radiative transfer codes do not incorporate. It shares with FASCODE: spherical geometry, single and multiple scattering (Rayleigh, Mie), default atmospheric profile descriptors (gases, aerosols, clouds, fogs, and rain), and molecular continua (H_2O, CO_2, O_3, O_2, N_2). In addition, it can calculate the solar/lunar direct and scattered radiation. MODTRAN3 was released to the general public in November 1994. It has several important features that the previous version, MODTRAN2, does not have. Chloro-fluorocarbon (CFC) and related heavy molecules (whose spectroscopic properties first appear on the HITRAN92 data base as temperature-dependent cross sections) have been incorporated into pseudo-band models, with provision for using both default and user supplied profiles. The addition of SO_2 and NO_2 in the UV, along with upgraded ozone Chappuis bands in the visible is also part of MODTRAN3. An improved multiple scattering algorithm, the DIScrete Ordinate Radiative Transfer (DISORT) (*Stamnes et al.*, 1988), has also been incorporated into MODTRAN3 (*Stamnes*, 1994). MODTRAN is very fast; simple timing runs of MODTRAN3 .vs. FASCOD3 show an improvement of more than a factor of 100 for a typical 500 cm^{-1} spectral interval and comparable vertical layering. Speed is an important consideration in heating/cooling rates calculations, where a large number of radiative transfer calculations are needed. The MODTRAN3 used in this study is based on HITRAN92, but as mentioned above, it will be upgraded to HITRAN94 upon its release at the end of 1994.

MODTRAN has been adopted by some researchers in the AVIRIS program as one radiative transfer code to derive surface reflectance from AVIRIS measurements. The accuracy of the code is very important because any errors in the radiative transfer calculation will directly translate into errors in the derived surface reflectance. In this paper, the new solar irradiance calculated by Kurucz (*Kurucz*, 1994), which is adopted in MODTRAN3, will be presented. Recent validations of MODTRAN3 with airborne high resolution interferometer measurements over ocean will be discussed. Good agreement between model calculations and measurements was achieved.

2. New High Resolution Solar Irradiance in MODTRAN3

An error in the solar irradiance data of MODTRAN2 was discovered by Green and Gao in 1993 (*Green and Gao*, 1993). They also proposed an update based on the Neckels and Labs continuum spectrum (*Neckels et al.*, 1984). In MODTRAN3, we adopted a new solar irradiance calculated by Kurucz. The resolution of solar irradiance is an input parameter in the MODTRAN3 control file 'tape5', and can be changed based on user requirements. Fig. 1. shows the solar irradiance at the top of the atmosphere and the transmitted solar irradiance calculated by MODTRAN3 and degraded to the average

resolution of AVIRIS from 0.4 - 2.4 μm (25,000 - 4167 cm^{-1}) of about 100.0 cm^{-1}. It seems that the problems with the old solar irradiance in MODTRAN2 discussed by Green and Gao are fixed in this new solar irradiance.

3. Comparisons of MODTRAN3 Calculations with Airborne Michelson Interferometer Measurements During Daytime

The data used for the validation of MODTRAN3 during daytime is the down-looking spectra taken by the High-resolution Interferometer Sounder (HIS) of CIMSS/University of Wisconsin (*Revercomb et al.*, 1988) and NWS balloon sonde data over the Eastern Pacific off the California coast on 14 April 1986. The reason for choosing the interferometer measurement over ocean is that the surface reflectance and emissivity are more uniform and easier to define compared with that of land surface. Since our primary objective is to validate MODTRAN3, it is not prudent to introduce the land surface reflectance/emissivity complication by using measurement over land. HIS is a Michelson interferometer, the spectral region from about 600 cm^{-1} to 2700 cm^{-1} is divided into 3 bands (*Revercomb et al.*, 1993). The spectral resolutions and maximum optical path differences of each band for the Eastern Pacific experiment are listed in Table 1.

In the MODTRAN3 calculations, the radiosonde profiles of temperature, H_2O, and O_3 were used. The profiles of the remaining radiatively important species (CO_2, CO, CH_4, N_2O, O_2) were defaulted to the 1976 U.S. Standard Atmosphere (model 6 in MODTRAN3). Heavy molecules, such as CCl_4, $CFC11$, $CFC12$, were not included in this calculation. The high resolution HIS spectra was degraded to 2.0 cm^{-1} using the FASCOD3 triangular scan function with a FWHM of 2.0 cm^{-1}. Figure 2 shows the HIS spectrum, MODTRAN3 calculated spectrum, and residual for the third band in the short IR (2000 cm^{-1} to 2700 cm^{-1}) with and without solar contribution. In the MODTRAN3 calculation with solar contribution, a sea surface albedo of 0.05, solar zenith angle of 38°, and day number of 104 corresponding to the day and time (14 April 1986, 1800 UTC, off the California coast at -120.5 longitude and +34.7 latitude) when the HIS spectra was taken, were used. Clearly much better agreement between model calculation and interferometer measurements was achieved by including the solar contribution. The remaining differences around 2400 cm^{-1} arise from difficulties in the band model parameterization at the sharp CO_2 band edge (*Anderson et al.*, 1994). The large residual close to the edge of HIS band III from 2640 cm^{-1} to 2700 cm^{-1} is likely due to instrument or calibration (*Knuteson and Revercomb, private communication*, 1994).

4. Summary and Conclusions

The new solar irradiance in MODTRAN3 was presented and discussed. Problems with the old solar irradiance in MODTRAN2 were solved. Good agreement between model calculation and airborne high resolution interferometer measurement was achieved. Validation of MODTRAN3 in the solar region and the spectral region of AVIRIS (0.4 - 2.4 μm) is in progress with measurements by the ground-based Solar Radiance Transmission Interferometer (SORTI) developed at the University of Denver (*Murcray, private communication* , Nov. 1994). We expect to show some preliminary results on the validation of MODTRAN3 against SORTI measurements in the solar region at the AVIRIS workshop.

5. Acknowledgments

6. References

Anderson, G. P., J. H. Chetwynd, F. X. Kneizys, L. M. Kimball, L. Bernstein, P. Acharya, A. Berk, D. C. Robertson, L. W. Abreu, E. P. Shettle, "MODTRAN2: Evolution and Applications", *SPIE Proceedings*, Vol. **2222**, 790-799, 1994.

Berk, A., L. S. Bernstein, and D. C. Robertson, "MODTRAN: A Moderate Resolution Model for LOWTRAN 7," GL-TR-89-0122, 1989.

Green, R.O., and Bo-Cai Gao, "A Proposed Update to the Solar Irradiance Spectrum Used in LOWTRAN and MODTRAN," *Summaries of the Fourth Annual JPL Airborne Geoscience Workshop*, October 25-29, 81-84, 1993.

Kneizys, F. X., E. P. Shettle, L. W. Abreu, J. H. Chetwynd, G. P. Anderson, W. O.Gallery, J.   E. Selby, S. A. Clough, "Users Guide to LOWTRAN 7," *AFGL-TR-88-0177*, 1988.

Kurucz, R. L., "The Solar Irradiance by Computation," to appear in *Proc. of the 17th Annual Review Conference on Atmospheric Transmission Models*, 7 June 1994, Geophysics Directorate/Phillips Laboratory, 1994.

Neckles, Heinz, and Dietrich Labs, "The Solar Radiation Between 3300 and 12500 Å.", Sol. Phys., **90**, 205-258, 1984.

Revercomb, H. E., H. Bujis, Hugh B. Howell, D. D. LaPorte, William L. Smith, and L. A. Sromovsky, "Radiometric calibration of IR Fourier transform spectrometers: solution to a problem with the High-Resolution Interferometer Sounder," *Appl. Opt.*, **27**, 3210-3218, 1988.

Revercomb, H. E., R. O. Knuteson, S. C. Lee, "Validation of FASCOD3P Using University of Wisconsin HIS Data," *Technical Report to Phillips Laboratory*, 1993.

Stamnes, K., S.-C. Tsay, W. J. Wiscombe, and K. Jayaweera, "Numerically stable algorithm for discrete-ordinate-method radiative transfer in multiple scattering and emitting layered media," *Appl. Opt.*, **27**, 2502-2509, 1988.

Stamnes, K., *Upgrade of FASCODE and MODTRAN to Full Soar Capability Including Multiple Scattering and Spherical Geometry*, Final Report to Air Force Phillips Laboratory/Geophysics Directorate, University of Alaska, 1994.

Table 1. Spectral resolution and maximum optical path difference of HIS for the Eastern Pacific flight on 14 April 1986 [*Revercomb et al.*, 1993b].

HIS band	Spectral resolution (cm^{-1})	Maximum optical path (cm)
I	0.3640322	1.3735050
II	0.6370564	0.7848598
III	0.6370564	0.7848598
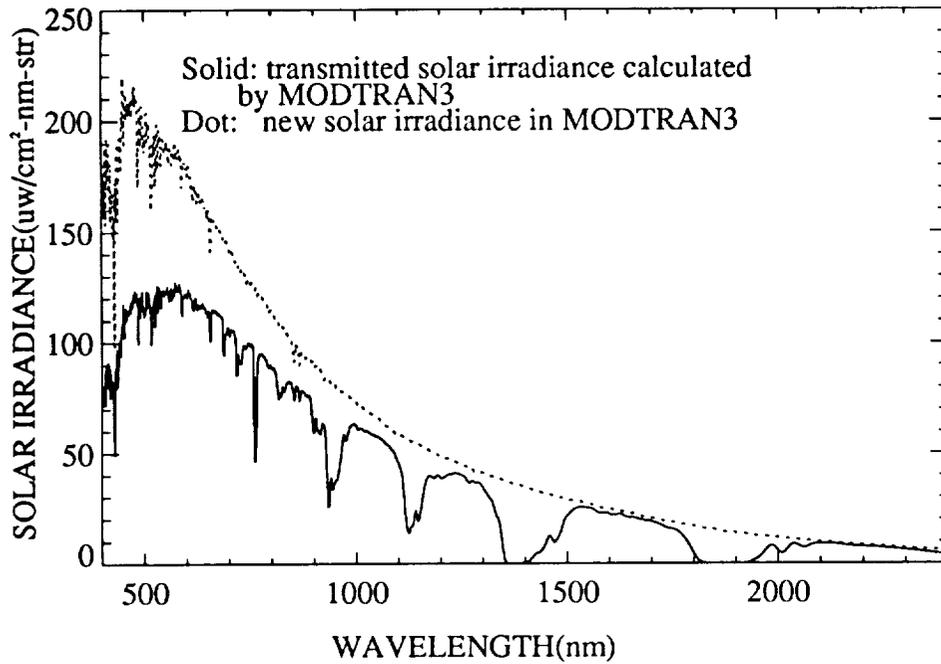
Fig. 1. New solar irradiance in MODTRAN3 based on the calculation by Kurucz.
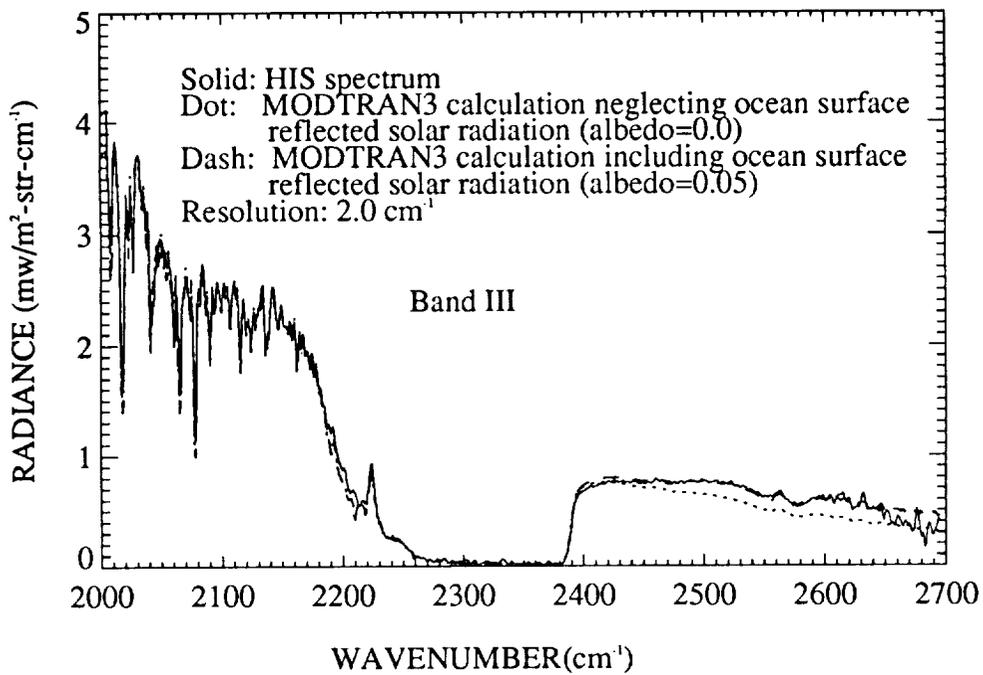
Fig. 2. Comparison between HIS measurement and MODTRAN3 calculations with and without solar contribution.

8

CHARACTERISTICS OF THE HYDICE SENSOR

R.W. Basedow and E. Zalewski
Hughes Danbury Optical Systems

Abstract

In 1992, in an effort to significantly improve knowledge in the field of hyperspectral imagery, the Naval Research Laboratories defined a set of requirements for a new generation sensor. Construction of this instrument, designated HYDICE, has recently been completed at Hughes Danbury Optical Systems. It is currently being flight tested on a Convair 580 operated by ERIM. This paper reports on some of the performance parameters measured to date. The majority of these are derived from laboratory test data. Optomechanical parameters include MTF, spatial co-registration, 'smile', spectral profile and spectral calibration. Detector-related parameters include system responsivity, signal to noise ratio, radiometric stability and gain linearity. The results are compared with the original system performance predictions.

QUANTITATIVE REMOTE SENSING OF AMMONIUM MINERALS, CEDAR MOUNTAINS, ESMERALDA COUNTY, NEVADA

William M. Baugh and Fred A. Kruse
Center for the Study of Earth from Space (CSES), CIRES,
University of Colorado, Campus Box 216, Boulder, CO, USA, 80309

1.   INTRODUCTION

Mineral-bound ammonium (NH_4^+) was discovered by the U.S. Geological Survey in the southern Cedar Mountains of Esmeralda County, Nevada in 1989. At 10 km in length, this site is 100 times larger than any previously known occurrence in volcanic rocks (Krohn, 1989). The ammonium occurs in two hydrothermally altered, crystal-rich rhyolitic tuff units of Oligocene age, and is both structurally and stratigraphically controlled. This research uses Advanced Visible/Infrared Imaging Spectrometer (AVIRIS) data to quantitatively map the mineral-bound ammonium (buddingtonite) concentration in the altered volcanic rocks.

Naturally occurring mineral-bound ammonium is fairly rare; however, it has been found to occur in gold-bearing hydrothermal deposits (Krohn et al., 1988). Because of this association, it is thought that ammonium may be a useful tool in exploration for gold and other metal deposits.

Mineral-bound ammonium is produced when an ammonium ion (NH_4^+) replaces the alkali cation site (usually K^+) in the crystal structure of silicate minerals such as feldspars, micas and clays (Krohn et al, 1988). Buddingtonite is an ammonium feldspar. The ammonium originates in buried organic plant matter and is transported to the host rock by hydrothermal fluids (Hallam and Eugster, 1976). Ammonium alteration does not produce visible changes in the rock, and it is barely detectable with standard x-ray diffraction methods. It is clearly identified, however, by absorption features in short wave-infrared (SWIR) wavelengths (2.0 - 2.5 μm). The ammonium absorption features are believed to be caused by N-H vibrational modes and are analogous to hydroxyl (O-H) vibrational modes, only shifted slightly in wavelength (Krohn et al., 1988). Buddingtonite absorption features in the near- and SWIR lie at 1.56, 2.02 and 2.12 μm. The feature at 2.12 μm is the strongest of the three and is the only one used in this study. The southern Cedar Mountains are sparsely vegetated and are an ideal site for a remote sensing study.

2.   LABORATORY MEASUREMENTS

Nitrogen content of 54 samples was determined by a combustion (Dumas) technique (Tabatabai and Bremner, 1991). The weight percent nitrogen is converted to percent ammonium by multiplying it by 1.286 (Kydd and Levinson, 1986). This method assumes that there is no other source for nitrogen in the rock.

The depth of the 2.12 μm ammonium absorption feature was measured on continuum-removed PIMA spectra for the same 54 samples. The PIMA is a hand-held field spectrometer that covers the range from 1.3 to 2.5 μm. It uses an internal light source so spectra may be acquired under cloud cover or even at night. An internal reflectance standard is scanned after each spectrum is taken to provide calibration.

The 2.12 μm, continuum-removed band depths and corresponding ammonium concentrations were plotted, and a linear relationship was observed. The equation of this linear relationship was used as a quantitative calibration for the remotely-sensed

spectra. With it, appropriate continuum-removed band depths can be converted to ammonium concentrations (Felzer, 1990).

3. DATA PROCESSING

AVIRIS data acquired during July 1990 were processed to create quantitative ammonium concentration maps. Field spectra of light and dark ground-targets were used to calibrate the data to reflectance with the empirical line method (Roberts et al., 1985). Buddingtonite occurrences and relative concentrations were established using a spectral matching program called the Spectral Angle Mapper (SAM) (Kruse et al., 1993a). The program determines the similarity of a test spectrum (from an AVIRIS pixel) to a reference spectrum (laboratory spectrum). The spectra are treated as vectors and a small angle between the spectral vectors indicates a better match. Output from the SAM consists of a gray scale image where higher values denote a better match with buddingtonite spectra.

To make quantitative measurements of buddingtonite concentration, band depth values from continuum-removed AVIRIS spectra had to found. Continuum removal was achieved with a prototype expert system called the General Use Expert System for Spectra (GUESS) (Kruse et al., 1993b). Depth of the buddingtonite absorption feature was measured at band 190 (2.119 μm) on the continuum-removed AVIRIS data and an image consisting of band depth values was produced.

To create an image showing ammonium concentration, the linear calibration was applied to the band depth image. The equation is:

$$Y = 13865X - 347.93$$

where X is the input band depth "DN" value and Y is the output ammonium concentration in ppm. After applying this equation to the AVIRIS data, each pixel is converted to an ammonium concentration in ppm. The ammonium concentration image was contoured to produce quantitative ammonium concentration maps (Figure 1).

On the concentration map, a few anomalously high ammonium values were indicated in a region that was known from field work to be barren. Inspection of several AVIRIS spectra from this region showed no buddingtonite features. The SAM results were used to construct a filter that masked these false high-ammonium values.

4. FIELD VERIFICATION

To test the accuracy of the AVIRIS concentration map, spectra were taken in the field with the PIMA spectrometer and a ground-truth concentration map was produced. An area covering about 620 AVIRIS pixels that showed the greatest ammonium concentration was chosen. In the field, spectra were measured on fresh and weathered surfaces on a regular grid of 40 m. Ammonium concentrations were derived using the linear calibration; and the ground-truth concentration map was contoured for comparison with the AVIRIS concentration map of the same area (Figure 1).

5. DISCUSSION

Comparison of the ground-truth concentration map and the AVIRIS concentration map demonstrates that ammonium can be quantitatively mapped with AVIRIS data (Figure 1). While the two maps are not identical, they do match in both magnitude and pattern. The AVIRIS map indicates that the region is dominantly greater than 4000 ppm and increases to 5500 ppm in the center. The ground-truth map shows less of the highest concentrations, yet it confirms that the region is dominantly greater than 4000 ppm and increases to 5500 ppm in the center. It must be remembered

that the ground truth map was sampled at points every 40 m while AVIRIS sampled every 20 m and averaged spectra from an approximately 400 m^2 area. We therefore may expect AVIRIS to give a more accurate representation of the buddingtonite concentration in this zone because it is not affected by the very small-scale variations that could deceive the pin-point ground sampling.

An interesting feature that appears on both maps is a small zone of no buddingtonite. It was masked by the SAM filter on the AVIRIS image and showed no ammonium on the ground survey. Inspection of the area revealed a 20 m by 5 m piece of ammonium-free rock that was faulted in place.

On a larger scale, AVIRIS showed that the buddingtonite occurs in two of four exposed volcanic tuff units, and forms isolated zones along the western mountain front. Within the ammonium zones, areas of high and low concentration are generally linear and are believed to correspond to fracture patterns. It is thought that these fractures were the passages along which ammonium-bearing hydrothermal fluids once flowed.

Field mapping indicates a relationship between buddingtonite and northeast-striking, high angle, dip-slip basin and range(?) faults. All of the high-ammonium zones inspected were on the northern, down-dropped side of these dip-slip faults. Within the buddingtonite zones the rock is broken by closely spaced fractures that are sub-parallel to the northeast striking faults.

Ammonium Ridge Area
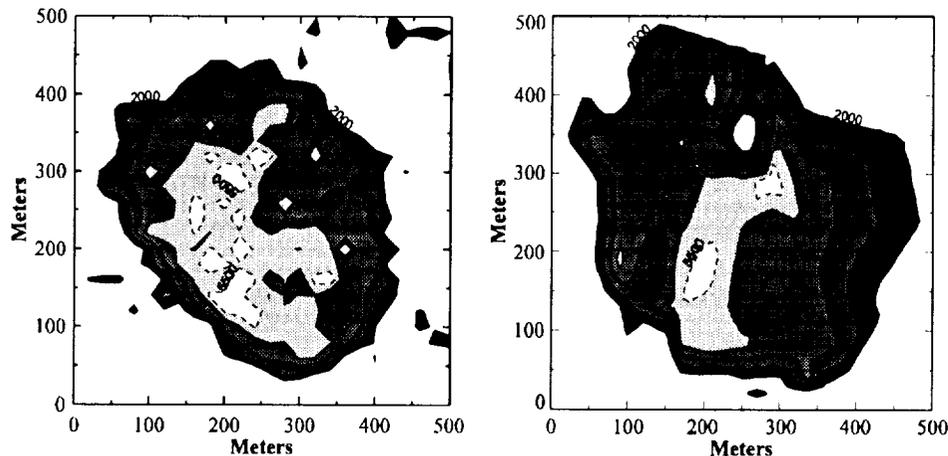
Figure1. AVIRIS (left) and ground-truth (right) NH$_4$ concentration maps: Contour interval is 1000 ppm, dashed contours are 5500 ppm

6. CONCLUSIONS

AVIRIS is capable of quantitatively mapping buddingtonite concentration in the southern Cedar Mountains, Nevada. This is accomplished by producing a calibration equation based on laboratory analysis and applying it to appropriately processed AVIRIS data. Buddingtonite is both stratigraphically and structurally controlled at this site, and is found commonly in concentrations up to 6000 ppm.

This method may be applicable to other hydroxyl minerals, found in hydrothermally altered rocks, that contain absorption features in the SWIR. Besides buddingtonite, other examples include alunite, kaolinite and jarosite. If these can be quantitatively mapped, not only can we determine the geometry of a fossil hot spring system, but we can infer much about the chemistry of the hydrothermal fluids that affected different parts of the system. Alunite would indicate low pH and more

13

oxidizing fluids, while buddingtonite denotes high pH and more reducing fluids. Kaolinite is formed by oxidizing fluids of an intermediate pH (Krohn, et al, 1988). Knowledge of fluid chemistry in fossil hot springs can aid in their study and be valuable in choosing prospecting sites.

7.   REFERENCES

Felzer, B.S., 1990, *Quantitative reflectance spectroscopy of buddingtonite from the Cuprite Mining District, Nevada*, Unpublished M. S. Thesis, University of Colorado, Boulder, 137p.

Hallam, M. and H.P. Eugster, 1976, "Ammonium silicate stability relations," *Contrib. Mineral. Petrol.*, vol. 57, pp. 227-244.

Krohn, M.D., S.P. Altaner, and D.O. Hayba, 1988, "Distribution of ammonium minerals at Hg/Au-bearing hot springs deposits: Initial evidence from near-infrared spectral properties," in Schaffer, R.W., Cooper, J.J., and Vikre, P.G., eds., *Proceedings of the bulk minable precious metal deposits of western United States symposium*, Geol Soc. Nevada, pp. 661-679.

Krohn, M.D., 1989, "Preliminary description of a mineral-bound ammonium locality in the Cedar Mountains, Esmeralda County, Nevada," *U.S. Geological Survey open-file-report #89-637.*

Kruse, F.A., K.S. Kierein-Young, and J.W. Boardman, 1990, "Mineral mapping at Cuprite, Nevada with a 63 channel imaging spectrometer," *Photogramm. Eng. Remote Sens.*, vol. 56, pp. 83-92.

Kruse, F.A., A.B. Lefkoff, J.W. Boardman, K.B. Heidebrecht, A.T. Shapiro, P.J. Barloon, and A.F.H. Goetz, 1993a, "The spectral image processing system (SIPS) - interactive visualization and analysis of imaging spectrometer data," *Remote Sens. Environ.*, vol. 44, pp. 145-163.

Kruse, F.A., A.B. Lefkoff, and J.B. Dietz, 1993b, "Expert system-based mineral mapping in northern Death Valley, California/Nevada, using the airborne visible/infrared imaging spectrometer (AVIRIS)," *Remote Sens. Environ.*, vol. 44, pp. 309-336.

Kydd, R.A., and A.A. Levinson, 1986, "Ammonium halos in lithogeochemical exploration for gold at the Horse canyon carbonate hosted deposit, Nevada, U.S.A.: use and limitations," *Applied Geochemistry*, vol. 1, pp. 407-417.

Roberts, D.A., Y. Yamaguchi, and R.J.P. Lyon, 1985, "Calibration of airborne imaging spectrometer data to percent reflectance using field spectral measurements," in *Proceedings, Nineteenth International Symposium on Remote Sensing of Environment*, Ann Arbor, Michigan, October 21-25, 1985.

Tabatabai, M.A., and J.M. Bremner, 1991, "Automated instruments for determination of total carbon, nitrogen, and sulfur in soils by combustion techniques," in Smith, K.A., ed., *Soil Analysis Modern Instrumental Techniques Second Edition*, Marcel Dekker, Inc., New York, pp. 261-286.

CNR LARA PROJECT, ITALY: AIRBORNE LABORATORY FOR ENVIRONMENTAL RESEARCH

R. Bianchi, R. M. Cavalli, L. Fiumi, C.M. Marino, S. Pignatti

CNR, Progetto LARA
00040 Pomezia (Roma), Italy

The increasing interest for the environmental problems and the study of the impact on the environment due to antropic activity produced an enhancement of remote sensing applications. The Italian National Research Council (CNR) established a new laboratory for airborne hyperspectral imaging, the LARA Project (Laboratorio Aereo per Ricerche Ambientali - Airborne Laboratory for Environmental Research), equipping its airborne laboratory, a CASA-212, mainly with the Daedalus AA5000 MIVIS (Multispectral Infrared and Visible Imaging Spectrometer) instrument. MIVIS's channels spectral bandwidths and locations are chosen to meet the needs of scientific research for advanced applications of remote sensing data. MIVIS can make significant contributions to solving problems in many diverse areas such as geologic exploration, land use studies, mineralogy, agricultural crop studies, energy loss analysis, pollution assessment, vulcanology, forest fire management and others. The broad spectral range and the many discrete narrow channels of MIVIS provide a fine quantization of spectral information that permits accurate definition of absorption features from a variety of materials, allowing the extraction of chemical and physical information of our environment. The availability of a such hyperspectral imager, that will operate mainly in the Mediterranean area, at the present represents a unique opportunity for those who are involved on environmental studies and land-management to collect systematically large-scale and high spectral/spatial resolution data of this part of the world. Nevertheless, MIVIS deployments will touch other parts of the world, where a major interest from the international scientific community is present.

MIVIS is a sensor with 4 spectrometers, that simultaneously sample and record 102 spectral bands. It is designed to collect radiation from the earth's surface in the Visible/Near-IR (20 channels from 0.43 - 0.83 μm), Near-IR (8 channels from 1.15 - 1.55 μm), Mid-IR (64 channels from 1.985 - 2.479 μm), and Thermal-IR (10 channels from 8.21 - 12.7 μm).

The MIVIS technical characteristics are (Daedalus Ent., 1994):
- *Two built in reference sources thermally controlled in the range 15°C below and 45°C above ambient temperature*
- *Spatial registration of all spectral bands due to a common field stop optical design (2.0 mrad IFOV)*
- *Sample rate (angular step): 1.64 mrad*
- *Digitized Field of View (FOV): 71.059°*
- *12 bits data quantization*
- *Pixels per scan line: 755*
- *Scan rotational speeds: 25, 16.7, 12.5, 8.3 and 6.25 scans/sec*
- *Computer aided data quality check for all 102 channels in real time*
- *Thermally compensated optical-mechanical design*
- *Large dynamic range: 1200°C maximum scene temperature*
- *Computer interfaced data recording system. VHS cassette media (10.2 Gbytes capacity)*
- *Built in aircraft Position and Attitude System (PAS) using a GPS receiver, a roll/pitch gyro and a flux gate compass for aircraft heading. Real time aircraft roll correction (±15°)*
- *Simple operator interface using a touch screen display and menu system*
- *Built in system monitors: Moving Window Display on CRT, and oscilloscope*
- *Automatic built in subsystems testing*

The complete scanner system consists of an electro-optical sensor assembly (Scan Head/Spectrometer) and four electronics chassis interconnected by electrical cables. The Scan Head/Spectrometer component is mounted to have a clear opening through the aircraft skin to the ground below. Data from the sensors is amplified in the spectrometer and passed to the electronics where it is digitized, combined with ancillary data and recorded. The electronics chassis contains the operator interface, the GPS receiver and other supporting subsystems. The principle MIVIS subsystem components are: Scan Head and Spectrometer, Moving Window Display and Monitor, Digitizer, VLDS (Very Large Data Store) Tape Recorder and the Power Distributor.

Three of the MIVIS subsystems contain embedded control computers that supervise and monitor operations for which that subsystem is responsible. Commands and status information is passed between these three subsystems through a local communication network. System startup automatically initiates a series of self tests to verify that the system is ready for use.

The Scan Head consists of the optical elements comprising the primary collecting telescope, a rotating scan mirror, the motor-encoder assembly, two controlled thermal references, and an Invar^R steel and aluminum structure. The scene energy collected by the scan mirror is focused by a paraboloid and directed onto the IFOV defining aperture. Energy passing through the aperture is collimated and reflected out of the scan head to the spectrometer. The two reference sources contained within the scan head are viewed once per scan mirror revolution.

The Spectrometer accepts the collimated energy from the Scan Head and divides it into 4 optical ports. Each port contains a diffraction grating, imaging lens, detector array and preamplifier electronics. Each spectrometer port uses optical materials, coatings and detectors that are optimized for its specific wavelength region of operation. Selectable electronic gains and/or optical attenuations are implemented in the spectrometer to maximize SNR for a wide range of input radiance levels. The output of the spectrometer is 102 electrical signals, each from a different detector, representing, as already seen, a segment of the spectrum between 0.43 and 12.7 μm.

The Moving Window Display (MWD) contains a CRT display monitor assembly, a wave-form monitoring oscilloscope, and a DC to AC power inverter. The principal function of this unit is to provide a visual real time image of the scene being recorded to the operator. This function serves to assess areal coverage, monitor the system integrity and provide an estimate of data quality. The MWD is capable of operating in either real time during the data collection, or after flight in data playback. Display functions are controlled by touch screen menu selections from digitizer system component.

The principle Digitizer function is to provide 102 channels of analog to 12 bit digital conversion, format this data and write it to tape. This process is synchronized to the scan mirror rotation by signals from the optical encoder on the motor. All Digitizer functions are supervised by an embedded computer and control software. The Digitizer contains the Touch Screen which is the principal interface to the instrument.The touch screen and display menu concept makes the control and monitoring of a such complex instrument relatively simple. Menus are presented on the screen to the operator, identifying what action will occur when a designed area on the screen is touched.

During recording time the operator through the MWD monitor continously check the Dynamic Range status of each channel in the form of a matrix of 102 numbers (one for each channel). The channel number will be illuminated when any of the above mentioned dynamic range errors occur.

The MIVIS system records all data for post flight production and analysis by means of an image processing system (MIDAS). The VLDS recorder is a digital magnetic tape drive using helical scan technology and tape cassettes similar to the home VCR. It enables MIVIS to store a large quantity of data (10.2 Gbytes per cassette) at high speed.

The MIDAS (Multispectral Interactive Data Analysis System) system has been developed to efficiently preprocess, analyze and visualize MIVIS data, and is written for portability to a large number of computer platforms. It has been designed for use on a wide variety of UNIX workstations that support X-Window System and the Application Visualization System (AVS) graphical programming environment. LARA project hosted MIDAS software on a UNIX Silicon Graphics SGI 4D/420VGXT based in Pomezia, a town close to Rome, in a configuration that is synthetically listed below:
- *Two 40 MHz CPUs*
- *128 Mbytes main memory*
- *Four 1.1 Gbytes IPI high-speed disks*
- *Two 1.2 Gbytes SCSI disks*
- *VLDS helical scan cartridge tape system*
- *Two 8 mm Exabyte tape drives (5 Gbytes capacity each)*
- *One 8 mm Exabyte tape drive (10 Gbytes capacity)*
- *1/4 inch cartridge tape drive (150 Mbytes capacity)*
- *Kodak Model XL-7700 film recorder*

A MIDAS Production Processor handles data ingestion, standardized processing (which include radiometric, geometric or atmospheric calibration), reformatting, archiving and dissemination. Raw data from MIVIS are ingested with the VLDS helical scan cartridge tape system and backuped on the 10 Gbytes 8mm Exabyte tape, while preprocessing, archiving, dissemination, and alternative data ingestion is via the two 5 Gbytes 8 mm Exabyte tape drives and the 1/4 inch cartridge tape drive.

The big capacity of this particular hardware and software configuration is the use of a flexible three-dimensional data structure that allows to rapidly move information from high speed disks to memory, so that arbitrarily large data volumes may be processed or interactively visualized (30 frames/sec) without regard to memory limitations. This allows a sensitive compression of times for ingestion, reformatting, validation and preprocessing of MIVIS data before their distribution. In fact, all modules in MIDAS handle hyperspectral data in the Volume Image Management System (VIMS) format greatly improving the system performance. MIDAS organizes data into volume elements (voxels), and uses the voxel bricking (an extension of the planar processing pixel tiling) reducing the disk thrashing problem (TASC, 1993).

Besides MIVIS data production, MIDAS offers to users a very powerful system for hyperspectral image processing. MIDAS provide all the standard functions of a software dedicated to image processing, but more, offer software tools to analyze data in the spectral domain and allow the possibility to develop new algorithms for particular user's analysis.

During the second half of last July 1994 LARA Project, in the framework of the final MIVIS/MIDAS testing and tuning, held a MIVIS test deployment in Sicily. The deployment was successful and more than 56 Gbytes of MIVIS data were collected in almost 5 hours of VLDS recording time.

This first MIVIS deployment has been carried out in Sicily in cooperation with national and international institutions on a variety of sites, including active volcanoes (Mt. Etna and Eolian Islands), coastlines (Gela, Acireale, Taormina), ocean (Messina Straits and Marsala lagoon), vegetated areas (Mt. Etna slopes), waste discharges (Acireale), and archeological sites (Selinunte, Alesa and Acireale).

During MIVIS data acquisition a contemporaneous ground data acquisition campaign has been carried out for most sites. For the surveys on volcanic areas CNR/IIV offered its ground support logistics in making measurements of plume SO_2 with its portable COSPEC instruments, while JPL, CNR/CSGDSA, ING, OGUM, and the Universtity of Palermo people launched radiosondes to measure H_2O profiles, used anemometers for wind speeds, a GER portable spectrometer to measure ground radiances, radiation thermometers and thermocouples for measurements of ground temperatures. CNR/IROE deployed by helicopter its FLIDAR instrument contemporaneously with MIVIS on Gela's coastline and on Mt. Etna's beech-woods. CNR/CST and the University

of Palermo made sea truths measurements with scientific boats on the Straits of Messina and inside/outside the Lagoon of Marsala.

After the Sicily 1994 MIVIS deployment an evaluation of MIVIS inflight performances has been done for thermal channels making statistics on a portion of the ocean West of Stromboli Island (6771 pixels). In Figure 1 the inflight NEΔT is shown.
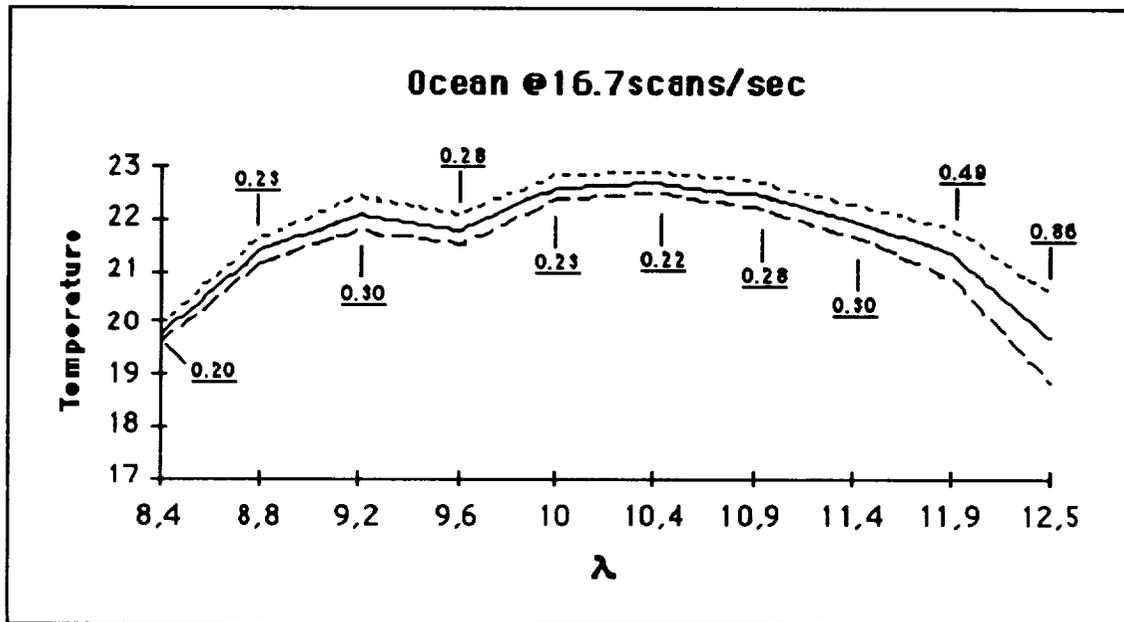
Figure 1 - Inflight NEΔT (underlined numbers on the plot) computed for the 10 MIVIS thermal channels on a portion of ocean target (6771 pixels), West of Stromboli Island.

Selected scenes of the Sicily 1994 MIVIS data will be extracted for general distribution under request starting from 1995.

REFERENCES

DAEDALUS Enterprises, 1994, *AA5000 MIVIS Operator Manual*, 6 volumes.
TASC Company, 1993, *MIDAS Data Center User's Manual*, 2 volumes.

USING DARK CURRENT DATA TO ESTIMATE AVIRIS NOISE COVARIANCE AND IMPROVE SPECTRAL ANALYSES

Joseph W. Boardman

Center for the Study of Earth from Space
Cooperative Institute for Research in the Environmental Sciences
Campus Box 216 University of Colorado
Boulder, CO 80309-0216

1.   INTRODUCTION AND RATIONALE

Starting in 1994, all AVIRIS data distributions include a new product useful for quantification and modeling of the noise in the reported radiance data. The "postcal" file contains approximately 100 lines of dark current data collected at the end of each data acquisition run. In essence this is a regular spectral-image cube, with 614 samples, 100 lines and 224 channels, collected with a closed shutter. Since there is no incident radiance signal, the recorded DN measure only the DC signal level and the noise in the system. Similar dark current measurements, made at the end of each line are used, with a 100 line moving average, to remove the DC signal offset. Therefore, the pixel-by-pixel fluctuations about the mean of this dark current image provide an excellent model for the additive noise that is present in AVIRIS reported radiance data. The 61,400 dark current spectra can be used to calculate the noise levels in each channel and the noise covariance matrix. Both of these noise parameters should be used to improve spectral processing techniques. Some processing techniques, such as spectral curve fitting, will benefit from a robust estimate of the channel-dependent noise levels. Other techniques, such as automated unmixing and classification, will be improved by the stable and scene-independent noise covariance estimate. Future imaging spectrometry systems should have a similar ability to record dark current data, permitting this noise characterization and modeling.

2.   DARK CURRENT DATA PROCESSING

2.1   Estimation of Noise Level and Covariance in Units of Raw DN

The postcal file reports 100 lines of dark current data, each with a full 614 samples and 224 spectral channels in units of raw DN. A measure of the background constant, or DC, signal offset is given by the mean of these spectra. Figure 1 shows one such mean for a 1994 scene. This mean is the average of the full 100 lines, similar to the offset spectrum subtracted in the standard AVIRIS data processing. An estimate of the noise level in the data is given by the standard deviation of the dark current data, with respect to the mean spectrum shown in Figure 1. The standard deviation spectrum for the same scene is shown in Figure 2.

The acquisition of over 60,000 dark current spectra permits a robust estimation of the full, 224-by-224 noise covariance matrix. The data are processed as 224-channel multivariate signals and covariance about the mean is calculated in the standard fashion. Figures 3 and 4 show the intriguing patterns evident in the dark current covariance images. These images are linearly stretched so that -0.02 and 0.15 correspond to black and white. Since these data are recorded with no incident signal, this covariance matrix

provides our best model for the noise statistics in the radiance data. Several interesting features are worthy of discussion.

First, note the overall similarity between the two images. These are from two different AVIRIS data acquisition runs, more than two months apart in the summer of 1994. The high degree of similarity is a testament to the stability of AVIRIS, even on the sub-DN level, throughout a flight season.

The patterns in the covariance matrix can be used to reveal and to understand the sources and the properties of the noise in AVIRIS data. The blocks defined by the four spectrometers are evident, as is a complex inter-relationship among their various sources of noise. The diagonal stripes and "plaid" effects reflect noise sources with varying frequencies and amplitudes, affecting the four spectrometers differently.

2.2 Conversion to Apparent Reflectance

Analysts typically process apparent reflectance data, not raw DN. So the noise model must be converted from units of raw DN to those of apparent reflectance. This is done in two steps: 1) DN to spectral radiance; 2) spectral radiance to apparent reflectance. The dark current data are reported as raw DN and must be multiplied by appropriate scale factors to convert them to units of spectral radiance. The scale factors, included in the AVIRIS radiometric calibration file, are the product of a constant factor of 500 and a spectrally-variable radiometric calibration function.

Conversion from spectral radiance to apparent reflectance is done by deriving the appropriate scale factors that match the reduction of the actual image data to apparent reflectance. Several methods (Gao et al., 1993; Green et al., 1993) are now available to reduce observed spectral radiance to apparent surface reflectance, accounting for atmospheric effects on a pixel-by-pixel basis. These data were reduced with ATREM (Gao et al., 1993) resulting in an almost a linear conversion. Suitable scale factors for the noise model are determined through a linear regression of the apparent reflectance and radiance data sets. The best-fit scale factors are then used to convert the radiance noise model to apparent reflectance units. The linear regressions for bands 22 and 60 are shown in Figures 5 and 6. Although the pixel-by-pixel water vapor removal has introduced some non-linearity in certain channels, the scale factors are still well-determined from the slopes of the scatter plots. Once reduced to apparent reflectance, the noise standard deviations can be used to estimate signal to noise ratios. Figure 7 shows the estimated signal to noise spectrum, for the particular scene, at a reference reflectance of 0.5.

3. APPLICATION TO SPECTRAL ANALYSES AND CONCLUSIONS

The noise modeling outlined above can be used to improve quantitative numerical analysis of AVIRIS spectra. The dark current standard deviation spectrum is a noise level estimate that should be used as an inverse weighting function. It will improve curve fitting procedures such as unmixing and spectral feature matching. In addition, the dark current covariance matrix is an estimate of the noise covariance in the observed data. This matrix can be used to precondition the data, through a series of affine transformations, to whiten the noise (Green et al., 1988; Lee et al., 1990). The noise-whitened data has unit-variance noise in all spectral channels and no correlation of noise between

20

channels. This noise modeling permits direct quantification of spectral discrimination and unmixing precision.

4. ACKNOWLEDGMENTS

5. REFERENCES

Gao, B-C, K. B. Heidebrecht and A. F. H. Goetz, 1993, Derivation of Scaled Surface Reflectances from AVIRIS Data, *Remote Sensing of Environment*, vol. 44, no. 2, pp. 165-178.

Green, A. A., M. Berman, P. Switzer and M. D. Craig, 1988, A Transformation for Ordering Multispectral Data in Terms of Image Quality with Implications for Noise Removal", *IEEE Transactions on Geoscience and Remote Sensing*, vol. 26, no. 1, pp. 65-74.

Green, R.O., J. E. Conel and D. A. Roberts, 1993, Estimation of Aerosol Optical Depth and Additional Parameters for the Calculation of Apparent Surface Reflectance form Radiance Measured by the Airborne Visible/Infrared Imaging Spectrometer, *4th Annual JPL Airborne Geoscience Workshop*, JPL Pub. 93-26, v. 1, pp. 73-76.

Lee, J.B., A.S. Woodyatt and M. Berman, Enhancement of High Spectral Resolution Remote Sensing Data by a Noise-Adjusted Principal Components Transform, *IEEE Transactions on Geoscience and Remote Sensing*, vol. 28, no. 3, pp. 295-304.
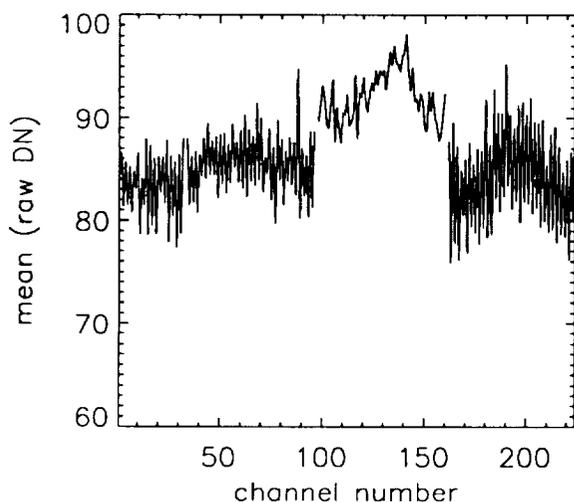
Figure 1. Mean of the dark current spectra.
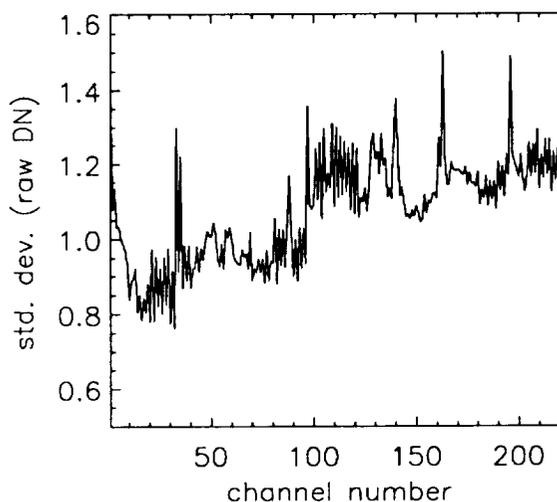
Figure 2. Standard deviation of the dark current.
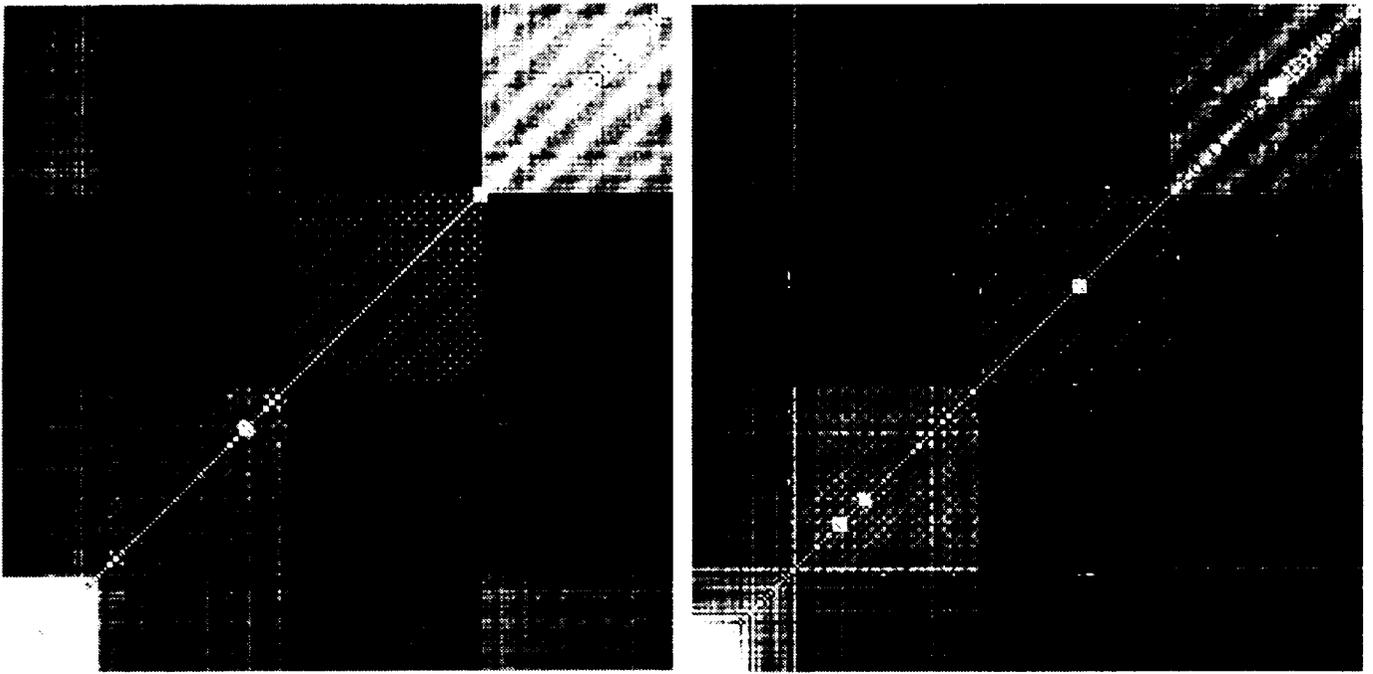
Figures 3 and 4. Dark current covariance images for two different AVIRIS runs.
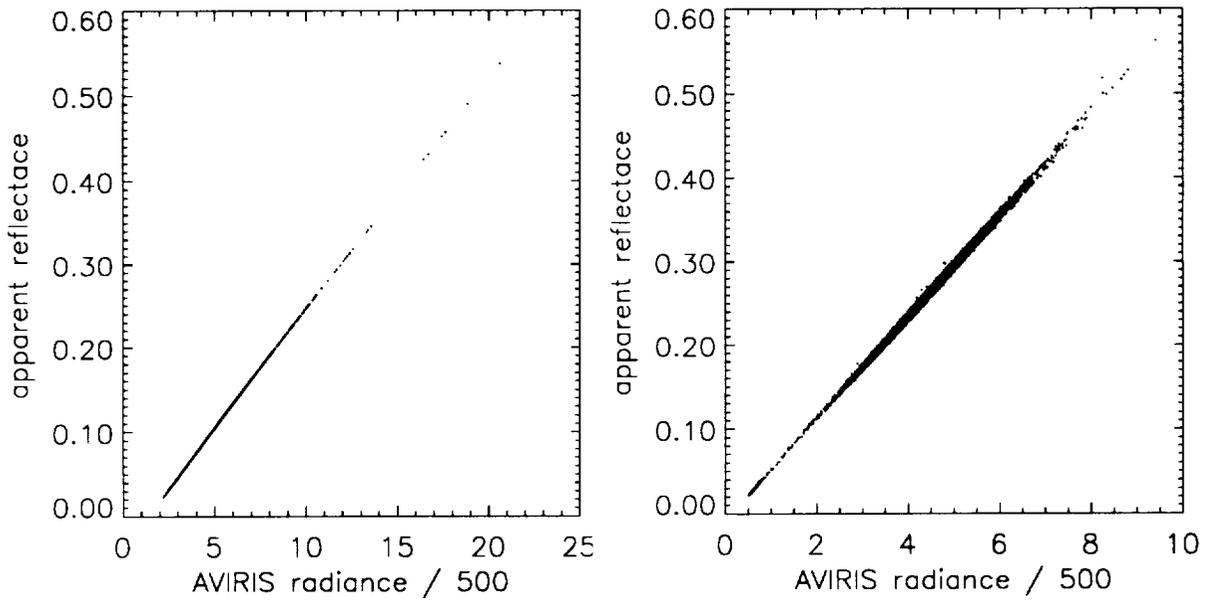
Figures 5 and 6. Scatterplots of apparent reflectance versus observed radiance, bands 22 and 60.
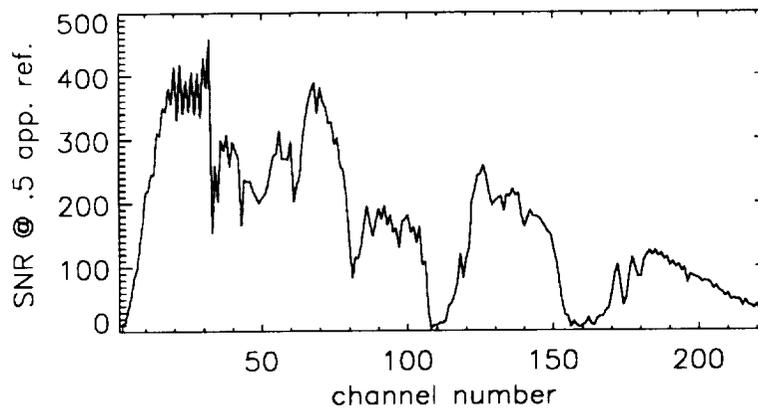
Figure 7. Predicted signal-to-noise ratio for the particular AVIRIS scene, based on a nominal 0.5 reflectance target.

MAPPING TARGET SIGNATURES
VIA PARTIAL UNMIXING OF AVIRIS DATA

Joseph W. Boardman[1], Fred A. Kruse[1,2], Robert O. Green[3]

1 Center for the Study of Earth from Space
Cooperative Institute for Research in the Environmental Sciences
Campus Box 216 University of Colorado, Boulder, CO 80309-0216

2 Geological Sciences Department
Campus Box 250 University of Colorado, Boulder, CO 80309-0250

3 Jet Propulsion Laboratory, California Institute of Technology, 4800 Oak Grove Dr.
Pasadena, CA 91109

1.   INTRODUCTION AND RATIONALE

A complete spectral unmixing of a complicated AVIRIS scene may not always be possible or even desired. High quality data of spectrally complex areas are very high dimensional and are consequently difficult to fully unravel. Partial unmixing provides a method of solving only that fraction of the data inversion problem that directly relates to the specific goals of the investigation. Many applications of imaging spectrometry can be cast in the form of the following question: "Are my target signatures present in the scene, and if so, how much of each target material is present in each pixel?" This is a partial unmixing problem. The number of unmixing endmembers is one greater than the number of spectrally defined target materials. The one additional endmember can be thought of as the composite of all the other scene materials, or "everything else".

Several workers have proposed partial unmixing schemes for imaging spectrometry data, but each has significant limitations for operational application. The low probability detection methods described by Farrand and Harsanyi (1993) and the foreground-background method of Smith et al. (1994) are both examples of such partial unmixing strategies. The new method presented here builds on these innovative analysis concepts, combining their different positive attributes while attempting to circumvent their limitations. This new method partially unmixes AVIRIS data, mapping apparent target abundances, in the presence of an arbitrary and unknown spectrally mixed background. It permits the target materials to be present in abundances that drive significant portions of the scene covariance. Furthermore it does not require *a priori* knowledge of the background material spectral signatures. Figure 1 illustrates the concept for a scene with five background materials and two targets of interest. The challenge is to find the proper projection of the data that hides the background variance while simultaneously maximizing the variance amongst the targets.

2.   METHOD OUTLINE

The data processing can be broken into three steps: reduction to apparent surface reflectance; pixel purity determination; and partial unmixing. The AVIRIS data are first reduced to apparent surface reflectance by a radiative transfer model approach (Gao et al., 1993; Green et al., 1993). This data reduction uses little, or no, ground data and removes the atmospheric, solar and instrument effects.

Next the data are subjected to a dimensionality analysis and noise whitening process, using the Minimum Noise Fraction (MNF) transform process (Green et al., 1988; Lee et al., 1990). Through a series of affine transforms, the data are translated to have zero mean and then rotated and scaled so that the noise in every band is uncorrelated and has unit variance.

Then the data are repeatedly projected onto random unit vectors. The extreme pixels in each projection are noted. A cumulative account records the number

of times each pixel is found to be extreme. This extremity-score can be shown to be related to pixel purity, via a convex geometry argument (Boardman, 1993). The purest pixels in the scene are rapidly identified.

The purest pixels in the scene are then compared against the target spectra. If any are close matches for the target materials they are identified and separated from the other purest pixels. This allows the method to work on major scene components. It is not limited to low-probability targets. All high-purity pixels that do not closely match a target spectrum are used to determine a subspace that spans the background. This obviates the need to know the specific background endmember spectra. We only require their spanning subspace, a much less restrictive requirement. Optimal projection vectors are directly calculated for the target-spanning subspace, perpendicular to the background-spanning subspace.

Automatic unmixing (Boardman, 1993) is applied to the data, after projection onto the optimal target subspace. Here the number of endmembers is one more than the number of targets, irrespective of the complexity of the background. Finally, the target apparent abundances are spatially mapped.

3.   AVIRIS EXAMPLES

We present three applications of the method: carbonate mapping at the North Grapevine Mountains (NGM), CA/NV; rare-earth mineral mapping at Mountain Pass, CA; and kaolinite mapping near Golden, CO. The carbonate example is shown here for illustration purposes. The NGM scene is fairly complicated and has a variety of surface mineralogies. Figure 2 shows the MNF-eigenvalues, indicating at least six-dimensional data. The targets of interest were calcite and dolomite, two carbonate minerals. The partial unmixing process was applied, and the results are shown in the following figures. Figure 3 shows the optimal projection of the data. The background composite endmember is centered at (0,0). The vertical axis corresponds to the separation between the targets and the background, the horizontal axis maps intertarget separation. The units are noise standard deviations. Figure 4 shows the MNF model of a target-free scene. The scatter in the null model corresponds to the noise in the data. The agreement between the observed data and the null hypothesis model indicates the successful derivation of the optimal projection. The targets are optimally separated, and the multi-component background is fully compressed.

Figures 5 and 6 show portions of the calcite dolomite abundance maps. For display, the apparent abundances are scaled from 0.10 to 0.50 and displayed in a gray scale from white to black respectively. The outcrop pattern of the two minerals and surface mixing is clearly defined. Figures 7 and 8 show the mean spectra of the 50 highest abundance pixels for each target. They are good matches to reference spectra of calcite and dolomite.

4.   CONCLUSIONS

We present a method for mapping target surface materials, based on their spectral signatures, in the presence of complicated and unknown backgrounds. The targets can be major scene components. The spectra of the background materials are not required. The complexity of the unmixing is driven by the number of targets, not by the number of total materials in the scene and background. This uncouples the processing complexity from the scene complexity. The method is rapid, automatic and repeatable.

5. ACKNOWLEDGMENTS

6. REFERENCES

Boardman, J. W., 1993, Automating Spectral Unmixing of AVIRIS Data Using Convex Geometry Concepts, *Summaries of the Fourth Annual JPL Airborne Geoscience Workshop*, JPL Pub. 93-26, Vol. 1, AVIRIS Workshop. Jet Propulsion Laboratory, Pasadena, CA, pp. 11-14.

Farrand, W.H. and J.C. Harsanyi, 1993, Discrimination of Poorly Exposed Lithologies in AVIRIS Data, *Summaries of the Fourth Annual JPL Airborne Geoscience Workshop*, JPL Pub. 93-26, Vol. 1, AVIRIS Workshop. Jet Propulsion Laboratory, Pasadena, CA, pp. 53-56.

Gao, B-C, K.B. Heidebrecht, and A.F.H. Goetz, 1993, Derivation of Scaled Surface Reflectances from AVIRIS Data, *Remote Sensing of Environment*, vol. 44, no. 2, pp. 165-178.

Green, A.A., M. Berman, P. Switzer, and M.D. Craig, 1988, A Transformation for Ordering Multispectral Data in Terms of Image Quality with Implications for Noise Removal, *IEEE Transactions on Geoscience and Remote Sensing*, vol. 26, no. 1, pp. 65-74.

Green, R.O., J.E. Conel, and D.A. Roberts, 1993, Estimation of Aerosol Optical Depth and Additional Atmospheric Parameters for the Calculation of Apparent Surface Reflectance from Radiance Measured by the Airborne Visible/Infrared Imaging Spectrometer, *Summaries of the Fourth Annual JPL Airborne Geoscience Workshop*, JPL Pub. 93-26, Vol. 1, AVIRIS Workshop, Jet Propulsion Laboratory, Pasadena, CA, pp. 73-76.

Lee, J.B., A.S. Woodyatt, and M. Berman, 1990, Enhancement of High Spectral Resolution Remote Sensing Data by a Noise-Adjusted Principal Components Transform, *IEEE Transactions on Geoscience and Remote Sensing*, vol. 28, no. 3, pp. 295-304.

Smith, M.C., D. Roberts, J. Hill, W. Mehl, B. Hosgood, J. Verdebout, G. Schmuck, C. Koechler, and J. Adams, 1994, A New Approach to Quantifying Abundances of Materials in Multispectral Images, *Proceedings of IGARSS 1994*, Jet Propulsion Laboratory, Pasadena, CA, pp. 2372-4.
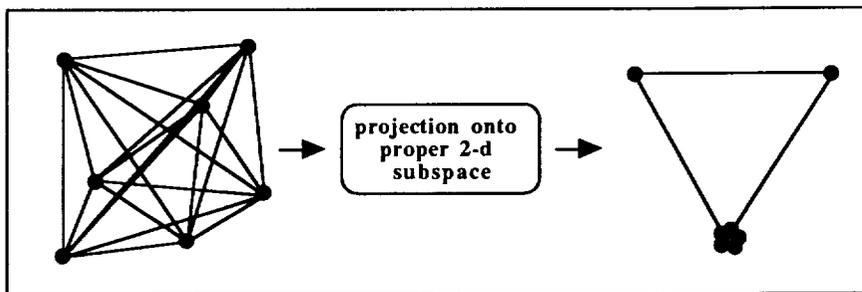
Figure 1. Schematic diagram of partial unmixing as a data projection.
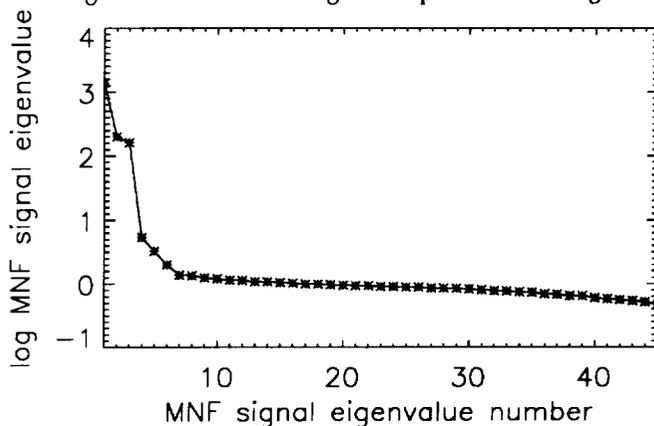
Figure 2. MNF signal eigenvalues of NGM data, showing at least 6 valid dimensions.
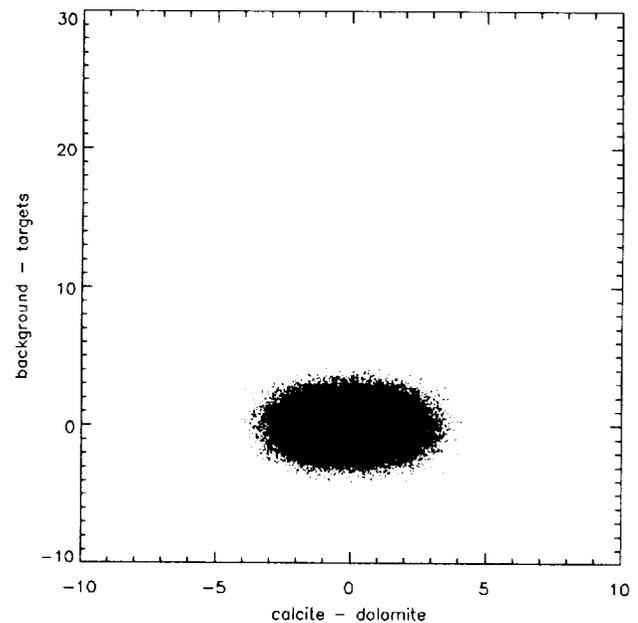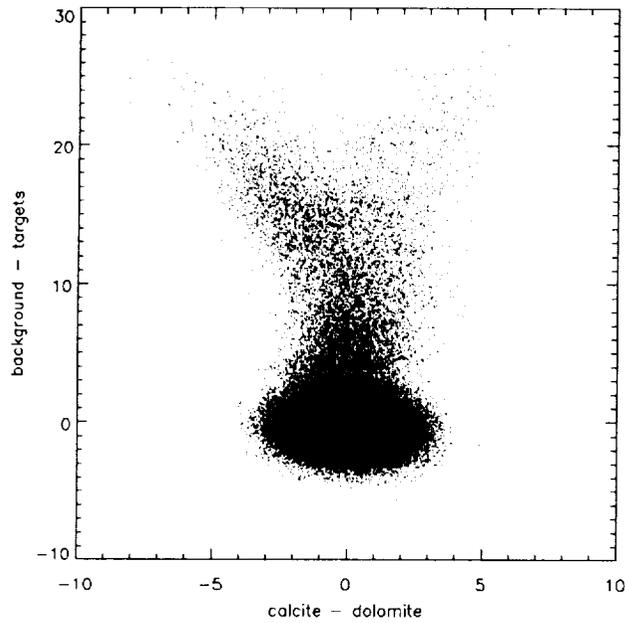
Figures 3 and 4. Optimally projected data and MNF-noise-model null hypothesis.
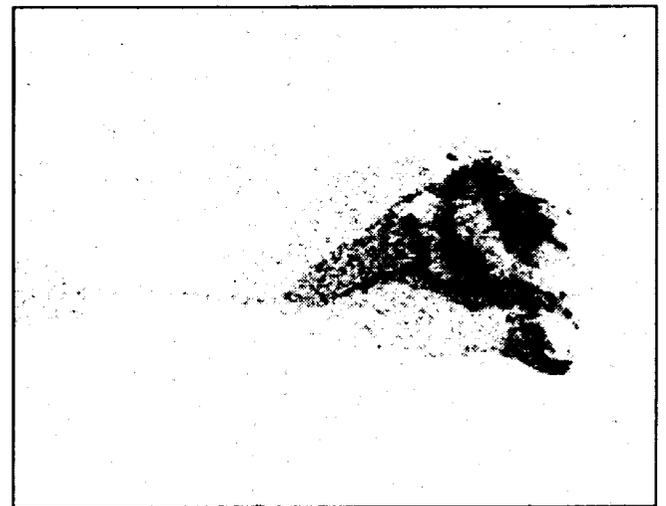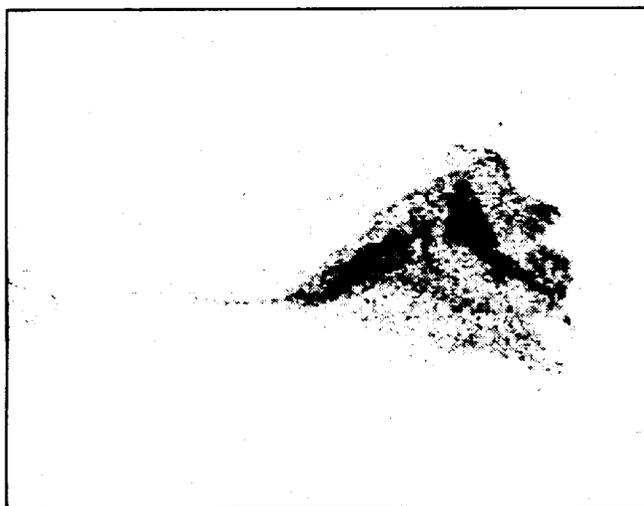
Figures 5 and 6. Apparent abundance of dolomite and calcite target materials.
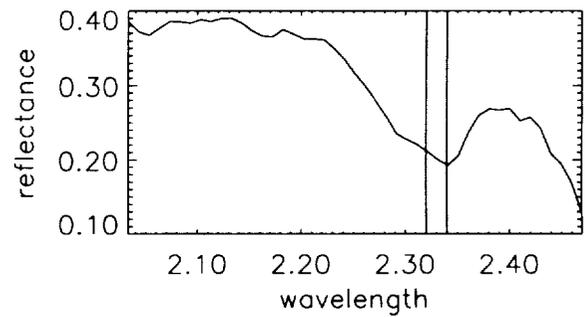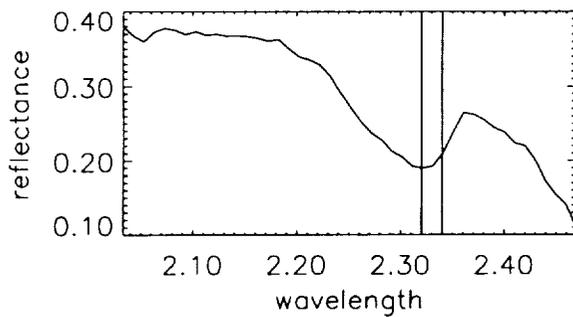
Figures 7. and 8. Mean spectra of 50 purest dolomite and calcite pixels.

COMBINED HYPERSPATIAL AND HYPERSPECTRAL IMAGING SPECTROMETER CONCEPT

Ian Burke and Harold Zwick
MacDonald Dettwiler and Associates, Ltd.
13800 Commerce Parkway, Richmond B.C., V6V 2J3

1. INTRODUCTION

There is a user need for increasing spatial and spectral resolution in Earth Observation (EO) optical instrumentation. Higher spectral resolution will be achieved by the introduction of spaceborne imaging spectrometers. Higher spatial resolutions of 1 - 3 m will be achieved also, but at the expense of sensor redesign, higher communications bandwidth, high data processing volumes, and therefore, at the risk of time delays due to large volume data-handling bottlenecks.

This paper discusses a design concept whereby the hyperspectral properties of a spaceborne imaging spectrometer can be used to increase the image spatial resolution, without such adverse cost impact.

2. HYPERSPATIAL IMAGE MERGING

An EO instrument may be designed so as to provide higher spatial resolution information through combining more than one "look" of a scene at different wavelengths. These multiple "looks" have subpixel offsets from each other. The composite image has a higher sampling density, and hence a higher spatial resolution if the system SNR is adequate. With the images combined from different wavelengths, the composite image represents what would have been measured by a high-resolution "pseudo-panchromatic band". Sharpe and Kerr (1991) had success in producing hyperspatial images from multispectral Landsat-5 TM data to verify this concept.

Figure 1 shows a process by which spatially offset multispectral images ("looks") can be combined to increase spatial resolution. Combining the single-band images from a multispectral sensor increases the number of samples, but the samples are taken from different parts of the spectrum. Consequently, the first step is *radiometric matching*, in which the radiance levels in each of the single-band images are modified, over localized regions, to simulate those in a reference band. The second step consists of merging the radiometrically matched images to form a composite image; this is called *band interleaving*. The third step is *geometric rectification*, where the composite image is resampled onto a uniform grid.

When the single-band images are combined, the distance between the pixels decreases, but the pixel size (amount of ground covered by each individual pixel) remains the same; consequently, the pixels are overlapped. *Pixel shrinking filters* (Wornell *et al.*, 1989) are then used to produce pixels that no longer overlap but are butted. This simulates an image that would have been measured with detectors having a pixel size equal to the new pixel spacing. The net result is a new composite image that has higher spatial detail, and may be said to have an effectively higher Modulation Transfer Function (MTF) than each original single-band image.

Spatially offset single-band images → Radiometric Matching → Band Interleaving → Geometric Rectification → Pixel Shrinking → High resolution pseudo-panchromatic composite image with uniform sampling
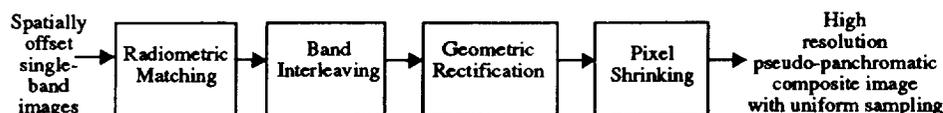
Figure 1 Hyperspatial Image Merging Process
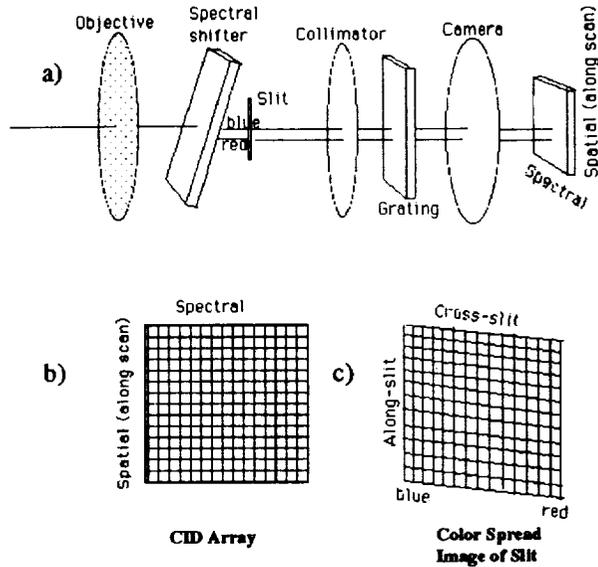
Figure 2   Hyperspatial Imaging Spectrometer Design

3.   HYPERSPATIAL IMAGING SPECTROMETER CONCEPT

This section shows that a hyperspatial-hyperspectral instrument can be readily designed. Figure 2a shows the optics layout for a typical Imaging Spectrometer (IS) (ignoring the "spectral shifter" and the fact that the array consists of Charge Injection Devices (CIDs) for the moment). The grating serves to disperse the light in the "spectral" dimension, projecting the various colors on different pixels as shown in Figure 2b. In order to allow the image merging process outlined in Figure 1 to be applied to this IS, spatial shifts between the different bands in the along-scan direction plus appropriate band-to-band time delayed readouts among the spectral bands for the across-scan direction are required.

The random access CID array is a detector readout addressable matrix, so that individual detectors and therefore bands can be read out under external control. This means that with a random access CID the spectral bands can be read out in whatever band sequence is desired and with selectable time delays between individual bands. The random access CID then can provide the necessary across-scan direction subpixel spatial shifts between the single-band images.

It is desirable to also introduce a differing subpixel shift between each single-band image in the along-scan direction (orthogonal to the grating dispersion). As the shift between band centres in the along-scan direction is not programmable by readout (only by unit detector sizes), it is necessary to introduce a spectral shifter to produce the required subpixel offsets. This device is shown near the slit in Figure 2a. This optical device creates a different relative subpixel image shift for each band (color) along the length of the slit. The color spread image of the slit is shown in Figure 2c, with the degree of along-slit displacement from the optical axis being proportional to the wavelength of observation.

The resulting single-band images are displaced from each other by subpixel amounts in both the along-scan and across-scan directions. The subpixel shifts can be made to be uniform in the across-scan direction by appropriate choices of the detector readout times. The subpixel shifts in the along-scan direction, on the other hand, are determined by the spectral dispersion of the spectral shifter for each band wavelength. This will be somewhat nonuniform, but the nonuniformity can be handled by subsequent processing.

28

1

0.8

0.6

System
MTF

0.4

0.2

0

———— Single-band MTF

_ _ _ _ Fifteen-band pseudo-panchromatic
MTF after pixel shrinking

0   0.5   1   1.5   2   2.5   3   3.5   4

Spatial Frequency (cycles/pixel)

Single-band   Fifteen-band
aliasing frequency   aliasing frequency
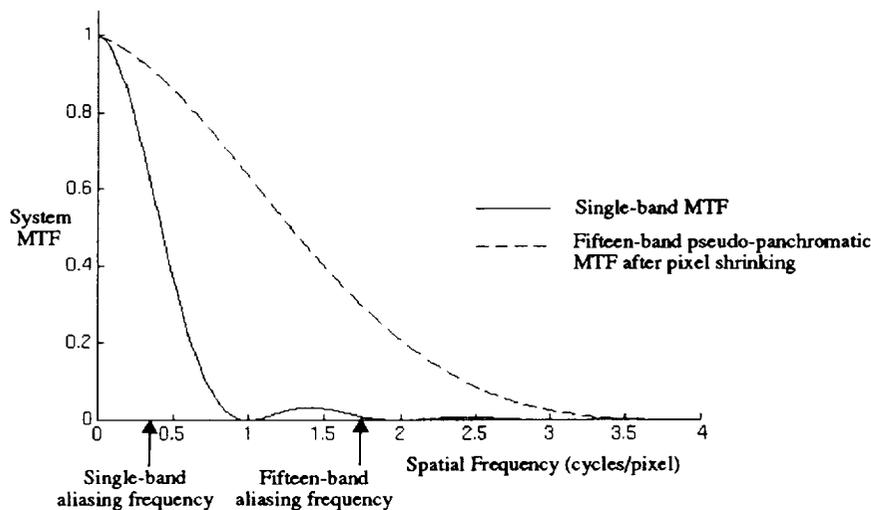
Figure 3 Simulated single-band and pseudo-panchromatic MTFs in the
across-scan direction (at 680 nm) for a 15-spectral band IS instrument

4.   HYPERSPATIAL RESOLUTION OF AN IMAGING SPECTROMETER

The quality of an imaging system can be described by two parameters: the system
MTF* and the aliasing frequency. The spatial frequency at which the first reflected branch
of the MTF (caused by sampling the image) is one-half of the fundamental branch (true
spectrum centered about zero) is called the *aliasing frequency*** . A convenient definition is
to set the *spatial resolution**** to be the inverse of the aliasing frequency.

In order to illustrate the benefits of the IS design shown in Figure 2, a 15-spectral
band silicon CID IS will be used as an example. Figure 3 shows the simulated system MTF
in the across-scan direction at 680 nm as a solid curve. If the sensor had its optics set up as
shown in Figure 2, there would be different subpixel displacements between all fifteen
spectral bands. Suppose the spectral shift and readout timing were coordinated so that all
fifteen single-band images were evenly offset from each other by subpixel amounts in both
the along-scan and across-scan directions**** . Processing these images through the
flowchart in Figure 1 up to the pixel shrinking algorithm would leave the MTF shape
unchanged and the aliasing frequency increased by a factor of about $\sqrt{15}$ (as shown in the
figure), since the sampling density has increased by this amount in both spatial directions.

A pixel shrinking filter is then used to change the single-band MTF to the fifteen
-band pseudo-panchromatic MTF (shown as a dotted curve in Figure 3). The result of these
operations is a better MTF with a higher aliasing frequency, yielding a significant increase
in spatial resolution and image quality. The increase in spatial resolution is limited by the
shape of MTF, and the SNR achieved. Combining N multispectral images evenly offset in
both spatial directions will yield an increase in resolution of about $\sqrt{N}$.

---

* The MTF is different in the along-scan and across-scan directions. The across-scan MTF is a function
of the detector size, optics, and sampling rate.

** This definition has the added provision that the reflected branch be, on average, greater than the fun-
damental branch for spatial frequencies above the aliasing frequency.

*** This definition of spatial resolution is very conservative; discernible detail will be noticeable be-
low this limit.

**** The bands are not expected to be evenly spaced in the spectrum so the subpixel displacement in
the along-scan direction will not be uniform.

5. USING AVIRIS DATA TO INVESTIGATE THE COSTS AND BENEFITS OF A HYPERSPATIAL IMAGING SPECTROMETER DESIGN

A hyperspatial-hyperspectral IS instrument has been conceptually modeled. The next stage in the analysis consists of testing the design concept proposed here with real data. Spaceborne IS data will be simulated from airborne IS data for these tests. Each band of the airborne data will be "smoothed" to the resolution of the proposed spaceborne sensor. During this process, the simulated bands will be offset by subpixel amounts. The pseudo-panchromatic composite image will be created from these simulated bands and directly compared with the original "unsmoothed" high resolution single-band images. The large spectral range and contiguous nature of the AVIRIS spectral bands make it well-suited to these tests, since they allow significant flexibility in the simulation of spaceborne imagery.

The main parameters to investigate are the spatial resolution of the pseudo-panchromatic composite image, the surface characteristic conditions under which hyperspatial image merging can be utilized, and the use of the high resolution pseudo-panchromatic image in typical applications. The spatial resolution of the pseudo-panchromatic composite image can be tested by comparing it to the individual smoothed single-band images to search for improved spatial detail, and by comparing it to the original unsmoothed high resolution images. The later tests will consist of comparing edge sharpness at feature edges, calculating rms differences, and visually comparing the simulated and original high resolution images.

Tests to determine the conditions under which hyperspatial image merging should be utilized, and its robustness in the presence of errors in data gathering and processing, should also be conducted. This will yield information about how the improvement in spatial detail varies with the number of bands merged, the effect of the accuracy of pixel location knowledge, and tolerance of the hyperspatial image merging process to different band wavelengths.

The limitations of implementing this new design also need to be addressed. This consists of investigating how the radiometric accuracy and SNR among single-band images are affected by subpixel displacements, and investigating whether image misregistration causes appreciable error in the derivation of standard thematic products, such as the Normalized Difference Vegetation Index (NDVI).

6. CONCLUSIONS AND RECOMMENDATIONS

The design concept presented in this paper uses the hyperspectral properties of an imaging spectrometer to achieve hyperspatial resolution. The benefits include better image spatial quality via a better MTF. The next stage consists of using airborne multispectral imagery to test the design concept for high spatial resolution spaceborne imaging spectrometers, and to test the limitations of the design. AVIRIS seems well-suited to these studies due to its wide spectral range and the contiguous nature of its spectral bands.

7. BIBLIOGRAPHY

Sharpe, B. and A. Kerr, 1991, "Multichannel Fusion Technique for Resolution Enhancement during Ground Processing", *Proceedings of IGARSS'91*, pp. 1459-1462.

Wornell, G. W., D. S. Kauffman, and B. Sharpe, 1989, "Minimum Mean-Square Error Resampling for Remotely Sensed Imagery", *Proceedings of IGARSS'89*, pp. 616-619.

Airborne Visible/Infrared Imaging Spectrometer (AVIRIS) Onboard Calibration System

Thomas G. Chrien, Mike Eastwood, Robert O. Green, Charles Sarture, Howell Johnson, Chris Chovit, and Pavel Hajek

Jet Propulsion Laboratory, California Institute of Technology
4800 Oak Grove Drive, Pasadena, California USA 91109

The AVIRIS instrument uses an onboard calibration system to provide auxillary calibration data. The system consists of a tungsten halogen cycle lamp imaged onto a fiber bundle through an eight position filter wheel. The fiber bundle illuminates the back side of the foreoptics shutter during a pre-run and post-run calibration sequence. The filter wheel contains two neutral density filters, five spectral filters and one blocked position. This paper reviews the general workings of the onboard calibrator system and discusses recent modifications.

INTRODUCTION

AVIRIS is an airborne sensor which measures high spatial resolution image data of the earth in 224 spectral channels in four spectrometers (A, B, C, and D) covering the range from 380 to 2500 nm. These data are spatially, spectrally and radiometrically calibrated (Vane, 1987, Chrien 1990, Chrien 1993b). Modifications to AVIRIS have resulted in substantial improvements in signal-to-noise ratio, calibration accuracy and operability of the sensor (Chrien, 1991, Chrien 1993a). Validation experiments are conducted to verify instrument performance and calibration in flight (Green, 1993a). The onboard calibration data can be used to correct for variations in the AVIRIS radiometric response (Green 1993b). Recent modifications to the onboard calibration system are discussed.

CALIBRATION REQUIREMENT

Imaging spectrometers are used to measure the contiguous spectral signature of the upwelling radiance reflected and emitted from the surface of the earth and its atmosphere. The information contained in this data is in general a non-linear mixture of atmospheric molecular absorptions and particle scattering signatures, surface reflected molecular absorption signatures and bidirectional reflectance properties and source spectral characteristics such as solar spectral radiance and surface temperatures. The scientific study of any one of these effects requires a separation of these complex interactions.

The instrument calibration of an imaging spectrometer removes an additional (and unnecessary) complication to the non-linear unmixing problem discussed above. In general, the requirement for calibration accuracy is determined by the tolerance of unmixing algorithms to residual calibration errors. This tolerance decreases as the signal-to-noise ratio of an imaging spectrometer increases in order to avoid unmixing that is instrument calibration error limited.

Recent improvements in both the signal-to-noise ratio of the AVIRIS instrument and the unmixing algorithms applied to AVIRIS data have prompted a re-evaluation of its calibration requirements. Of primary interest are improvements to the current instrument radiometric accuracy of 5% absolute and spectral accuracy of 1 to 2 nanometers.

ONBOARD CALIBRATION SYSTEM

In 1991 the onboard calibrator under went a major modification (Chrien, 1991) that routed light into the four AVIRIS spectrometers by illuminating the back of the closed foreoptics shutter. A color balance filter (2 mm Schott KG-2) was installed to provide good detector response across the 224 spectral channels of

the sensor. An improved current stabilized lamp drive circuit was also installed. These changes greatly improved the utility of the onboard calibrator data to correct for residual drifts in the radiometric response of the sensor. Since that time a number of addition improvements have been made.

End of Run Dark Images

The AVIRIS instrument now records 100 lines of dark imagery at the end of each run of data. The fore-optics shutter is closed during this time as it is during end-of-line dark measurements. It is expected that this dark image will provide a data set on which to base coherent noise level measurements and to enable the construction of coherent noise filters for the data. A high resolution counter (HRC) has been added to the engineering telemetry to measure the number of instrument clock cycles between successive lines (which varies due to roll correction). The high resolution counter provides a way to time code detector reads from line to line and may prove useful in filtering time dependent noise sources.

Onboard Calibration Lamp

Prior to the 1994 flight season the OBC lamp was replaced with a 5000 hour rated lifetime bulb. Unfortunately, during the 1994 flight season the onboard calibrator experienced an excessive number of lamp failures. The first ocurred just before shipping AVIRIS to Ames. Two other failures occurred during the flight season. These failures occured at a fraction of the 5000 hour life of the bulb. Upon visual inspection, no fracture or burn-through of the filament was visible, and indeed, the second lamp that failed in AVIRIS lit right up in the lab.

The failed bulbs were returned to the manufacturer for autopsy, and the cause of failure was found to be degradation of the pigtail-wire-to-lamp-pin crimp-weld connections owing to corrosion. The corrosion arose from chemical byproducts from the heat degradation of shrink tubing placed over the crimp-welds before the lamp was potted in its metal base. This corrosion caused the wire-to-pin connections to rise in resistance beyond what the OBC constant-current power supply could handle (owing to an upper limit on the voltage it was able to supply to the bulb and wires combination), and hence the bulbs failed to light. The bulb intensity was probably unstable for some time before the resisitance due to the crimp-weld rose so far as to preclude the lamp from lighting at all.

The corrosion explanation fit well with the observed lamp behavior before failure, and with lamp "filament" resistance measurements after failure. The manufacturer uses teflon tubing for all its higher-wattage lamps, but for this 10 watt lamp typical electronic-cabling-variety shrink tubing was used. The manufacturer did not forsee the lamp base getting very hot, but we had taken steps to make sure that the lamp did get to at least 250 degrees C in order to keep the lamp's internal halogen cycle effective and hence maximize the life and the light output stability of the bulb. The manufacturer has fabricated new lamps for the AVIRIS OBC application which incorporate the high temperature tolerant teflon tubing around the crimp-welds. We expect these to survive our nominal operating temperature.

31

Also included in this year's changes is a conversion from a constant-current power supply to a constant-light-output power supply. We have mounted a silicon photodiode/amplifier hybrid (Model #UDT-455) on the top of the OBC lamp housing. The lamp filament is imaged onto the photodiode active area through a 543nm narrow-pass filter. The resulting signal is fed back to the lamp power supply to maintain constant light output from the bulb.

Currently an investigation of lamp stability over operating temperature is underway. Historical data show that the temperature internal to the OBC remains between 20° C and 30° C over the course of a flight season. Narrow-banding the light hitting the detector minimizes the effect of the silicon photodiode's spectrally-dependent responsivity drift with temperature.

Spectral Calibration Filters

Four new spectral filters have been designed for the onboard calibration source filter wheel. The filter wheel has been modified to accommodate the additional filters. The new filters consist of a birefringent material sandwiched between linear polarizers to make a single stage Lyot filter. The transmission of a Lyot filter varies as the cosine squared of one over the wavelength depending on the filter retardance. The four filters are designed to have a period of approximately 20 nanometers at the short wavelength end of each AVIRIS spectrometer. This insures that there will be sharply sloping spectral features across the entire 0.4 to 2.5 μm spectrum.

The spectral transmittance of the four filter set is shown in Figure 1. Measured data is shown for the first three filters which cover the 0.4 to 1.9 μm range, while the predicted performance is shown for the fourth 1.7 to 2.5 μm filter. A temperature sensor placed on the filter wheel housing updates the engineering telemetry once per second with a 0.3°C precision.
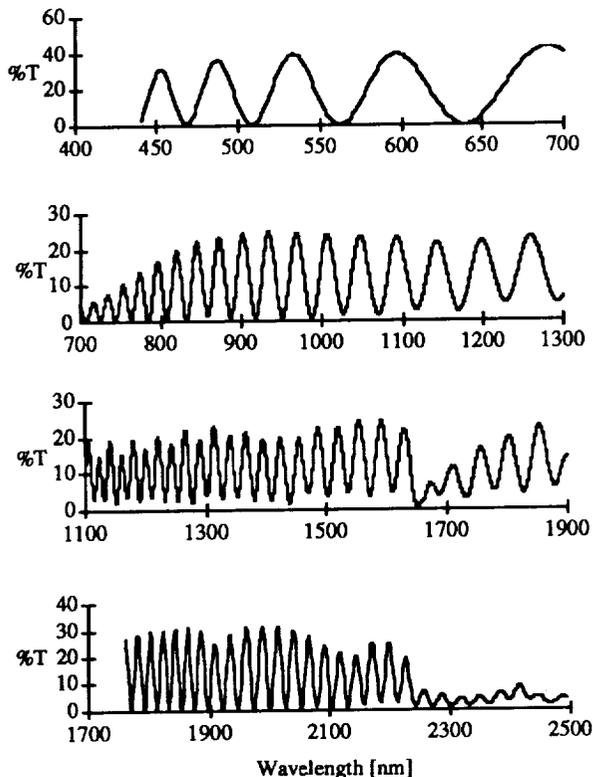
Figure 1. Lyot spectral calibration filter set

The data from the onboard calibrator is converted to spectral transmittance by dividing the Lyot minus Dark filter wheel spectra by the High minus Dark spectra. The sharply sloping transmittance features provide high sensitivity to spectral shifting inflight. Preliminary analysis shows that a 0.1 nm shift in spectral response is detectable using these filters.

REFERENCES

Chrien, T. G., R. O. Green, and M. L. Eastwood, "Accuracy of the Spectral and Radiometric Laboratory Calibration of the Airborne Visible/Infrared Imaging Spectrometer", Proc. SPIE Conference on Aerospace Sensing, Imaging Spectroscopy of the Terrestrial Environment, Orlando, Florida, 16-20 April, 1990.

Chrien, Thomas G., Michael L. Eastwood, Charles M. Sarture, Robert O. Green, and Wallace M. Porter, "Current Instrument Status of the Airborne Visible/Infrared Imaging Spectrometer (AVIRIS)", Proc. Third AVIRIS Workshop, JPL Publication 91-28, Jet Propulsion Laboratory, Pasadena, CA, pp. 302-313, 1991.

Chrien, Thomas G., R. O. Green, "Instantaneous Field of View and Spatial Sampling of the Airborne Visible/Infrared Imaging Spectrometer (AVIRIS)," Summaries of the Fourth Annual JPL Airborne Geoscience Workshop, JPL Publication 93-26, Vol. 1, Jet Propulsion Laboratory, Pasadena, CA, 1993a.

Chrien, Thomas G., R. O. Green, C. M. Sarture, C. Chovit, M. L. Eastwood, and B. T. Eng, "Airborne Visible/Infrared Imaging Spectrometer (AVIRIS): Recent Improvements to the Sensor," Summaries of the Fourth Annual JPL Airborne Geoscience Workshop, JPL Publication 93-26, Vol. 1, Jet Propulsion Laboratory, Pasadena, CA, 1993b.

Green, Robert O., James E. Conel, Mark Helmlinger, Jeannette van den Bosch, Chris Chovit and Tom Chrien, "Inflight Calibration of AVIRIS in 1992 and 1993," Summaries of the Fourth Annual JPL Airborne Geoscience Workshop, JPL Pub. 93-26, Vol. 1, Jet Propulsion Laboratory, Pasadena, CA, 1993a.

Green, Robert O., "Use of Data from the AVIRIS Onboard Calibrator," Summaries of the Fourth Annual JPL Airborne Geoscience Workshop, JPL Publication 93-26, Vol. 1, Jet Propulsion Laboratory, Pasadena, CA, 1993b.

Vane, Gregg, T. G. Chrien, E. A. Miller, and J. H. Reimer, "Spectral and radiometric calibration of the Airborne Visible/Infrared Imaging Spectrometer (AVIRIS)," Proc. SPIE, 834, (1987).

New Calibration Techniques for the Airborne Visible/Infrared Imaging Spectrometer (AVIRIS)

Thomas G. Chrien, Robert O. Green, Chris Chovit, Mike Eastwood, Jessica Faust,
Pavel Hajek, Howell Johnson, H. Ian Novack, and Charles Sarture

Jet Propulsion Laboratory, California Institute of Technology
4800 Oak Grove Drive, Pasadena, California USA 91109

Recent laboratory calibrations of the Airborne Visible/Infrared Imaging Spectrometer (AVIRIS) include new methods for the characterization of the geometric, spectral, temporal and radiometric properties of the sensor. New techniques are desired in order to: (1) increase measurement accuracy and precision, (2) minimize measurement time and expense (3) prototype new field and inflight calibration systems, (4) resolve measurement ambiguities and (5) add new measurement dimensions. One of the common features of these new methods is the use of the full data collection and processing power of the AVIRIS instrument and data facility. This allows the collection of large amounts of calibration data in a short period of time and is well suited to modular data analysis routines.

INTRODUCTION

AVIRIS is an airborne sensor which measures high spatial resolution image data of the earth in 224 spectral channels in four spectrometers (A, B, C, and D) covering the range from 380 to 2500 nm. These data are spatially, spectrally and radiometrically calibrated (Vane, 1987, Chrien 1990, Chrien 1993b). Modifications to AVIRIS have resulted in substantial improvements in signal-to-noise ratio, calibration accuracy and operability of the sensor (Chrien, 1991, Chrien 1993a). Validation experiments are conducted to verify instrument performance and calibration in flight (Green, 1993a).

Recent improvements in both the signal-to-noise ratio of the AVIRIS instrument and the unmixing algorithms applied to AVIRIS data have prompted a re-evaluation of its calibration requirements. Of primary interest are improvements to the current instrument radiometric accuracy of 5% absolute and spectral accuracy of 1 to 2 nanometers. This paper describes new calibration techniques tried during a recent laboratory calibration. Preliminary results from these measurements will be shown.

CALIBRATION DIMENSIONS

The process by which instrument response is converted to units of spectral radiance is generally called calibration. The precision and accuracy of this calibration must be sufficient to avoid calibration errors that show up as systematic noise in subsequent data analysis. The frequency of the calibration is determined by the instrument stability such that residual response drift is also sufficiently small.

Each spectral-spatial channel responds to the input spectral radiance with some digitized number (DN) output. The DN responds to both signal and non-signal sources such as thermal background and dark current. A shuttered detector sample is used to subtract this non-signal component. The remaining relationship between DN and signal photons is the radiometric response function. If the response is linear, and dark subtraction is done properly, the radiometric calibration is reduced to a single gain coefficient for each detector channel. If linearity does not apply, then more coefficients are required.

The number of received signal photons, Φ, is also determined by the temporal, spectral and spatial characteristics of the sensor as shown by the following equation:

$$\Phi := \int L \cdot A \cdot \Omega \cdot \Delta\lambda \cdot t \cdot \frac{\lambda}{hc} \; dL \; dA \; d\Omega \; d\lambda \; dt$$

where L is the spectral radiance field presented to the sensor, A is the aperture response function, Ω is the geometric response function, $\Delta\lambda$ is the spectral response function, t is the temporal response function, and λ/hc converts energy into the number of photons of wavelength λ.

A complete calibration must measure each of the above response functions for each spectral-spatial channel and show the relative relationship between adjacent response functions. In the extreme case, each image cube element has a unique set of response functions to describe its calibration. Fortunately, parameters can be used to approximate the response functions and their interrelations. The goal is to measure the pertinent calibration coefficients, to an adequate accuracy, in a time and cost effective manner.

Radiometric Calibration

The standard method of AVIRIS radiometric calibration is based upon the radiance standard constructed out of a calibrated reflectance panel and an irradiance standard lamp (Chrien, 1990). A Spectroradiometer is used to transfer this radiance to a large integrating sphere which has uniform output over the 30 degree field-of-view of the AVIRIS scan mirror. The error associated with the intermediate calibration and radiometric stability of the integrating sphere is estimated to be 1.1%.

Direct observation of the radiance target has been proposed as a method for eliminating this error source. An early attempt at this revealed a significant increase in stray light from the irradiance lamp. An investigation of scattered light sources has led to a radiance target design which uses baffles and an off-axis look angle.

An additional requirement for the direct radiance standard was that it be field portable. The desire was to have the capability to place a ground based radiometric calibration on the AVIRIS instrument while it is on deployment away from JPL.

As an additional experiment, data was collected at a number of lamp current levels. Past experience shows that the lamp irradiance spectrum closely matches that of a blackbody. The assumption is that other current levels will also correspond to blackbody temperatures. The spectral ratio between any two of these level will be a good test of band-to-band radiometry, spectral calibration accuracy, and linearity of the radiometric system response.

The irradiance accuracy of the calibrated lamp source is the dominant uncertainty term in the short-wave infrared. In order to improve the absolute accuracy in this spectral range, a cavity blackbody source was used. Data was collected at cavity

temperatures between 100°C and 1000°C in roughly 100°C intervals. Ratios of these cavity temperatures will also be investigated.

Spectral Calibration

The standard method for spectral calibration consists of using a scanning Monochromator which is calibrated using spectral emission lamps. A new method bypasses the Monochromator and uses the emission lamps directly. The lamps were placed at the collimator focus and data was collected with the scanning mirror disabled. The following lamps were used: krypton, argon, helium, neon, deuterium, xenon, hydrogen, carbonic acid, carbon dioxide, mercury vapor, iodine, bromine, water vapor and nitrogen. A related method uses rare earth oxides (Holmium Oxide, Erbium Oxide, and Dysprosium Oxide) embedded in a sintered halon base in a reflectance configuration.

Several different approaches to using a scanning Monochromator with an embedded spectral sync pulse have been investigated. The general approach is to mix in a known spectral source such as an emission lamp or laser line. As the Monochromator scans, the current wavelength position is also encoded into the sensor data by way of the spectral sync pulse.

A Michaelson interferometer was also used as a wavelength input source. The interferometer is scanned through the zero path length to a path length that is unresolved in the spectral domain. The resultant inteferogram is collected during the scan. The Fourier transform of the inteferogram is used to determine the spectral response function of the individual spectral channels.

Geometric Calibration

The standard method for geometric calibration is to scan a narrow slit at a fixed rate across the focal plane of a collimator. This measures the relative shape of the geometric response function as well as the sampling interval between spatial pixels. A new variant of this technique use a double slit. Careful measurement of the slit spacing, collimator focal length, and instrument timing information is used to place an accurate angle calibration on the geometric response function data. A similar set of experiments was performed with an extra wide slit, which presented two edge response functions at a known spacing.

The field of view of a scanner is simply the number of cross track pixels times the sampling interval between adjacent pixels. The scanning slit technique works well for measuring the sampling interval, but only for a few nadir pixels. In order to test that the sampling interval was constant over the full scan field-of-view, a new technique was developed. The technique uses a HeNe laser passed through a Ronchi ruling transmittance grating. Carefully aligned, this configuration produces a large number of pulses spaced across the full scanned field-of-view. Standard diffraction theory is used to compute the angular spacing of each of the diffracted orders.

In a related test, a full-aperture Ronchi ruling was placed between the instrument aperture and a collimator projected a white light illuminated slit. We expect to find an interesting combination of spatial and spectral calibration data from the resultant data set.

Temporal Calibration

In order to investigate the temporal spacing between spectral channels, data were collected of a strobe light source at a range of strobe frequencies. The phase delay between adjacent channels within a spectrometer and across spectrometers boundaries provides insight to these relationships.

CONCLUSIONS

The new techniques discussed here are all relatively easy to implement. Data collection is done in the natural imaging mode of the instrument under test. Results from the new techniques presented here are still pending data analysis. The accuracy that results from the new techniques as well as the ease of processing this data will be used to decide the value of the new approaches.

REFERENCES

Chrien, T. G., R. O. Green, and M. L. Eastwood, "Accuracy of the Spectral and Radiometric Laboratory Calibration of the Airborne Visible/Infrared Imaging Spectrometer", Proc. of the SPIE Conference on Aerospace Sensing, Imaging Spectroscopy of the Terrestrial Environment, Orlando, Florida, 16-20 April, 1990.

Chrien, Thomas G., Michael L. Eastwood, Charles M. Sarture, Robert O. Green, and Wallace M. Porter, "Current Instrument Status of the Airborne Visible/Infrared Imaging Spectrometer (AVIRIS)", Proc. of the Third AVIRIS Workshop, JPL Publication 91-28, Jet Propulsion Laboratory, Pasadena, CA, pp. 302-313, 1991.

Chrien, Thomas G., R. O. Green, C. M. Sarture, C. Chovit, M. L. Eastwood, and B. T. Eng, "Airborne Visible/Infrared Imaging Spectrometer (AVIRIS): Recent Improvements to the Sensor," Summaries of the Fourth Annual JPL Airborne Geoscience Workshop, JPL Publication 93-26, Vol. 1, Jet Propulsion Laboratory, Pasadena, CA, 1993b.

Green, Robert O., James E. Conel, Mark Helmlinger, Jeannette van den Bosch, Chris Chovit and Tom Chrien, "Inflight Calibration of AVIRIS in 1992 and 1993", Summaries of the Fourth Annual JPL Airborne Geoscience Workshop, JPL Pub 93-26, Jet Propulsion Laboratory, Pasadena, CA, Vol. 1, 1993a.

Vane, Gregg, T. G. Chrien, E. A. Miller, and J. H. Reimer, "Spectral and radiometric calibration of the Airborne Visible/Infrared Imaging Spectrometer (AVIRIS)," Proc. of the SPIE, 834, (1987).

ACKNOWLEDGMENTS

INITIAL VEGETATION SPECIES AND SENESCENCE/STRESS INDICATOR MAPPING IN THE SAN LUIS VALLEY, COLORADO USING IMAGING SPECTROMETER DATA

By
Roger N. Clark, Trude V.V. King, Cathy Ager and Gregg A. Swayze
U. S. Geological Survey
Mail Stop 964
Box 25046 Federal Center
Denver, CO 80225

INTRODUCTION

Vegetation covers a large portion of the Earth's land surface. Obtaining quantitative information about vegetation with remote sensing has proven difficult. To first order, all vegetation is chemically similar, and most healthy plants are green showing absorption bands that are almost identical. Plant species are generally characterized by the leaf and flower or fruit morphology, not by remote sensing spectral signatures. However, to the human eye, many plants show varying shades of green, so there is direct evidence for spectral differences between plant types. Quantifying these subtle differences in a predictable manner has not been easy, and has been made more difficult by lack of adequate instrumentation.

Clark et al., (1990a, 1991) developed a new analysis algorithm that uses a digital spectral library of known materials and a fast, modified-least-squares method of determining if a single spectral feature for a given material is present. This algorithm, now called "tricorder," compares continuum-removed spectral features (Clark and Roush, 1984) from the imaging spectrometer data set to corresponding continuum-removed spectral features from a reference spectral library. Multiple features from multiple materials are compared and the closest match is selected. The algorithm does not force a detection like many other algorithms. For example, many algorithms take a set of curves and best fit them to the observed data, often requiring a set of parameters (like mineral fraction) to sum to one. The tricorder algorithm has no such constraint. If the materials do not exist in a given pixel, such that there are no spectral features from those or similar materials, the algorithm produces zeros, indicating they are not detected.

The human eye sees different plant leaves as shades of green, as characterized by the "green peak" in reflectance spectra. The eye/brain color system differentiates shades of green under different lighting conditions. For example, under indoor incandescent light, there is a strong red slope to the spectral signal received by the eye due to the red spectral shape of the light source (as compared to the same plant in direct sunlight). We are still able to distinguish the plant as green and distinguish different plants as various shades of green.

The tricorder algorithm is very sensitive to the shape of spectral features and has the potential to distinguish more subtle differences in the visible spectrum of plants than the human eye. We have applied this method, along with reference spectra of specific plants, to map vegetation species in AVIRIS scenes.

The continuum removal to isolate diagnostic spectral features is an important step, particularly when a pixel contains spectral information from green plants, dry vegetation, and soil. In such a case, the combination of materials within a pixel changes the color perceived by the human eye. However, by isolating absorption features with continuum removal, the position and shape of the continuum removed spectral feature remains constant, although its depth changes with absorber fractional areal coverage in the pixel. The tricorder algorithm normalizes the absorptions so that overall shape is compared.

IMAGING SPECTROMETER DATA

We analyzed AVIRIS data obtained over agricultural areas in the San Luis Valley of Colorado. The data were acquired on September 3, 1993. A combined method of radiative transfer modeling and ground calibration site reflectance was used to correct the flight data to surface reflectance (Clark et al., 1994a). This method, called Radiative Transfer Ground Calibration, or RTGC, corrects for variable water vapor in the atmosphere and produces spectra free of artifacts with spectral channel to channel noise approaching the signal to noise of the raw data. The calibration site soil samples were obtained on the day of the overflight and measured on our laboratory spectrometer

(Clark *et al*, 1990b). The site was near the center of the AVIRIS scene and the spectra of the soil is spectrally bland, especially in the region of the chlorophyll absorption in the visible portion of the spectrum.

The center of the scene is located at approximately 106° 03' longitude, 37° 23' latitude, and the scene covers about 92 square kilometers. This scene is one of 28 in the area for a general project to study the Summitville abandoned mine site, located in the mountains west of the San Luis Valley, and its effects on the surrounding environment.

VEGETATION SPECIES AND REFERENCE SPECTRA

The study area includes farmland producing potatoes, alfalfa, barley, oat hay, canola, and open fields containing chico, and other unidentified weeds. Ideally, one would have a digital spectral library of reference spectra of the plant species to be mapped. Such a library does not exist for vegetation, as it does for minerals (e.g. Clark *et al.*, 1993b). It is not known how many spectra as a function of growing season would be required to represent the changing spectral signatures of plants.

Some plant species were measured with a portable field spectrometer, but due to windy conditions and limited availability of the instrument, sufficient data to form a library of all crops could not be obtained. The main objective of the field operations was to provide spectral information on sites with detailed geochemical analysis. Because of the limitation of obtaining field spectra, reference spectra were obtained for sites of known species directly from the AVIRIS data. AVIRIS, having been well calibrated to surface reflectance, is an excellent field spectrometer, providing data for large areas. The alfalfa, canola, oat hay, and nugget potato spectra show the plants to be green and healthy. The barley had lost all its chlorophyll signature. The Norkotah potatoes were not being irrigated as they were about to be harvested, and consequently they showed weak chlorophyll and cellulose absorptions with soil (clay) absorptions from exposed soil. These potatoes were also being sprayed with a defoliant. Thus, they should show decreased chlorophyll absorption along with a shift of the red edge of the absorption to shorter wavelengths. The chico and pasture spectra show combinations of chlorophyll and cellulose (dry vegetation) absorptions. There was rain in the valley in the few days before the flight so the chico/pasture may not show much water deprivation stress (being native plants they are hardy and can also withstand some reduced precipitation compared to the crops).

TRICORDER ANALYSIS

The continuum-removed chlorophyll-containing spectra are shown in Figure 1. The shape differences between each species enable the tricorder algorithm to discriminate between them. The tricorder algorithm produced maps of the distribution of each material. If there are other plants present in the image with similar spectral features, they could be misidentified as one of those in set of spectra used in the mapping. Thus, it is important to have a complete set of reference spectra. The extensive work by many workers on the Summitville project provided knowledge of the crops in the area, thus our spectral library for this case should be complete for crops. As the time of data acquisition was early fall for this mountain valley (elevation ~7650 feet, 2330 meters), some crops and/or pasture were senescing. Since the crops were changing spectrally, it was not known how representative a single reference spectrum for each crop would be. Each crop exists in several fields, each of which may have been in a different stage of senescence.

The tricorder algorithm examines the spectrum of each pixel in the image and chooses the best match to the set of reference spectra. The images from each crop/soil/pasture match were then color coded and a color coded map produced (AVIRIS Workshop Slide 1). Results of field checking of crops in the area were used to produce a color coded answer map for comparison. Field verification data was supplied by Maya ter Kuile of Argo Engineering (1993, personal communication), and our own work. Every crop and field could not be checked due to limited resources for this large area.

Examination of the results shows the tricorder-derived map to be highly accurate. Of 43 verification fields (not including chico/pasture), 7 included the sites of our reference spectra, 33 were identified correctly, another 3 were identified as mixed by the tricorder analysis (but were indicated as one crop type in the field data), and no fields were incorrect. The fields identified as mixed were of two species, one of which was correct in each case. The field check was done by driving the roads and identifying the crops visually. Because of the time required to develop this analysis (AVIRIS data receipt followed by calibration to surface reflectance in January, 1994, initial mapping in February, 1994), and the fact that it was winter, we were unable to investigate the cause of the discrepancies in the three fields mapped as mixed. If we give a score of half to the three fields identified as mixed,

the success score of 96% shows the method is accurate.

The accuracy is made even more impressive when one considers several fields were mapped correctly even though they had already been harvested. There was apparently enough plant material still left on the fields to still make a correct identification. This is again possible because the algorithm normalizes the absorptions, so even though the vegetation cover may be only a few percent, a correct identification can be made. The harvested areas can be identified in the data as circular plots where the colored pixels are sparse and/or low in intensity. Clark *et al.*, (1992) was also able to differentiate vegetation communities on the arid Colorado Plateau, another sparsely vegetated case. The harvested areas should also be under stress, and are indicated as such in the senescence/stress map.

Canola was mapped in many of the areas known to be pasture. While it is possible that canola seeds have been blown into surrounding fields and are growing, it is more likely that the canola spectral signature is close to other (native?) plants in those open fields. Complete discrimination of crops and surrounding wild vegetation requires a more complete set of reference spectra, beyond the scope of this initial study.

SENESCENCE/STRESS MAPPING

The long-wavelength side of the chlorophyll absorption (~0.68 to ~0.73 μm) forms one of the most extreme slopes found in spectra of naturally occurring common materials, plant or mineral. The absorption is usually very intense, ranging from a reflectance low of less than 5% (near 0.68 μm) to a near infrared reflectance maximum of ~50% or more at ~0.73 μm). The properties of reflectance spectra (e.g. Clark and Roush, 1984) indicate such an absorption band is "saturated." In such a case, the absorption band minimum will not change much with increased or decreased absorption, but the wings of the absorption will change. When the chlorophyll absorption in the plant decreases, the overall width of the absorption band decreases. The short wavelength side of the chlorophyll absorption is not observed in reflectance like that of the long wavelength side, because of other absorptions in the ultraviolet (UV). The result of this combination appears as a shift to shorter wavelengths as the chlorophyll absorption decreases. This has popularly become known as the "red-edge shift" or the "blue shift of the red edge" and can be caused by natural senescence, water deprivation, or toxic materials (e.g. Collins *et al.*, 1983; Rock *et al.*, 1986).

The ratio of two spectra, one shifted in wavelength, the other not, and each with steep slopes as seen at the "red edge," will produce a spurious feature when there is only a small shift between the two. If the blue shifted spectrum is divided by an unshifted spectrum, a peak will be observed in the ratio. For a spectrum of green vegetation, a 1 nm shift will produce a residual feature of about 6%. The AVIRIS data have a signal to noise of several hundred in this spectral region, so red-edge shifts of less than 0.1 nm are possible to detect. We used field spectrometer spectra for the San Luis data set, and computed a ratio cube which would show a peak when a shift occurs.

The red-edge shift was mapped using the tricorder algorithm. The fact that the resulting image shows no horizontal scan line striping attests to the superb wavelength stability of the AVIRIS instrument. As indicated earlier, the senescence/stress crop fields are those which have been harvested, sprayed with a defoliant, deprived of water, or may have other toxic influences. The area covered by this scene is not affected by acid mine drainage from the Summitville mine, thus it provides a control for the region of what might be expected under normal agricultural conditions.

CONCLUSIONS

Vegetation species mapping is possible with high precision using spectral feature analysis of data from airborne imaging spectrometers. Once calibrated, and after reference spectra have been selected, species mapping, along with senescence/stress indicator mapping can be achieved in less than 1 second of CPU time per square kilometer per species (or soil/mineral) on a 10 million floating point operation per second (MFLOP) workstation.

Imaging spectroscopy data can be used for environmental application, monitoring vegetation cover and its health, monitoring vegetation species, and providing a rapid overview of large areas. When applied to large areas, the cost to derive these maps is low in cost relative to field checking and monitoring on the ground. The species maps might be used for more accurate crop yield predictions.

Space limitations prevent us from presenting the entire AVIRIS data set of the Summitville and San Luis Valley study area in this paper, and processing is not yet complete. Additional areas, including vegetation species and senescence/stress indicator maps for more of the study area will be shown at the meeting.

37

REFERENCES

Collins, W., S.H. Chang, G. Raines, F. Canney, and R. Ashley, Airborne biogeochemical mapping of hidden mineral deposits: *Econ. Geol.*, **78**, p. 737, 1983.

Clark, R.N. and T.L. Roush, Reflectance Spectroscopy: Quantitative Analysis Techniques for Remote Sensing Applications: *J. Geophys. Res.*, **89**, p. 6329-6340, 1984.

Clark, R.N., A.J. Gallagher, and G.A. Swayze, Material absorption band depth mapping of imaging spectrometer data using a complete band shape least-squares fit with library reference spectra: *Proceedings of the Second Airborne Visible/Infrared Imaging Spectrometer (AVIRIS) Workshop*, JPL Publication 90-54, p. 176-186, 1990a.

Clark, R.N., T.V.V. King, M. Klejwa, G. Swayze, and N. Vergo, High Spectral Resolution Reflectance Spectroscopy of Minerals: *J. Geophys Res.* **95**, p. 12653-12680, 1990b.

Clark, R.N., G.A. Swayze, A. Gallagher, N. Gorelick, and F. Kruse, Mapping with Imaging Spectrometer Data Using the Complete Band Shape Least-Squares Algorithm Simultaneously Fit to Multiple Spectral Features from Multiple Materials: *Proceedings of the Third Airborne Visible/Infrared Imaging Spectrometer (AVIRIS) Workshop*, JPL Publication 91-28, p. 2-3, 1991.

Clark, R.N., G.A. Swayze, C. Koch, A. Gallagher, and C. Ager, Mapping Vegetation Types with the Multiple Spectral Feature Mapping Algorithm in both Emission and Absorption: Summaries of the Third Annual JPL Airborne Geosciences Workshop, Volume 1: AVIRIS Workshop. JPL Publication 92-14, p. 60-62, 1992.

Clark, R.N., G.A. Swayze, and A. Gallagher, Mapping Minerals with Imaging Spectroscopy: *U.S. Geological Survey, Office of Mineral Resources Bulletin 2039*, p. 141-150, 1993a.

Clark, R.N., G.A. Swayze, A. Gallagher, T.V.V. King, and W.M. Calvin, The U. S. Geological Survey, Digital Spectral Library: Version 1: 0.2 to 3.0 μm: *U.S. Geological Survey, Open File Report 93-592*, 1340 pages, 1993b. (Also being published as a USGS Bulletin, 1300+ pages, 1994 in press.)

Clark, R.N., G.A. Swayze, K. Heidebrecht, R.O. G.A.F.H. Goetz: Calibration to Surface Reflectance of Terrestrial Imaging Spectrometry Data: Comparison of Methods: *Applied Optics* in review, 1994a.

Rock, B.N., J.E. Vogelmann, D.L. Williams, A.F. Voglemann, T. Hoshizaki, Remote detection of forest damage: *Bio. Sci.* **36**, p. 439, 1986.
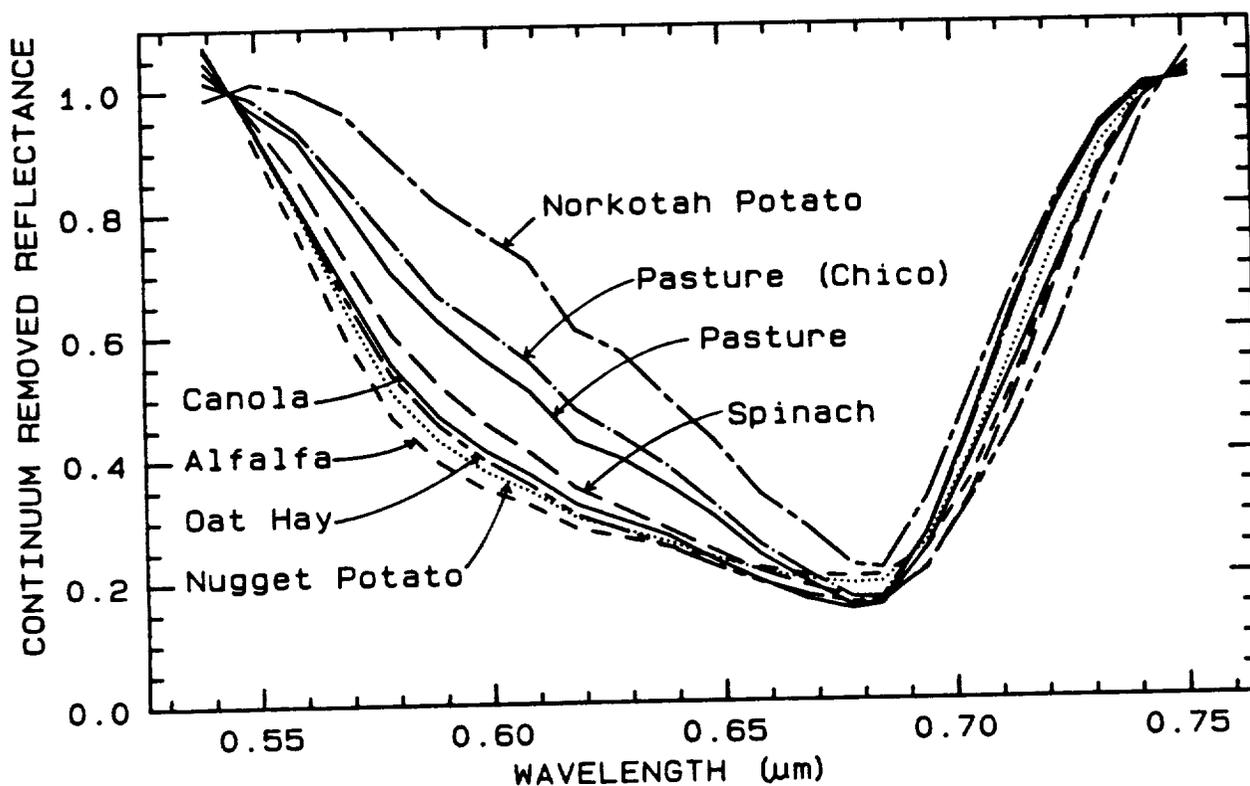
Figure 1. The continuum-removed chlorophyll absorption spectra are compared. Note the subtle changes in the shapes of the absorption between species.

Mapping Minerals, Amorphous Materials, Environmental Materials, Vegetation, Water, Ice and Snow, and Other Materials: The USGS Tricorder Algorithm

Roger N. Clark and Gregg A. Swayze

U.S. Geological Survey
Box 25046 Federal Center
Denver, CO 80225

Introduction

One of the challenges of Imaging Spectroscopy is the identification, mapping and abundance determination of materials, whether mineral, vegetable, or liquid, given enough spectral range, spectral resolution, signal to noise, and spatial resolution. Many materials show diagnostic absorption features in the visual and near infrared region (0.4 to 2.5 μm) of the spectrum. This region is covered by modern imaging spectrometers such as AVIRIS. The challenge is to identify the materials from absorption bands in their spectra, and determine what specific analyses must be done to derive particular parameters of interest, ranging from simply identifying its presence to deriving its abundance, or determining specific chemistry of the material.

Recently, a new analysis algorithm was developed that uses a digital spectral library of known materials and a fast, modified-least-squares method of determining if a single spectral feature for a given material is present (Clark *et al.*, 1990). Clark *et al.* (1991) made a another advance in the mapping algorithm: simultaneously mapping multiple minerals using multiple spectral features. This was done by a modified-least-squares fit of spectral features, from data in a digital spectral library, to corresponding spectral features in the image data. This version has now been superseded by a more comprehensive spectral analysis system called Tricorder.

Tricorder: New Features

The mapping of materials now includes a) pre-processing, b) specific algorithm selection, c) case-specific analyses, d) "not" features, e) spectral thresholding operations, and f) band constraints:

Preprocessing steps within Tricorder can include conversion of radiance data to reflectance data on the fly, ratioing to ground calibration target spectra or other reference spectra, and uncompressing data. The ability to correct the imaging data within Tricorder saves both time and disk space while eliminating the need for time-consuming manual file management.

The Tricorder concept is a simulation of the scientist's spectroscopic analysis method: it does the same operations you would do to analyze a spectrum. After preprocessing, Tricorder offers a selection of the algorithms that allow analysis of special cases. For instance, the first step in your analysis would be to decide which spectral features are present. Say, for example, that you determine there are both chlorophyll absorptions and clay mineral absorptions in a spectrum. Your next step might be to determine the relative areal coverage of the plants, and then to determine the water content of the plant leaves, remove this component and calculate the lignin/nitrogen ratio. You could also analyze the chlorophyll absorption for stress-induced red edge shift, and determine the plant species. Once the plant component is removed you could use the resulting unmixed soil spectrum to search for additional minerals that might have been concealed by the vegetation's spectral features.

Tricorder has the capability to analyze spectra stepwise, making specific decisions on what to do first, then based on the result, what to do next. This is achieved with a case sequence. For instance, if material "A" is found, do case 3, and when case 3 is complete, use the resulting answer to derive parameter "B," etc.

The new "not" feature is used for distinguishing between materials that have identical dominant spectral features but diagnostic subordinate features. The spectra of montmorillonite and muscovite are good examples. Both have nearly identical absorption features near 2.2 μm. However, muscovite has additional, weaker absorptions at longer wavelengths (near 2.3 μm). To be certain that montmorillonite is identified correctly, the 2.3-μm muscovite

bands must not be present. The "not" features allows tricorder to distinguish between materials like montmorillonite and muscovite.

Other new concepts include fit, band depth, and continuum thresholding. For example, fit thresholding evaluates the value of the correlation coefficient from the least squares analysis. If the fit is too low to reasonably identify any of a given set of materials, the pixel can be rejected from further analysis. Band depth thresholding works in a similar fashion. Continuum thresholding prevents material identifications in pixels with very low continuum levels where noise could resemble weak absorptions. In addition, by knowing the continuum value, you can often determine if the spectrum represents an area in a shaded region, over water, or in a region covered by a cloud.

Some materials have less-intense subordinate absorptions in addition to strong diagnostic absorptions. While the diagnostic absorptions may be detectable if abundance is high enough, the subordinate absorptions might be concealed by absorptions from other materials or might be too weak to be detected. Tricorder now uses diagnostic and optional absorption band assignments for each material which allow for the concealment or absence of these weaker absorptions during the fitting process. This band constraint feature has proven especially useful for mapping pixels containing mixed materials.

Use and Availability

We have developed Tricorder command files that are now analyzing for over 120 materials (including minerals, amorphous materials like weathering products, environmental materials like mine waste, vegetation, ice and snow, mineral mixtures, etc.). As the Tricorder code is refined, and as the number of spectra in our libraries increase, we will map for hundreds to thousands of materials at a time. Tricorder can now analyze individual laboratory spectra, field spectrometer data, as well as imaging spectrometer data like that from AVIRIS or other imaging spectrometers.

Because of the complexity involved in spectroscopic analysis, and therefore the necessary sophistication of Tricorder, having expert knowledge of spectroscopy is important to successfully use this algorithm. In addition, users must be knowledgeable with the Specpr software package (Clark, 1993). The user's guide for Tricorder is currently being written, and as soon as it is complete, the user's guide and the Tricorder code will be released. We anticipate that this release will occur in the first half of 1995, pending funding to complete the project. The capabilities of Tricorder, and examples of Tricorder products will be shown at the workshop.

References

Clark, R.N., A.J. Gallagher, and G.A. Swayze, Material absorption band depth mapping of imaging spectrometer data using a complete band shape least-squares fit with library reference spectra: *Proceedings of the Second Airborne Visible/Infrared Imaging Spectrometer (AVIRIS) Workshop*, JPL Publication 90-54, p. 176-186, 1990.

Clark, R.N., G.A. Swayze, A. Gallagher, N. Gorelick, and F. Kruse, Mapping with Imaging Spectrometer Data Using the Complete Band Shape Least-Squares Algorithm Simultaneously Fit to Multiple Spectral Features from Multiple Materials, *Proceedings of the Third Airborne Visible/Infrared Imaging Spectrometer (AVIRIS) Workshop*, JPL Publication 91-28, 2-3, 1991.

Clark, R.N., G.A. Swayze, A. Gallagher, T.V.V. King, and W.M. Calvin, The U. S. Geological Survey, Digital Spectral Library: Version 1: 0.2 to 3.0 µm, *U.S. Geological Survey, Open File Report 93-592*, 1340 pages, 1993. (Also being published as a USGS Bulletin, 1300+ pages, 1995 in press).

Calibration to Surface Reflectance of Terrestrial Imaging Spectrometry Data: Comparison of Methods

Roger N. Clark[1], Gregg A. Swayze[1], Kathy Heidebrecht[2],
Robert O. Green[3] and Alexander F.H. Goetz[2],

[1]U.S. Geological Survey
MS 964 Box 25046 Federal Ctn., Denver, CO 80225

[2]Center for the Study of Earth from Space (CSES)
Cooperative Institute for Research in Environmental Sciences (CIRES)
University of Colorado, Boulder, CO 80309-0449

[3]Jet Propulsion Laboratory
California Institute of Technology
4800 Oak Grove Drive, Pasadena, CA 91109

Many algorithms for spectral analysis of imaging spectroscopy data of the Earth's surface require that the data be calibrated to surface reflectance. Calibration requires removing instrumental response, solar irradiance, atmospheric transmittance, and atmospheric scattering from the radiance detected at the sensor. Depending on the amount of support data, this can be a formidable task. This paper examines four methods of calibration: 1) a radiative transfer model from the University of Colorado (ATREM: Gao and Goetz, 1990; Gao et al., 1992), 2) a MODTRAN-based method developed at the Jet Propulsion Lab by Green et al., (1991), 3) a ground calibration using known sites as standards, and 4) a combined approach using radiative transfer methods and ground calibration. Data from the Airborne Visual and Infra-Red Imaging Spectrometer (AVIRIS) instrument were evaluated from data sets obtained over multiple years and multiple sites.

Models that rely on solar irradiance alone contain serious errors. Experience with solar irradiance problems has led to a modification of the ATREM algorithm in 1993 to empirically correct for such problems. To date, the published solar irradiance spectra have disagreements of greater than $\pm 7\%$ at AVIRIS 1992 resolution and sampling. Unfortunately, these disagreements create spectral features of similar magnitude in calibrated spectra. Further, it is not clear which, if any, of the published solar irradiance measurements is correct. It is even possible that some of the spectral features in the solar spectrum are variable.

In general, the radiative transfer models produce good corrections of atmospheric transmission as a function of elevation throughout the scene. However, because of small errors in wavelength precision and resolution, a perfect correction will be difficult to achieve, even if the radiative transfer code predicted atmospheric transmission perfectly. Unknowns in the solar irradiance spectra add to the difficulty in achieving accurate calibration, as do errors in the instrument radiance calibration. The channel to channel variations in the radiative transfer methods limit effective signal to noise to about 30 to 60 for the current ATREM and 50 to 110 for Green's method (using 1993 data), depending on the wavelength region. Analysis of 1994 AVIRIS data, collected over Mountain Pass, California and calibrated using Green's method, show the effective signal to noise to be significantly higher. The advantage of the radiative transfer model is that it can be relatively quick computationally, and takes the least effort of the methods compared in this paper. We have also encountered conditions where the simplistic scattering treatment in the radiative transfer models was not sufficient to correct for the scattering observed in AVIRIS data.

The ground calibration method uses targets at the surface with known reflectance as standards and provides locally the best calibration to ground reflectance. Its inability to properly correct for topographic variations in atmospheric path results in elevation dependent residual atmospheric absorptions. It also requires high quality spectra (field or laboratory) of the ground sites, and 1 to 2 person-months of effort per calibration.

The hybrid method of radiative transfer model plus ground calibration produces the best overall result, providing good correction as a function of elevation, while removing artifacts from errors in the radiative models and solar spectrum. It requires the most effort.

References

Gao, B.C. and A.F.H. Goetz, C., "Column Atmospheric Water Vapor and Vegetation Liquid Water Retrievals From Airborne Imaging Spectrometer Data," *J. Geophys. Res.* **95**, 3549-3564.

Gao, B.C., K.B. Heidebrecht, A.F.H. Goetz, *ATmospheric REMoval Program (ATREM) User's Guide*, version 1.1, Center for the Study of Earth From Space, University of Colorado, 24pp., 1992.

Green, R.O., J.E. Conel, J.S. Margolis, C.J. Bruegge, and G.L. Hoover, "An Inversion Algorithm for Retrieval of Atmospheric and Leaf Water Absorption From AVIRIS Radiance With Compensation for Atmospheric Scattering," in *Proceedings of the Third Airborne Visible/Infrared Imaging Spectrometer (AVIRIS) Workshop*, JPL Pub. 91-28, Jet Propulsion Laboratory, Pasadena, CA, 51-61, 1991

Acknowledgement

CAUSAL CORRELATION OF FOLIAR BIOCHEMICAL CONCENTRATIONS WITH AVIRIS SPECTRA USING FORCED ENTRY LINEAR REGRESSION

Terence P. Dawson and Paul J. Curran
Department of Geography, University of Southampton, Southampton SO17 1BJ, UK.

John A. Kupiec
Scottish Natural Heritage, 2 Anderson Place, Edinburgh EH6 5NP, UK.

"Unguided multiple linear regression methods lack consistency in wavelength selection for a given constituent and can result in over-fitting of the data" (Aber, 1994).

1.0   Introduction

A major goal of airborne imaging spectrometry is to estimate the biochemical composition of vegetation canopies from reflectance spectra (Curran, 1994). Remotely-sensed estimates of foliar biochemical concentrations of forests would provide valuable indicators of ecosystem function at regional and eventually global scales. Empirical research has shown a relationship exisits between the amount of radiation reflected from absorption features and the concentration of given biochemicals in leaves and canopies (Matson et al., 1994, Johnson et al., 1994). A technique commonly used to determine which wavelengths have the strongest correlation with the biochemical of interest is unguided (stepwise) multiple regression. Wavelengths are entered into a multivariate regression equation, in their order of importance, each contributing to the reduction of the variance in the measured biochemical concentration. A significant problem with the use of stepwise regression for determining the correlation between biochemical concentration and spectra is that of 'overfitting' as there are significantly more wavebands than biochemical measurements. This could result in the selection of wavebands which may be more accurately attributable to noise or canopy effects. In addition, there is a real problem of collinearity in that the individual biochemical concentrations may covary. A strong correlation between the reflectance at a given wavelength and the concentration of a biochemical of interest, therefore, may be due to the effect of another biochemical which is closely related. Furthermore, it is not always possible to account for potentially suitable waveband omissions in the stepwise selection procedure.

This concern about the suitability of stepwise regression has been identified and acknowledged in a number of recent studies (Wessman et al., 1988, Curran, 1989, Curran et al., 1992, Peterson and Hubbard, 1992, Martin and Aber, 1994, Kupiec, 1994). These studies have pointed to the lack of a physical link between wavelengths chosen by stepwise regression and the biochemical of interest, and this in turn has cast doubts on the use of imaging spectrometry for the estimation of foliar biochemical concentrations at sites distant from the training sites. To investigate this problem, an analysis was conducted on the variation in canopy biochemical concentrations and reflectance spectra using forced entry linear regression.

2.0   Methods and Results

Our analysis was based upon an AVIRIS data set, together with foliage samples, collected from Gainesville, Florida in 1992. This site, comprising slash pine, provided 14 sample plots: 7 control and 7 fertilised. The biochemicals of interest were

nitrogen, lignin and cellulose and the concentration of these biochemicals, together with others, were measured from the 360 foliar samples using wet chemical assay techniques at the University of New Hampshire (Curran and Kupiec, 1995).
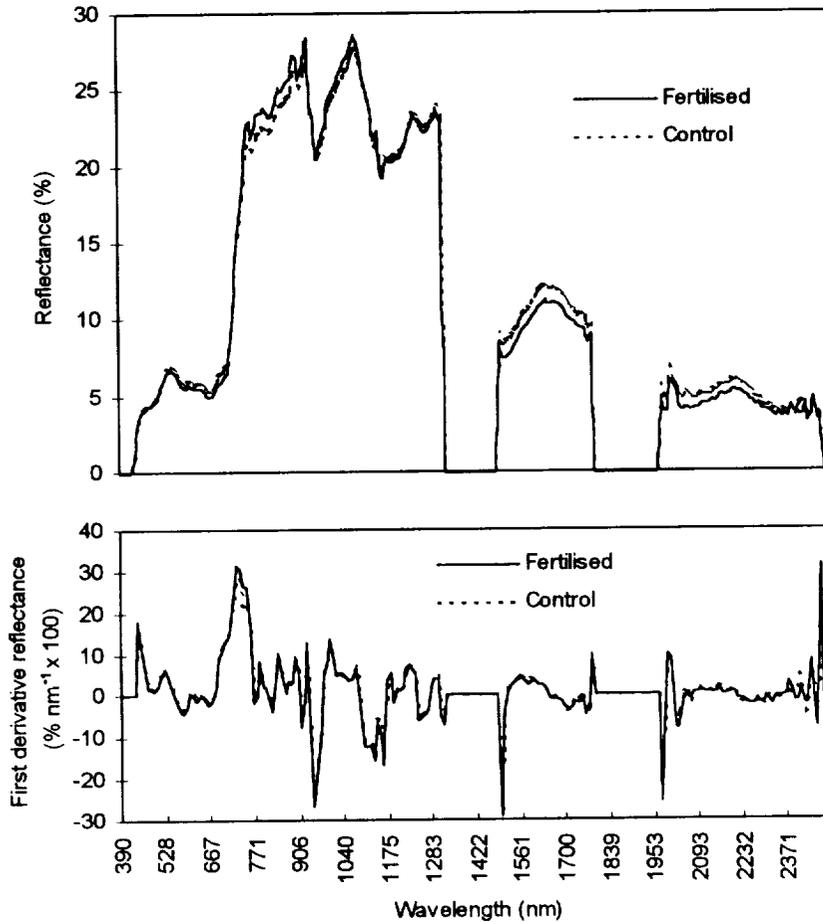
AVIRIS averaged spectra of slash pine.

Selected wavebands identified by Himmelsbach et al. (1988) were entered into a forced entry multivariate linear regression procedure (Norusis, 1992) for analysis of the AVIRIS data set. Himmelsbach's chemometric approach to the interpretation of spectral reflectance and associated biochemical absorption features is highly reliable and consistant having been derived from years of laboratory spectrophotometric experiments by the United States Department of Agriculture (USDA). These wavelengths are the known consequence of bending and stretching vibrations of the chemical bonds, together with their harmonics and overtones, between hydrogen and carbon, nitrogen and oxygen atoms causing spectral absorption in the 400 - 2400 nm spectral region. The five wavebands used were those with both (i) a known causal relationship between biochemical bond and reflectance and (ii) the largest partial correlation coefficient with the biochemical of interest. For the spectral data, a first derivative transformation was made on the selected AVIRIS imagery. This process reduces the effects caused by illumination changes and is widely used although there is an increase in the signal-to-noise ratio. The chosen AVIRIS data channels were within 10 nm of the 'Himmelsbach wavelengths'.

44

Nitrogen - Correlation coefficient, $R^2 = 0.85$

AVIRIS 1st derivative wavelength (nm)	'Himmelsbach wavelengths' (nm)	Chemical bond
1184.27 ± 8.98	1188	C-H Str. 2nd OT
1222.60 ± 8.98	1230	C-H Str. 2nd OT
1700.28 ± 9.81	1690	C-H Str. 1st OT
2162.56 ± 14.43	2168	2X Amide I + Amide III
2301.45 ± 14.58	2294	N-H Bend NH2 2nd OT

Lignin - Correlation coefficient, $R^2 = 0.83$

AVIRIS 1st derivative wavelength (nm)	'Himmelsbach wavelengths' (nm)	Chemical bond
1193.86 ± 8.98	1192	C-H Str. 2nd OT
1541.59 ± 9.63	1542	C=O Str. 3rd OT Aromatic O-H Str. 1st OT
2043.10 ± 14.19	2048	C=O Str. 2nd OT
2102.88 ± 14.32	2106	2X O-H Def. + 2X
2380.58 ± 14.62	2380	Aliphatic C-H Str. + Def.

Cellulose - Correlation coefficient, $R^2 = 0.48$

AVIRIS 1st derivative wavelength (nm)	'Himmelsbach wavelengths' (nm)	Chemical bond
1193.86 ± 8.98	1194	C-H Str. 2nd OT
1541.59 ± 9.63	1536	O-H Str. 1st OT (Intra H bond)
1739.90 ± 9.84	1736	C-H Str. 1st OT
1768.60 ± 9.86	1772	C-H Str. 1st OT
2350.92 ± 14.61	2356	C-H Dev. 2nd OT

3.0 Discussion

The use of airborne spectrometry for the investigation of canopy biochemical concentrations has raised questions about the statistical techniques used for locating those spectral absorption features that are related to biochemical concentrations. Using forced entry linear regression, based upon known absorption features, it has been possible to account for much of the variation in lignin and nitrogen concentrations and about half of the variation in cellulose concentration can be accounted for using the AVIRIS first derivative spectral reflectance. A problem with the AVIRIS data is that some of the important waveband features identified in the laboratory on dry samples could not be selected due to the lack of data in the major water absorption wavelengths (figure). It is interesting to note that other combinations of wavebands identified by Hemmelsbach can produce similar correlation coefficients for the above biochemicals. Whether this is the result of co-linear harmonics requires further investigation but increasing the number of identified wavebands in the regression equation does increase the R^2 suggesting that there may be a possibility that biochemical concentrations can indeed be reliably detected in airborne spectrometry reflectance. Future research requires the development of radiative tranfer models incorporating foliar biochemistry at the leaf and canopy scales to help our understanding of those effects.

45

4.0   Acknowledgements

5.0   References

Aber J. (ed.), 1994, *Accelerated Canopy Chemistry Program Final Report to NASA-EOS-IWG*, NASA - Washington, DC.

Curran P.J. and Kupiec J., 1995, "Imaging spectrometry: a new tool for ecology" In Danson F.M. and Plummer S.E. (eds) *Advances in Environmental Remote Sensing*, Wiley & Sons, Chichester (in press).

Curran P.J., 1994, "Imaging Spectrometry", *Progress in Physical Geography*, 18, 247-266.

Curran P.J., Dungan J.L., Macler B.A., Plummer S.E. and Peterson D.L., 1992, "Reflectrance spectroscopy of fresh whole leaves for the estimation of chemical concentration", *Remote Sensing of Environment*, 39, 153 - 166.

Curran P.J., 1989, "Remote sensing of foliar chemistry", *Remote Sensing of Environment*, 30, 271 - 278.

Himmelsbach D.S., Boer H., Akin D.E. and Barton II F.E., 1988, "Solid-state carbon-13 NMR, FTIR and NIR spectroscopic studies of ruminant silage digestion" in C.S. Erand and A.M.D. Davies (eds.), *Analytical Applications of Spectroscopy*, Royal Society of Chemistry, London, England, 410-413.

Johnson L.F., Hlavka C.A. and Peterson D.L., 1994, "Multivariate analysis of AVIRIS data for canopy biochemical estimation along the Oregon transect", *Remote Sensing of Environment*, 47, 216 - 230.

Kupiec J.A., 1994, *The Remote Sensing of Foliar Chemistry*, Ph.D. Thesis, University College of Wales, Swansea.

Martin M.E. and Aber J.D., 1994, "The Study of Forest Ecosystems Through the Remote Sensing of Canopy Chemistry", *Accelerated Canopy Chemistry Program Final Report to NASA-EOS-IWG*, NASA - Washington, DC.

Matson P., Johnson L.F., Billow C., Miller J. and Pu R., 1994, "Seasonal patterns and remote spectral estimation of canopy chemistry across the Oregon transect", *Ecological Applications*, 4, 280 - 298.

Norusis M.J., 1992, *SPSS for Windows Base Systems User's Guide 5.0*, Prentice Hall, London, 303 - 357.

Peterson D.L. and Hubbard S., 1992, "Scientific issues and potential remote-sensing requirements for plant biochemical content", *Journal of Imaging Science and Technology*, 36, 5, 446 - 456.

Peterson D.L., 1991, *"Report on the Workshop Remote Sensing of Plant Biochemical Content: Theoretical and Empirical Studies"*, NASA-Ames Research Center, Mountain View, CA.

Wessman C.A., Aber J.D., Peterson D.L. and Melillo J.M., 1988, "Remote sensing of canopy chemistry and nitrogen cycling in temperate forest ecosystems", *Nature* 335, 8, 154-156.

MINERALOGIC VARIATIONS IN FLUVIAL SEDIMENTS CONTAMINATED BY MINE TAILINGS AS DETERMINED FROM AVIRIS DATA, COEUR D'ALENE RIVER VALLEY, IDAHO

W.H. Farrand[1] and Joseph C. Harsanyi[2]

1) Science Applications International Corporation
1710 Goodridge Drive, P.O. Box 1303, M.S. E-7-3
McLean, VA 22102

2) Applied Signal and Image Technology Co.
9193 Rolling Meadow Run
Pasadena, MD 21122

1.0 INTRODUCTION

The success of imaging spectrometry in mineralogic mapping of natural terrains (e.g., Clark et al., 1992) indicates that the technology can also be used to assess the environmental impact of human activities in certain instances. Specifically, this paper describes an investigation into the use of data from the Airborne Visible/Infrared Imaging Spectrometer (AVIRIS) for mapping the spread of, and assessing changes in, the mineralogic character of tailings from a major silver and base metal mining district.

The area under investigation is the Coeur d'Alene river valley in northern Idaho. Mining has been going on in and around the towns of Kellogg and Wallace, Idaho since the 1880's. In the Kellogg-Smelterville Flats area, west of Kellogg, mine tailings were piled alongside the South Fork of the Coeur d'Alene River. Until the construction of tailings ponds in 1968 much of these waste materials were washed directly into the South Fork. The Kellogg-Smelterville area was declared an EPA Superfund site in 1983 and remediation efforts are currently underway. Recent studies (e.g., Horowitz et al., 1992) have demonstrated that sediments in the Coeur d'Alene River and in the northern part of Lake Coeur d'Alene, into which the river flows, are highly enriched in Ag, Cu, Pb, Zn, Cd, Hg, As, and Sb. These trace metals have become aggregated in iron oxide and oxyhydroxide minerals and/or mineraloids. Reflectance spectra of iron-rich tailing materials are shown in Figure 1. Also shown in Figure 1 are spectra of hematite and goethite. The broad bandwidth and long band center (near 1 μm) of the Fe^{3+} crystal-field band of the iron-rich sediment samples combined with the lack of features on the Fe^{3+}-O^{2-} charge transfer absorption edge indicates that the ferric oxide and/or oxyhydroxide in these sediments is poorly crystalline to amorphous in character. Similar features are seen in poorly crystalline basaltic weathering products (e.g., palagonites).

The problem of mapping and analyzing the downriver occurences of iron rich tailings in the Coeur d'Alene (CDA) River Valley using remotely sensed data is complicated by the full vegetation cover present in the area. Because exposures of rock and soil were sparse, the data processing techniques used in this study were sensitive to detecting materials at subpixel scales. The methods used included spectral mixture analysis (Adams et al., 1993) and a constrained energy minimization technique (Farrand and Harsanyi, 1994a).

2.0 DATA

The CDA River Valley is currently under investigation by the Spokane field office of the USGS (C. Smith, pers. comm.). In a cooperative endeavor between the USGS, the EPA and the Naval Research Laboratory's HYDICE (Hyperspectral Digital Imagery Collection Experiment) Project Office an AVIRIS flight was scheduled over the

CDA River Valley. Data was collected on May 24, 1993 at 21:40 UTC. Incomplete coverage of the target area led to a reflight on September 17 at 19:40 UTC. An earlier paper (Farrand and Harsanyi, 1994b) presented a preliminary examination of two scenes from the May collection. The current paper considers three scenes from the September collection that cover an area extending down river from approximately Smelterville to Killarney Lake (see Figure 2).

The reflectance of samples collected in the field were measured in the laboratory. A subset of the samples were measured at Brown University's RELAB. The majority of the samples were measured on the USGS Reston Beckman (UV5240).

The AVIRIS data were analyzed in a radiometrically calibrated format and also in a format with DN equal to apparent surface reflectance. The conversion from radiance to reflectance was done using both surface reflectance data and the ATREM (Gao et al., 1993) radiative transfer based approach. First the data were converted to apparent surface reflectance through the use of ATREM which effectively removed atmospheric variability. This was followed by the application of a modified flat field (MFF) method (Farrand, 1992) applied to the ATREM corrected data which acted to remove instrumental noise that is retained in the ATREM correction.

3.0   ANALYSIS

The AVIRIS radiance data were initially examined with spectral mixture analysis. An iterative approach utilizing several runs and successive examination of the resulting RMS error images (Adams et al., 1993) suggested four endmembers: shade, vegetation, an agricultural soil, and an iron oxide or oxyhydroxide rich soil. As was discussed above, the iron-rich soil is the most likely candidate for bearing heavy metals leached from the mine tailings. In the fraction image for this endmember, other materials besides the ferruginous soil (for instance, the pavement on I-90) appeared bright on the fraction image.

In order to cut down on the false alarm rate, a recently developed detection algorithm that has already shown good success in detecting distributed subpixel target materials, the constrained energy minimization (CEM) technique (Farrand and Harsanyi, 1994b), was applied to the data. The key to the CEM technique is to determine a vector operator, w composed of weights ($w_1...w_m$) that suppresses the unknown and undesired background spectra while enhancing the target spectrum d. The summed pixel energy can be represented by a scalar value y_i. The CEM operator is defined by two constraints. The first constraint, for any given pixel, is to minimize the energy summed across the wavelength range (e.g., minimize y_i). The second constraint is that when applied to the target spectrum, $y_i = 1$, e.g., $w^Td=1$.

CEM was applied to subsections of the three AVIRIS scenes. The target spectrum for input to the CEM routine was derived from the data itself. Three pixels most like the BH-3 sample spectrum shown in Figure 1 were identified. The radiance spectra of these pixels were then extracted from a radiance data set that was subsectioned to 188 bands to exclude several of the shortest and longest wavelength bands, spectrometer overlap regions and atmospheric water absorptions at 1.4 and 1.9 μm. These radiance spectra were averaged and the average was used as input to the CEM routine. As might be expected, the resulting CEM component images showed that the iron-rich sediments are concentrated primarily along the CDA River. There were also known concentrations of tailings in a dump west of Smelterville. Weaker responses are returned from some fields in the CDA River Valley.

The CEM routine identified 159 pixels in the three scenes that were most like the iron-rich sediments at Cataldo Flats. These pixels were then extracted from the ATREM+MFF corrected data cube and transformed via a principal components analysis (PCA). The PCA was applied in two parts. 88 VNIR channels were analyzed separately

48

from 45 SWIR channels. This was done because iron bearing minerals primarily have features in the VNIR and clay minerals primarily have features in the SWIR. By separating the analyses, the resulting intrinsic dimensionality of the data set could be kept to a manageable number of endmembers (e.g., 3 to 4). For purposes of brevity only the VNIR analysis will be discussed here.

The first three principal components of the VNIR analysis were examined interactively using the "XGobi" data visualization program (Swayne et al., 1992). By rotating the data cloud, spectrally extreme endmember pixels could be identified. Two distinct linear trends revealed themselves outlining two ridges of a tetrahedron. Pixel spectra from the ends of these trends (i.e., the vertices of the tetrahedron) are shown in Figure 3. Although the PCA was done on only the first 88 channels, the full spectral range is shown in Figure 3 since, as it turns out, there is extra information to be gained from the SWIR region as well. Figure 3 reveals two similar appearing, but nonetheless distinct, sets of spectra. Both trends have one endmember with a strong "1 μm" Fe crystal field absorption feature and one with only a weak absorption at that wavelength. The spectra, t2em1 and t2em2 appear to be wetter with stronger 1.4 and 1.9 μm absorption features. These spectra also display absorptions indicative of gypsum at 1.48, 1.53 and longwards of 1.7 μm. The presence of the sulfate mineral, gypsum, lends further credence to the interpretation that the ferruginous sediments are contaminated by mine wastes.

4.0   CONCLUSIONS

These results provide encouragement that imaging spectrometer data can be used effectively both to track the spread of fluvially distributed mine tailings and to provide insight into changes in their mineralogic character. An enabling algorithm that aids significantly in this process is the constrained energy minimization technique which, in this instance, provided a unique identification of the ferruginous sediments associated with mine waste contamination.

5.0   REFERENCES

Adams, J.B., M.O. Smith, and A.R. Gillespie,1993, Imaging spectroscopy: Interpretation based on spectral mixture analysis. in *Remote Geochemical Analysis: Elemental and Mineralogical Composition*, (C.M. Pieters and P.A.J. Englert, ed.s), Cambridge University Press, New York, pp. 145-166.

Clark, R.N., G.A. Swayze, and A.J. Gallagher, 1992, Mapping the mineralogy and lithology of Canyonlands, Utah with imaging spectrometer data and the multiple spectral feature matching algorithm. in *Summaries of the Third Annual JPL Airborne Geoscience Workshop: AVIRIS* JPL Publ. 92-14, 11-13.

Farrand, W.H., 1992, A comparison of methods for retrieving apparent surface reflectance from hyperspectral data. *Proceedings of the International Symposium on Spectral Sensing Research*, pp.1154-1164.

Farrand, W.H. and J.C. Harsanyi, 1994a, Mapping distributed geological and botanical targets through constrained energy minimization. *Proc. Thematic Conf. Geol. Remote Sens. 10th*, 419-429.

Farrand, W.H. and J.C. Harsanyi, 1994b, An examination of mine waste contamination in the Coeur D'Alene River Valley, Idaho using imaging spectrometer data. in *Proc. ISSSR '94* (in press).

Gao, B.-C., K.B. Heidebrecht, and A.F.H. Goetz, 1993, Derivation of scaled surface reflectances from AVIRIS data. *Rem. Sens. Env.* **44**, 165-178.

Horowitz, A., K.A. Elrick, and R.B. Cook, 1992, Effect of mining related activities on the sediment trace element geochemistry of Lake Coeur d'Alene, Idaho, USA: Part 1. Surface sediments, U.S. Geological Survey Open-file Report 92-109, 30 pp.

Swayne, D.F., D. Cook and A. Buja, 1992, User's manual for XGobi, *Bellcore Technical Memorandum*
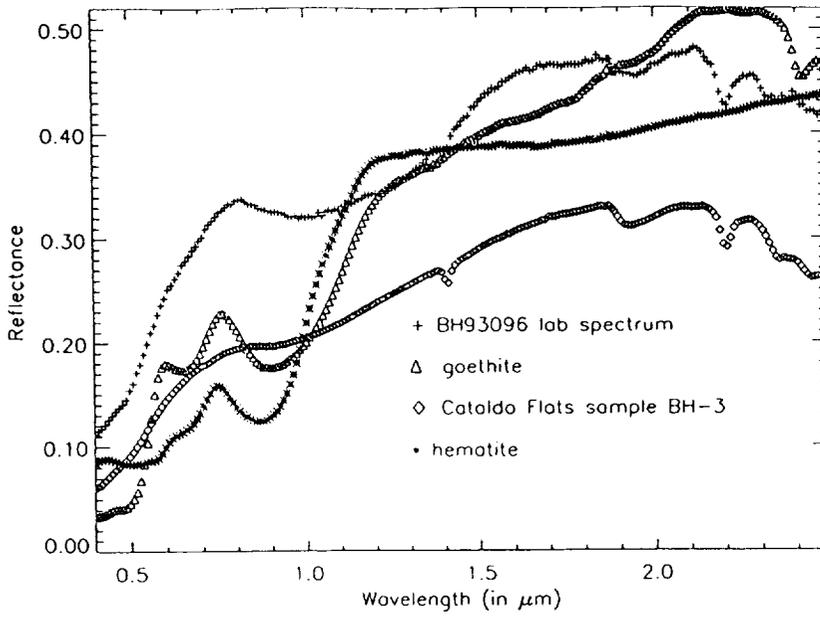
Figure 1. Laboratory reflectance spectra of iron-rich sediments collected near the Coeur d'Alene River compared against library spectra of goethite and hematite.
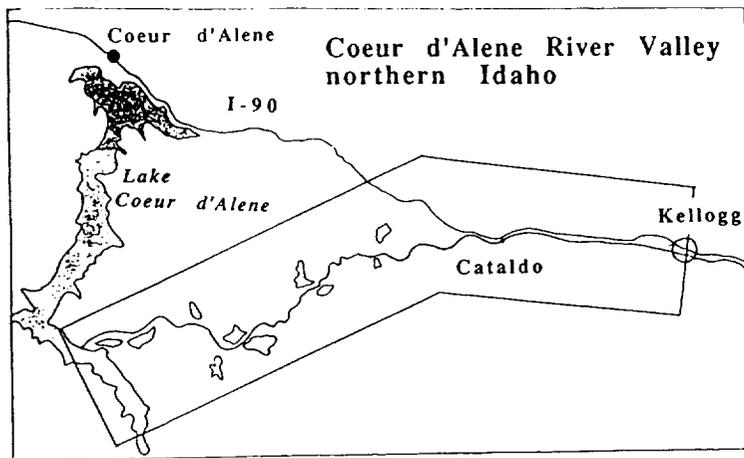
Figure 2. Sketch map of Coeur d'Alene River Valley in northern Idaho. The AVIRIS flightlines are outlined by the box.
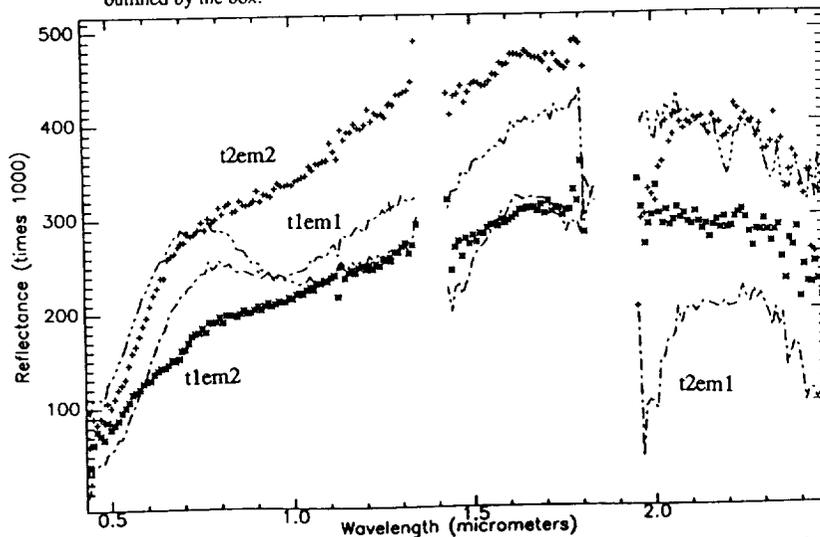
Figure 3. Iron-rich sediment endmembers determined from PCA of VNIR channels and interactive data analysis.

50

A LAYERED APPROACH TO TECHNOLOGY TRANSFER OF AVIRIS BETWEEN EARTH SEARCH SCIENCES, INC. AND THE IDAHO NATIONAL ENGINEERING LABORATORY

James S. Ferguson, JoAnne E. Ferguson, John Peel, III., and Larry Vance

1. GENERAL

Since initial contact between Earth Search Sciences, Inc. (ESSI) and the Idaho National Engineering Laboratory (INEL) in February, 1994, at least seven proposals have been submitted in response to a variety of solicitations to commercialize and improve the AVIRIS instrument. These proposals, matching ESSI's unique position with respect to agreements with the National Aeronautics and Space Administration (NASA) and the Jet Propulsion Laboratory (JPL) to utilize, miniaturize, and commercialize the AVIRIS instrument and platform, are combined with the applied engineering of the INEL. Teaming ESSI, NASA/JPL, and INEL with diverse industrial partners has strengthened the respective proposals. These efforts carefully structure the overall project plans to ensure the development, demonstration, and deployment of this concept to the national and international arenas.

The objectives of these efforts include:

- developing a miniaturized commercial, real-time, cost effective version of the AVIRIS instrument
- identifying multiple uses for AVIRIS
- integrating the AVIRIS technology with other technologies
- gaining the confidence/acceptance of other government agencies and private industry in AVIRIS, and
- increasing the technology base of U.S. industry.

1.1 History.

The initial contact between ESSI and INEL began in February 1994, as ESSI was involved in discussions with the Idaho Department of Commerce (IDOC). ESSI, a small business within the state, approached the IDOC with a need for assistance from a large institution with the capability to develop a miniaturized version of the AVIRIS instrument that could be deployed on a commercial airborne platform. ESSI had an agreement under the Space Act to utilize the AVIRIS instrument for mineral exploration since 1987. ESSI had been working with NASA and JPL to improve the instrument, verifying and validating the results of the overflights as they were made. ESSI also concluded an agreement with NASA/JPL to re-deploy the AVIRIS from the ER-2 flight platform to NASA's C-130, fuse the AVIRIS data with that of other sensors on the C-130 platform, and to miniaturize and commercialize the instrument for use throughout the world. With an array of industrial partners in the U.S. and from other countries, ESSI assembled a world class team of potential partners who can provide unique capabilities for applications. TRW, Inc. joined the group in May 1994. In June, 1994, Tetra Tech, Inc., joined the ESSI and INEL efforts, adding their significant remote sensing and environmental reputation and expertise to the efforts. Tetra Tech is rated seventh of the top 200 small businesses in the United States by Forbes Magazine. Lockheed and several other firms followed Tetra Tech in October 1994, forming a team to use AVIRIS in Kazakhstan as a major cornerstone in the United States policy to convert defense industries to commercial entities. This has

been followed by the U.S. Environmental Protection Agency participating in a demonstration of the technology for environmental assessment and monitoring of large areas in place of traditional sampling methods. U.S. commercial and agricultural industries also expressed an interest in using the same technology to assess areas prior to purchase and to monitor existing operations. Today, the education community is attracted to the field of remote sensing and is using AVIRIS as a technical cornerstone to establish an international Remote Sensing Center of Excellence accompanied by graduate degree programs and a dedicated testing center in excess of 4,000 square miles at the University of Idaho.

1.2 Teaming.

As a small business, publicly-held, but sold in the penny stock market, ESSI has severely-limited funds to bring to the venture. Seeking funds from other partners or through joint solicitations with other federal agencies and federal entities is the primary means of securing capital. Signing Memorandums of Agreement (MOA), negotiating Cooperative Research and Development Agreements (CRADAs), and concluding Teaming Agreements with government and private industry has been the preferred route for ESSI to protect the intellectual property rights to the technology. These arrangements have increased the leveraging of funds and expanded the potential business opportunities. Business plans between team members are used to share the division of labor and profit.

2. PROPOSAL SOLICITATIONS

2.1 Advanced Projects Research Agency (ARPA) Technology Reinvestment Project (TRP).

This proposal was initiated to develop dual-use hyperspectral instruments for environmental, agricultural, mining, forestry and specific Department of Defense applications requiring unique signature identification. This $6M proposal involves the design and construction of a real-time, miniaturized, commercial prototype hyperspectral instrument and developing a new family of hyperspectral instruments with industrial firms, including: TRW, Inc., Earth Search Science, Inc. (ESSI), National Aeronautic and Space Administration (NASA), Jet Propulsion Laboratories (JPL), WJT Software, Integrated Spectronics PTY, CALTECH, and EG&G Idaho. A MOA between TRW, Inc, Earth Search Science, Inc., NASA/JPL, and EG&G Idaho, Inc., was concluded between the partners. Upon award, a Teaming Agreement and a Business Plan will be produced.

2.2 Rocky Flats Request for Proposals.

This request resulted in another proposal entitled "Aerial Multispectral Sensor Platform for the Detection of Rocky Flats Hazardous (including Radiological) and Toxic Wastes". This $1.4M effort proposes to characterize both hazardous (including radiological) and toxic wastes surveyed from an airborne multisensor platform at hovering altitudes, mid-level altitudes (30,00 ft.), and high altitudes (>60,00 ft.). The airborne platforms will be enhanced with non-radiological sensing capability, including, but not limited to, thermal imaging to detect vegetal stress, seeps, and other hydrological features; laser induced fluorescence; and electromagnetic imaging/magnetometer/ground penetrating radar coupled to video to provide better arrays and overcome the limitations of separate sensors. Data fusion, data compression, and data management are project keystones. All data collected in the flyovers will be fused into a geographic information system (GIS) data base. These

data will be used in the site-wide management information system affecting the environmental remediation of Rocky Flats Plant. A MOA was concluded between the partners. When an award is announced, a CRADA with the INEL will be executed.

2.3 Environmental Protection Agency (EPA) Environmental Technology Initiative (ETI).

This is a $700K proposal to use the Fort Hall Indian Reservation as a demonstration site to evaluate the current monitoring capabilities and development needs of hyperspectral instruments used for environmental purposes. The technology demonstration will also be used to identify the extent of recurring pollution on the reservation (nitrates, ethylene dibromide, and assorted pesticides and herbicides). Non-point-source pollution cannot be adequately addressed by traditional sampling methods. Partners include the Shoshone-Bannock Tribe, the INEL, EPA, NASA/JPL, and Earth Search Sciences, Inc. (ESSI). EPA funding is being leveraged with ESSI providing $3.5K. An MOA was concluded by the team to demonstrate the airborne multisensor platform and train Shoshone-Bannock Tribe personnel to use GIS to manage the reservation resources. When an award is announced, a CRADA will be executed.

2.4 EPA Requested Flyover of the San Jacinto River.

In October 1994, EPA requested ESSI's assistance to use the AVIRIS to assess the environmental impact of a gasoline pipeline break in the Houston, Texas area. With demonstration of the technology for environmental purposes over large land areas, EPA has indicated that remote sensing may be substituted for traditional, expensive and time-consuming sampling procedures. This may include monitoring the environmental status of the Gulf of Mexico coast and the U.S.-Mexico border area.

2.5 Retrofit of the AVIRIS to the NASA/JPL C-130 Multisensor Platform.

In October 1994, ESSI obtained JPL support to retrofit the AVIRIS instrument to the NASA C-130 aircraft. This will enable the AVIRIS instrument to collect 5 by 5 meter pixel data flying at 5,000 meter AGL, a 16-fold increase in spatial resolution over the resolution available currently with the ER-2 aircraft.

2.6 International Remote Sensing Center of Excellence.

The international Remote Sensing Center of Excellence's mission is to support watershed/river basin management as it affects all biota. Idaho was selected because the state is rich in potential sensor services users and developers and offers a natural laboratory for sensor platform testing and evaluation. The potential client base includes agriculture, range management, fisheries, mining, forestry, wildlife management, and human engineering.

2.7 Defense Nuclear Agency Defense Industry Conversion Solicitation.

This $11M proposal is to use hyperspectral and multispectral imaging to explore for minerals, perform environmental assessments, manage national industries, such as agriculture and forestry, natural resource management, and land use planning for the Republic of Kazakhstan. The teaming arrangement, which consists of Lockheed Environmental Systems and Technologies, ESSI, Tetra Tech, Inc., Ramparts Technologies, Lockheed Idaho Technologies Company, NASA/JPL, EG&G Measurements, Las Vegas, Bishop Associates, SEMTECH (Kazakhstan industry partner), and Scientech, plans to begin operations in January 1995.

53

2.8 Latin America Initiative.

Several proposals have been developed to partner with industry, universities, and State and Federal agencies to develop, package, and deliver Department of Energy and ESSI competitive advanced technology products/services. This approach provides solutions to critical environmental restoration and waste management problems while furthering national business and technology goals. The proposals include providing environmental management education and training services to build an infrastructure in Mexico and are planned for expansion to Chile and Argentina. Use of the AVIRIS and other non-intrusive remote sensing technologies provides the technical foundation for this effort.

3. FUTURE PLANS

3.1 Solicitation Plans.

Through teaming with other firms, ESSI plans to continue to respond to future solicitations. This allows them to identify possible technology applications for remote sensing which far exceed it current capability to fulfill. Current partners include three firms based in the Washington DC area. One centers its efforts on federal government opportunities, the second focuses on international opportunities, and the third on major corporations which have remote sensing requirements. Where possible, these firms are included as teaming partners in proposals. None require up front financing to obtain potential remote sensing applications. All potential partners agree to allow ESSI to establish offices with little or no overhead costs, gain access to new markets, and obtain the services of other firms' marketing capabilities of products and services.

3.2 Relocation Plans.

ESSI is evaluating opportunities in relocating to southeast Idaho to more fully use national laboratory assets. National laboratories now offer a variety of services to small businesses. These range from CRADAs to use of the laboratory's staff and laboratories to being awarded contracts identified solely for small business. Ten percent of INEL's FY-95 $1B budget is committed to small and minority businesses.

4. INTELLECTUAL PROPERTY PROTECTION IN US AND INTERNATIONAL ARENAS

ESSI current projects and outstanding funding proposals were reviewed by patent attorneys to determine appropriate actions to protect their intellectual property through patents, trademarks, an copyrights. Applications have been initiated to obtain patents for equipment, processes, and new applications of single and multiple remote sensing systems. Protection of intellectual property has been included in all Memorandums of Agreement, Teaming Agreements, and proposals. Other methods are also being used, such as the CRADA which allows commercially valuable data generated to be withheld from public release for up to five years, and teaming with firms currently doing business in international arenas.

5. CONCLUSION

ESSI has developed an approach to a costly technology development program that fully leverages the resources of others while retaining ownership, technical application and control, and management direction.

EVALUATION OF THE PHOTOCHEMICAL REFLECTANCE INDEX IN AVIRIS IMAGERY

John A. Gamon[1], Dar A. Roberts[2], and Robert O. Green[3]

[1]Department of Biology & Microbiology
California State University, Los Angeles
5151 State University Drive
Los Angeles, CA 90032

[2]Department of Geography
University of California, Santa Barbara
Santa Barbara, CA 93106

[3]Jet Propulsion Laboratory
California Institute of Technology
4800 Oak Grove Drive
Pasadena, CA 91109

1. INTRODUCTION

In this paper, we evaluate the potential for extracting the "photochemical reflectance index" (PRI; previously called the "physiological reflectance index") from AVIRIS data. This index, which is derived from narrow-band reflectance at 531 and 570 nm, has proven to be a useful indicator of photosynthetic function at the leaf and canopy scales (Gamon and Field 1992, Gamon et al. 1992, Peñuelas et al. *in review*).

At the leaf level, PRI varies with photosynthetic capacity, radiation-use efficiency, and vegetation type (unpublished data). This finding is consistent with the hypothesis that vegetation types exhibiting chronically reduced photosynthesis during periods of stress (e.g. drought-tolerant evergreens) invest proportionally more in photoprotective processes than vegetation with high photosynthetic capacity (e.g. crops or deciduous perennials).

Vertical transects in tropical and boreal forest canopies have indicated declines in PRI associated with downregulation of photosynthesis at the canopy tops under sunny, dry midday conditions (unpublished data). This reduced PRI in upper canopy levels provides a further basis for examining this signal with the "view from above" afforded by aircraft overflights.

Although many factors could confound interpretation of a subtle physiological signal at the landscape scale, we conducted a preliminary examination of PRI extracted from existing AVIRIS imagery of Stanford University's Jasper Ridge Biological Preserve obtained on the June 2nd, 1992, overflight. The goal was to use the hyperspectral capabilities of AVIRIS to evaluate the potential of this index for obtaining useful physiological data at the landscape scale. The expectation based on leaf- and canopy-level studies was that regions containing vegetation of reduced photosynthetic capacity (e.g. chaparral or evergreen woodland) would exhibit lower PRI values than regions of high capacity (e.g. deciduous woodland).

2. METHODS

In this study, PRI was calculated as follows:

$$PRI = (R_{528} - R_{567})/(R_{528} + R_{567}) \qquad (1)$$

Where R_{528} and R_{567} indicate reflectance at AVIRIS bands 15 (528 nm) and 19 (567 nm), respectively. These represent the AVIRIS bands closest to 531 and 570 nm, which are typically used for this index.

The Normalized Difference Vegetation Index (NDVI), a widely used canopy greenness indicator, was calculated as:

$$NDVI = (R_{831} - R_{667})/(R_{831} + R_{667})$$ (2)

Where R_{831} and R_{667} indicate reflectance at AVIRIS bands 49 (831 nm) and 29 (667 nm), respectively. A portion of an AVIRIS spectrum for the deciduous woodland is illustrated in Figure 1, along with the bands used for calculating PRI and NDVI.

Reflectance images were derived using the approach described by Green et al. (1993a &b). This approach uses MODTRAN II radiative transfer code to generate a series of look-up tables for an AVIRIS scene collected at a specific latitude and longitude on a specific date. Look-up tables are generated for a black target and for a 25% reflective target. Radiance estimated for the black target provides an estimate of the additive path radiance. For this analysis aerosol optical depth was estimated and assumed to be constant across the scene. Once the look-up tables are generated a non-linear least squares fitting routine is employed to invert radiance measured at the sensor and solve for atmospheric column water vapor abundance and liquid water absorption. This approach is applied to each element in the scene to produce images showing liquid water and water vapor abundance. Once atmospheric column water vapor abundance has been determined for a specific element, reflectance can be retrieved using the general equation:

$$R_{ij\lambda} = 0.25 \times (L_{ij\lambda} - L_{\lambda_{p'}})/(L_{\lambda'} - L_{\lambda_{p'}})$$ (3)

Where $R_{ij\lambda}$ indicates reflectance at sample i, line j, and wavelength λ; $L_{ij\lambda}$ is the measured radiance at the sensor; $L_{\lambda_{p'}}$ is the modeled path radiance; and $L_{\lambda'}$ is the modeled radiance at the sensor for a 25% reflective target (at an estimated water vapor abundance). For this analysis water vapor was estimated from the 940 nm water vapor band.

3. RESULTS & DISCUSSION

As predicted, the PRI values from the Jasper Ridge AVIRIS scene were lower in vegetation with reduced photosynthetic capacity (e.g. chaparral and evergreen woodland) than in the high-capacity vegetation (deciduous woodland). The two grassland types, which were largely comprised of senescent vegetation by this date, had the lowest PRI values (Figure 2). These results were consistent with the hypothesis (based on prior, leaf-level studies) that PRI scales with photosynthetic capacity and radiation-use efficiency in a wide variety of species.

In addition to photosynthetic function, many other factors (including canopy structure, phenology, and atmospheric effects) could explain the PRI patterns in Jasper Ridge imagery. PRI varied with canopy "greenness" (measured by NDVI; Figure 2), suggesting that PRI was strongly influenced by canopy structure and phenology at the landscape scale. Clearly, the spectral region (AVIRIS bands 15 and 19) used for PRI calculation presents technical challenges to a simple interpretation of this index in landscape imagery. Until these confounding issues are resolved, PRI appears to be more directly applicable to laboratory and ground-based field studies than to landscape-level remote sensing.

Further research will clarify the relative influence of photosynthetic regulation, canopy structure and phenology, atmospheric effects, and other factors on PRI. Approaches for resolving these issues might include mixture modeling or other image classification methods. Application of canopy radiative transfer models could also be of use. Further field experiments combining ground optical sampling (e.g. using access towers) with CO_2 flux measurements (e.g. eddy covariance) are also warranted. Our current plans are to address some of these remaining issues using AVIRIS imagery and other measurements obtained from recent Jasper Ridge and boreal forest overflights.

4. REFERENCES

Gamon, J.A. and Field, C.B. (1992) Tracking photosynthetic efficiency with narrow-band spectroradiometry. *Summaries of the Third Annual JPL Airborne Geoscience Workshop*, Vol. 1, JPL Pub. 92-14, Jet Propulsion Laboratory, Pasadena, CA, June 1992, pp. 95–97.

Gamon, J.A., Peñuelas, J., and Field, C.B. (1992) A narrow-waveband spectral index that tracks diurnal changes in photosynthetic efficiency. *Remote Sensing of Environment.* Vol. 41, pp. 35–44.

Green, R.O., Conel, J.E., and Roberts, D.A., 1993a, Estimation of aerosol optical depth pressure elevation, water vapor and calculation of apparent surface reflectance from radiance measured by the Airborne Visible-Infrared Imaging Spectrometer (AVIRIS) using MODTRAN2, SPIE Conference Vol. 1937 (Imaging Spectrometry of the Terrestrial Environment), pp. 2–11.

Green, R.O., Conel, J.E., and Roberts, D.A., 1993b, Estimation of aerosol optical depth and additional atmospheric parameters for the calculation of apparent reflectance from radiance measured by the Airborne Visible/Infrared Imaging Spectrometer, Summaries of the 4th Annual JPL Airborne Geoscience Workshop, Oct. 25–29, 1993, Washington, D.C., JPL Pub. 93-26, Jet Propulsion Lab, Pasadena, CA, Vol. 1. AVIRIS Workshop, pp. 73–76.

Peñuelas, J., Filella, I., and Gamon, J.A.. (in review) Assessment of photosynthetic radiation-use efficiency with spectral reflectance, *Plant, Cell and Environment.*
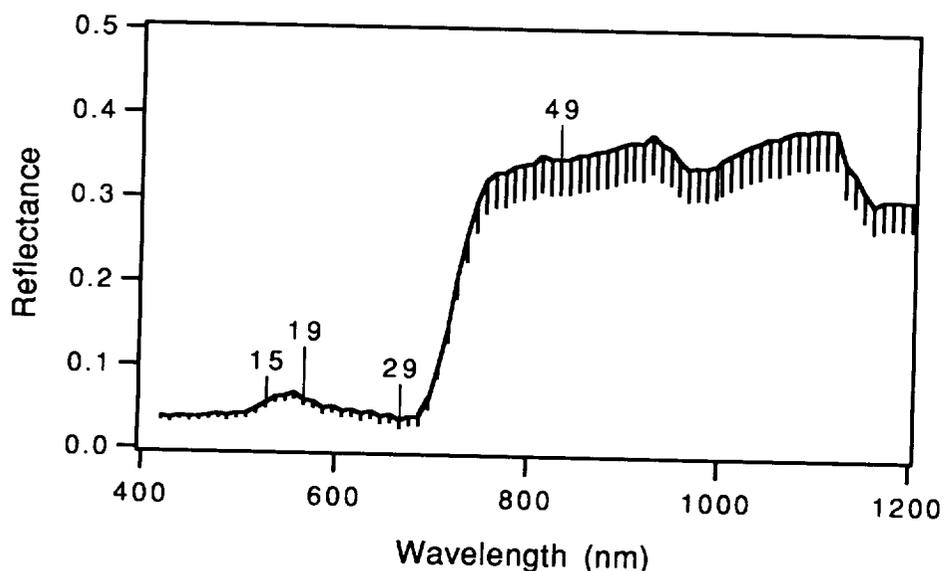
Figure 1. Representative AVIRIS spectrum (average of 10 pixels) for a deciduous woodland at Jasper Ridge. The AVIRIS bands used for calculating PRI (bands 15 and 19) and NDVI (bands 29 and 49) are indicated. Error bars indicate 1 standard error of the mean (SEM).
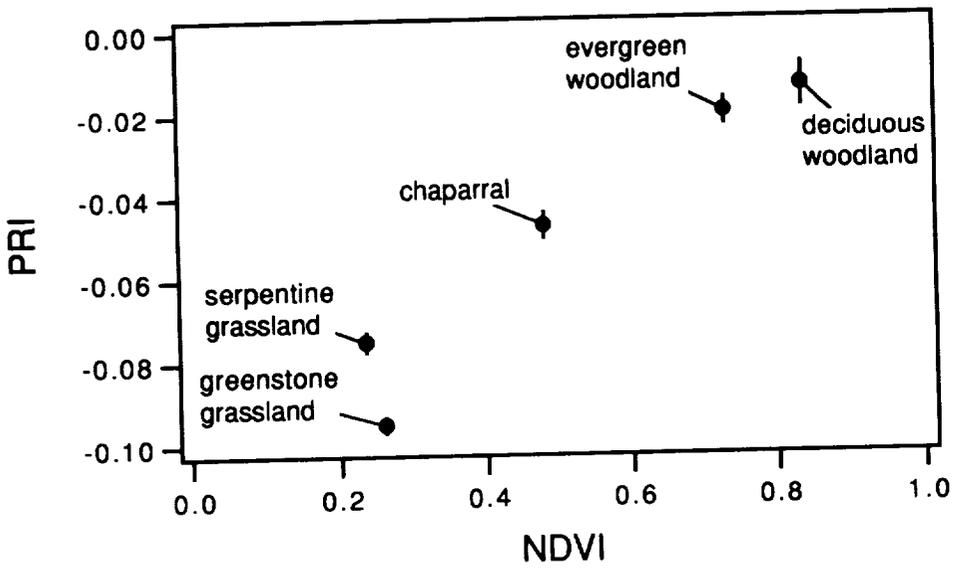
Figure 2. Comparison of PRI with NDVI values for five vegetation types at Jasper Ridge. Each point represents the mean ($\pm$ 1 SEM) for 10 pixels. As predicted from leaf-level studies (not shown), PRI increases with photosynthetic capacity and radiation-use efficiency, with woodland vegetation exhibiting relatively high capacity and efficiency compared to chaparral or grassland. However, the correlation of PRI with NDVI suggests that the relationship between PRI and photosynthetic function is largely driven by green canopy structure in this AVIRIS image.

5. ACKNOWLEDGMENT

CORRECTION OF THIN CIRRUS EFFECTS IN AVIRIS IMAGES USING THE SENSITIVE 1.375-μm CIRRUS DETECTING CHANNEL

Bo-Cai Gao[1], and Yoram J. Kaufman[2]

[1]USRA, Code 913, NASA Goddard Space Flight Center, Greenbelt, MD 20771
[2]Climate and Radiation Branch, Code 913, NASA/GSFC, Greenbelt, MD 20771

1. INTRODUCTION

Using spectral imaging data acquired with the Airborne Visible Infrared Imaging Spectrometer (AVIRIS) from an ER-2 aircraft at 20 km altitude during various field programs, it was found that narrow channels near the center of the strong 1.38-μm water vapor band are very effective in detecting thin cirrus clouds (Gao et al., 1993). Based on this observation from AVIRIS data, Gao and Kaufman (1994) proposed to put a channel centered at 1.375 μm with a width of 30 nm on the Moderate Resolution Imaging Spectrometer (MODIS) (Salomonson et al., 1989) for remote sensing of cirrus clouds from space. The sensitivity of the 1.375-μm MODIS channel to detect thin cirrus clouds during the day time is expected to be one to two orders of magnitude better than the current infrared emission techniques. As a result, much larger fraction of the satellite data is expected to be identified as being covered by cirrus clouds; some of them so thin that their obscuration of the surface is very small. In order to make better studies of surface reflectance properties, thin cirrus effects must be removed from satellite images. Therefore, there is a need to study radiative properties of thin cirrus clouds, so that a strategy for correction or removal of the thin cirrus effects, similar to the correction of atmospheric aerosol effect (e.g., Kaufman and Sendra, 1988), can be formed. In this extended abstract, we describe an empirical approach for removing/correcting thin cirrus effects in AVIRIS images using channels near 1.375 μm - one step beyond the detection of cirrus clouds using these channels.

2. BACKGROUND

Cirrus clouds consist of ice particles having different sizes and shapes. The "effective" particle sizes are usually greater than 5 μm. We illustrate the scattering and absorption properties of cirrus clouds through examples. Figure 1 shows two AVIRIS spectra (in reflectance units) acquired over areas covered by thick and thin cirrus clouds above Monterey Bay in California on September 4, 1992. The spectra below 0.5 μm are not shown here due to calibration problems. For each spectrum, the reflectances of ice particles in the 0.5 - 1.1 μm spectral region are constant with wavelength, because ice particle sizes are much greater than wavelengths. The larger apparent reflectances in the 0.5 - 0.6 μm region are due to Rayleigh scattering. Beyond 1.1 μm, ice absorption effects, for example the ice bands centered near 1.5 and 2.0 μm, are seen in the two spectra. The ice absorption effects near 1.24 μm are weak. Near 1.375 μm, both water vapor and ice particles have absorptions. The ice absorption effects near 1.375 μm are comparable to those near 1.24 μm, because imaginary parts of ice refractive indices at both wavelengths are about the same.

At present, accurate modeling of cirrus scattering and absorption effects is still very difficult. Our knowledge on cirrus particle size distributions and optical properties are not sufficient (King, 1993). Cirrus spatial inhomogeneity and adjacency effects are also difficult to be treated properly in radiative transfer models. In view of these difficulties, we propose to establish empirical relationships among remote sensing measures to characterize the main cirrus properties, and then to develop an empirical cirrus correction/removal technique.
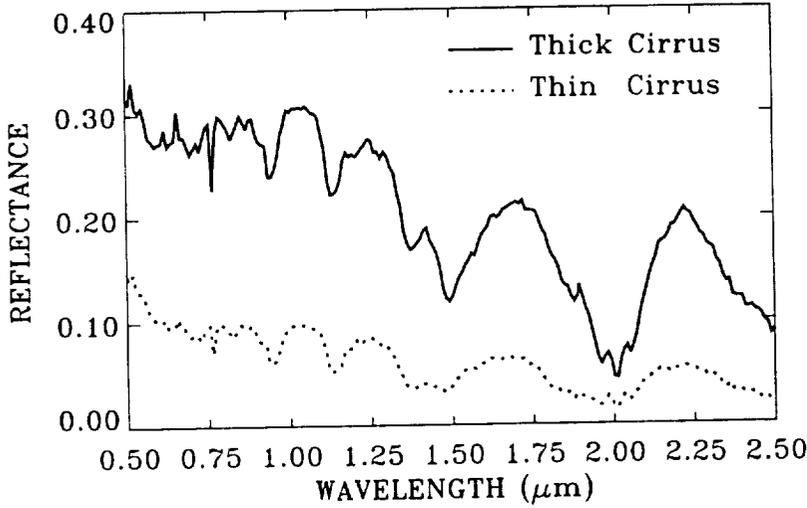
Fig. 1. Examples of AVIRIS spectra over thick and thin cirrus clouds.

3. THE EMPIRICAL APPROACH

For thin cirrus clouds, we assume that a homogeneous thin cirrus layer is located above a virtual "surface", which includes the effects of Rayleigh scattering and bottom surface reflection and scattering. With these assumptions, we have the following relationship (similar to descriptions of aerosol scattering, e.g., Fraser and Kaufman, 1985):

$$\rho_\lambda^* = \rho_{c\lambda} + T_{c\lambda} \rho_\lambda / (1 + S_{c\lambda} \rho_\lambda) \qquad (1)$$

where ρ_λ^* is the measured spectral radiance (normalized to reflectance units), ρ_λ is the reflectance of the virtual "surface", $\rho_{c\lambda}$ is the atmospheric path radiance due to the cirrus cloud (radiation backscattered by the cloud), $T_{c\lambda}$ is the two way transmission (direct + diffuse) through the cloud, and $S_{c\lambda}$ is the cloud scattering of upward radiation back to the surface. $S_{c\lambda} \rho_\lambda \ll 1$ for thin cirrus, and Eq. (1) can be simplified to:

$$\rho_\lambda^* = \rho_{c\lambda} + T_{c\lambda} \rho_\lambda \qquad (2)$$

In order to correct ρ_λ^* for the cirrus effect, namely to derive ρ_λ based on Eq. (2), cirrus path radiance $\rho_{c\lambda}$ and transmittance $T_{c\lambda}$ must be known.

Analyzing AVIRIS data, we have found that cirrus path radiances $\rho_{c\lambda}$ for AVIRIS channels between 0.4 and 1.1 μm are linearly related to $\rho_{c\ 1.375\ \mu m}$,

$$\rho_{c\lambda} = \rho_{c\ 1.375\mu m} / t_{CO} \qquad (3)$$

where t_{CO} is less than 1 due to ice and water vapor absorption at 1.375 μm and can be derived from AVIRIS data themselves. For thin cirrus clouds, $T_{c\lambda}$ is usually greater than 0.9. Correction of cirrus path radiances can be made relatively easily. Substitute Eq. (3) into Eq. (2), we obtain:

$$T_{c\lambda} \rho_\lambda = \rho_\lambda^* - \rho_{c\ 1.375\mu m} / t_{CO} \qquad (4)$$

Images of $T_{c\lambda} \rho_\lambda$ are cirrus path radiance corrected images. Because of the large transmittance of thin cirrus, images of $T_{c\lambda} \rho_\lambda$ are very similar to images of ρ_λ.

60
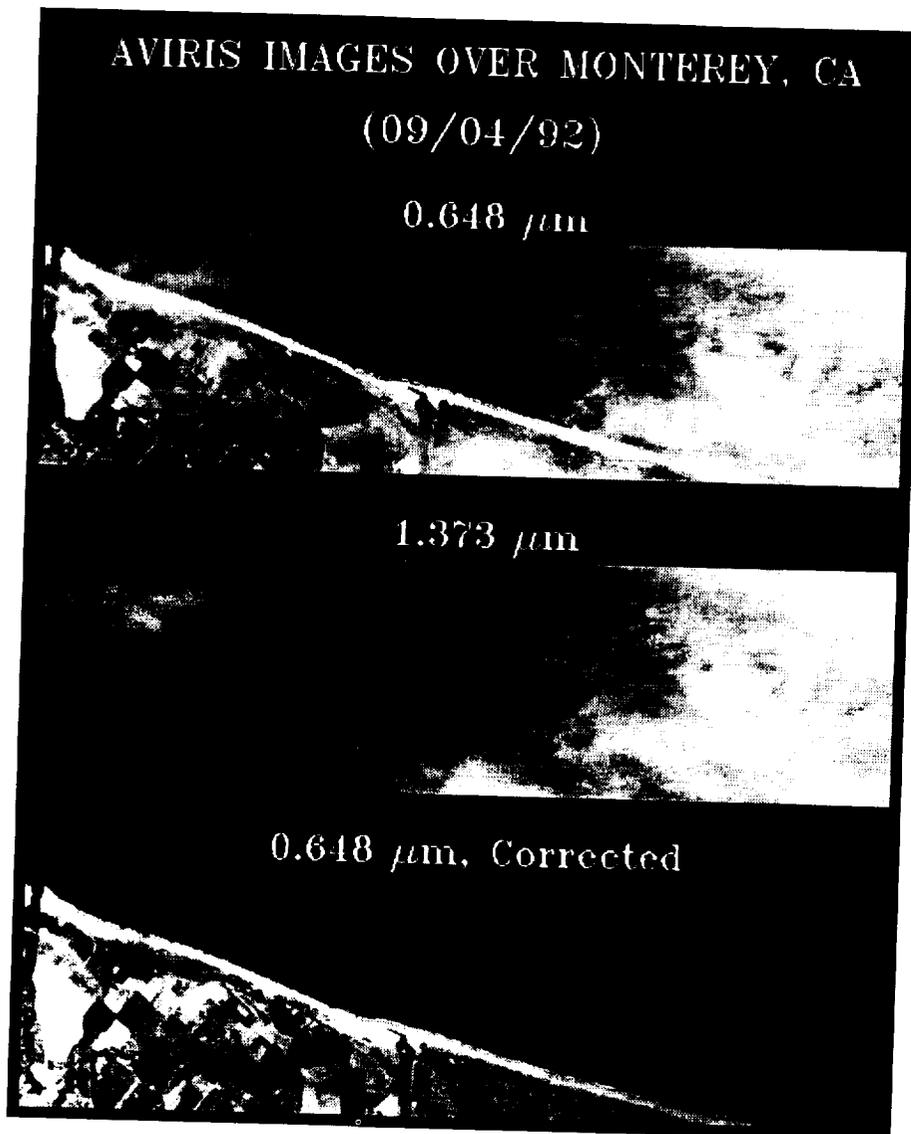
Fig. 2. A 0.648 μm AVIRIS image (top plot), 1.373 μm image (middle plot), and cirrus path radiance corrected 0.648 μm image (bottom plot).

Corrections of the cirrus transmittances $T_{c\lambda}$ are practically more difficult than the corrections of path radiances. The solar radiation on the two-way path (Sun-cirrus-surface-cirrus-sensor) encounters cirrus clouds at different spatial locations. Due to the non-local nature of $T_{c\lambda}$, it is difficult to make accurate derivation of $T_{c\lambda}$ from AVIRIS images. Nevertheless, we are making progress in deriving a quantity from AVIRIS images that would characterize the main properties of $T_{c\lambda}$.

4. RESULTS AND DISCUSSION

Figure 2 shows an example of our correction of thin cirrus effects. The top plot shows the 0.648-μm image. The image was acquired over Monterey, CA on September 4, 1992. The image covers both land and ocean areas. A number of land surface features are blurred due to the presence of thin cirrus clouds. The middle plot of Fig. 2 shows the 1.373-μm image over the same area. Only cirrus clouds are seen. Fig. 3 shows a scatter plot of $\rho^*_{1.373\mu m}$ versus $\rho^*_{1.043\mu m}$ for many pixels over the ocean. The straight line

61
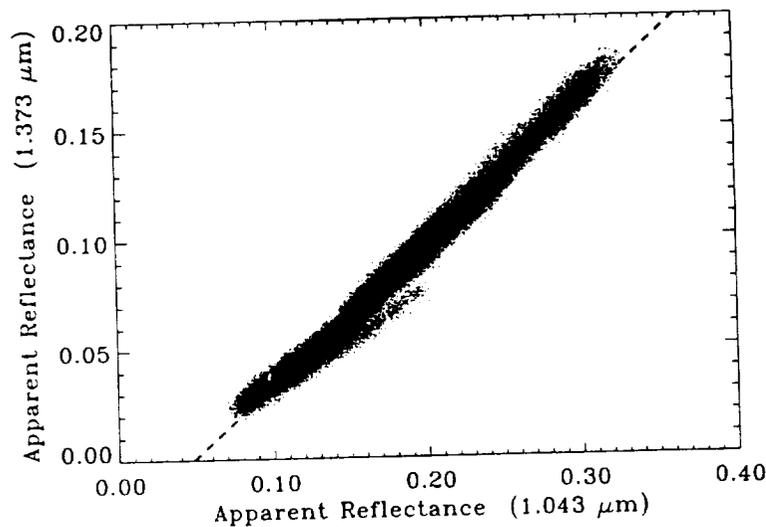
Fig. 3. A scatter plot of apparent reflectances at 1.373 μm vs those at 1.043 μm.

is a linear fit to all the points. The slope, 0.635, of the fitted line can be considered as good estimate of t_{CO} (see Eq. 3). The bottom plot of Fig. 2 shows our path radiance corrected image. Most of the cirrus clouds over the ocean are removed. Land features are far less blurred than those in the top plot.

As expected, the AVIRIS images in Figure 2 were contaminated by stratospheric aerosols resulted from Mt. Pinatubo volcano eruption in 1991. As a result, the minimum reflectance of the 1.373-μm is about 0.02, not zero.

5. SUMMARY

We have developed an empirical technique that is successful in removing the cirrus path radiances in AVIRIS images between 0.4 and 1.1 μm. The derivation of two-way cirrus transmittance factor is more difficult because of the non-local nature of the two-way transmittance. *The authors would like to express appreciation to J. Von Den Bosch of Jet Propulsion Laboratory for providing the AVIRIS data used in this study.*

6. REFERENCES

Fraser, R.S. and Y.J. Kaufman, 1985: 'The relative importance of aerosol scattering and absorption in remote sensing', *IEEE J. Geosc. Rem. Sens.*, GE-23, 525-633.

Gao, B.-C., A. F. H. Goetz, and W. J. Wiscombe, 1993, Cirrus cloud detection from airborne imaging spectrometer data using the 1.38 μm water vapor band, Geophys. Res. Lett., 20, 301-304.

Gao, B.-C., and Y. J. Kaufman, Selection of the 1.375-μm MODIS channel for remote sensing of cirrus clouds and stratospheric aerosols from space, Submitted to J. Atmos. Sci. in June, 1994.

Kaufman, Y.J. and C. Sendra, 1988: Satellite mapping of aerosol loading over vegetated areas. Ed. P. V. Hobbs and M. P. McCormick, *Aerosols and Climate*, A. Deepak Publ., Hampton, VA., 51-67.

King, M. D., 1993, Radiative Properties of Clouds, in *Aerosol-Cloud-Climate Interactions*, (P. Hobbs editor), Academic Press, 123-149.

Salomonson, V. V., W. L. Barnes, P. W. Maymon, H. E. Montgomery, and H. Ostrow, 1989, MODIS: Advanced facility instrument for studies of the earth as a system, IEEE Trans. Geosci. Remote Sens., 27, 145-153.

REMOTE SENSING OF SMOKE, CLOUDS, AND RADIATION USING AVIRIS DURING SCAR EXPERIMENTS

Bo-Cai Gao[1], Lorraine Remer[2], and Yoram J. Kaufman[3]

[1]USRA, Code 913, NASA Goddard Space Flight Center, Greenbelt, MD 20771
[2]SSAI, Code 913, NASA Goddard Space Flight Center, Greenbelt, MD 20771
[3]Climate and Radiation Branch, Code 913, NASA/GSFC, Greenbelt, MD 20771

1. INTRODUCTION

During the past two years, researchers from several institutes joined together to take part in two SCAR experiments. The SCAR-A (Sulfates, Clouds And Radiation - Atlantic) took place in the mid-Atlantic region of the United States in July, 1993. Remote sensing data were acquired with the Airborne Visible Infrared Imaging Spectrometer (AVIRIS), the MODIS Airborne Simulator (MAS), and a RC-10 mapping camera from an ER-2 aircraft at 20 km. In situ measurements of aerosol and cloud microphysical properties were made with a variety of instruments equipped on the University of Washington's C-131A research aircraft. Ground based measurements of aerosol optical depths and particle size distributions were made using a network of sunphotometers. The main purpose of SCAR-A experiment was to study the optical, physical and chemical properties of sulfate aerosols and their interaction with clouds and radiation. Sulfate particles are believed to affect the energy balance of the earth by directly reflecting solar radiation back to space and by increasing the cloud albedo.

The SCAR-C (Smoke, Clouds And Radiation - California) took place on the west coast areas during September - October of 1994. Sets of aircraft and ground based instruments, similar to those used during SCAR-A, were used during SCAR-C. Remote sensing of fires and smoke from AVIRIS and MAS imagers on the ER-2 aircraft was combined with a complete in situ characterization of the aerosol and trace gases from the C-131A aircraft of the University of Washington and the Cesna aircraft from the U. S. Forest Service.

The comprehensive data base acquired during SCAR-A and SCAR-C will contribute to a better understanding of the role of clouds and aerosols in global change studies. The data will also be used to develop satellite remote sensing algorithms from MODIS on the Earth Observing System.

2. PRELIMINARY RESULTS

The AVIRIS data acquired during SCAR-A have been used in the intercomparison of radiometric calibrations among AVIRIS, MAS, and Landsat TM5. The AVIRIS data have also been used in developing an operational algorithm for retrieving aerosol optical depths from MODIS visible and near-IR channels. In this MODIS algorithm, the 2.13-μm MODIS channel is used to find areas covered by dark, green vegetation. The MODIS channels at 0.47 and

0.65 μm are then used to derive aerosol optical depths over vegetated areas (Kaufman and Sendra, 1988).

Figures 1a and 1b show how the AVIRIS data can be used to improve algorithms for retrieving tropospheric aerosols. In Fig. 1a, an AVIRIS 0.557-μm image acquired over an area in North Carolina on July 22, 1993 during SCAR-A is shown. Surface features were blurred. At first, we thought the whole image was covered by thin cirrus clouds. In Fig. 1b, a 1.372-μm image over the same area is shown. The 1.372-μm channel sees only the upper portion of the atmosphere; cirrus clouds and contrails from a twin engine aircraft are sharply delineated. Only the lower portion of the image was covered by thin cirrus clouds. The upper portion was actually covered by a dense haze layer with an optical depth (at 0.55 μm) of approximately 1.0, based on ground based sunphotometer observations. By applying a cirrus mask derived from the 1.372-μm image to the 0.557-μm image, areas of cirrus can be eliminated from the 0.557-μm image, so that a better retrieval of tropospheric aerosol optical depths can be made.

3. DISCUSSION

Although we have received many AVIRIS data sets measured during SCAR-A, we are still in the very early stage of analyzing these data sets. We hope to fly AVIRIS during SCAR-B to be conducted in Brazil in August - September of 1995.

4. ACKNOWLEDGMENTS

The authors are grateful to Robert O. Green at Jet Propulsion Laboratory for encouraging and helping in the AVIRIS participation and for providing the AVIRIS data.

5. REFERENCES

Kaufman, Y.J. and C. Sendra, 1988: Satellite mapping of aerosol loading over vegetated areas. Ed. P. V. Hobbs and M. P. McCormick, *Aerosols and Climate*, A. Deepak Publ., Hampton, VA., 51-67.
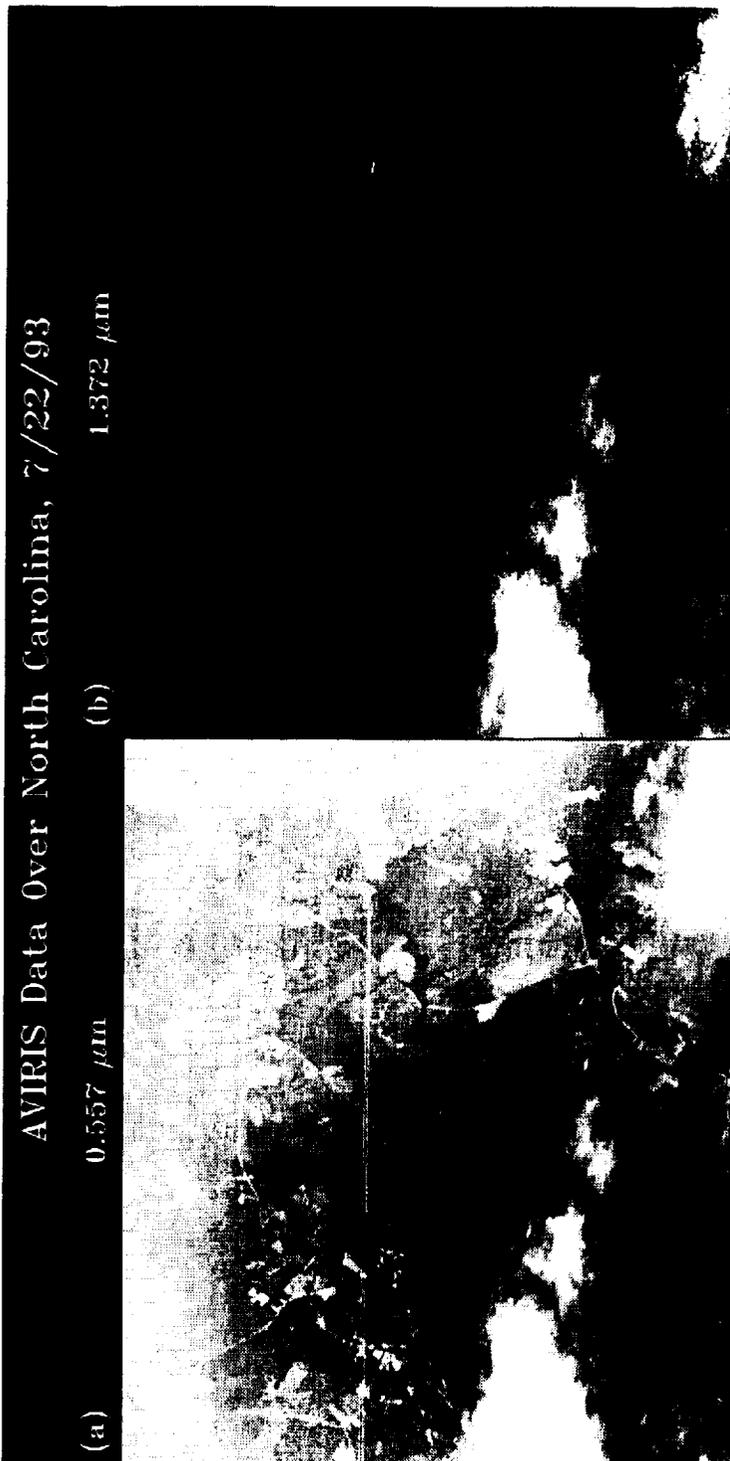
Fig. 1: 0.557-μm and 1.372-μm AVIRIS images acquired over an area in North Carolina on July 22, 1993 during the SCAR-A (Sulfate, Cloud, And Radiation - Atlantic) experiment. Surface features in the 0.557-μm image are blurred because of large amount of haze in the lower atmosphere. The 1.372-μm image sees the thin cirrus clouds and aircraft contrails and does not see the lower level haze layer.

High Accuracy In-Flight Wavelength Calibration of Imaging Spectrometry Data

Alexander F.H. Goetz[1,2], Kathleen B. Heidebrecht[1] and Thomas G. Chrien[3]

[1]Center for the Study of Earth from Space/CIRES, University of Colorado
[2]Department of Geological Sciences, University of Colorado
Boulder, Colorado
[3]Jet Propulsion Laboratory, California Institute of Technology
Pasadena, California

1. INTRODUCTION

Accurate wavelength calibration of imaging spectrometer data is essential if proper atmospheric transmission corrections are to be made to obtain apparent surface reflectance (Gao et al., 1993). Accuracies of 0.1 nm are necessary for a 10 nm-sampling instrument in order to match the slopes of the deep atmospheric water vapor features that dominate the 0.7-2.3 μm region (Goetz et al., 1991).

The Airborne Visible/Infrared Imaging Spectrometer (AVIRIS) (Vane et al., 1993) is calibrated in the laboratory to determine the wavelength position and full-width-half-maximum (FWHM) response for each of the 224 channels (Chrien et al., 1990). The accuracies are limited by the quality of the monochromator used as a source. The accuracies vary from ±0.5 to ±1.5 nm depending on the wavelength region, in general decreasing with increasing wavelength. Green et al. (1990; 1992) make corrections to the wavelength calibrations by using the known positions of 14 atmospheric absorption features throughout the 0.4-2.5 μm wavelength region. These features, having varying width and intensity, were matched to the MODTRAN model (Berk et al., 1989) with a non-linear least squares fitting algorithm. A complete calibration was developed for all 224 channels by interpolation.

Instrument calibration cannot be assumed to be stable to 0.1 nm over a flight season given the rigors of thermal cycling and launch and landing loads. The upcoming sensor HYDICE (Rickard et al., 1993) will require a means for in-flight spectral calibration of each scene because the calibration is both temperature and pressure sensitive. In addition, any sensor using a two-dimensional array has the potential for systematic wavelength shifts as a function of cross-track position, commonly called "smile" (Goetz et al., 1991). Therefore, a rapid means for calibrating complete images will be required. The following describes a method for determining instrument wavelength calibration using atmospheric absorption features that is efficient enough to be used for entire images on workstations. This study shows the effect of the surface reflectance on the calibration accuracy and the calibration history for the AVIRIS B spectrometer over the 1992 flight season.

2. METHOD

The O_2 absorption feature, centered at 762 nm, was used here to test various methods for instrument calibration. The data used came from eight flights spanning the 1992 flight season for AVIRIS. Since only the 762 nm band was used, only the B spectrometer calibration of AVIRIS was tested.

The standard models, such as ATREM (Gao et al., 1993), used for radiometric correction are based on spectral atmospheric transmission values given in HITRAN (Rothman et al., 1987). In ATREM the HITRAN data are resampled to provide an equal wavelength spacing of 2.5 nm. Therefore, we chose to represent the O_2 feature with 2.5 nm samples, deemed adequate given the AVIRIS FWHM of 9 nm and sampling of approximately 10 nm (fig. 1). Three AVIRIS channels are affected by the O_2 band, but the shape of the band is dependent on the wavelength position of each individual detector (fig. 2).

C - 2

The apparent shape of the O_2 band is dependent not only on the individual detector wavelength and spectrometer resolution, but also on the shape of the spectral reflectance curve within the three channels affected (fig. 3). This effect has been recognized by others (Gao and Goetz, 1990; Carrere and Conel, 1993) and accounted for in the non-linear least squares fitting routines. However, non-linear least squares is a computing intensive technique, not suitable for processing large image data sets rapidly.

The method chosen here makes use of the slopes of the spectral curves about the band-center wavelength channel (fig. 4). The model spectrum is resampled using 100 different sets of wavelengths, each differing by 0.1 nm. Ratios of slope(left)/slope(right) are taken and the results for all possible ratios are shown in figure 5. The procedure for determining the actual wavelength of the center channel is as follows: (1) Divide the AVIRIS radiance spectrum by the exo-atmospheric solar irradiance spectrum. (2) Correct for the slope of the surface spectral reflectance by assuming a linear change in reflectance between the channels adjacent to the channels affected by the O_2 absorption. (3) Calculate the ratio of the slopes of the two sides of the O_2 feature. (4) Determine the center wavelength from the look-up table, the values of which are plotted in figure 5.

3. RESULTS

Figure 6 shows the results of an analysis of a full scene of data from the June 21, 1992 coverage of Blackhawk Island, Wisconsin. The histograms show the distribution of calculated center-channel wavelength values for data with and without surface reflectance corrections. The separation between the two peaks is the greatest for vegetated areas because the 762 nm band lies at the shoulder of the near infrared (NIR) plateau in vegetation reflectance. The width of the distributions can be attributed to system noise and variations in surface materials. Therefore, it is important to calculate the band center for a large number of pixels to get an accurate wavelength value. Figure 7 shows the results calculated from vegetated and unvegetated areas within the Blackhawk Island image. The offset between the two curves is 0.4 nm, and can be attributed to the assumption of a linear surface reflectance curve over the 50 nm wavelength region bridging the O_2 absorption feature. The width of each distribution can be attributed to system noise.

A number of images from the 1992 AVIRIS flight season were processed. The center wavelength position was constant for scenes from two different overflights taken on the same day. Figure 8 shows the variation of the center wavelength position of channel 42 with time. The wavelength calibration file accompanying the image data gives a value of 764.0 nm. The maximum variation is only 3 nm, but this becomes significant when atmospheric correction is attempted. Figure 9 shows the results of the application of the ATREM program to data from Gainesville, Florida taken July 8 under very high humidity conditions. The proper calibration is most important here because of the great depth of the unsaturated atmospheric water absorption features. The properly calibrated data set has far fewer artifacts than the one using the published wavelength values. AVIRIS contains an onboard calibration capability using filters. The data have not yet been checked to confirm the shift.

4. CONCLUSIONS

We have shown that, at least for the 762 nm O_2 absorption band, it is possible to calibrate AVIRIS, using in-flight data, to an accuracy of ±0.2 nm regardless of the surface reflectance. This technique could be extended to other atmospheric features in the wavelength range covered by AVIRIS and HYDICE. The rapid analysis made possible by our algorithm will make it feasible to analyze each image from sensors such as HYDICE, for which systematic wavelength calibration changes during flight are anticipated.

5. ACKNOWLEDGMENT

6. REFERENCES

Berk, A., L.S. Bernstein and D.C. Robertson, 1989, "MODTRAN: a moderate resolution model for LOWTRAN 7," Air Force Geophysical Laboratory, Hanscom AFB, MA. 42 pp.

Carrere, V. and J.E. Conel, 1993, "Recovery of Atmospheric Water Vapor Total Column Abundance from Imaging Spectrometer Data around 940 nm - Sensitivity Analysis and Application to Airborne Visible/Infrared Imaging Spectrometer (AVIRIS) Data," *Remote Sens. Environ.*, vol. 44, no. 2/3, pp. 179-204.

Chrien, T.G., R.O. Green and M.L. Eastwood, 1990, "Accuracy of the Spectral and Radiometric Laboratory Calibration of the Airborne Visible/Infrared Imaging Spectrometer (AVIRIS)," *Proc. Second Airborne Visible/Infrared Imaging Spectrometer (AVIRIS) Workshop*, JPL Pub. 90-54, Jet Propulsion Laboratory, Pasadena, CA, pp. 1-14.

Gao, B.-C. and A.F.H. Goetz, 1990, "Column Atmospheric Water Vapor and Vegetation Liquid Water Retrievals From Airborne Imaging Spectrometer Data," *J. Geophys. Res.*, vol. 95, no. D4, pp. 3549-3564.

Gao, B.-C., K.B. Heidebrecht and A.F.H. Goetz, 1993, "Derivation of Scaled Surface Reflectances from AVIRIS Data," *Remote Sens. Environ.*, vol. 44, no. 2/3, pp. 165-178.

Goetz, A.F.H., C.O. Davis, J.D. Aber, K.L. Carder, R.N. Clark, J. Dozier, S.A.W. Gerstl, H. Kieffer, D.A. Landgrebe, J.M. Melack, L.C. Rowan, S.L. Ustin, R.M. Welch and C.A. Wessman, 1991, "High Resolution Imaging Spectrometer (HIRIS) Science Requirements," HIRIS Science Team and Jet Propulsion Laboratory. (JPL internal document) Jet Propulsion Laboratory, Pasadena, CA, 30 pp.

Green, R.O., J.E. Conel, C.J. Bruegge, J.S. Margolis, V. Carrere, G. Vane and G. Hoover, 1992, "In-flight calibration of the spectral and radiometric characteristics of AVIRIS in 1991", *Summaries of the Third Annual JPL Airborne Geoscience Workshop*, JPL Pub. 92-14, vol. 1, AVIRIS Workshop, Jet Propulsion Laboratory, Pasadena, CA, pp. 1-4.

Green, R.O., J.E. Conel, V. Carrère, C.J. Bruegge, J.S. Margolis, M. Rast and G. Hoover, 1990, "Determination of the in-flight spectral and radiometric characteristics of the Airborne Visible/Infrared Imaging Spectrometer (AVIRIS)," *Proc. Second AVIRIS Workshop*, JPL Pub. 90-54, Jet Propulsion Laboratory, Pasadena, CA, pp. 15-34.

Rickard, L.J., R.W. Basedow, E.F. Zalewski, P.R. Silverglate and M. Landers, 1993, "HYDICE: an airborne system for hyperspectral imaging," *Proc. SPIE - Imaging Spectrometry of the Terrestrial Environment*, SPIE, Orlando, FL, vol. 1937, pp. 173-179.

Rothman, L.S., R.R. Gamache, A. Goldman, L.R. Brown, R.A. Toth, H.M. Pickett, R.L. Poynter, J.-M. Flaud, C. Camy-peyret, A. Barbe, N. Husson, C.P. Rinsland and M.A.H. Smith, 1987, "The HITRAN database: 1986 edition," *Appl. Opt.*, vol. 26, no. 19, pp. 4058-4097.

Vane, G., R.O. Green, T.G. Chrien, H.T. Enmark, E.G. Hansen and W.M. Porter, 1993, "The Airborne Visible/Infrared Imaging Spectrometer," *Remote Sens. Environ.*, vol. 44, no. 2/3, pp. 127-143.
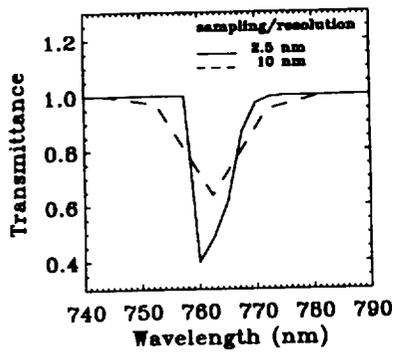
Figure 1. The oxygen feature at HITRAN and AVIRIS resolution and sampling.
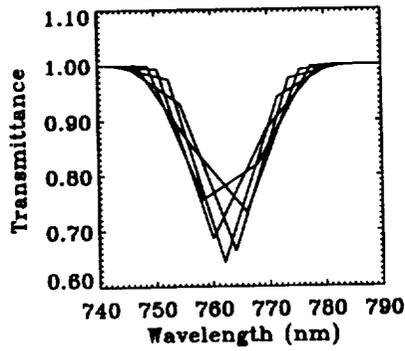
Figure 2. Oxygen band with sensor center wavelengths varying by 2 nm.
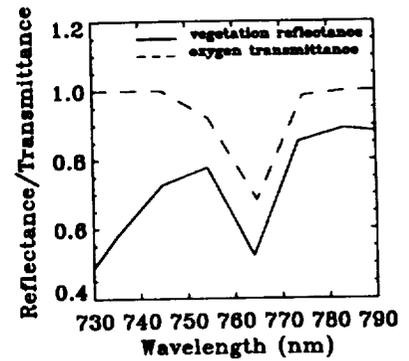
Figure 3. Oxygen transmittance and vegetation reflectance spectra. Note the increasing slope in the vegetation spectrum.
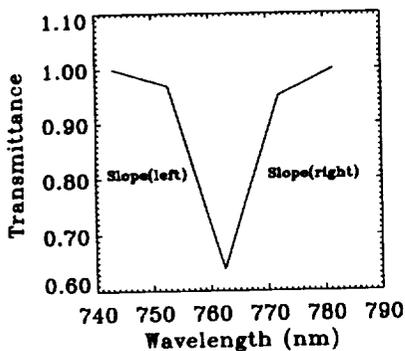
Figure 4. The left and right sides of the oxygen feature are used in calculating the ratio.
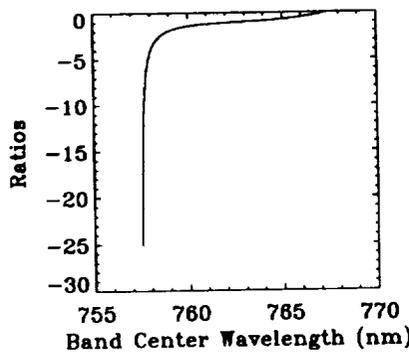
Figure 5. Ratios of two sides of the oxygen feature for 100 different sensor wavelength calibrations.
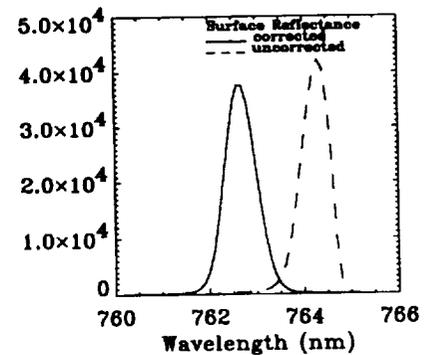
Figure 6. Oxygen band center histograms for the full Blackhawk Island scene, corrected and uncorrected for surface reflectance.
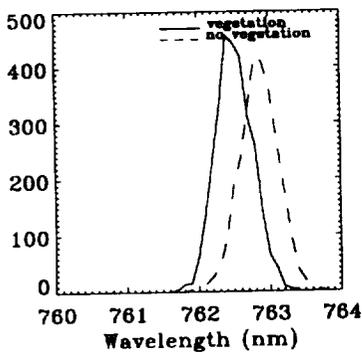
Figure 7. Histograms of the oxygen band centers for vegetated and nonvegetated areas near Blackhawk Island.
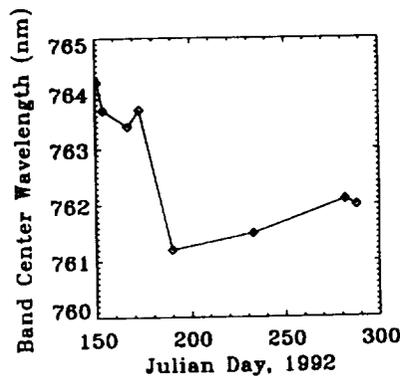
Figure 8. Calculated oxygen band center wavelengths for eight scenes over the 1992 flight season.
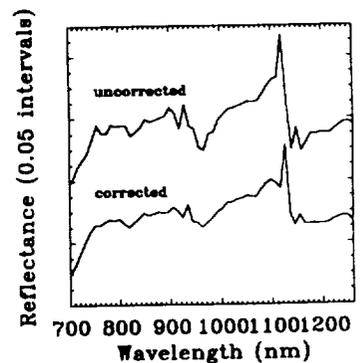
Figure 9. Reflectance spectra in AVIRIS spectrometer B calculated using ATREM from Gainesville, Florida. Wavelengths for the corrected spectrum were shifted by 2.8 nm.

70

DETERMINATION OF THE IN-FLIGHT SPECTRAL CALIBRATION OF AVIRIS USING ATMOSPHERIC ABSORPTION FEATURES

Robert O. Green

Jet Propulsion Laboratory, California Institute of Technology, Pasadena, CA 91109
and
University of California, Santa Barbara, CA 93106

1.   IN-FLIGHT SPECTRAL CALIBRATION

Spectral calibration of the Airborne Visible/Infrared Imaging Spectrometer (AVIRIS) as data are acquired in flight is essential to quantitative analysis of the measured upwelling spectral radiance (Green, 1995). In each spectrum measured by AVIRIS in flight, there are numerous atmospheric gas absorption bands that drive this requirement for accurate spectral calibration. If the surface and atmospheric properties are measured independently, these atmospheric absorption bands may be used to deduce the in-flight spectral calibration of an imaging spectrometer (Conel et al., 1988, Green et al., 1988, 1993).

Both the surface and atmospheric characteristics were measured for a calibration target during an in-flight calibration experiment held at Lunar Lake, Nevada on April 5, 1994 (Green et al., 1995). This paper uses upwelling spectral radiance predicted for the calibration target with the MODTRAN radiative transfer code (Berk et al., 1989) to validate the spectral calibration of AVIRIS in flight.

Surface reflectance, atmospheric optical depths, and water vapor measurements were used to constrain the MODTRAN and predict at high spectral resolution the upwelling radiance at AVIRIS over the in-flight calibration target (Figure 1). To compare this MODTRAN radiance with AVIRIS radiance, MODTRAN must be convoluted to the AVIRIS spectral channels (Figure 2). The radiance reported by the AVIRIS channels in the vicinity of each atmospheric absorption is strongly dependent on the laboratory-calibrated (Chrien et al., 1990) spectral wavelength position of each AVIRIS channel. An algorithm was developed in 1988 to derive the in-flight spectral calibration of AVIRIS using these atmospheric absorption bands (Green et al., 1988). This algorithm optimizes the agreement between the AVIRIS-measured spectrum and the MODTRAN-predicted spectrum across a single absorption band by varying the AVIRIS channel spectral calibration characteristics (Figures 3 through 6). Results for this algorithm, when applied to the April 1994 calibration experiment data, are given in Table 1. The spectral locations of the atmospheric band, the band source, the AVIRIS spectrometer affected, the AVIRIS channel spectral shift from laboratory calibration, and the confidence level are given.

Table 1. AVIRIS In-Flight Spectral Calibration

Wave Length, nm	Source	Spectro-meter	Shift from Lab, nm	Confidence, nm
430	Solar	A	-0.3	±2.0
520	Solar	A	+0.4	±2.0
620	H_2O	A	-0.4	±2.0
650	H_2O	A	+1.2	±2.0
690	H_2O	B	-0.6	±2.0
730	H_2O	B	+0.4	±2.0
760	O_2	B	-0.7	±1.0
820	H_2O	B	+0.3	±2.0
940	H_2O	B	-0.5	±1.0
1140	H_2O	B	+0.0	±1.0
1260	O_2	C	+0.0	±2.0
1470	H_2O	C	-0.2	±2.0
1580	CO_2	C	+1.2	±2.0
1610	CO_2	C	-0.9	±2.0
2020	CO_2	D	-0.3	±1.0
2060	CO_2	D	-0.8	±1.0
2350	CH_4	D	+0.2	±2.0
2380	CH_4	D	-0.8	±2.0
2420	CH_4	D	+0.0	±2.0
2460	CH_4	D	-0.1	±2.0

In this analysis, none of the derived in-flight spectral channel calibrations exceeded the uncertainty of the algorithm. The uncertainty, or confidence level, is based on the spectral contrast of the absorption band. Contrasts of the absorption band *minima to continua* of greater than 25 percent are given a confidence of ± 1.0 nm. Bands with less than 25 percent contrast are given a ± 2.0 nm confidence. Levels of 1.0 and 2.0 nm are estimated based on confidence in the MODTRAN model, AVIRIS radiometric stability, and in situ measurement. These confidence levels are supported in the algorithm results by the discrepancy for pairs of absorption bands in the same spectrometer. For example, the strong CO_2 bands at 2020 and 2060 nm give differing results of 0.5 nm and the results for the week CO_2 bands at 1580 and 1610 differ by 2.1 nm. In overview, this analysis shows that the in-flight spectral calibration had not changed with respect to the laboratory spectral calibration at the level of confidence in the algorithm.

2. ACKNOWLEDGMENTS

3. REFERENCES

Berk, A., L. S. Bernstein, and D.C. Robertson, "MODTRAN: A moderate resolution model for LOWTRAN 7," Final report, GL-TR-0122, AFGL, Hanscom AFB, MA, 42 pp., 1989.

Chrien, T.G., R.O. Green, and M. Eastwood, Laboratory spectral and radiometric calibration of the Airborne Visible/Infrared Imaging Spectrometer (AVIRIS), SPIE Vol. 1298, Imaging spectroscopy of the terrestrial environment, 1990.

Conel, J.E., R.O. Green, R.E. Alley, C.J. Bruegge, V. Carrere, J.S. Margolis, G. Vane, T.G. Chrien, P.N. Slater, S.F. Biggar, P.M. Teillet, R.D. Jackson and M.S. Moran, In-flight radiometric calibration of the Airborne Visible/Infrared Imaging Spectrometer (AVIRIS), SPIE Vol. 924, Recent advances in sensors, radiometry and data processing for remote sensing, 1988.

Green, R.O., G. Vane, and J.E. Conel, "Determination of in-flight AVIRIS spectral, radiometric, spatial and signal-to-noise characteristics using atmospheric and surface measurements from the vicinity of the rare-earth-bearing carbonatite at Mountain Pass, California," Proc. Airborne Visible/Infrared Imaging Spectrometer (AVIRIS) Performance Evaluation Workshop, JPL Pub. 88-38, Jet Propulsion Laboratory, Pasadena, CA, 162-184, 1988.

Green, R.O., J.E. Conel, M. Helmlinger, J. van den Bosch, C. Chovit and T. Chrien, "Inflight Calibration of AVIRIS in 1992 and 1993," Summaries of the Fourth Annual JPL Airborne Geoscience Workshop, Vol. 1, AVIRIS Workshop, JPL Pub. 93-26, Jet Propulsion Laboratory, Pasadena, CA, 69-72, 1993.

Green, R. O., "An Improved Spectral Calibration Requirement for AVIRIS," Summaries of the Fifth Annual JPL Airborne Earth Science Workshop, JPL 95-1, Vol. 1, AVIRIS Workshop, Jet Propulsion Laboratory, Pasadena, CA, January 23, 1995 (this volume).

Green, R. O., J. E. Conel, M. Helmlinger, and J. van den Bosch, "Inflight Radiometric Calibration of AVIRIS in 1994," Summaries of the Fifth Annual JPL Airborne Earth Science Workshop, JPL 95-1, Vol. 1, AVIRIS Workshop, Jet Propulsion Laboratory, Pasadena, CA, January 23, 1995 (this volume).

4.   FIGURES
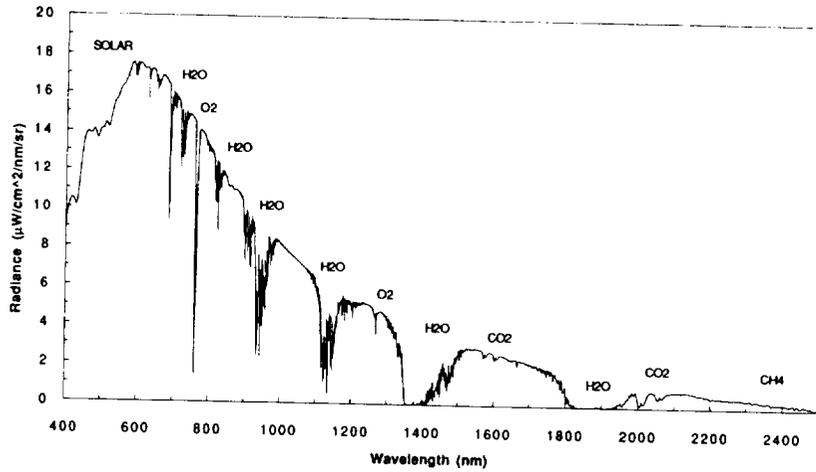
Figure 1. Upwelling spectral radiance predicted by MODTRAN for the AVIRIS over flight of Lunar Lake, NV on April 5, 1994.
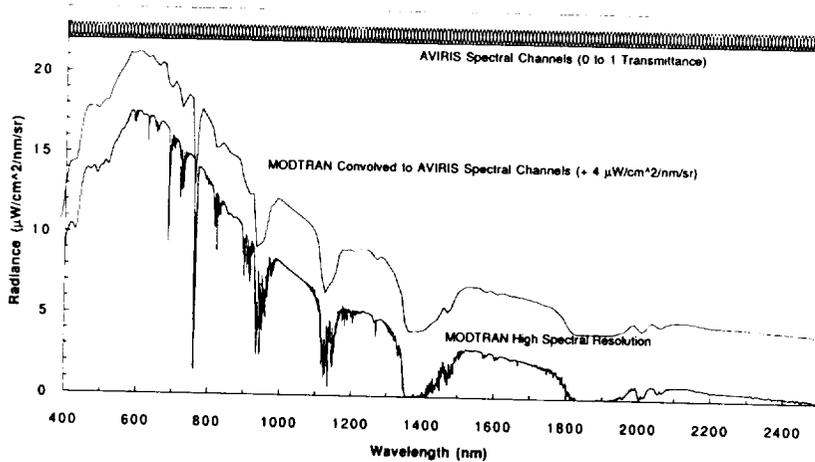
Figure 2. Convolution of MODTRAN to AVIRIS spectral channel characteristics.
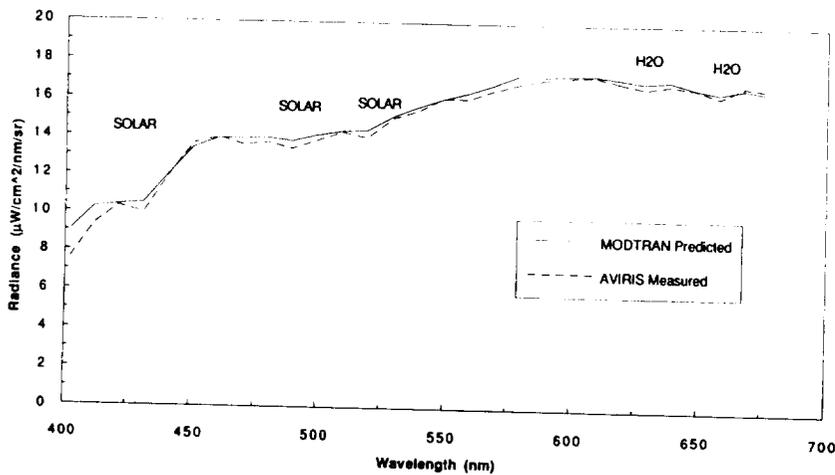
Figure 3. AVIRIS-measured and MODTRAN-predicted radiance for the A spectrometer, based on the laboratory spectral calibration.

73
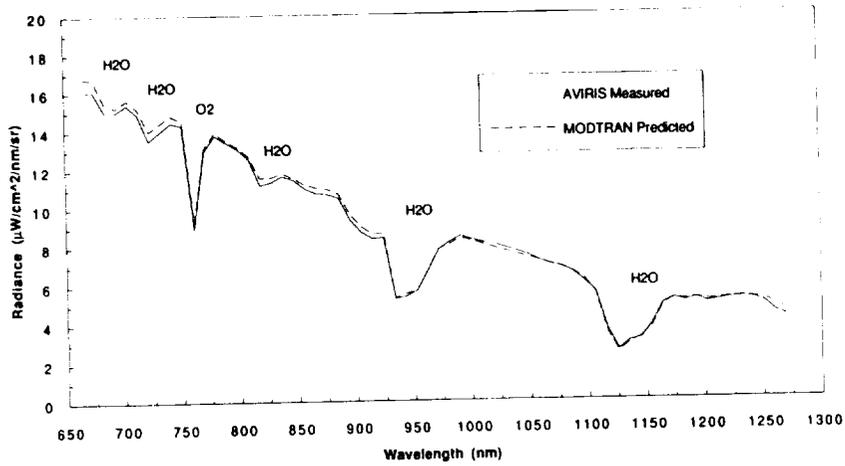
Figure 4. AVIRIS-measured and MODTRAN-predicted radiance for the B spectrometer, based on the laboratory spectral calibration.
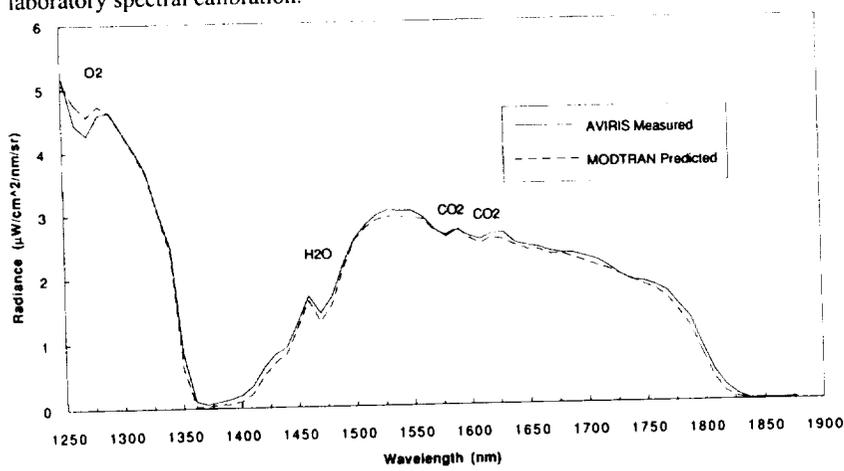
Figure 5. AVIRIS-measured and MODTRAN-predicted radiance for the C spectrometer, based on the laboratory spectral calibration.
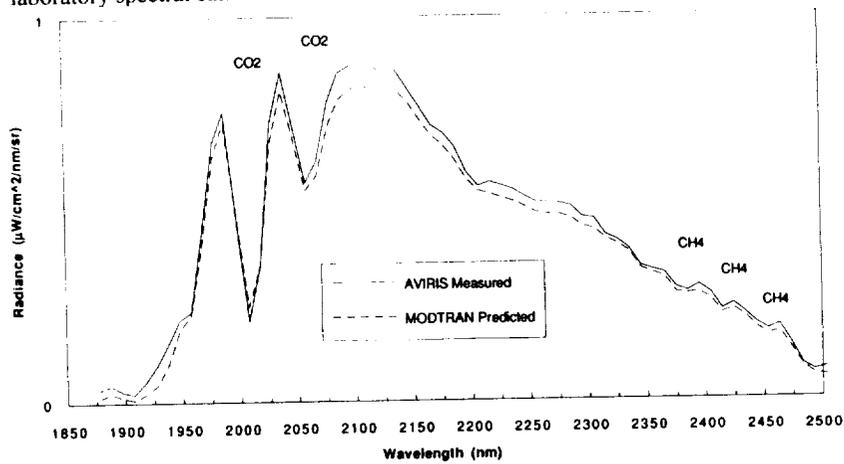
Figure 6. AVIRIS-measured and MODTRAN-predicted radiance for the D spectrometer, based on the laboratory spectral calibration.

AN IMPROVED SPECTRAL CALIBRATION REQUIREMENT FOR AVIRIS

Robert O. Green

Jet Propulsion Laboratory, California Institute of Technology, Pasadena, CA 91109
and
University of California, Santa Barbara, CA 93106

1.   INTRODUCTION

The Airborne Visible/Infrared Imaging Spectrometer (AVIRIS) measures spectra from 400 to 2500 nm through 224 contiguous spectral channels. These spectra are used to identify and determine the abundances of constituents of the Earth's surface and atmosphere through the analysis of spectral molecular absorptions and scattering properties of materials. Spectral calibration of the AVIRIS is required to pursue these determinations, which are based on these fundamental spectral characteristics.

The spectral calibration of AVIRIS consists of a description of the spectral response function for each of the 224 spectral channels. The spectral response function of AVIRIS channels was measured in the laboratory and shown to be Gaussian in shape (Chrien et al. 1990). Figure 1 shows a subset of nine AVIRIS spectral channels with channel centers at 10 nm intervals and channel shapes of Gaussian form with 10 nm full width and half maximum (FWHM). For AVIRIS the spectral calibration is described by the spectral center and FWHM of a Gaussian function for each channel. Uncertainty in the determination of the spectral center and FWHM for each channel are also reported.

This paper presents results from an investigation of the sensitivity of AVIRIS-measured upwelling radiance to errors in spectral calibration. Based on this sensitivity analysis in conjunction with earlier work (Green et al., 1990), an improved spectral calibration requirement for AVIRIS is proposed.

2.   AVIRIS MEASURED RADIANCE

AVIRIS measures the upwelling spectral radiance from the sun that was reflected by the surface as well as absorbed and scattered by the intervening atmosphere. To investigate the effect of spectral calibration on measurement of the upwelling radiance, a high resolution spectrum of the radiance arriving at
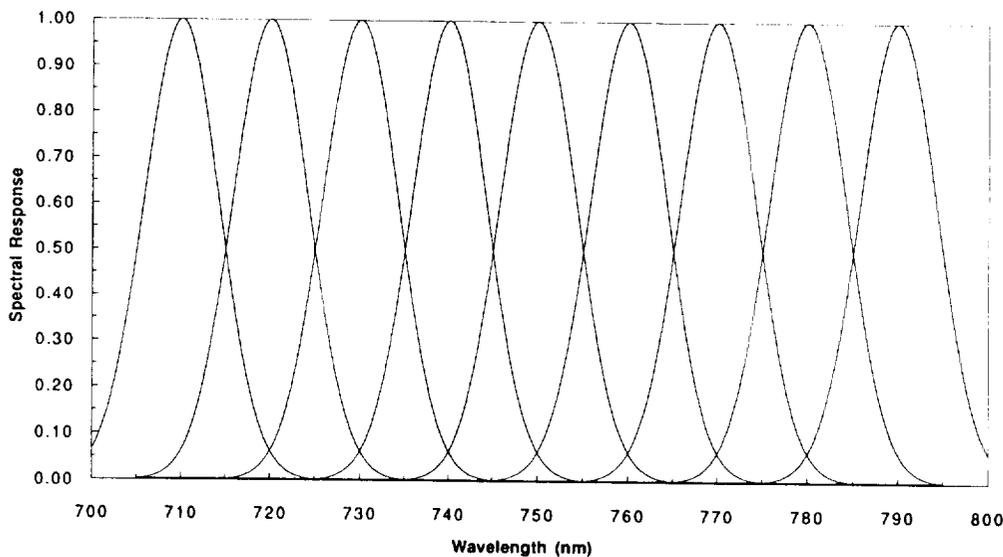
Figure 1. Modeled spectral response functions of 9 AVIRIS channels.

AVIRIS was generated by the MODTRAN radiative transfer code (Berk, et al. 1989). Figure 2 shows the modeled upwelling radiance arriving at AVIRIS at 2 wave-number spectral resolution with a 0.25 reflectance surface, 45 degree solar zenith angle, and the mid-latitude summer atmospheric model. Across this spectral range, the upwelling radiance is dominated by narrow atmospheric and solar absorptions as indicated on the figure.

The radiance reported by each AVIRIS channel is the result of the convolution of the upwelling spectral radiance with the spectral response function of each channel. This spectral convolution is given in equation 1. For each spectral channel, the measured radiance L_i is the product of the channel spectral response function $f(\lambda_i - \lambda)$ and the upwelling spectral radiance $L(\lambda)$ at each wavelength $d\lambda$:

$$L_i = \int f(\lambda_i - \lambda)*L(\lambda)d\lambda \qquad (1)$$

In Figure 3, the AVIRIS radiance convolved through 10 nm FWHM Gaussian spectral channels is given. Because the upwelling spectral radiance contains numerous narrow solar and atmospheric
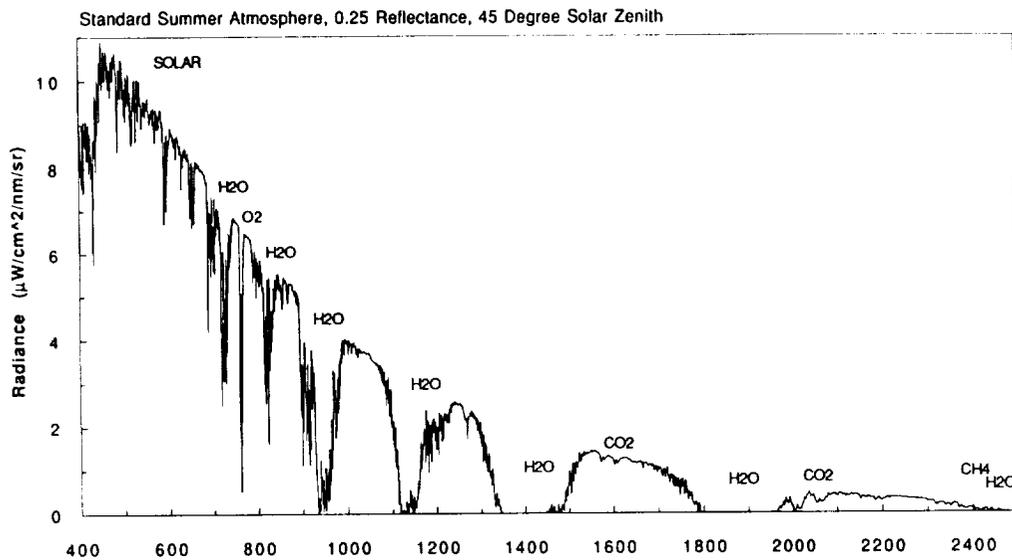
Figure 2. MODTRAN radiative transfer code modeled upwelling spectral radiance.
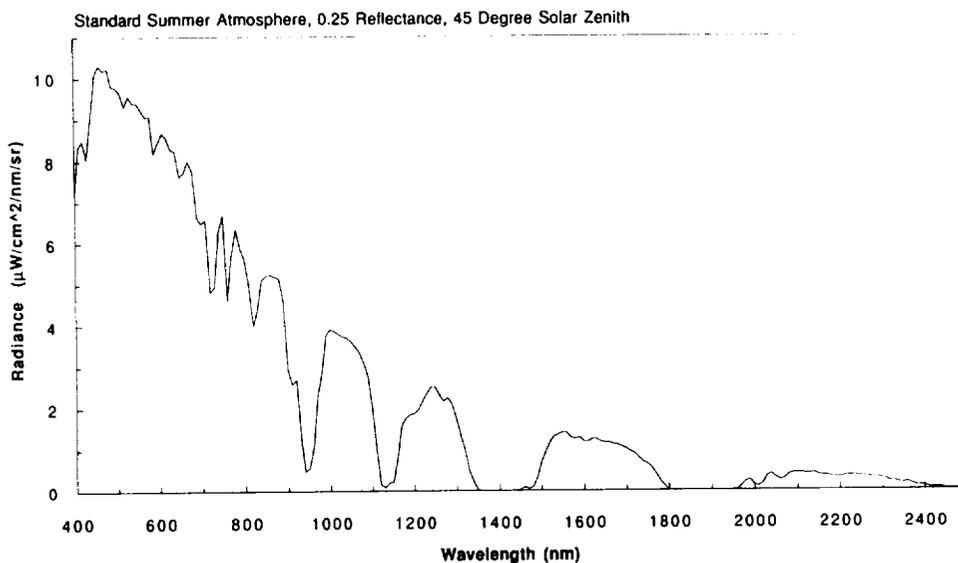
Figure 3. Result of the convolution of the MODTRAN radiance spectrum by the AVIRIS spectral channels.

absorptions, the spectrum in Figure 3 is strongly dependent on the spectral position and FWHM of each of the AVIRIS channels.

3.   AVIRIS SPECTRAL CALIBRATION SENSITIVITY ANALYSIS

To understand the sensitivity of the AVIRIS measured radiance to the spectral calibration, a sensitivity analysis was performed. For this analysis, errors in both channel center and FWHM were evaluated. The effects of error in channel center position were investigated by introducing a systematic spectral shift across the spectral range. For FWHM investigation, errors of systematic broadening were introduced. Sensitivity to these spectral calibration errors was assessed as the percent difference in radiance measured through a spectral channel with and without the spectral calibration error.

Sensitivity in calibration of the channel center position was tested by calculating the convolved radiance for shifts in spectral channel positions of 1.0, 0.5, and 0.1 nm. These errors correspond to 10, 5, and 1 percent of the nominal 10 nm AVIRIS spectral resolution. The percent difference in radiance between the error free and spectrally shifted spectra is shown in Figure 4. Spectrally distinct errors throughout the spectral range increase as the errors in calibration of the spectral channel center position grow. For example, at 930 nm, an error of 1.0 nm in channel position caused a –15 percent error in measured radiance. At 930 nm, a 0.5 nm shift caused a –8 percent error in radiance and a 0.1 nm shift caused a –1.5 percent error.

An analysis of the sensitivity of channel FWHM calibration was performed through calculation of the percent error in radiance for errors in the spectral FWHM of 1.0, 0.5, and 0.1 nm. These results are shown in Figure 5. As with errors in channel position, errors in the calibration of channel shape cause errors in the sensor measured radiance. At 1120 nm, errors in channel width calibration of 1.0 nm, 0.5 nm, and 0.1 nm result in radiance errors of 11.3, 5.6, and 1.1 percent, respectively.

Spectral calibration errors of a given percentage of the spectral resolution are shown to cause errors of a greater percentage in measured radiance in spectral regions with strong narrow absorptions in the upwelling radiance. Errors in the measured radiance directly propagate to calculations of apparent reflectance. Errors in measured radiance impact algorithms that use spectral fitting to known reference spectra as well as algorithms that derive parameters from computational models. Furthermore, the spectrally sharp nature of these errors mimics and modifies actual molecular absorptions and consequently undermines the general spectral measurement objectives of imaging spectrometry.
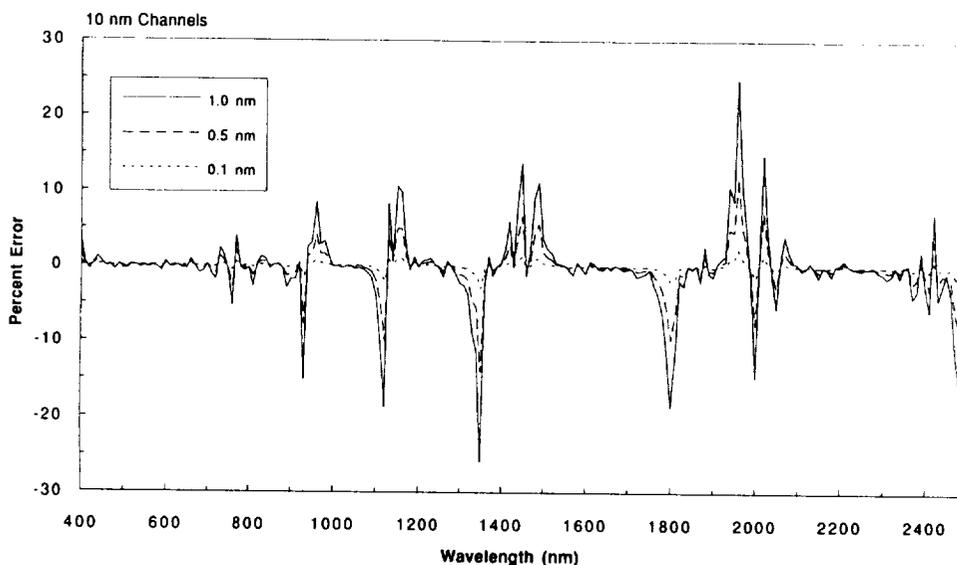
Figure 4. Error in AVIRIS modeled upwelling radiance with errors of 1.0, 0.5 and 0.1 nm in the calibration of channel center position.

77

4. CONCLUSION

These sensitivity analyses show that the ubiquitous narrow solar and atmospheric absorptions in the upwelling spectral radiance drive the requirement for spectral calibration of AVIRIS. The original spectral calibration requirement for AVIRIS was ±5.0 nm for spectral position and FWHM. Based on these analyses, a spectral calibration requirement of 5 percent (0.5 nm) and goal of 1 percent (0.1 nm) of the spectral resolution are justified to provide AVIRIS spectra that are free of significant spectral calibration induced errors.

5. ACKNOWLEDGMENTS

This research was carried out at the Jet Propulsion Laboratory, California Institute of Technology, under contract with the National Aeronautics and Space Administration. Computer and analysis support was also provided through the Center for Remote Sensing and Environmental Optics at the University of California, Santa Barbara.

6. REFERENCES

Berk, A., L. S. Bernstein, and D.C. Robertson, 1989, "MODTRAN: A moderate resolution model for LOWTRAN 7," Final report, GL-TR-0122, AFGL, Hanscom AFB, MA, 42 pp.

Chrien, T.G., R. O. Green, and M. Eastwood, "Laboratory spectral and radiometric calibration of the Airborne Visible/Infrared Imaging Spectrometer (AVIRIS)," SPIE, Vol. 1298, Imaging spectroscopy of the terrestrial environment, 1990.

Green, R. O., J. E. Conel, J. S. Margolis, V. Carrere, C. J. Bruegge, M. Rast, G. Hoover, "In-flight validation and calibration of the spectral and radiometric characteristics of the Airborne Visible/Infrared Imaging Spectrometer (AVIRIS)", SPIE, Vol. 1298, Imaging spectroscopy of the terrestrial environment, 1990.
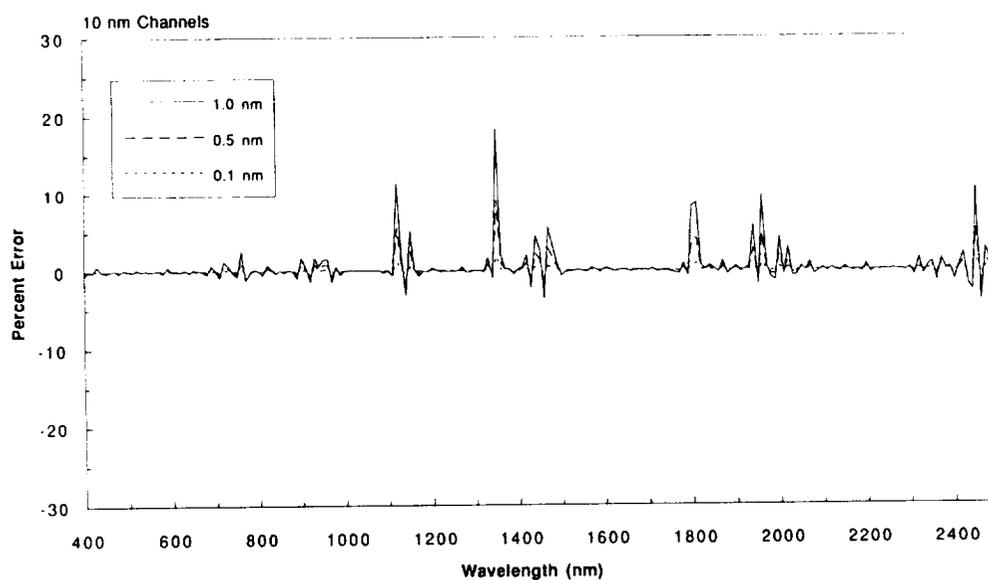
Figure 5. Error in modeled AVIRIS upwelling radiance with errors of 1.0, 0.5 and 0.1 nm in the calibration of channel FWHM.

MOVEMENT OF WATER VAPOR IN THE ATMOSPHERE MEASURED BY AN IMAGING SPECTROMETER AT ROGERS DRY LAKE, CA

Robert O. Green[1,2] and James E. Conel[1]

[1]Jet Propulsion Laboratory, California Institute of Technology, Pasadena CA 91109
[2]University of California at Santa Barbara, CA 93106

1.   INTRODUCTION

Movement of water as vapor in the atmosphere is a fundamental process in the Earth's hydrological cycle. Investigations of spatial and time scales of water vapor transport in the atmosphere are important areas of research.

Water vapor transmits energy as a function of its abundance across the spectrum. This is shown in the 400- to 2500-nm spectral region where the transmission of the terrestrial atmosphere has been modeled using the MODTRAN radiative transfer code (Berk et al., 1989) for a range of water vapor abundances (Figure 1). Based on these model results, spectra measured by the Airborne Visible/Infrared Imaging Spectrometer (AVIRIS) have been used to investigate the movement of water vapor at 20-m spatial resolution over an 11-by-30-km area at approximately 15-minute time intervals (1.25 hours total). AVIRIS measures the upwelling spectral radiance from 400 to 2500 nm at 10-nm spectral intervals and collects images of 11-by-up-to-1000 km at 20-m spatial resolution. Data are collected at a rate of 1 km of flight line per 4.5 seconds. A set of five AVIRIS flight lines was acquired in rapid succession over Rogers Dry Lake, CA on May 18, 1993 at 18:59, 19:13, 19:29, 19:47, and 19:59 UTC (Figure 2). Rogers Dry Lake is located 2 hours north of Los Angeles, California at 34.84 degrees north latitude and 117.83 degrees west longitude in the Mojave Desert.

2.   MEASUREMENT OF ATMOSPHERIC WATER VAPOR

AVIRIS measures the upwelling spectral radiance that has been reflected by the surface and transmitted and scattered by the atmosphere. The change in radiance as a function of the abundance of water vapor in the atmosphere has been modeled with MODTRAN for a terrestrial atmosphere ranging from 0 to 36.5 precipitable mm of water vapor (Figure 3). This plot shows that the water absorption bands at 940 nm and 1140 nm are strongly sensitive to water vapor over the range of abundances encountered in the terrestrial atmosphere. Absorption bands at shorter wavelengths are less sensitive and those at longer wavelengths saturate for this range of water vapor. A model (Green et al., 1991 and 1993) of the upwelling radiance at AVIRIS in the 940-nm region as a function of water vapor has been developed incorporating MODTRAN. This model was inverted using a nonlinear least squares spectral fitting approach to determine the water vapor abundance for the spectrum of each AVIRIS spatial element. A sample spectral fit from the first spatial element in the first flight line is used to derive a water vapor column abundance of 14.39 precipitable mm (Figure 4). The average residual radiance error across the spectral fit is 1.1 percent.

This algorithm has been applied to the five AVIRIS flight lines over Rogers Dry Lake (Figure 5). The spatial coverage of these images is the same as presented in the radiance images. In each image the water vapor varies from approximately 12 mm to 16 mm precipitable water vapor, which represents a 25-percent variation in water vapor throughout the image. Spatial patchiness and lateral variation of water vapor are shown at scales from less than 200 m to greater than 5000 m. Through these five images, the spatial distribution of water vapor changes significantly between each 15-minute observation. However, several dominant features are observed to persist and drift from image to image. Overall, there is a trend towards decreasing water vapor through the observation time interval. For this test case at Rogers Dry Lake, CA, these images demonstrate the high spatial and temporal variability of water vapor in the terrestrial atmosphere.

3. CONCLUSION

Water vapor in the atmosphere has been derived from the AVIRIS spectra measured in five overpasses above Rogers Dry Lake, CA. The abundance of water vapor in these data is shown to be spatially heterogeneous at the 25-percent level over a range of spatial scales. Temporal variation is also shown through the changing water vapor distribution in the five data sets acquired at 15-minute intervals. Imaging spectrometer data provide a unique means of rapidly measuring quantitatively the spatial distribution and movement of water vapor in the terrestrial atmosphere at high spatial resolution and over large areas.

4. FUTURE WORK

A future water vapor mass balance calculation will be performed to characterize the rate of change in water vapor in the atmosphere in this data set. Mapping features in the water vapor between overpasses will be used to investigate water vapor diffusion rates from the data themselves.

5. ACKNOWLEDGMENTS

6. REFERENCES

Berk, A., L. S. Bernstein, and D. C. Robertson, 1989, *MODTRAN: A moderate resolution model for LOWTRAN 7, Final Report, GL-TR-0122*, AFGL, Hanscomb AFB, MA, 42 pp.

Green, R. O., J. E. Conel, J. S. Margolis, C. J. Bruegge, and G. L. Hoover, 1991, "An Inversion Algorithm for Retrieval of Atmospheric and Leaf Water Absorption From AVIRIS Radiance With Compensation for Atmospheric Scattering," *Proc. Third Airborne Visible/Infrared Imaging Spectrometer (AVIRIS) Workshop*, JPL Publication 91-28, Jet Propulsion Laboratory, Pasadena, California, pp. 51-61.

Green, R. O., J. E. Conel, and D. A. Roberts, 1993, "Estimation of aerosol optical depth, pressure elevation, water vapor and calculation of apparent surface reflectance from radiance measured by the Airborne Visible/Infrared Imaging Spectrometer (AVIRIS) using a radiative transfer code," *SPIE, Vol. 1937, Imaging Spectrometry of the Terrestrial Environment*, pp. 2-11.

Figure 1. Decrease in transmittance of the atmosphere as a function of increase in the abundance of water vapor.
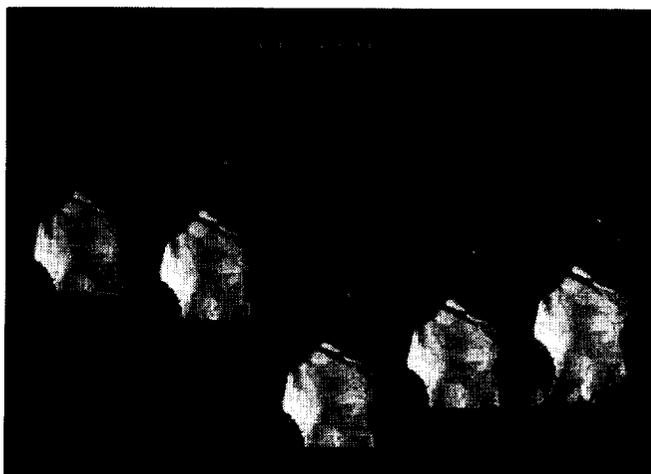
Figure 2. Radiance images of AVIRIS flight lines over Rogers Dry Lake, CA, acquired on May 18, 1993 (see AVIRIS Workshop Slide 2).
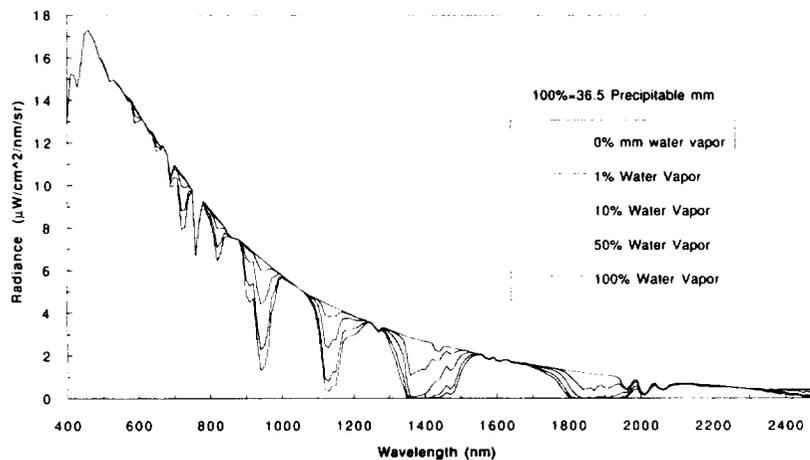
Figure 3. MODTRAN-modeled decrease in radiance with increase of water vapor over the range of abundances encountered in the terrestrial atmosphere.

81
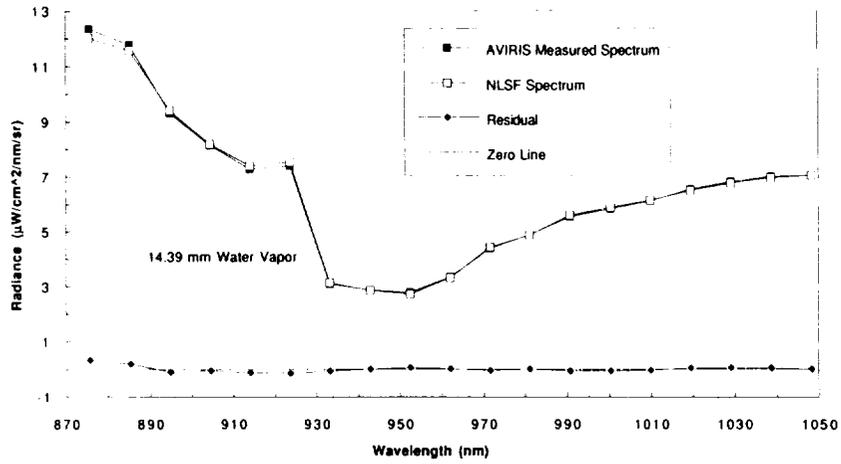
Figure 4. AVIRIS-measured spectrum and a model spectrum for determination of water vapor abundance.

Figure 5. AVIRIS-derived water vapor for the five flight lines acquired over Rogers Dry Lake, CA (see AVIRIS Workshop Slide 2).

IN-FLIGHT RADIOMETRIC CALIBRATION OF AVIRIS IN 1994

Robert O. Green[1,2], James E. Conel[1], Mark Helmlinger[1],
Jeannette van den Bosch[1] and Pavel Hajek[1]

[1]Jet Propulsion Laboratory, California Institute of Technology, Pasadena, CA 91109
[2]University of California, Santa Barbara, CA 93106

1. INTRODUCTION

The AVIRIS sensor must be calibrated at the time it measures spectra from the ER-2 airborne platform in order to achieve research and application objectives that are both quantitative and physically based. AVIRIS is radiometrically calibrated in the laboratory prior to each flight season (Chrien, 1990). However, the operational environment inside the Q-bay of the ER-2 at 20 km altitude differs from that in the AVIRIS laboratory with respect to temperature, pressure, vibration and high-frequency electromagnetic fields. Experiments at surface calibration targets are used in each flight season to confirm the accuracy of AVIRIS in-flight radiometric calibrations (Conel et al., 1988; Green et al., 1988, 1990, 1992, 1993). For these experiments, the MODTRAN radiative transfer code (Berk et al., 1989) is constrained by using in situ measurements to independently predict the upwelling spectral radiance arriving at AVIRIS for a specific calibration target. AVIRIS calibration is validated in flight by comparing the MODTRAN-predicted radiance to the laboratory-calibrated radiance measured by the AVIRIS sensor for the same time over the calibration target. In this paper, we present radiometric calibration results for the AVIRIS in-flight calibration experiment held at the beginning of the 1994 flight season.

2. IN-FLIGHT CALIBRATION EXPERIMENT

On April 5, 1994 an in-flight calibration experiment was held at Lunar Lake, Nevada located 130 km east of Tonopah at 38.38 degrees north latitude and 115.98 degrees west longitude. Lunar Lake is a small dry lake approximately 3 km in diameter at 1600 m elevation. This dry lake was selected because it is one of the highest dry lakes in North America. The high elevation assures an atmosphere that is straightforward to model, with less water vapor and aerosols than lower sites.

On a portion of the dry lake surface, a calibration target was designated for comparison of the MODTRAN-predicted radiance to the AVIRIS-measured radiance. This target was 40 by 200 m in dimension, with the long axes parallel and in the center of the AVIRIS flight line. In the half hour preceding and following the AVIRIS data acquisition, the surface spectral reflectance was measured using a field spectrometer that covers the AVIRIS spectral range. A total of 40 measurements were acquired; these were evenly spaced over the target and averaged to determine the calibration target spectral reflectance (Figure 1).
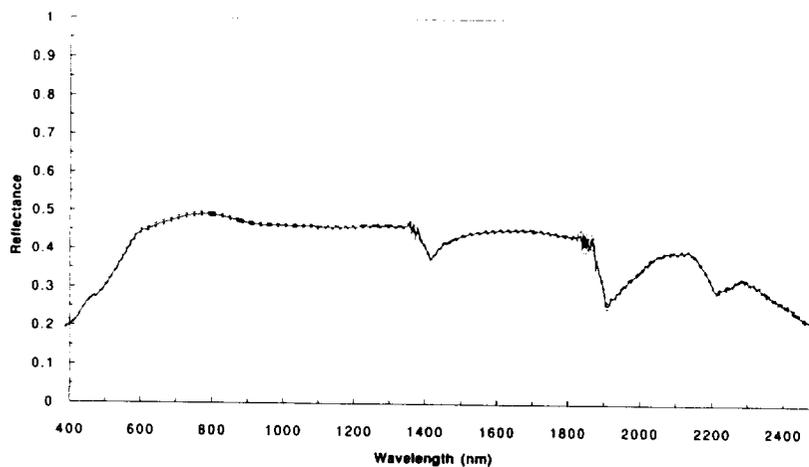
Figure 1. Average calibration target spectral reflectance ± 1 standard deviation.

At the calibration target solar radiometer, measurements were acquired from sunrise through local solar noon with a solar radiometer that measures 10 discrete spectral channels in the range from 370 to 1050 nm. These data were reduced with the Langley technique to generate atmospheric optical depths for the calibration target. The optical depths were used to select the midlatitude summer atmospheric model and adjust the visibility to 250 km in MODTRAN. With these constraints the MODTRAN atmospheric model optical depths agreed closely with the measured optical depths (Figure 2). Data from the radiometer channel centered at 940 NM were analyzed to derive the total column water vapor (Reagan et al., 1987, Bruegge et al., 1990). A value of 4.9 ± 0.2 precipitable mm was determined and used to constrain the water vapor profile in MODTRAN. MODTRAN was run with the spectral surface reflectance, optical depth and water vapor determined to predict the upwelling spectral radiance at the time of the AVIRIS over flight of the target at 18:10 UTC (Figure 3). An updated exo-atmospheric solar irradiance spectrum (Green and Gao, 1993) was used in MODTRAN. The MODTRAN-predicted radiance and AVIRIS spectral resolution were convolved and compared to the AVIRIS laboratory calibrated radiance for the calibration target (Figure 4). An absolute average agreement across the spectral range was 95.3 percent, excluding the regions of near-zero radiance at 1400 and 1900 nm.
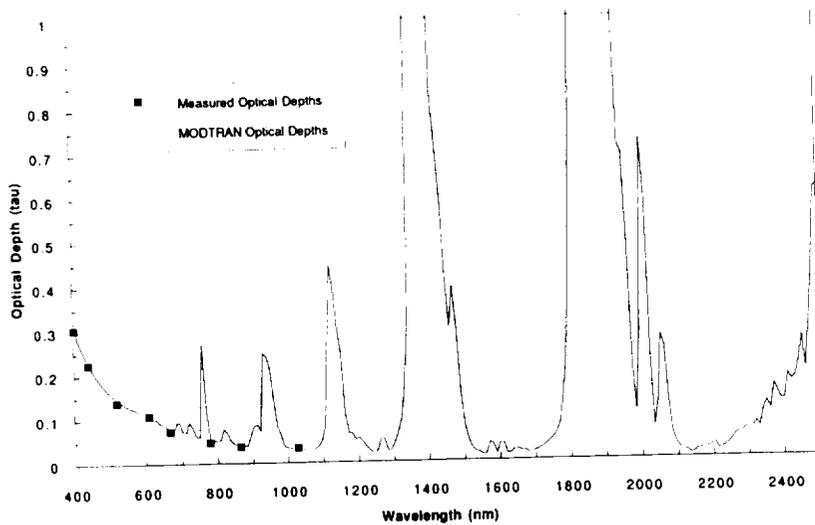
Fig. 2. Measured discrete optical depths with the MODTRAN spectral optical depths for the calibration experiment atmosphere.
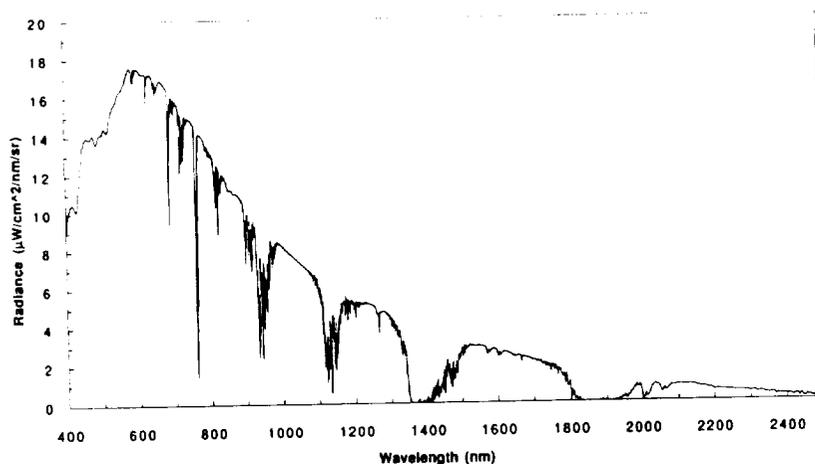
Fig. 3. MODTRAN-predicted radiance for the calibration target at the time of AVIRIS over flight.

AVIRIS in-flight radiometric precision (signal-to-noise ratio) was also determined with data from this calibration experiment. Noise was estimated as the standard deviation of the dark spectra measured at the end of each image line. An uncalibrated AVIRIS signal was taken from the Lunar Lake calibration target. This signal was scaled to the AVIRIS reference radiance (Green et al., 1988) and divided by the noise to give the AVIRIS in-flight signal-to-noise ratio for 1994, compared to that of 1993 (Figure 5). In 1994, the signal-to-noise ratio in the 400- to 600-nm spectral region is shown to be significantly improved due to the installation of a new focal plane in the first spectrometer. AVIRIS continues to show exceptionally high in-flight signal-to-noise performance across the spectral range. This performance is expected to further improve with installation of new focal planes for the 1995 flight season.

3. RADIOMETRIC CALIBRATION ERROR DISCUSSION

The residual 4.7-percent disagreement in radiometric calibration shown between the AVIRIS laboratory-calibrated radiance and MODTRAN-predicted radiance for the calibration target is attributed to several sources: 1) AVIRIS laboratory standard and calibration procedure errors, 2) errors in the in situ measurements and data reduction and, 3) imprecision in the MODTRAN model and calculation of upwelling spectral radiance.
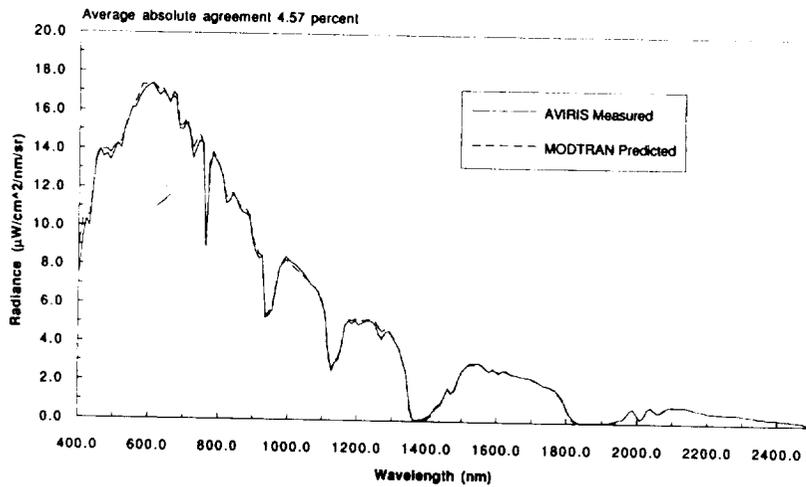
Fig. 4. Comparison of the MODTRAN-predicted radiance and AVIRIS laboratory-calibrated radiance for the Lunar Lake calibration target at 18:10 UTC on April 5, 1994.
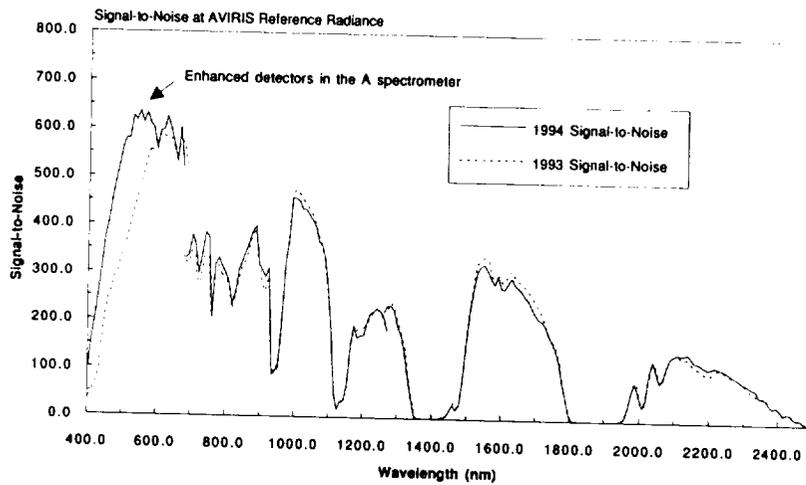
Fig. 5. AVIRIS in-flight 1994 signal-to-noise ratio compared to 1993 AVIRIS reference radiance.

85

4. CONCLUSION

The in-flight calibration experiment at Lunar Lake, Nevada on April 5, 1994 shows 95.3-percent agreement at the calibration target between the MODTRAN-predicted radiance and AVIRIS laboratory-calibrated radiance. The 1994 in-flight signal-to-noise ratio is shown to equal the 1993 performance over most of the spectral range, and to have improved between 400 and 600 nm. The AVIRIS sensor continues to demonstrate high in-flight radiometric calibration accuracy and precision across the spectral range. This level of radiometric performance is required to achieve the physically based objectives of research and application with AVIRIS-measured spectra. Work continues on improving the radiometric calibration accuracy and precision of AVIRIS.

5. REFERENCES

Berk, A., L.S. Bernstein, and D.C. Robertson, "MODTRAN: A moderate resolution model for LOWTRAN 7," Final report, GL-TR-0122, AFGL, Hanscom AFB, MA, 42 pp., 1989.

Bruegge, C.J., J.E. Conel, J.S. Margolis, R.O. Green, G. Toon, V. Carrere, R.G. Holm, and G. Hoover, In-situ atmospheric water-vapor retrieval in support of AVIRIS validation, SPIE Vol. 1298, Imaging spectroscopy of the terrestrial environment, 1990.

Chrien, T.G., R.O. Green, and M. Eastwood, Laboratory spectral and radiometric calibration of the Airborne Visible/Infrared Imaging Spectrometer (AVIRIS), SPIE Vol. 1298, Imaging spectroscopy of the terrestrial environment, 1990.

Conel, J.E., R.O. Green, R.E. Alley, C.J. Bruegge, V. Carrere, J.S. Margolis, G. Vane, T.G. Chrien, P.N. Slater, S.F. Biggar, P.M. Teillet, R.D. Jackson and M.S. Moran, In-flight radiometric calibration of the Airborne Visible/Infrared Imaging Spectrometer (AVIRIS), SPIE Vol. 924, Recent advances in sensors, radiometry and data processing for remote sensing, 1988.

Green, R.O., G. Vane, and J.E. Conel, Determination of in-flight AVIRIS spectral, radiometric, spatial and signal-to-noise characteristics using atmospheric and surface measurements from the vicinity of the rare-earth-bearing carbonatite at Mountain Pass, California, in Proceedings of the Airborne Visible/Infrared Imaging Spectrometer (AVIRIS) Performance Evaluation Workshop, JPL Pub. 88-38, Jet Propulsion Laboratory, Pasadena, California, 162-184, 1988.

Green, R.O., J.E. Conel, V. Carrere, C.J. Bruegge, J.S. Margolis, M.Rast, and G. Hoover, "In-flight Validation and Calibration of the Spectral and Radiometric Characteristics of the Airborne Visible/Infrared Imaging Spectrometer (AVIRIS)," Proc. SPIE Conference on Aerospace Sensing, Imaging Spectroscopy of the Terrestrial Environment, Orlando, Florida, 16-20 April 1990.

Green, R. O., J. E. Conel, C. J. Bruegge, J. S. Margolis, V. Carrere, G. Vane and G. Hoover, "In-flight Calibration of the Spectral and Radiometric Characteristics of AVIRIS in 1991," Summaries of the Third Annual JPL Airborne Geoscience Workshop, JPL Publication 92-14, Vol. 1., pp. 1-4, Jet Propulsion Laboratory, Pasadena, CA, 1992.

Green, R. O. and B.-C. Gao, "A Proposed Update to the Solar Irradiance Spectrum Used in LOWTRAN and MODTRAN," Summaries of the Fourth Annual JPL Airborne Geoscience Workshop, JPL 93-26, Vol. 1, pp 81-84, Jet Propulsion Laboratory, Pasadena, CA, Oct. 25, 1993.

Reagan, J.A., K. Thome, B. Herman, and R. Gall, Water vapor measurements in the 0.94 micron absorption band: calibration, measurements and data applications, Proc. IGARSS, Ann Arbor, 18-21 May 1987.

6. ACKNOWLEDGEMENTS

MEASUREMENT OF ATMOSPHERIC WATER VAPOR, LEAF LIQUID WATER AND REFLECTANCE WITH AVIRIS IN THE BOREAL ECOSYSTEM-ATMOSPHERE STUDY: INITIAL RESULTS

Robert O. Green[1,2] James E. Conel[1] and Dar A. Roberts[2]

[1]Jet Propulsion Laboratory, California Institute of Technology, Pasadena CA 91109
[2]University of California, Santa Barbara, CA 93106

1.   INTRODUCTION

The Airborne Visible/Infrared Imaging Spectrometer (AVIRIS) acquired data as part of the Boreal Ecosystem-Atmosphere Study (BOREAS) in 1994. Flights occurred over the Northern Study Area (NSA) in the region of 56 degrees north latitude and 98.5 degrees west longitude and over the Southern Study Area (SSA) at 54 degrees north latitude and 105 degrees west longitude (Table 1).

Table 1. Acquisition of AVIRIS data for BOREAS in 1994.

Southern Study Area	19 April 1994
Northern Study Area	20 April 1994
Northern Study Area	28 April 1994
Northern Study Area	8 June 1994
Southern Study Area	21 July 1994
Northern Study Area	4 August 1994
Northern Study Area	8 August 1994
Southern Study Area	16 September 1994

These data will be used to directly derive spectral properties of the surface and atmosphere and to provide supporting data for other instruments, models, and experiments in support of the BOREAS objectives. In this paper we present a preliminary evaluation of the AVIRIS data collected in BOREAS in terms of the AVIRIS-derived parameters: water vapor, leaf water, and apparent spectral reflectance.

2.   WATER VAPOR, LEAF WATER, AND REFLECTANCE

AVIRIS data were acquired over the Old Jack Pine (OJP) site at 53.88 degrees north latitude and 104.92 degrees west longitude on July 21, 1994, at 16:55 UTC (Figure 1). These data, including the data over the SSA OJP site, were calibrated from the AVIRIS-measured signal to upwelling spectral radiance (Figure 2). From the upwelling radiance the atmospheric water vapor was derived with a nonlinear least squares spectral fitting algorithm (Green et al., 1991, 1993) employing the MODTRAN radiative transfer code (Berk et al., 1989). For the SSA OJP site an abundance of 23.8 ±0.5 precipitable mm of water vapor was determined (Figure 3). The algorithm was applied to the entire SSA OJP AVIRIS scene (Figure 4). A range of water vapor from 22.5 to 25.5 precipitable mm was mapped. Absorption of leaf liquid water was simultaneously derived from the water vapor with the water vapor algorithm. At the SSA OJP a value of 2.6 ±0.1 mm equivalent path transmittance leaf liquid water was required (Figure 5). Values from 0.0 to 4.5 mm of equivalent path transmittance leaf liquid water were derived for the entire AVIRIS data set (Figure 6). Over areas of open water the derived water vapor is high and leaf water is low due to the dominance of multiple scattering of light and minimal surface reflectance at 940 nm in the AVIRIS spectrum. Using the derived water vapor in conjunction with AVIRIS-based estimates of the aerosol scattering, the upwelling spectral radiance for the SSA OJP site measured by AVIRIS was inverted to apparent spectral reflectance (Green, 1990; Green et al., 1993) (Figure 7). Examination of the inverted spectrum shows good agreement with that expected for a coniferous vegetation spectrum.

3.   CONCLUSION

In 1994, AVIRIS measured images of upwelling spectral radiance for BOREAS during 8 different flights, including both southern and northern areas. Spectral fitting and inversion algorithms were applied to spectra measured over the SSA OJP region on July 21, 1994 to evaluate the calibration and quality of the AVIRIS data. Water vapor, leaf liquid water, and apparent surface reflectance were directly derived from the measured spectra, indicating good calibration. Based on

this AVIRIS calibration, research may proceed with the derived atmospheric and surface parameters to address the objectives of BOREAS.

4.   FUTURE WORK

AVIRIS-derived atmospheric and surface parameters will be compared to equivalent parameters measured by in situ instrumentation. Data acquisitions spanning the eight AVIRIS flights and two regions will be further evaluated with respect to calibration and inter-comparability.

5.   ACKNOWLEDGMENTS

The research described in this paper was carried out in part at the Jet Propulsion Laboratory, California Institute of Technology, under a contract with the National Aeronautics and Space Administration.

6.   REFERENCES

Berk, A., L. S. Bernstein, and D. C. Robertson, 1989, *MODTRAN: A moderate resolution model for LOWTRAN 7, Final Report, GL-TR-0122*, AFGL, Hanscom AFB, MA, 42 pp.

Green, R. O., 1990, "Radiative-transfer-based retrieval of reflectance from calibrated radiance imagery measured by an imaging spectrometer for lithological mapping of the Clark Mountains, California," *SPIE, Vol. 1298, Imaging Spectroscopy of the Terrestrial Environment*, pp. 213-221.

Green, R. O., J. E. Conel, J. S. Margolis, C. J. Bruegge, and G. L. Hoover, 1991, "An Inversion Algorithm for Retrieval of Atmospheric and Leaf Water Absorption From AVIRIS Radiance With Compensation for Atmospheric Scattering," *Proc. Third Airborne Visible/Infrared Imaging Spectrometer (AVIRIS) Workshop, JPL Publication 91-28*, Jet Propulsion Laboratory, Pasadena, CA, pp. 51-61.

Green, R. O., J. E. Conel, and D. A. Roberts, 1993, "Estimation of aerosol optical depth, pressure elevation, water vapor and calculation of apparent surface reflectance from radiance measured by the Airborne Visible/Infrared Imaging Spectrometer (AVIRIS) using a radiative transfer code," *SPIE, Vol. 1937, Imaging Spectrometry of the Terrestrial Environment*, pp. 2-11.

Figure 1. AVIRIS image of SSA Old Jack Pine region (see AVIRIS Workshop Slide 3).
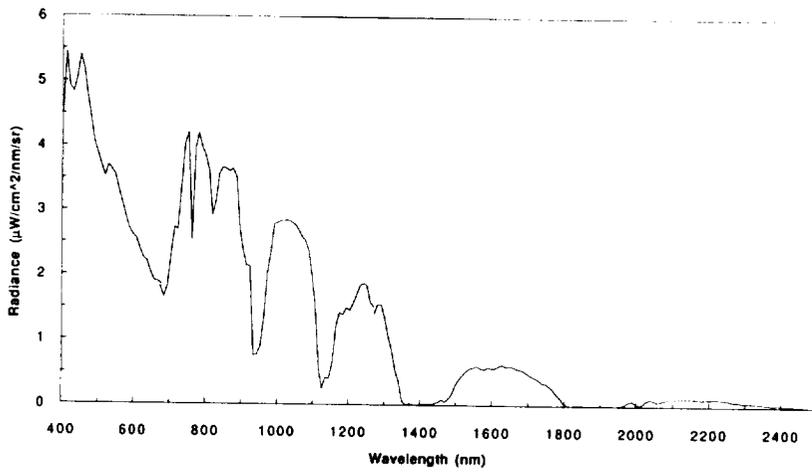
Figure 2. Upwelling spectral radiance measured by AVIRIS for the Old Jack Pine site on 21 July 1994.
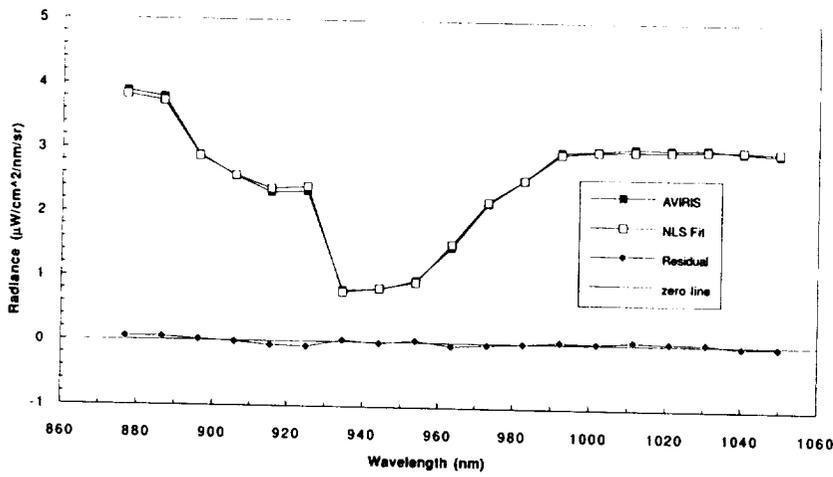
Figure 3. Nonlinear least squares spectral fit for determination of water vapor.
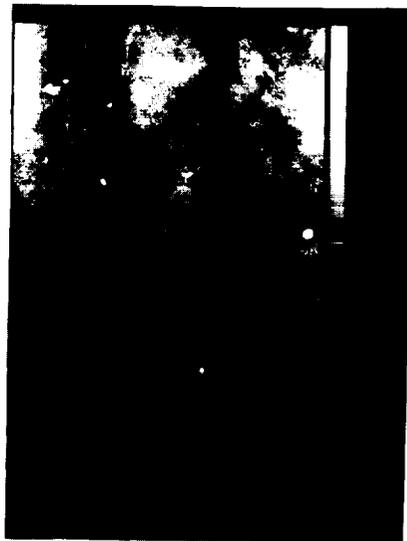
Figure 4. Image of water vapor over the SSA Old Jack Pine site (see AVIRIS Workshop Slide 3).
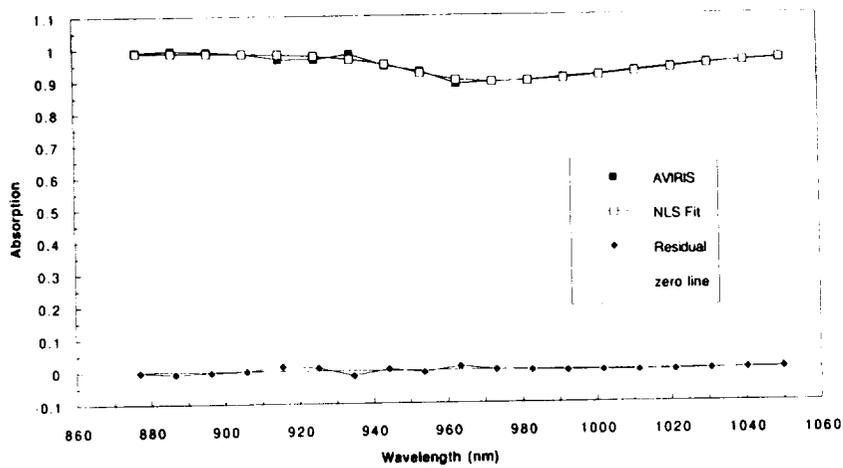
Figure 5. Nonlinear least squares spectral fit for determination of absorption due to leaf liquid water.

Figure 6. Image of leaf liquid water absorption, derived from AVIRIS spectral data (see AVIRIS Workshop Slide 3).
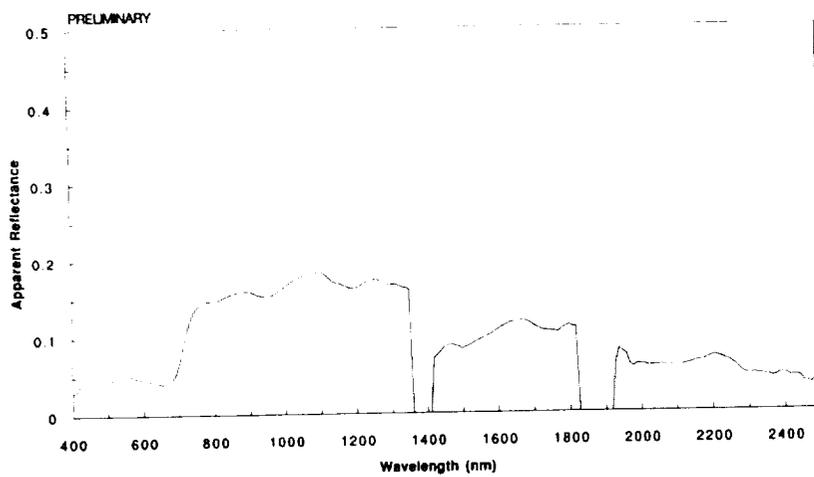
Figure 7. RTC-derived surface reflectance for SSA Old Jack Pine site, from AVIRIS on 21 July 1994.

90

MEASUREMENT OF THE SPECTRAL ABSORPTION OF LIQUID WATER IN MELTING SNOW WITH AN IMAGING SPECTROMETER

Robert O. Green[1,2] and Jeff Dozier[2]

[1]Jet Propulsion Laboratory, California Institute of Technology, Pasadena, CA 91109
[2]University California at Santa Barbara, CA 93106

1. INTRODUCTION

Melting of the snowpack is a critical parameter that drives aspects of the hydrology in regions of the Earth where snow accumulates seasonally. New techniques for measurement of snow melt over regional scales offer the potential to improve monitoring and modeling of snow-driven hydrological processes. In this paper we present the results of measuring the spectral absorption of liquid water in a melting snowpack with the Airborne Visible/Infrared Imaging Spectrometer (AVIRIS).

AVIRIS data were acquired over Mammoth Mountain, in east central California on 21 May 1994 at 18:35 UTC (Figure 1). The air temperature at 2926 m on Mammoth Mountain at site A was measured at 15-minute intervals during the day preceding the AVIRIS data acquisition. At this elevation, the air temperature did not drop below freezing the night of the May 20 and had risen to 6 degrees Celsius by the time of the overflight on May 21. These temperature conditions support the presence of melting snow at the surface as the AVIRIS data were acquired.

2. OPTICAL PROPERTIES OF LIQUID WATER AND ICE

The basis for the spectral measurement of liquid water is derived from the optical properties of liquid water in the 400- to 2500-nm range. To spectrally measure liquid water in snow, its absorption must be separable from the absorption due to frozen water. The complex refractive indices (Warren, 1982; Kou et al., 1993) were used to model the spectral properties of liquid water and ice. The complex refractive indices of these two phases of water are similar in overall magnitude and spectral trend. However, in detail these physical constants differ due to the different molecular bond energies of water in the liquid and solid state.

To investigate the contrast in spectral absorption between liquid water and ice, the transmittance of a 10-mm path through these materials was calculated (Figure 2). The spectral absorptions are overlapping, but displaced in both the 1000- and 1200-nm spectral regions. The 1000-nm spectral region is selected for this research because snow is more reflective at these wavelengths and path lengths of 10 mm are expected in the snowpack (Dozier, 1989).

3. AVIRIS MEASUREMENTS AND TRANSMITTANCE MODEL

AVIRIS measures the upwelling spectral radiance from 400 to 2500 nm at 10-nm intervals and collects images of 11 by up to 1000 km at 20-m spatial resolution. AVIRIS radiance spectra acquired over Mammoth Mountain were inverted to apparent spectral reflectance (Green, 1990; Green et al., 1993). An equivalent path transmittance model was developed for liquid water and ice in the 1000 nm spectral region. The model was inverted using a nonlinear least squares fitting routine to derive the equivalent path length transmittance of liquid water and ice for each spectrum measured by AVIRIS. A linear spectral albedo term is included in the model to compensate for illumination. For the AVIRIS spectrum in open snow below and adjacent to site A, the inverted spectral model returned values of 1.9 ± 0.1 mm liquid water and 13.3 ± 0.7 mm ice (Figure 3). The presence of liquid water due to surface melting at this elevation is consistent with the temperature prior to the AVIRIS acquisition. For site B to the north of the summit of Mammoth Mountain, the inverted model returned equivalent path transmittance of 0.0 mm liquid water and 20.1 ± 0.9 mm (Figure 4). At the 3362 m summit, the temperature is calculated to be 2.6 degrees Celsius colder. Snow at these higher elevations and north facing slopes had not commenced surface-melting at the time of AVIRIS data acquisition.

This equivalent path transmittance model was inverted for the entire AVIRIS scene of Mammoth Mountain (Figure 5). Absorption due to ice in snow is measured at Mammoth Mountain and to the higher elevations in the northwest. At this late spring date, absorption due to ice was not measured at the lower elevations to the east and in the valley to the west of the mountain. The equivalent path transmittance due to liquid water was derived for the AVIRIS scene (Figure 6). Liquid water is measured in the AVIRIS spectrum in the snow at the lower elevations at Mammoth Mountain. As expected, liquid water is absent at the highest elevations of Mammoth Mountain where the snow is fully frozen. At low elevations, liquid water is also measured in the leaves of vegetation (Green et al., 1991). Liquid water in melting snow is

spectrally distinguishable from liquid water in vegetation, based either on the absorption of ice in snow or chlorophyll in vegetation.

4. CONCLUSION

Examination of the optical constants of liquid and solid water shows that in the 1000 nm region these two phases of water are separable, based upon their spectral properties. Measurement of these two phases of water requires spectral modeling of the overlapping absorptions of the liquid water absorption centered at 970 nm and the ice absorption at 1030 nm. An equivalent-path transmittance model was developed for liquid water and ice. This model was inverted using a nonlinear, least-squares spectral fitting approach for Mammoth Mountain AVIRIS data. Liquid water and ice were measured in melting snow below 2926 m based on spectral properties. Near the summit at 3362 m, only the absorption due to ice was measured. The occurrence of fully frozen snow at high elevations and melting snow at intermediate and low elevations is consistent with measured temperatures and elevations at the time and date of the AVIRIS acquisition.

This first-time remote measurement of the spectral absorption of liquid water in a melting snowpack will lead to new algorithms for the measurement, modeling and monitoring of snow-driven hydrological processes.

5. FUTURE WORK

Future research will focus on development of a radiative transfer model of the snowpack when both the liquid and solid phases of water are present. In 1995 additional AVIRIS flights with in situ measurements will be used to further validate the measurement of these two phases of water in the snowpack.

6. ACKNOWLEDGMENTS

7. REFERENCES

Dozier, J., 1989, "Remote Sensing of Snow in Visible and Near-Infrared Wavelengths," in Theory and Applications of Optical Remote Sensing, G. Asrar, ed., pp. 527-547, Wiley and Sons.

Green, R. O., 1990, "Radiative-transfer-based retrieval of reflectance from calibrated radiance imagery measured by an imaging spectrometer for lithological mapping of the Clark Mountains, California," SPIE Vol. 1298, Imaging Spectroscopy of the Terrestrial Environment.

Green, Robert O., James E. Conel, Jack S. Margolis, Carol J. Bruegge, and Gordon L. Hoover, 1991, "An Inversion Algorithm for Retrieval of Atmospheric and Leaf Water Absorption From AVIRIS Radiance With Compensation for Atmospheric Scattering," Proc. Third AVIRIS Workshop, JPL Publication 91-28, Jet Propulsion Laboratory, Pasadena, California, pp. 51-61.

Green, R. O., J. E. Conel, D. A. Roberts, 1993, "Estimation of Aerosol Optical Depth, Pressure Elevation, Water Vapor and Calculation of Apparent Surface Reflectance from Radiance Measured by the Airborne Visible/Infrared Imaging Spectrometer (AVIRIS) using a Radiative Transfer Code," SPIE, Vol. 1937, Imaging Spectrometry of the Terrestrial Environment, p. 2-11.

Kou, L., D. Labrie, and P. Chylek, 1993, "Refractive indices of water and ice in the 0.65- to 2.5-μm spectral range," Applied Optics, Vol. 32, No. 19, P. 3531-3540.

Warren, S. G., 1982, "Optical Properties of Snow," Reviews of Geophysics and Space Physics, vol. 20, pp. 67-89.

8. FIGURES
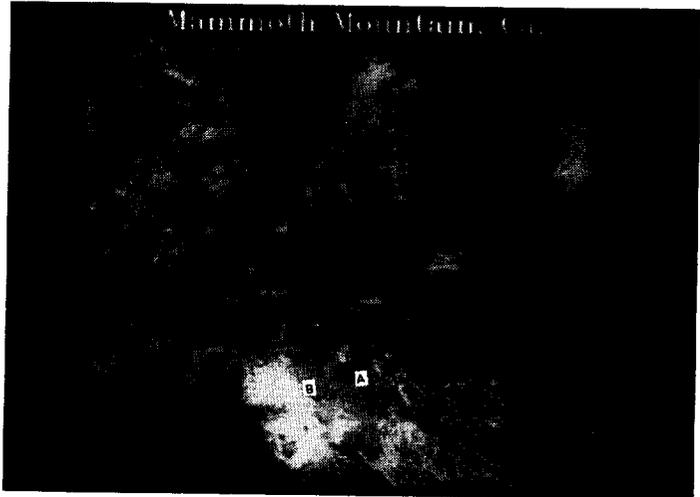
Figure 1. AVIRIS image of Mammoth Mountain with ski runs in the lower center of the image. North is to the top. (See AVIRIS Workshop Slide 4.)
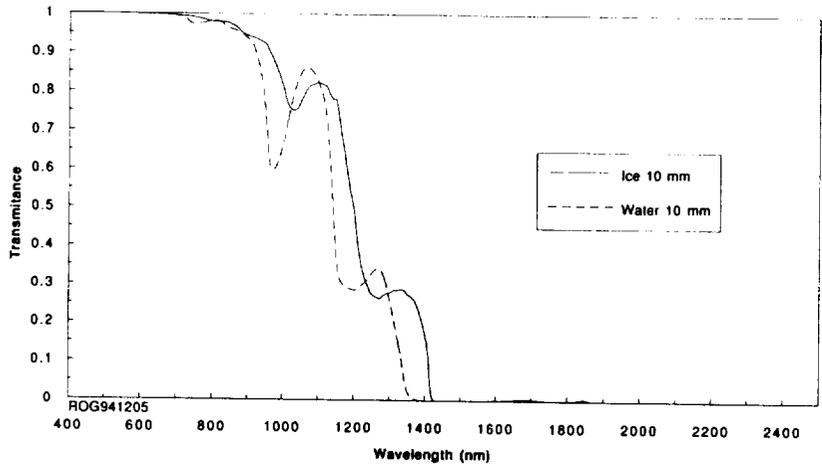
Figure 2. Transmission of light through 10 mm of water and ice.
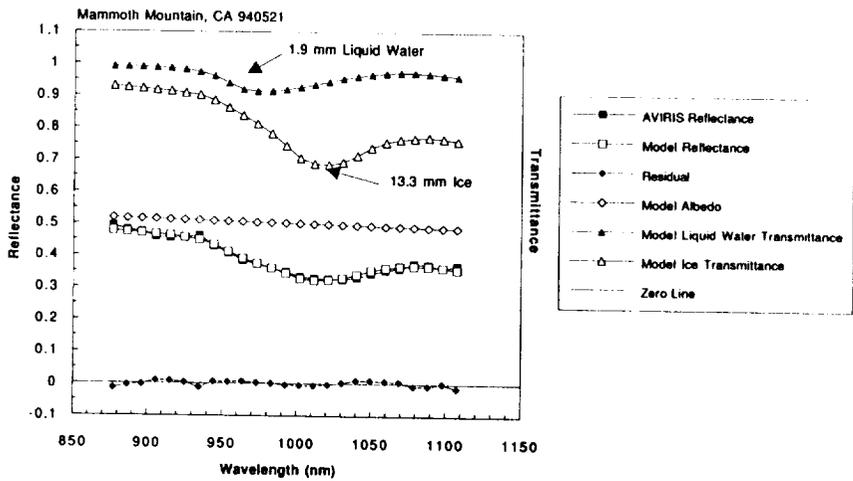
Figure 3. For site A at Mammoth Mountain, CA, the AVIRIS-measured spectrum and modeled spectrum when both liquid water and ice are present. Also shown is the residual disagreement and components of the model.

93
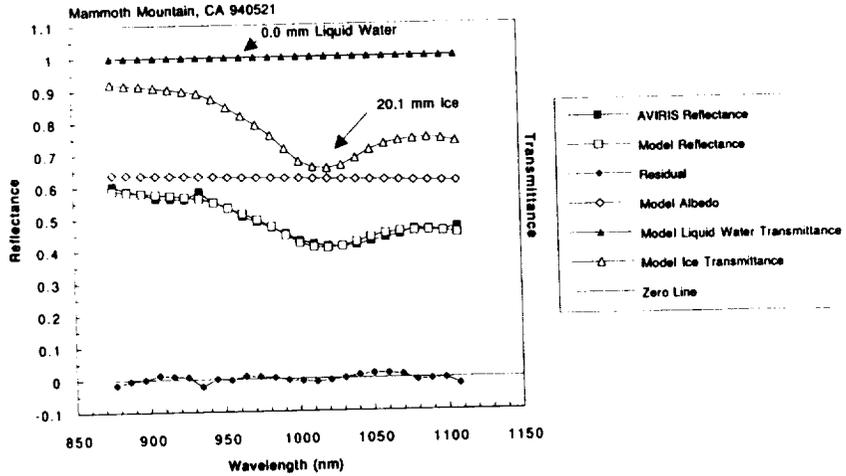
Figure 4. For site B, the AVIRIS-measured spectrum and modeled spectrum when ice is present, but liquid water is absent.

Figure 5. AVIRIS-derived path equivalent transmittance image for ice at Mammoth Mountain, CA. Ice is present only on the higher elevation in the May data set. (See AVIRIS Workshop Slide 4.)
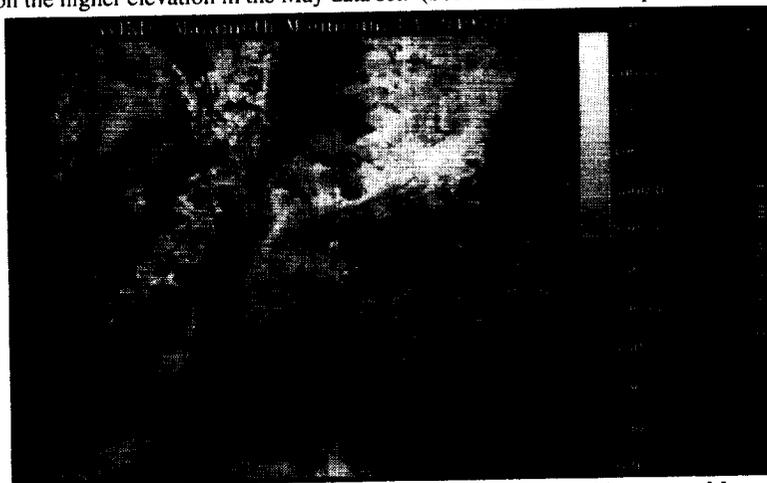
Figure 6. AVIRIS-derived path equivalent transmittance image for liquid water at Mammoth Mountain, CA. Liquid water is present on the lower snow slopes of the mountain where the snow is melting. Liquid water is also measured in healthy vegetation. (See AVIRIS Workshop Slide 4.)

94

VEGETATION SPECIES COMPOSITION AND CANOPY ARCHITECTURE INFORMATION EXPRESSED IN LEAF WATER ABSORPTION MEASURED IN THE 1000 nm AND 2200 nm SPECTRAL REGION BY AN IMAGING SPECTROMETER

Robert O. Green[1,2] and Dar A. Roberts[2]

[1]Jet Propulsion Laboratory, California Institute of Technology, Pasadena, CA 91109
[2]University of California at Santa Barbara, CA 93106

1.   INTRODUCTION

Plant species composition and plant architectural attributes are critical parameters required for the measuring, monitoring, and modeling of terrestrial ecosystems. Remote sensing is commonly cited as an important tool for deriving vegetation properties at an appropriate scale for ecosystem studies, ranging from local to regional and even synoptic scales (e.g., Wessman, 1992). Classical approaches rely on vegetation indices such as the Normalized Difference Vegetation Index (NDVI) to estimate biophysical parameters such as leaf area index or intercepted photosynthetically active radiation (IPAR). Another approach is to apply a variety of classification schemes to map vegetation and thus extrapolate fine-scale information about specific sites to larger areas of similar composition. Imaging spectrometry provides additional information that is not obtainable through broad-band sensors and that may provide improved inputs both to direct biophysical estimates as well as classification schemes. Some of this capability has been demonstrated through improved discrimination of vegetation (e.g., Roberts et al., 1992, 1993a), estimates of canopy biochemistry (e.g., Wessman et al., 1988) and liquid water estimates from vegetation (Green et al., 1991, 1993, and Roberts et al., 1993b, 1994). In this paper we investigate further the potential of leaf water absorption estimated from Airborne Visible/Infrared Imaging Spectrometer (AVIRIS) data as a means for discriminating vegetation types and deriving canopy architectural information. We expand our analysis to incorporate liquid water estimates from two spectral regions, the 1000-nm region and the 2200-nm region.

The study was conducted in the vicinity of Jasper Ridge, California, which is located on the San Francisco peninsula to the west of the Stanford University campus. AVIRIS data were acquired over Jasper Ridge, CA, on June 2, 1992, at 19:31 UTC (Figure 1). Spectra from three sites in this image were analyzed. These data are from an area of healthy grass, oak woodland, and redwood forest, respectively. For these analyses, the AVIRIS-measured upwelling radiance spectra for the entire Jasper Ridge scene were transformed to apparent surface reflectance using a radiative transfer code-based inversion algorithm (Green, 1990; Green et al., 1993).

2.   LEAF LIQUID WATER DETERMINATIONS

The absorption of water expressed in the reflectance of leaves in the AVIRIS spectra was modeled as the equivalent path transmittance through liquid water. For this model, the absorption coefficient for water was used to fit the expressed absorption of water and a linearly varying spectral albedo parameter was used to account for the spectrum brightness. Liquid water was estimated from two spectral regions, the 1000-nm region, where absorption is low, and the 2200-nm region, where leaf water absorption ranges from moderate to high.

A nonlinear least squares algorithm was developed to fit the modeled spectrum to the measured spectrum, minimizing the residual over a specified spectral range. Results are first presented for the 1000-nm region. For the healthy grass, an equivalent path of 1.83 mm was determined for liquid water as the best fit between the AVIRIS spectrum and the model (Figure 2). This path results from a combination of transmittance and scattering from single leaves as well as from multiple scattering within the grass canopy. In comparison, fitted leaf water for evergreen oak woodland was 2.16 mm, and for redwood forest, it was 3.48 mm (Figure 2). Large differences in equivalent path transmittance of liquid water expressed in the spectra were shown for these three species types. These differences result from the species' leaf thickness as well as from canopy architecture. The trend shown is for the equivalent path transmittance of liquid water to increase as

the species type changes from thin to thick leaves, and as the canopy changes from shallow to deep.

The leaf water equivalent path transmittance model has been inverted for the entire AVIRIS scene using a 1000-nm spectral region (Figure 3). This image shows a number of distinct contiguous plant communities mapped in terms of the expressed leaf water. The equivalent path transmittance model was applied to these same spectra in the 2200-nm spectral region. Resulting estimates of leaf water path were considerably lower in the 2200-nm region when compared to the 1000-nm region, producing estimates of 0.37, 0.81, and 1.03 mm for the healthy grass, evergreen oak woodland, and redwood forest, respectively (Figure 4). In this spectral region, strong absorption results in reduced transmittance and scattering of light at the individual leaf and canopy scales; this results in reduced overall brightness and reduced expression of the liquid water absorption. Contrast in the 2200-nm region may be further reduced by spectral reflection off leaf surfaces which, in regions of low spectral reflectance, may constitute a majority of the reflected signal. The difference in total expressed water between species in conjunction with the contrast in expressed water between spectral regions provides information on both the plant species composition and plant architectural attributes.

3.   CONCLUSION

Expressed leaf water derived from AVIRIS spectra using an equivalent path transmittance model was compared for three communities consisting of markedly different plant species with divergent plant architectures. A difference in expressed water derived from the 1000-nm spectral region was shown for the healthy grass, evergreen oak woodland, and redwood forest sites in AVIRIS data from Jasper Ridge. The expressed leaf water was determined for the full AVIRIS image, showing the differentiation of plant communities based on this parameter. Furthermore, there were differences between the expressed liquid water in the 1000-nm and 2200-nm spectral region for these communities. These results are consistent with differences in plant leaf and canopy architecture properties between these vegetation types. Derivation of plant species type and canopy architectural information through imaging spectrometer measurements provides a new approach for determining these vegetation parameters remotely at a range of scales. Future work will incorporate leaf and canopy optical models to more quantitatively relate the expressed leaf water in different portions of the spectrum to the physical properties of the vegetation.

4.   ACKNOWLEDGMENTS

5.   REFERENCES

Green, R. O., 1990, "Radiative-transfer-based retrieval of reflectance from calibrated radiance imagery measured by an imaging spectrometer for lithological mapping of the Clark Mountains, California," *SPIE, Vol. 1298, Imaging Spectroscopy of the Terrestrial Environment,* pp. 213-221.

Green, R. O., J. E. Conel, J. S. Margolis, C. J. Bruegge, and G. L. Hoover, 1991, "An Inversion Algorithm for Retrieval of Atmospheric and Leaf Water Absorption From AVIRIS Radiance With Compensation for Atmospheric Scattering," *Proc. Third Airborne Visible/Infrared Imaging Spectrometer (AVIRIS) Workshop, JPL Publication 91-28,* pp. 51-61.

Green, R. O., J. E. Conel, and D. A. Roberts, 1993, "Estimation of aerosol optical depth, pressure elevation, water vapor and calculation of apparent surface reflectance from radiance measured by the Airborne Visible/Infrared Imaging Spectrometer (AVIRIS) using a radiative transfer code," *SPIE, Vol. 1937, Imaging Spectrometry of the Terrestrial Environment,* pp. 2-11.

Roberts, D. A., M. O. Smith, D. E. Sabol, J. B. Adams, and S. Ustin, 1992, "Mapping the Spectral Variability in Photosynthetic and Non-photosynthetic Vegetation, Soils and Shade Using

AVIRIS," *JPL Publication 92-14, Summaries of the Third Annual JPL Airborne Geoscience Workshop, Vol. 1 (AVIRIS Workshop)*, Jet Propulsion Laboratory, Pasadena, CA, pp. 38-40.

Roberts, D. A., M. O. Smith, and J. B. Adams, 1993a, "Green vegetation, non-photosynthetic vegetation and soils in AVIRIS data," *Rem. Sens. Environ., 44: 2/3*, pp. 255-270.

Roberts, D. A., R. O. Green, D. E. Sabol, and J. B. Adams, 1993b, "Temporal changes in endmember abundances, liquid water and water vapor over vegetation at Jasper Ridge," *JPL Publication 93-26, Summaries of the Fourth Annual JPL Airborne Geoscience Workshop, Vol. 1 (AVIRIS Workshop)*, Oct. 25-29, pp. 153-156.

Roberts, D. A., R. O. Green, J. B. Adams, J. S. Cothern, D. E. Sabol, and M. O. Smith, 1994, "Temporal and spatial relationships between topography, atmospheric water vapor, liquid water and vegetation endmember fractions determined using AVIRIS," *1994 International Geoscience and Remote Sensing Symposium (IGARSS'94), Vol. IV*, Pasadena, CA, Aug. 8-12, pp. 2366-2368.

Wessman, C.A., 1992, "Spatial scales and global change: Bridging the gap from plots to GCM grid cells," *Annual Review of Ecology and Systematics, 23*: 175-200.

Wessman, C.A., J. D. Aber, D. L. Peterson, and J. M. Mellilo, 1988, "Remote sensing of canopy chemistry and nitrogen cycling in temperate forest ecosystems," *Nature, 335(8):* 154-156.
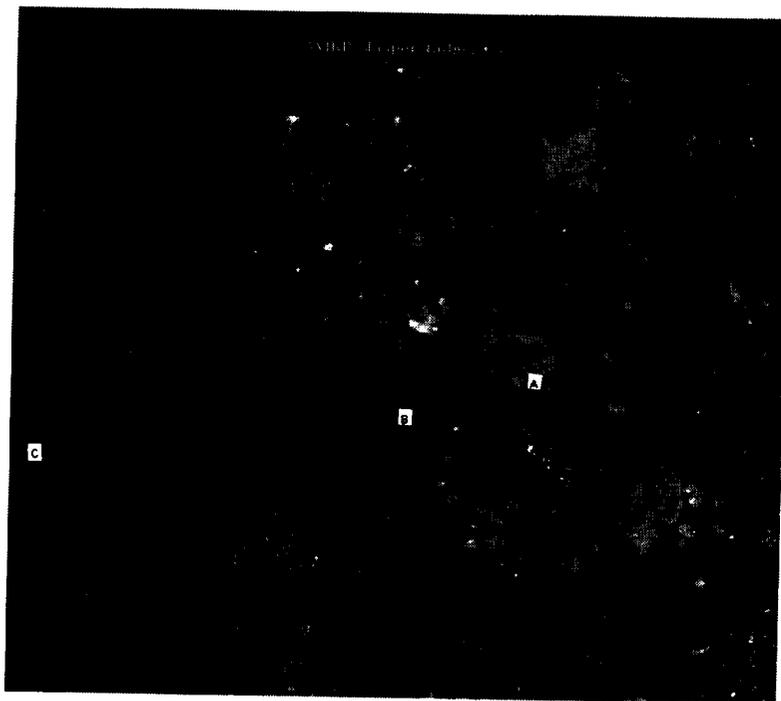
Figure 1. AVIRIS image of Jasper Ridge, CA, acquired on June 2, 1992 at 19:31 UTC. Sites A, B, and C show the locations of the healthy grass, oak woodland, and redwood forest plant communities, respectively (see AVIRIS Workshop Slide 5).
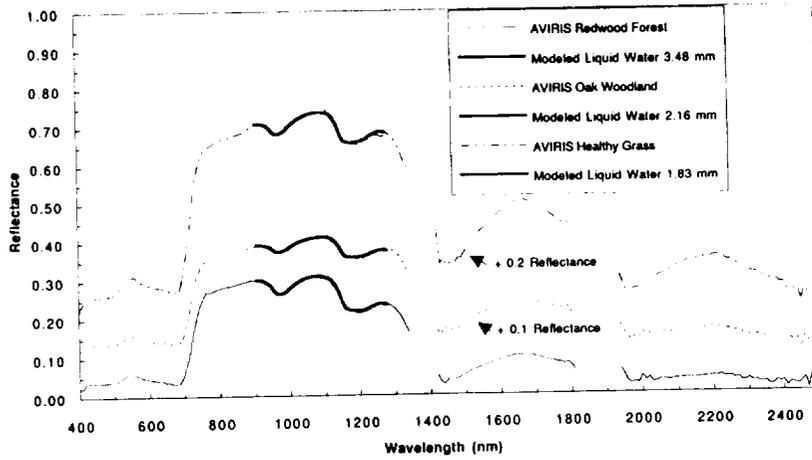
Figure 2. Equivalent path transmittance leaf water for healthy grass, oak woodland, and redwood forest in the 1000-nm spectral region.

Figure 3. Image of liquid water equivalent path transmittance for the Jasper Ridge AVIRIS scene in microns (see AVIRIS Workshop Slide 5).
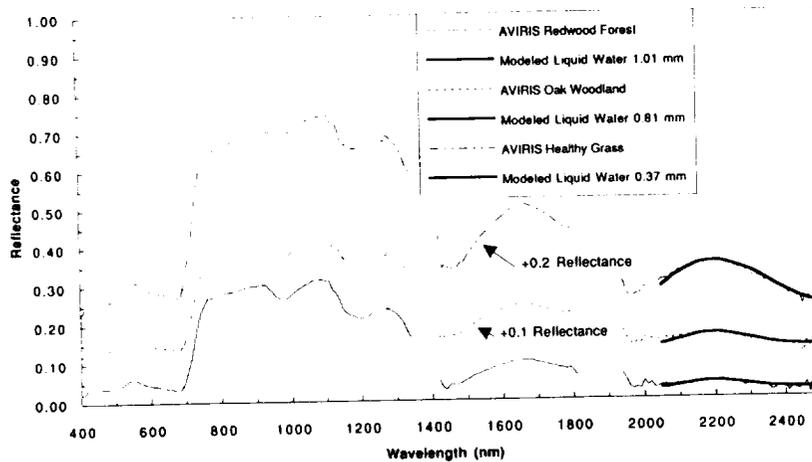
Figure 4. Expressed leaf water for healthy grass, oak woodland, and redwood forest at 2200 nm.

PROSPECT REDUX

S. Jacquemoud[1], S.L. Ustin[1], J. Verdebout[2], G. Schmuck[2], G. Andreoli[2], B. Hosgood[2]

[1] University of California, Land, Air, and Water Resources, Davis, CA 95616, USA
[2] Joint Research Centre, IRSA/AT, 21020 Ispra (VA), Italy

1. INTRODUCTION

The remote estimation of leaf biochemical content from spaceborne platforms has been the subject of many studies aimed at better understanding of terrestrial ecosystem functioning. The major ecological processes involved in exchange of matter and energy, like photosynthesis, primary production, evapotranspiration, respiration, and decomposition can be related to plant properties e.g., chlorophyll, water, protein, cellulose and lignin contents (Peterson, 1991). As leaves represent the most important plant surfaces interacting with solar energy, a top priority has been to relate optical properties to biochemical constituents. Two different approaches have been considered: first, statistical correlations between the leaf reflectance (or transmittance) and biochemical content, and second, physically based models of leaf scattering and absorption developed using the laws of optics. Recently reviewed by Verdebout et al. (1994), the development of models of leaf optical properties has resulted in better understanding of the interaction of light with plant leaves.

Present radiative transfer models mainly use chlorophyll and / or water contents as input parameters to calculate leaf reflectance or (Jacquemoud and Baret, 1990; Fukshansky et al., 1991; Yamada and Fujimura, 1991; Martinez v. Remisowsky et al., 1992). Inversion of these models allows to retrieve these constituents from spectrophotometric measurements. Conel et al. (1993) recently proposed a two-stream Kubelka-Munk model to analyse the influence of protein, cellulose, lignin, and starch on leaf reflectance, but in fact, the estimation of leaf biochemistry from remote sensing is still an open question. In order to clarify it, a laboratory experiment associating visible / infrared spectra of plant leaves both with physical measurements and biochemical analyses was conducted at the Joint Research Centre during the summer of 1993. This unique data set has been used to upgrade the PROSPECT model (Jacquemoud and Baret, 1990) by including leaf biochemistry.

2. THE EXPERIMENT

The LOPEX (Leaf Optical Properties Experiment) is detailed in Jacquemoud et al. (1994); it consists of a wide range of variation in leaf internal structure, pigments, water, and biochemistry contents. In total, about 70 leaf samples representing 50 woody and herbaceous species were obtained from trees and crops near the Joint Research Centre in Italy. The hemispherical reflectance (R), transmittance (T), and infinite reflectance (R∞) of fresh and dry leaves were measured using a Perkin Elmer Lambda 19 spectrophotometer over the 400-2500 nm wavelength interval.

Many physical and biological measurements were performed on leaf samples: blade thickness, specific leaf area (SLA = dry weight per unit leaf area), equivalent water thickness (EWT = water mass per unit leaf area), photosynthetic pigments (chlorophyll a, b, and total carotenoids), biochemical components (total proteins, cellulose, lignin, and starch), and finally elementary composition (C, H, O, N). Table 1 gives descriptive statistics and illustrates the range in leaf biophysical characteristics. Good relationships among some biochemicals were established, including leaf thickness

	range	mean	std
thickness (μm)	86.4 – 780.0	194.7	114.9
SLA (cm^2.g^{-1})	73.9 – 535.3	224.6	93.4
EWT (g.cm^{-2})	0.0046 – 0.0405	0.0115	0.0067
Chl. a (μg.cm^{-2})	12.8 – 64.2	36.9	11.4
Chl. b (μg.cm^{-2})	3.7 – 21.3	11.7	3.8
Carot. (μg.cm^{-2})	3.7 – 19.4	10.5	3.6
Proteins (% MS)	7.4 – 36.7	20.0	7.0
Cellulose (% MS)	9.1 – 37.2	19.7	6.4
Lignin (% MS)	1.1 – 27.5	10.2	6.5
Starch (% MS)	0.0 – 10.0	1.9	2.1
Carbon (% MS)	38.5 – 52.3	47.1	2.9
Nitrogen (% MS)	1.2 – 5.9	3.4	1.1

Table 1. Leaf biophysical measurements.

and EWT, proteins and SLA or total chlorophylls. The strongest relationships were obtained between nitrogen and proteins, and between carbon and cellulose + lignin (Figure 1). This equivalence is very important because the C/N ratio which drives the decomposition rates of forest litter, affecting nutrient cycling and trace gas fluxes, can be replaced by the cellulose + lignin over protein ratio.
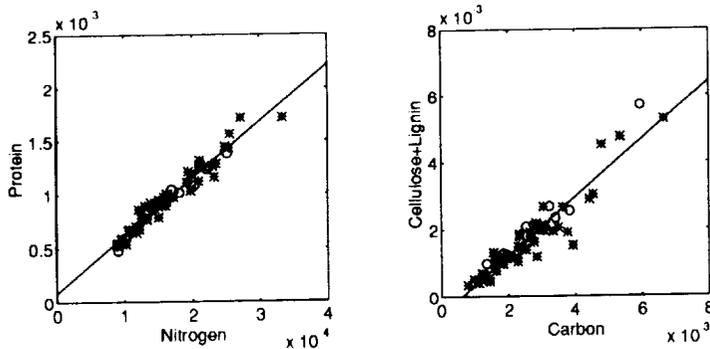
Figure 1. Comparison between a) nitrogen and protein concentrations b) carbon and cellulose+lignin concentrations (g.cm^{-2}). Circles indicate Monocots and stars Dicots.

3. CONSTRUCTION OF THE MODEL

PROSPECT is a radiative transfer model which calculates the leaf spectral reflectance and transmittance from 400 to 2500 nm. Scattering is described by the refractive index (n) of leaf materials and by a parameter characterizing the leaf mesophyll structure (N). Absorption is modeled using pigment concentration (C$_{ab}$), water depth (C$_w$ ⟷ EWT), and the corresponding specific absorption coefficients (K$_{ab}$ and K$_w$).

Modeling absorption processes implies that the effects of mesophyll structure in the NIR (780–920 nm) are accounted for. The reflectance and transmittance levels in the NIR are driven by the parameter N, number of stacked elementary layers. In the basic version of PROSPECT, the absorption by one elementary layer was small and was assumed to be constant (ko=0.0134). The origin of this absorption is uncertain but it cannot be attributed to either chlorophyll or water. Hypothesizing that NIR radiation is absorbed by the cell walls, then leaf optical properties must be explained by the N parameter and the absorption coefficient ko of the elementary layer. Neglecting the contributions of water and starch which are very small, ko can be written both as a function of N and the protein and cellulose+lignin concentrations expressed in g.cm^{-2}.

$$ko = \frac{k_1.[\text{protein}] + k_2.[\text{cellulose} + \text{lignin}]}{N}$$

The N parameter has been adjusted for each leaf while a global value for the two specific absorption coefficients was determined (k1=12.10 and k2=6.92). In that way, leaf reflectance and transmittance in the NIR are well modeled with a root mean square error $rmse$ = 0.0243. The ko values range from 0.0050 to 0.0275 with an average of 0.0135 which is very close to the constant provided by Jacquemoud and Baret (1990); in consequence, if leaf biochemistry is unknown, the coefficient ko=0.0135 can be used with reasonable results ($rmse$=0.0250).

The wavelength independent mesophyll structure parameter N is used to invert the Stokes equations: using measured reflectance and transmittance, the compact layer is easily calculated, permitting the determination of a spectral absorption coefficient $ko(\lambda)$. If the assumption is made that the leaf is a homogeneous mixture of biochemical components, the absorption coefficient can be written as:

$$ko(\lambda) = ke(\lambda) + \frac{k1(\lambda).[protein] + k2(\lambda).[cellulose + lignin] + k3(\lambda).[water] + k4(\lambda).[pigments]}{N}$$

where λ is the wavelength, $k1(\lambda)...k4(\lambda)$ are respectively the specific absorption coefficients for protein, cellulose+lignin, water, and photosynthetic pigments (chlorophyll a+b and total carotenoids). $ke(\lambda)$ explains the non-zero absorption of an albino leaf under 500 nm. Assuming that the specific absorption coefficients are known, one can predict the constituent concentrations and compare them with measured ones. For various reasons, this method is difficult to apply so another strategy was adopted: using the absorption coefficients $ko(\lambda)$ and the measured concentrations, we deduced the specific absorption coefficients of leaf biochemical components.
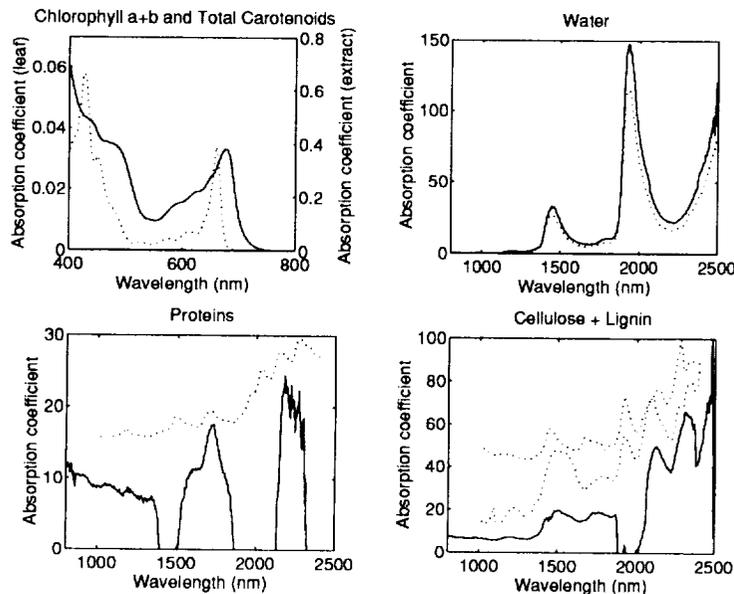
Figure 2. Specific absorption coefficients of a) photosynthetic pigments [the dotted points correspond to pigments in acetone, Lichtenthaller, 1987] b) water [the dotted points correspond to pure liquid water, Curcio and Petty, 1951] c) protein [the dotted points correspond to pure powdered material, Wessman, 1990] d) cellulose+lignin [the dotted points correspond to pure powdered material, Wessman, 1990].

Figure 2 shows that k3(λ) agrees very well with the fundamental constants published for pure liquid water. For pigments, the specific absorption coefficient k4(λ) displays classical features with some spectral shifts of the principal absorption peaks compared to *in vitro* observations. Results are less convincing for protein and cellulose+lignin: in particular, absorption peaks for protein are not well represented. Cellulose+lignin is better reproduced with some characteristic spectral features.

4. VALIDATION

Before a model can be used with confidence it must be validated. We tested our model in direct mode, by simulating reflectance and transmittance of 63 fresh leaves using the measured concentrations of pigments, water, protein, cellulose+lignin, and the estimated values of the mesophyll structure parameter N; the spectral *rmse* is low (<0.02) except in the absorption peaks of the visible where it equals 0.03. The transmittance, which is generally more sensitive to the model parameters than the reflectance, is surprisingly better simulated. The validation was carried out with the same data set. In Figure 3 the values provided by the model inversion are plotted against measured values: the high correlation for pigments and water shows that the procedure is successful in retrieving major leaf components whose effects predominate. Concerning minor ones, we notice that there is no sensitivity for protein but that cellulose+lignin is well estimated. In terms of reflectance and transmittance reconstruction, the very low spectral *rmse* (<0.01) demonstrates the capability of this new version of the PROSPECT model to accurately synthesize the whole leaf spectrum for widely different kinds of plant leaves using only 5 parameters.
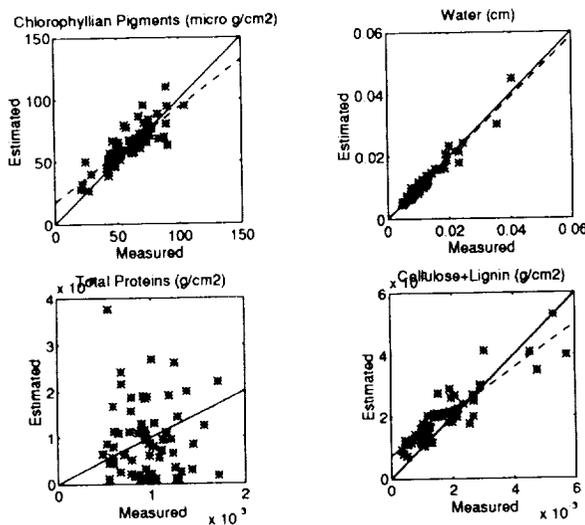
Figure 3.
Comparison between measured and estimated leaf biochemical parameters a) pigments b) water c) proteins d) cellulose+lignin.

5. CONCLUSION

In spite of the difficulties to derive specific absorption spectra in agreement with the literature, these results are very promising. It indicates that water does not obstruct all of the signal in the SWIR and that leaf biochemistry is potentially attainable from remote sensing data. The extension of the PROSPECT model to important constituents other than chlorophyll or water, i.e. proteins and cellulose+lignin, should help us to understand their specific effects on the radiometric signal. Finally, the search for the best specific absorption curves is certainly not ended.

102

REFERENCES

Conel, J.E., J. van den Bosch, and C.I. Grove, 1993, "Application of a two-stream radiative transfer model for leaf lignin and cellulose concentrations from spectral reflectance measurements. Parts 1 & 2", in *Proc. 4th Annual JPL Airborne Geoscience Workshop. Vol. 1. AVIRIS Workshop* (R.O. Green, Ed), 25-29 October 1993, Washington (DC), NASA-JPL Publication 93-26, pages 39-51.

Curcio, J.A., C.C. Petty, 1951, "The near infrared absorption spectrum of liquid water", *J. Opt. Soc. Am.*, vol. 41, no. 5, pp. 302-304.

Fukshansky, L., N. Fukshansky-Kazarinova, and A. Martinez v. Remisowsky, 1991, "Estimation of optical parameters in a living tissue by solving the inverse problem to the multiflux radiative transfer", *Appl. Opt.*, vol. 30, no. 22, pp. 3145-3153.

Jacquemoud, S. and F. Baret, 1990, "PROSPECT: a model of leaf optical properties spectra", *Remote Sens. Environ.*, vol. 34, pp. 75-91.

Jacquemoud, S., J. Verdebout, G. Schmuck, G. Andreoli, and B. Hosgood, 1994, "Investigation of leaf biochemistry by statistics", *Remote Sens. Environ.*, submitted.

Lichtenthaler, H.K., 1987, "Chlorophylls and carotenoids: pigments of photosynthetic biomembranes", *Methods Enzymol.*, vol. 148, pp. 350-382.

Martinez v. Remisowsky, A., J.H. McClendon, and L. Fukshansky, 1992, "Estimation of the optical parameters and light gradients in leaves: multi-flux *versus* two-flux treatment", *Photochem. Photobiol.*, vol. 55, no. 6, pp. 857-865.

Peterson, D.L., 1991, *Report on the workshop remote sensing of plant biochemical content: theoretical and empirical studies*, Marshall (CA), 18-20 March 1991, 50 pages.

Verdebout, J., S. Jacquemoud, and G. Schmuck, 1994, "Optical properties of leaves: modelling and experimental studies", in *Imaging Spectrometry - a Tool for Environmental Observations* (J. Hill & J. Mégier, Eds), ECSC, EEC, EAEC, Brussels and Luxembourg, pages 169-191.

Wessman, C.A., 1990, "Evaluation of canopy biochemistry", in *Remote Sensing of Biosphere Functioning* (R.J. Hobbs & H.A. Mooney, Eds), Springer-Verlag (New York), pp. 135-156.

Yamada, N. and S. Fujimura, 1991, "Nondestructive measurement of chlorophyll pigment content in plant leaves from three-color reflectance and transmittance", *Appl. Opt.*, vol. 30, no. 27, pp. 3964-3973.

AVIRIS USER'S GUIDE[*]

Howell K. Johnson and Robert O. Green

Jet Propulsion Laboratory, California Institute of Technology
4800 Oak Grove Drive, Pasadena CA 91109 USA

1. Introduction

This paper serves as a brief overview of the AVIRIS instrument (Airborne Visible/Infrared Imaging Spectrometer) and its role in the field of imaging spectrometry. Mission planning and flight operations are discussed, and recommendations are given regarding the deployment of ground truth experiments.

1.1 Objectives of imaging spectrometry with AVIRIS

The AVIRIS sensor collects data that can be used for quantitative characterization of the Earth's surface and atmosphere from geometrically coherent spectroradiometric measurements. This data can be applied to studies in the fields of oceanography, environmental science, snow hydrology, geology, volcanology, soil and land management, atmospheric and aerosol studies, agriculture, and limnology. Applications under development include the assessment and monitoring of environmental hazards such as toxic waste, oil spills, and land/air/water pollution.

1.2 Description of sensor system

The AVIRIS instrument, built and operated by the Jet Propulsion Laboratory (JPL), is a nadir-viewing whiskbroom scanner that operates unattended in the instrument bay of a NASA ER-2 high altitude aircraft. AVIRIS measures upwelling ground radiance from a nominal altitude of 20 kilometers. With proper calibration and correction for atmospheric effects, the measurements are converted to ground reflectance data which can then be used for quantitative characterization of surface features.

The spatial response of AVIRIS is 1.0 mrad, forming a "pixel" 20m by 20m on the ground. The image width (swath) is 11 km wide, and the image length is typically 10 to 100km. The spectral response ranges from blue-green to near-infrared (400 to 2450 nm). The light entering the instrument is divided between four grating spectrometers and is broken down into 224 contiguous spectral channels approximately 10 nm wide using linear arrays of InSb and Si detectors. Data quantization is 10 bits (upgrading to 12 bits in 1995 - see Sarture et al., 1995). Data from the 4 spectrometers is interleaved with instrument telemetry and aircraft navigation data, then sent out at a rate of 17 Mbits/sec (20 Mbits/sec in 1995). The data is stored on a 10-gigabyte Metrum high density tape storage unit. This allows AVIRIS to collect about 850 km of ground track data per flight.

Calibration of the sensor is maintained by several methods. First is an onboard calibrator that provides a continuous spectral and radiometric reference during data collection. Second is an intensive laboratory calibration that is performed twice each year whereby spectral, radiometric, and geometric aspects of AVIRIS data are compared with laboratory standards. Finally, an in-flight calibration is performed three times each year whereby performance is compared to theoretical predictions based on atmospheric measurements, surface reflectance measurements, and radiative transfer models.

An engineering field team monitors instrument health by performing preflight and postflight diagnostics. All data produced by the sensor is sent to the AVIRIS data processing facility at JPL. This facility performs the functions of monitoring instrument performance, archiving the data, applying instrument-specific calibration, transforming the data into a user-compatible format, and distributing the data products to investigators. Distribution of data more than one year old is handled by the EROS data center (Earth Resource Observation System) through an agreement with JPL.

The ER-2 aircraft, the airborne platform used for AVIRIS data collection, is a high altitude aircraft with a ground speed of 734 km/h, an altitude of 20 km, and a range of about 2200 km. It seats a crew of one person who serves as pilot, navigator, and instrument operator. The ER-2 is operated by the Ames Research Center in Mountain View, CA.

---

[*] This paper was prepared by the Jet Propulsion Laboratory, California Institute of Technology, under a contract with the National Aeronautics and Space Administration.

1.3 Project management

Operation of the AVIRIS instrument and collection of AVIRIS data aboard the ER-2 is funded primarily through the project office of Mission to Planet Earth at NASA Headquarters in Washington, D.C. This office also reviews experiment proposals and selects the experiments which it will fund. The High Altitude Missions Branch of NASA-Ames Research Center receives flight requests for experiments requiring AVIRIS/ER-2 data collection and, in collaboration with NASA Headquarters, drafts aircraft deployment schedules. The AVIRIS project operates under the Observational Systems Division of the Jet Propulsion Laboratory. In addition to operating and maintaining the sensor, the AVIRIS project works to insure that experiment requirements are met for each flight and that users are satisfied with data quality and the level of service provided.

2. The data collection process

All groups and agencies interested in acquiring AVIRIS data must submit an experiment proposal to NASA headquarters and a flight request to Ames Research Center. These items should be submitted well in advance of the time period for which data collection is desired. Each experiment must designate a Principal Investigator who will serve as a single point of contact for headquarters, Ames, and JPL.

Experiment proposals are reviewed by headquarters, and selections are made based on merit and the program goals of the Mission to Planet Earth office. Once the selection process is completed, the High Altitude Missions Branch at Ames Research Center iteratively designs an aircraft schedule that best accommodates the geographic and seasonal requirements for the suite of approved experiments. An alternative to seeking Headquarters funding for an AVIRIS/ER-2 flight is to contract directly with Ames Research Center on a cost-reimbursable basis. Such arrangements, however, must be approved by NASA headquarters individually.

After the aircraft schedule is drafted, it is distributed to all Principal Investigators. One month prior to the beginning of their experiments, investigators will be contacted by the AVIRIS experiment coordinator to verify experiment requirements and to discuss schedules and arrangements for calibration/validation activities that will accompany data collected during flight operations. The experiment coordinator will also assist investigators in fine-tuning experiment requirements and logistics to insure the likelihood of a successful mission.

3. Flight operations

3.1 Mission planning and execution

AVIRIS experiment requirements are transformed into flight plans by the ER-2 operations team. This team integrates AVIRIS requirements with requirements of other sensors being used by the ER-2 platform. Whenever possible, multiple experiments are combined into a single mission. The personnel involved in a typical AVIRIS mission include two pilots, a NASA representative, a 7-person aircraft ground crew, an AVIRIS experiment coordinator, two AVIRIS engineers, and engineers for any other instruments onboard the ER-2.

During flight operations, the primary contact for investigators will be the experiment coordinator. The duty of the experiment coordinator is to route all pertinent and time-critical information from/to ER-2 operations to/from the community of AVIRIS investigators. All changes to experiment requirements must be submitted in writing to the experiment coordinator and/or pilot at least 24 hours before they can be implemented. Late submission of requirements changes could result in missed flight opportunities for an experiment.

The day before a flight, a nominal set of target sites is selected. This selection is based on weather predictions, experiment requirements, ground team status, and other operational considerations. The ground teams involved with these experiments are alerted to the possibility of a flight, and the requirements for these experiments are frozen. The launch time is determined from the timing requirements and geographic locations of all experiments considered.

On flight day, three hours before the scheduled launch, a team of key people gathers to make the launch decision. This team consists of the pilot, the ER-2 ground crew chief, the AVIRIS experiment coordinator, the NASA representative, and one or more engineers representing each instrument on the ER-2. The pilot then makes a launch decision based on immediate considerations of weather, aircraft readiness, instrument readiness, and experiment ground team readiness. The pilot also considers long term factors such as weather patterns, ground team logistical problems, and schedules of other observation platforms used by the investigators.

Occasionally, a conflict arises whereby two different experiments have good flight conditions, but due to their geographic separation they cannot both be flown on the same day. In this situation the priority of the experiment, designated by NASA headquarters or other sponsoring agency, will be taken into account. In the absence of a designated priority, logic will dictate which site gets flown - i.e., the site that has a short time

window, a large and expensive field team, or rare opportunities for good weather. ER-2 Operations and the Experiment Coordinator go to great lengths to head off potential conflicts and to insure that all experiments receive equal consideration. Investigators can take comfort in the knowledge that, in the vast majority of cases, the factors of weather and experiment timing requirements eliminate all conflict between experiments.

After the launch decision is issued, the affected ground teams are notified, and preparation is begun on the aircraft and instruments. The pilot drafts a flight plan and files it with Air Traffic Control. One hour before launch, the pilot dons a pressure suit and breathes oxygen to purge nitrogen from his or her body. If the launch is aborted due to aircraft/instrument anomalies or new weather information, the affected ground teams are again notified. Ground teams will receive confirmation at the time of launch, if so requested. Coordination of multiple NASA aircraft (DC-8, C-130) is handled by the NASA representative. All other aircraft coordination should be handled by the investigator or designated field contact.

During the flight, the experiment coordinator gathers information from unaffected ground teams regarding ground conditions and operational readiness. Investigators are also contacted to discuss deployment status and any operational concerns of the experiment coordinator. After the flight is completed, the pilot briefs the experiment coordinator on the significant events of the mission, emphasizing any anomalous conditions of weather, aircraft performance, instrument performance, or any other conditions that would affect a data run. The experiment coordinator then fills out the AVIRIS flight log based on information from the flight plan and the post-flight briefing. The data tape and flight log are then shipped by express courier to JPL for processing.

3.2 Ground truth experiments: recommendations

The chief purpose of ground truth data collection for AVIRIS experiments is to provide input parameters to radiative transfer or other models that remove the effects of atmospheric absorption and scattering, ultimately converting the radiance data measured by AVIRIS into reflectance data. The ground truth data can also be used to validate the results of AVIRIS data analysis. This section discusses logistics and management issues of ground truth experiments; it is not intended as a guide for designing such experiments. For this information, the reader is referred to the literature (Green et al., 1990, Bruegge et al., 1990, Conel et al., 1988).

Experiment teams are advised to establish reliable pathways of communication and to test these pathways prior to the start of operations. If the experiment site is in a remote location, it is well worth investing in a portable phone or a radio with phone-patch access. One person or one telephone number should be designated as the central point of contact for the group. A regular call-in schedule for key team members is also recommended, especially during initial deployment and during rotation of field personnel.

A time window of at least two weeks' duration is recommended for each experiment to allow for uncertainties in weather patterns and possible equipment failures. In addition to weather, aircraft, and AVIRIS, there are other factors including air traffic control problems, investigator instruments (damaged, lost, or borrowed), and investigator observation platforms such as ships, balloons, and low-altitude aircraft.

Each team should secure a core set of instruments for which it has exclusive use during the entire deployment, especially those instruments used for simultaneous ground truth (e.g., radiometer, sun photometer, radiosonde). For various reasons, an investigator will have to shift or extend the experiment time window. This can create a serious conflict between groups sharing the same instrument if their time windows suddenly overlap.

Creating separate teams for simultaneous and non-simultaneous measurements can reduce personnel costs, thereby allowing a longer experiment window. Typically, the team performing simultaneous measurements is small and operates the set of instruments described in the preceding paragraph. Once the overflight has occurred, the rest of the team travels to the site to perform non-simultaneous ground truth measurements. Costs may reduce the simultaneous measurement team to a single person with one radiometer; however, this is preferable to missing a flight opportunity simply because nobody was in the field.

Accepting early data also helps insure a successful experiment. A compromise in data quality that results from flying at a different time of the month or a different hour of the day is preferable to the possibility of no data at all. An investigator who insists on ideal conditions often ends up, out of desperation, accepting data with 50% cloud cover on the last day of the deployment. Note: this sudden relaxation of requirements is referred to as the "data panic curve."

Field team members should recognize that weather appearing to be clear from the ground may still be unacceptable to an airborne sensor, due either to cloud shadow, near-invisible cirrus, or haze. The ER-2 operations team has full access to satellite images and terminal forecast networks and is very experienced at making weather decisions. Casual observations of the sky by field teams ("It's really clearing up - you people

better fly over here!") are generally not useful due to the limited horizon of a ground-based observer. Field teams can, however, assist the weather decision process by providing information on local diurnal weather patterns.

4. Data processing and distribution

All AVIRIS data is processed by the AVIRIS Data Facility at JPL. After data is collected and a flight log is prepared, the data tape and flight log are sent by overnight courier to the data facility. Two hours after receipt of the tape (19 hours after data collection), the data facility generates a performance evaluation of the sensor based on preliminary analysis of the data. This performance evaluation will reveal any anomalies that were not detected by the preflight and postflight diagnostics performed in the field.

Within 72 hours of data collection, the data facility will have archived the data and generated quick-look data products. An assessment of data quality (i.e., cloud cover) can also be performed during this period if arrangements have been made through the AVIRIS Experiment Scientist or the Experiment Coordinator. Every Friday, the quick-look data is placed online via an anonymous FTP (File Transfer Protocol) server. An e-mail message is sent to the Principal Investigator announcing the availability of the data and describing the procedure for downloading it via FTP. If needed, the quick-looks can be sent as hard copy through the mail.

After inspecting the quick-looks, the investigator can place an order for the portions of data he/she would like retrieved from the archive. The data can be delivered as raw or calibrated radiance (this is the instrument-specific calibration, not an atmospheric calibration). In either case, a file is provided that describes the calibration parameters. The investigator has a choice of three mediums: 8 millimeter, 4 millimeter, or 9-track tape. At the present time, data processing is performed on a set of SUN workstations capable of processing 1000 AVIRIS scenes per year. The data volume produced by AVIRIS in 1994 was on the order of 2000 scenes, resulting (unfortunately) in significant lag times for data delivery. A hardware upgrade is scheduled for 1995 that should provide at least a partial remedy to this situation.

5. References

Bruegge, C.J., J.E. Conel, J.S. Margolis, et al., "In-situ Atmospheric Water-vapor Retrieval in Support of AVIRIS Validation," Proc. SPIE, Vol. 1298, Imaging Spectroscopy of the Terrestrial Environment, April 1990, pp. 150-163.

Conel, J.E., R.O. Green, R.E. Alley, et al., "In-flight Radiometric Calibration of the Airborne Visible/Infrared Imaging Spectrometer (AVIRIS)," Proc. SPIE, Vol. 924, Recent Advances in Sensors, Radiometry and Data Processing for Remote Sensing, 1988.

Green, R.O., J.E. Conel, V. Carrere, C.J. Bruegge, J.S. Margolis, M. Rast, and G. Hoover, "Inflight Validation and Calibration of the Spectral and Radiometric Characteristics of the Airborne Visible/Infrared Imaging Spectrometer (AVIRIS)," Proc. SPIE, Vol. 1298, Imaging Spectroscopy of the Terrestrial Environment, April 1990, pp. 18-36.

Sarture, C.M., T.G. Chrien, R.O. Green, M.L. Eastwood, J.J. Raney, and M.A. Hernandez, "Airborne Visible/Infrared Imaging Spectrometer (AVIRIS): Sensor Improvements for 1994 and 1995," Summaries of the Fifth Annual JPL Airborne Earth Science Workshop (this volume), JPL Pub. 95-1, Vol. 1, Jet Propulsion Laboratory, Pasadena, CA, Jan. 23, 1995.

6. Bibliography

Bosch, J., van den, C.O. Davis, C.D. Mobley, and W.J. Rhea, "Atmospheric Correction of AVIRIS Data of Monterey Bay Contaminated by Thin Cirrus Clouds," Summaries of the Fourth Annual JPL Airborne Geoscience Workshop, Vol. 1, Pub. 93-26, Jet Propulsion Laboratory, Pasadena, CA, 1993, pp. 185-188.

Nielsen, P.J., R.O. Green, A.T. Murray, B.T. Eng, H.I. Novack, M. Solis, and M. Olah, "The Data Facility of the Airborne Visible/Infrared Imaging Spectrometer (AVIRIS)," Summaries of the Fourth Annual JPL Airborne Geoscience Workshop, Vol. 1, JPL Pub. 93-26, Jet Propulsion Laboratory, Pasadena, CA, 1993, pp. 133-136.

Porter, W.M., and H.T. Enmark, "A System Overview of the Airborne Visible/Infrared Imaging Spectrometer (AVIRIS)," Proc. SPIE Vol. 834, Imaging Spectroscopy II, 1987, pp. 22-29.

Swayze, G., R.N. Clark, F. Kruse, S. Sutley, and A. Gallagher, "Ground-Truthing AVIRIS Mineral Mapping at Cuprite, Nevada," Summaries of the Third Annual JPL Airborne Geoscience Workshop, Vol. 1, Pub. 92-14, Jet Propulsion Laboratory, Pasadena, CA, 1992, pp. 47-49.

INTEGRATION OF AIRSAR AND AVIRIS DATA FOR TRAIL CANYON ALLUVIAL FAN, DEATH VALLEY, CALIFORNIA

Kathryn S. Kierein-Young

Center for the Study of Earth from Space (CSES)/CIRES
Department of Geological Sciences
University of Colorado, Campus Box 216, Boulder, CO 80309-0216

1. INTRODUCTION

Combining quantitative geophysical information extracted from the optical and microwave wavelengths provides complementary information about both the surface mineralogy and morphology. This study combines inversion results from two remote sensing instruments, a polarimetric synthetic aperture radar, AIRSAR, and an imaging spectrometer, AVIRIS, for Trail Canyon alluvial fan in Death Valley, California. The NASA/JPL Airborne Synthetic Aperture Radar (AIRSAR) is a quad-polarization, three frequency instrument (van Zyl et al., 1992). AIRSAR collects data at C-band=5.66 cm, L-band=23.98 cm, and P-band=68.13 cm. The data are processed to four-looks and have a spatial resolution of 10 m and a swath width of 12 km. The AIRSAR data used in this study were collected as part of the Geologic Remote Sensing Field Experiment (GRSFE) over Death Valley on 9/14/89 (Evans and Arvidson, 1990). The Airborne Visible/Infrared Imaging Spectrometer (AVIRIS) is a NASA/JPL instrument that flies in an ER-2 aircraft at an altitude of 20 km (Vane et al., 1993). AVIRIS uses four spectrometers to collect data in 224 spectral channels from 0.4 μm to 2.45 μm. The width of each spectral band is approximately 10 nm. AVIRIS collects data with a swath width of 11 km and a pixel size of 20 m. The AVIRIS data used in this study were collected over Death Valley on 5/31/92.

2. GEOLOGY

Trail Canyon alluvial fan is located on the west side of Death Valley, California at the base of the Panamint Range. It is a large fan that is 7 km long and 450 m high. The northern part of the fan contains gravels derived from a carbonate dominant source material and the southern part of the fan has gravels derived from a quartzite source material. The quartzite and carbonate gravel mineralogies are not separated on the existing geologic map, which shows three gravel facies (Hunt and Mabey, 1966). The oldest gravel forms a smooth desert pavement of varnished rock fragments which covers approximately 30% of the fan. The younger gravel forms a rough surface of heavily varnished cobbles and covers about 50% of the fan. The youngest gravel is located in the more recent washes, does not have desert varnish, and covers about 20% of the fan. The base of the fan was covered by a lake during the Holocene and is mapped as a carbonate impregnated sand facies.

This study identified seven different surfaces on Trail Canyon alluvial fan based on the AIRSAR and AVIRIS data sets and the geologic map. These surfaces could not all be separated and identified by using only one data source. The surfaces include four facies on the quartzite source part of the fan: desert pavement (q-dp); a middle aged surface (q-m); a younger surface (q-y); and the current washes (q-c). A desert pavement (c-dp) and younger surface (c-y) were identified on the carbonate source part of the fan. The base of the fan (b) where the recent lake reached was also studied.

3. AIRSAR ANALYSIS

The AIRSAR data were calibrated using in-scene trihedral corner reflectors to allow for the extraction of accurate values of backscatter, polarization information, rms surface roughness, dielectric constants, and fractal dimensions. The calibration included an altitude correction, because the aircraft was flying over the mountains and imaging the valley, and a topographic correction using a digital elevation model (Kierein-Young, 1993; van Zyl et al., 1992).

Images of HH, VV, HV, and total power were synthesized for each of the three bands and placed into a "cube" of radar data. Mean frequency-polarization spectra were extracted from this AIRSAR data cube for the seven sites described above. The spectra fall into two main groups. The rougher surfaces include the quartzite middle (q-m), younger (q-y), current washes (q-c), and carbonate younger (c-y) sites. The smoother surfaces include the desert pavements (q-dp and c-dp) and the base of the fan (b).

The first-order small perturbation model (Evans et al., 1992; van Zyl et al., 1991; Barrick and Peake, 1967) was used to estimate the surface power spectral density and the dielectric constant at every pixel by performing an inversion of the AIRSAR data. The fractal dimension and rms surface roughness were calculated using the slope and intercept of the power spectrum obtained from the inversion model (Kierein-Young, 1993; Kierein-Young and Kruse, 1992). Table 1 shows the rms surface roughness, fractal dimension, and dielectric constants obtained from the small perturbation inversion model for the seven sites. These data show that the carbonate derived gravel is smoother than the quartzite derived gravel overall, the carbonate desert pavement (c-dp) is rougher than the quartzite desert pavement (q-dp), and the base of the fan (b) is the smoothest surface. The fractal dimension generally increases as the surface roughness decreases, and the dielectric constant is highest for the desert pavement surfaces.

Table 1. Small perturbation model inversion results for Trail Canyon fan.

Site	rms (cm)	Fractal dimension	Dielectric Constants C	L	P
q-c	15.2	2.13	3.9	3.6	3.0
q-y	14.0	2.14	4.6	3.7	3.0
q-m	15.2	2.105	4.0	3.4	3.0
q-dp	4.4	2.25	6.1	4.3	3.0
c-y	13.5	2.14	4.4	4.6	3.0
c-dp	6.3	2.20	5.1	5.1	3.0
b	2.8	2.405	4.1	3.0	3.0

4. AVIRIS ANALYSIS

The AVIRIS data were converted from radiance to reflectance using an atmospheric correction program, ATREM, to allow for accurate mineralogical determinations (Gao et al., 1992; Gao et al., 1993). The AVIRIS data allow discrimination of the quartzite and carbonate derived parts of the fan based on spectral characteristics. Mean reflectance spectra were extracted from the AVIRIS data and used to identify the surface mineralogy for the seven sites described above. Two dominant mineralogies are seen in the spectra, illite clay and a mixture of dolomite and illite. In addition, the areas that have desert varnish on the surface appear very dark in the images and have a lower reflectance in the shorter wavelengths than those surfaces without desert varnish. Only four general groups of surfaces are distinguishable in the spectra, the current wash, the carbonate part of the fan, the quartzite parts with heavy desert varnish, and the quartzite fan without heavy varnish. The AVIRIS images do not allow for the

discrimination of the smooth desert pavement surfaces from the other varnished rough surfaces. This is because the fan albedo is related to the amount of desert varnish on the gravels and not to the roughness of the surfaces. There is no desert varnish on the base of the fan, therefore it is brighter than the surfaces above the upper reaches of the ancient lake.

Automated spectral unmixing was performed on the AVIRIS data for Trail Canyon fan using five endmembers. Every pixel in an image contains a mixture of materials due to its spatial size. Spectral unmixing determines the percentage abundance of each material, or endmember, within a pixel (Boardman and Goetz, 1991). An automated technique was used to determine the mixing endmembers on Trail Canyon fan from only the input data and a geometric model (Boardman, 1993; Boardman, 1994). This method involved first performing a maximum noise fraction (MNF) transform, determining the number of unique endmembers, and using a convex geometric approach to find the endmembers. The first five derived endmembers, corresponding to bright illite, darker illite, illite with desert varnish, dolomite, and shadow were used to generate spatial endmember abundance images. Table 2 shows the results of the automatic unmixing using the AVIRIS data.

Table 2.   Unmixing results from the MNF automatic unmixing.

Site	% bright illite	% darker illite	% illite w/ dv	% dolomite	% shadow
q-dp	8.5	13.2	43.4	12.1	21.1
q-m	7.4	21.7	37.6	9.3	24.1
q-y	17.1	33.2	17.5	10.5	18.0
q-c	36.2	19.2	6.7	8.4	11.7
c-dp	8.2	17.3	29.0	34.2	11.3
c-y	7.4	22.5	14.5	32.2	23.4
b	24.6	23.4	10.7	5.8	35.5

5.   DATA INTEGRATION

Integration of the data sets was done by performing classification techniques on combined bands of AVIRIS and AIRSAR data. An accurate map of the seven surfaces on Trail Canyon fan was obtained by using a minimum distance classification technique on the co-registered AVIRIS automatic unmixing endmember images and the AIRSAR frequency-polarization cube. This combination of data gives the most accurate results because the unmixing endmembers show the best separation of the mineralogies, and the AIRSAR cube discriminates well between the smooth and rough surfaces. Figure 1 (AVIRIS Workshop Slide 6) shows the map generated from this classification. Classifications based on only one data set did not produce as accurate a map as the combined data.

6.   CONCLUSIONS

The results of the data integration show that the morphology of Trail Canyon fan is dependent on the age and mineralogical makeup of the surfaces. The AIRSAR data show the variation in surface roughness, and, in general, the smoother surfaces are older. The roughest area is the current wash which is the youngest part of the fan. The two middle aged surfaces of the fan have about the same surface roughness and cannot be separated in the AIRSAR data alone. The smoothest surfaces on the fan are the desert pavement areas which are the oldest deposits on the fan. The addition of AVIRIS data to the AIRSAR data allows for the separation of the two middle aged surfaces by the amount of desert varnish. The older surface has much more desert varnish than the younger washes. However, the desert pavement and varnished rough surfaces cannot be separated by using the AVIRIS data alone. Therefore, it is necessary to use both the AIRSAR and

111

AVIRIS data to correctly map and determine the relative ages of the surfaces of Trail Canyon fan.

7. ACKNOWLEDGMENTS

8. REFERENCES

Barrick, D. E. and W. H. Peake, 1967. Scattering from surfaces with different roughness scales: Analysis and interpretation, Research Report No. BAT-197A-10-3, Battelle Memorial Institute, Columbus Laboratories, Columbus, Ohio, AD 662751, 63 p.

Boardman, J. W. and A. F. H. Goetz, 1991. Sedimentary facies analysis using imaging spectrometry: A geophysical inverse problem, in *Proceedings of the Third AVIRIS Workshop*, JPL Publication 91-28, pp. 4-13.

Boardman, J. W., 1993. Automating spectral unmixing of AVIRIS data using convex geometry concepts, in *Summaries of the Fourth Annual JPL Airborne Geoscience Workshop*, JPL Publication 93-26, Vol. 1, pp. 11-14.

Boardman, J. W., 1994. Geometric mixture analysis of imaging spectrometry data, in Proceedings IGARSS '94, IEEE Catalog No. 94CH3378-7, Vol. IV, pp. 2369-2371.

Evans, D. L. and R. E. Arvidson, 1990. The Geologic Remote Sensing Field Experiment (GRSFE): Overview of initial results, IGARSS '90, University of Maryland, College Park, MD, IEEE Catalog Number 90CH2825-8, pp. 1347.

Evans, D. L., T. G. Farr, and J. J. van Zyl, 1992. Estimates of surface roughness derived from synthetic aperture radar (SAR) data, IEEE Transactions on Geoscience and Remote Sensing, Vol. 30, No. 2, pp. 382-389.

Gao, B-C., K. B. Heidebrecht and A. F. H. Goetz, 1992. Atmosphere removal program (ATREM) user's guide, CSES, University of Colorado, 24 p.

Gao, B-C., K. B. Heidebrecht and A. F. H. Goetz, 1993. Derivation of scaled surface reflectances from AVIRIS data, *Remote Sensing of Environment*, Vol. 44, No. 2, pp. 165-178.

Hunt, C. B. and D. R. Mabey, 1966. Stratigraphy and Structure Death Valley, California, U. S. Geological Survey Professional Paper 494-A, 162 p.

Kierein-Young, K. S., 1993. Comparison of inversion models using AIRSAR data for Death Valley, California, in Summaries of the Fourth Annual JPL Airborne Geoscience Workshop, JPL Publication 93-26, Vol. 3, pp. 25-28.

Kierein-Young, K. S., and F. A. Kruse, 1992. Extraction of quantitative surface characteristics from AIRSAR data from Death Valley, California, in Summaries of the Third Annual JPL Airborne Geoscience Workshop, JPL Publication 92-14, Vol. 3, pp. 46-48.

van Zyl, J. J., C. F. Burnette, and T. G. Farr, 1991. Inference of surface power spectra from inversion of multifrequency polarimetric radar data, Geophysical Research Letters, Vol. 18, No. 9, pp. 1787-1790.

van Zyl, J. J., B. D. Chapman, P. C. Dubois, and A. Freeman, 1992. Polcal User's Manual, JPL D-7715, version 4.0.

van Zyl, J. J., R. Carande, Y. Lou, T. Miller, and K. Wheeler, 1992. The NASA/JPL three-frequency polarimetric AIRSAR system, IGARSS '92, Houston, Texas, IEEE Catalog Number 92CH3041-1, pp. 649-651.

Vane, G., R. O. Green, T. G. Chrien, H. T. Enmark, E. G. Hansen, and W. M. Porter, 1993. The Airborne Visible/Infrared Imaging Spectrometer (AVIRIS), Remote Sensing of Environment, Vol. 44, No. 2/3, pp. 127-143.

REMOTE MINERAL MAPPING USING AVIRIS DATA AT SUMMITVILLE, COLORADO AND THE ADJACENT SAN JUAN MOUNTAINS

Trude V.V. King, Roger N. Clark, Cathy Ager, and Gregg A. Swayze
U.S. Geological Survey
P.O. Box 25046 MS 964
Denver, CO 80225

INTRODUCTION

From 1985 through 1992, the Summitville open-pit mine produced gold from low-grade ore using cyanide heap-leach techniques, a method to extract gold whereby the ore pile is sprayed with water containing cyanide, which dissolves the minute gold grains. Environmental problems at Summitville include significant increases in acidic and metal-rich drainage from the site, leakage of cyanide-bearing solutions from the heap-leach pad into an underdrain system and several surface leaks of cyanide-bearing solutions into the Wightman Fork of the Alamosa River. The mine's operator had ceased active mining and begun environmental remediation, including treatment of the heap-leach pile and installation of a water-treatment facility, when it declared bankruptcy in December 1992 and abandoned the mine site. The EPA immediately took over the Summitville site under EPA Superfund Emergency Response authority. Summitville was added to the EPA National Priorities List in late May 1994.

Summitville has focused nationwide public attention on the environmental effects of modern mineral-resource development. Soon after the mine was abandoned, Federal, State, and local agencies, along with Alamosa River water users and private companies, began extensive studies at the mine site and surrounding areas. These studies included analysis of water, soil, livestock and vegetation. The role of the U.S. Geological Survey (USGS) was to provide geologic and hydrologic information about the mine and surrounding area and to describe and evaluate the environmental condition of the Summitville mine and the downstream effects of the mine on the San Luis Valley. The environmental condition of the Summitville area is a result of the geologic evolution of this area that culminated in the formation of precious-metal mineral deposits and a result of the mining activity. Understanding the geologic and hydrologic history of this area is a critical piece to understanding the environmental puzzle at Summitville.

IMAGING SPECTROMETER DATA

To address these geologic and hydrologic problems, we analyzed AVIRIS data for the Summitville mining district and the adjacent San Luis Valley, in Colorado. The data were acquired on September 3, 1993. A combined method of radiative transfer modeling and empirical ground calibration site reflectance were used to correct the flight data to surface reflectance (Clark et al., 1994). This method corrects for variable water vapor in the atmosphere and produces smooth spectra with spectral channel to channel noise approaching the signal to noise of the raw data. Thus, the data can be compared to standard laboratory measurements. The calibration site is a plowed field approximately 18 kilometers SW of Alamosa. The calibration site soil samples were obtained on the day of the overflight and measured on the USGS laboratory spectrometer (Clark et al, 1990b). The spectra of the calibration field are spectrally bland and serve as an ideal calibration standard.

TRICORDER ANALYSIS

Clark et al., (1990a, 1991) developed a new analysis algorithm that uses a digital spectral library of known

reference materials and a fast, modified-least-squares method of determining if a diagnostic spectral feature for a given material is present in the image. This algorithm is called "tricorder." The tricorder analysis compares continuum-removed spectra (Clark and Roush, 1984) from the remotely sensed data, to a database of continuum-removed spectral features from the reference spectral library (Clark et al., 1993). Multiple features from multiple materials are compared and the material with the closest match is mapped. The algorithm does not force a positive match which makes if different from many other algorithms in use. The tricorder algorithm attempts to map only minerals included in the reference database.

For the present study we mapped minerals based on the presence of absorption features in the ~0.45 μm to ~1.0 μm, 1.5μm, and 2.2 μm to 2.3 μm wavelength region, which represent the visible and near-infrared portions of the electro magnetic spectrum. In this dataset we looked for 64 different minerals.

Absorption bands in the visible portion of the spectrum (~0.4-0.8μm) are caused by electronic processes including crystal field effects, charge transfer, color-centers, and conduction bands. The absorptions resulting in the visible portion of the spectrum involve elements of the first transition series which have an outer unfilled d-shell in their electronic distribution. The energy levels are determined by the valence state of the element, its coordination number and its site symmetry. Differences in these parameters are manifested in individual diagnostic absorption bands. Absorptions in this wavelength region are commonly associated with the presence of iron in the mineral structure.

Near-infrared radiation (1-2.45 μm, in this study) absorbed by a mineral is converted into molecular vibrational energy. The frequency or wavelength of the absorption depends on the relative masses and geometry of the atoms and the force constants of the bonds. There are two main types of molecular vibrations: stretching and bending. A stretching vibration is a movement along the bond axis which either increases or decreases the interatomic distances. Bending vibrations consist of a change in the angle between bonds with a common atom or the movement of a group of atoms with respect to the remainder of the molecule, but without movement of the atoms in the group with respect to one another (Silverstein et al., 1981). Only vibrations that result in a change in the dipole-moment of the molecule will be infrared active.

Absorption features in the 2.2 to 2.3-μm region result from a combination of the OH-stretching fundamental with either the Al-O-H bending mode absorbing at approximately 2.2 μm, or Mg-O-H bending mode absorption at 2.3 μm. At high resolution these bands also appear as characteristic multiple, complex absorption features. Based on previous work (King and Clark,1989, Clark et al., 1990b, Clark et al., 1993), it is known that the strength, position and shape of these features is a function of the mineral chemistry.

In this study we searched for 22 minerals with absorption features at wavelengths near or less than 1.0 μm. We successfully mapped 7 of these 22 potential minerals. The minerals we detected include: amorphous iron-hydroxide, ferrihydrite, goethite, hematite, K-jarosite, Na-jarosite, and an Fe-bearing material that spectrally matches the processed sludge removed from the Reynolds Tunnel. AVIRIS Workshop Slide 7 shows their distribution at, and near, the Summitville mine. Comparison of spectra of these minerals extracted from the remotely sensed data with our laboratory standards shows no differences. We have detected spectral differences that allow us to discriminate between the amorphous iron-hydroxide and ferrihydrite, based on our laboratory standards, however, it is possible that these two materials are chemically similar. It should be noted that the most reliable method of identifying amorphous iron oxides is mossbauer spectroscopy.

Samples of the processed Reynolds Tunnel sludge, collected at the mine site, were used as laboratory standards to identify this material in the remotely sensed data. In AVIRIS Workshop Slide 7, its distribution is depicted in yellow. In this case the algorithm maps solid Fe-bearing material and red-stained water puddles in the mine pit. Several days of rain occurred prior to the day of data acquisition, thus it is likely there was standing water in the pit. Other investigators have reported the occurrence of red-puddles in the pit resulting from precipitation or melting snow.

To detect the presence of minerals that have absorption features in the 2.2-2.3 μm wavelength region we used 48 mineral standards. These 48 standards included phyllosilicates, sulphates, carbonates, and cyanide compounds. Of these 48 standard minerals we detected 8 different phases of significant areal extent. Subtle spectral differences allow for the discrimination between K and Na alunites and poorly-crystalline and highly-crystalline kaolinites. However, because of spectral similarities and limitations of the mapping algorithm, some of the material mapped as Na-montmorillonite may be muscovite or sericite. Recent modifications to the mapping algorithm have eliminated this inconsistency.

Spectral data contained in the AVIRIS pixels are very similar to the spectral standards measured in the laboratory. Figure 1 shows the spectrum of a montmorillonite pixel detected near Alum Creek compared to a

laboratory spectrum of a standard montmorillonite. Breaks in the spectra of the AVIRIS data occur at the wavelengths where absorptions from atmospheric gases occur. The absorption features in the montmorillonite spectrum from the AVIRIS data are identical to the diagnostic absorption features in the laboratory standard at wavelengths near 2.2 μm. The AVIRIS data shows that the montmorillonite is mixed with an Fe-bearing mineral phase because of an absorption near 0.8 μm (this absorption feature would be mapped with the Fe-bearing minerals).

The mapping of the halloysite or kaolinite-smectite mixtures from the AVIRIS data has been less certain because of inconsistencies in both the spectral data and supporting x-ray analysis. Initially, the halloysite was mapped based on laboratory standards. However, X-ray data indicated that the material contained kaolinite and other unidentified phases, but did not contain either halloysite or illite (Stephen Huebner, USGS, personal communication, 1994). The spectral data of the material (collected in the field) clearly indicates that crystalline kaolinite is not present and that absorption features very similar to illite and halloysite are present. Thus, we believe that the material is likely to be a supergene weathering product, a mineral for which we do not have either spectral or X-ray standards, or a new mineral. Therefore, caution should be applied in interpretating the presently-mapped areal distribution of this phase.

DISCUSSION

Imaging spectroscopy data of the Summitville mine and the Iron, Alum and Bitter Creek basins were used to identify minerals associated with alteration. Hydroxyl-bearing materials, including clays, show discrete distribution patterns at both the mine site and within the Iron, Alum and Bitter Creek basins. Mineralogic differences between the open pit and the heap leach pile at the mine site can be distinguished and discrete mineralogical boundaries in the Iron, Alum and Bitter Creek basins can also be detected.

Perhaps the most interesting observation is that the Summitville mine apparently does not contribute OH-bearing minerals via the Wightman Fork to the Alamosa River. In contrast the mineralized area in Iron, Alum and Bitter Creek basins do contribute OH-bearing minerals to the Alamosa River. This observation is based on the spectral characteristics of the exposed fluvial sediments along Alum Creek and Bitter Creek and lack of OH-bearing fluvial sediment along the Wightman Fork. The unmined mineralized areas are believed to contribute OH-bearing materials to the Alamosa River due to the porous character of the well-exposed rock, which allows altered materials to be eroded easily and deposited along the stream banks. If hydroxyl-bearing materials, and associated contaminants, are being supplied to the Wightman Fork by the Summitville mine, the material must be carried as a very fine-grained aqueous suspension which cannot settle onto the creek banks.

Images show that both the Summitville mine and Iron, Alum and Bitter Creek basins are sources of iron-bearing sediments to the Alamosa River (AVIRIS Workshop Slide 7). These sediments give a reddish-brown color to stream banks, a characteristic typically associated with acid drainage, and are potential carriers of heavy metals to locations downstream. Consequently, in assessing the environmental impact of mining at Summitville, it is important to recognize that both the Summitville mine site and the Iron, Alum and Bitter Creek basins contribute this type of sediment to the Alamosa River.

SUMMARY

In summary, we have demonstrated the unique utility of imaging spectroscopy in mapping mineral distribution. In the Summitville mining region we have shown that the mine site does not contribute clay minerals to the Alamosa River, but does contribute Fe-bearing minerals. Such minerals have the potential to carry heavy metals. This application illustrates only one specific environmental application of imaging spectroscopy data. For instance, the types of minerals we can map with confidence are those frequently associated with environmental problems related to active and abandoned mine lands. Thus, the potential utility of this technology to the field of environmental science has yet to be fully explored.
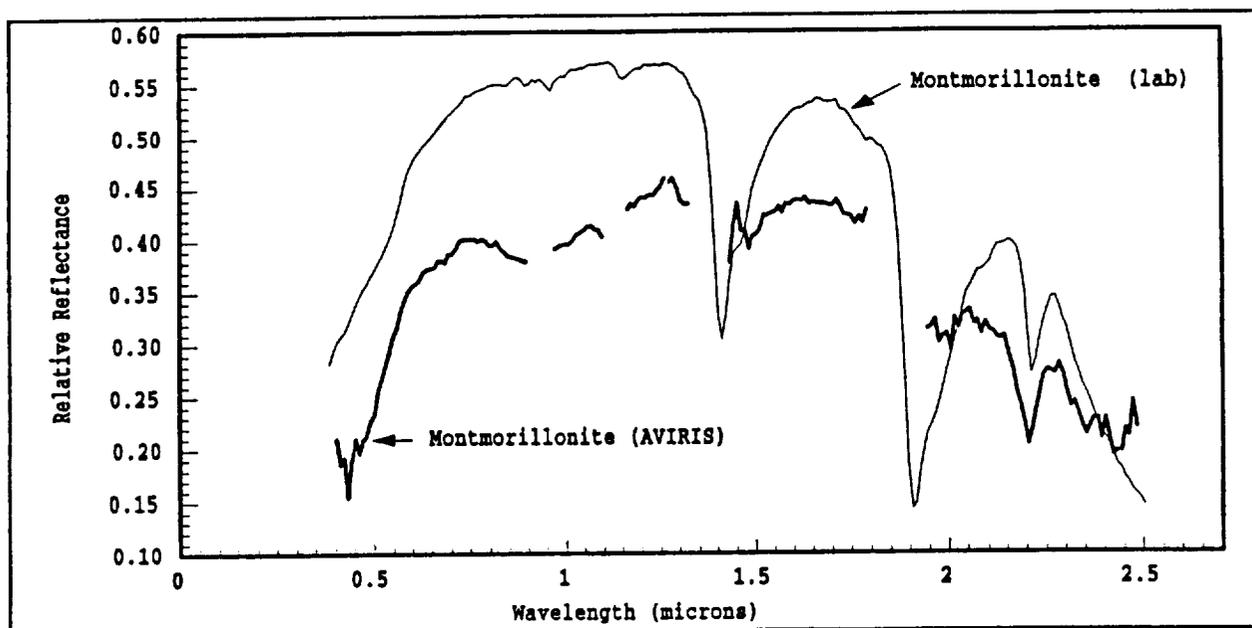
Figure 1. Spectra of montmorillonite measured in the laboratory and montmorillonite detected by AVIRIS near Alum Creek.

REFERENCES

Clark, R.N. and T.L. Roush, Reflectance Spectroscopy: Quantitative Analysis Techniques for Remote Sensing Applications, *J. Geophys. Res.*, **89**, 6329-6340, 1984.

Clark, R.N., A.J. Gallagher, and G.A. Swayze, Material absorption band depth mapping of imaging spectrometer data using a complete band shape least-squares fit with library reference spectra: *Proceedings of the Second Airborne Visible/Infrared Imaging Spectrometer (AVIRIS) Workshop*, JPL Publication 90-54, p. 176-186, 1990a.

Clark, R.N., T.V.V. King, M. Klejwa, G. Swayze, and N. Vergo, High Spectral Resolution Reflectance Spectroscopy of Minerals: *J. Geophys Res.* **95**, 12653-12680, 1990b.

Clark, R.N., G.A. Swayze, A. Gallagher, N. Gorelick, and F. Kruse, Mapping with Imaging Spectrometer Data Using the Complete Band Shape Least-Squares Algorithm Simultaneously Fit to Multiple Spectral Features from Multiple Materials, *Proceedings of the Third Airborne Visible/Infrared Imaging Spectrometer (AVIRIS) Workshop*, JPL Publication 91-28, 2-3, 1991.

Clark, R.N., G.A. Swayze, A. Gallagher, T.V.V. King, and W.M. Calvin, The U. S. Geological Survey, Digital Spectral Library: Version 1: 0.2 to 3.0 μm, *U.S. Geological Survey, Open File Report 93-592*, 1340 pages, 1993b. (Also being published as a USGS Bulletin, 1300+ pages, 1994 *in* press.)

Clark, R.N., G.A. Swayze, K. Heidebrecht, R.O. G.A.F.H. Goetz: Calibration to Surface Reflectance of Terrestrial Imaging Spectrometry Data: Comparison of Methods, *Applied Optics in* review, 1994a.

King, T.V.V. and R.N. Clark, Spectral Characteristics of Chlorites and Mg-Serpentines Using High-Resolution Reflectance Spectroscopy. *J. Geophys. Res.*, **94**, 13,997-14,008, 1989.

Silverstein, R.M., G.C. Bassler, and T.C. Morrill, Spectrometric Identification of Organic Compounds. John Wiley, New York, New York, 442p., 1981.

116

AIRCRAFT SCANNER DATA AVAILABILITY
VIA THE
VERSION 0 INFORMATION MANAGEMENT SYSTEM

G. R. Mah
Hughes STX
Land Processes Distributed Active Archive Center
USGS EROS Data Center, Sioux Falls, SD 57198

1.   Introduction

As part of the Earth Observing System Data and Information System (EOSDIS) development, NASA and other government agencies have developed an operational prototype of the Information Management System (IMS). The IMS provides access to the data archived at the Distributed Active Archive Centers (DAAC's) that allows users to search through metadata describing the [image] data. Criteria based on sensor name or type, date and time, and geographic location are used to search the archive. Graphical representations of coverage and browse images are available to further refine a user's selection.

Previously, the EROS Data Center (EDC) DAAC had identified the Advanced Solid-state Array Spectrometer (ASAS), Airborne Visible and infrared Imaging Spectrometer (AVIRIS), NS-001, and Thermal Infrared Multispectral Scanner (TIMS) as precursor data sets similar to those the DAAC will handle in the Earth Observing System era. Currently, the EDC DAAC staff, in cooperation with NASA, has transcribed TIMS, NS-001, and Thematic Mapper Simulator (TMS) data from Ames Research Center and also TIMS data from Stennis Space Center. During the transcription process, the IMS metadata and browse images were created to populate the inventory at the EDC DAAC. These data sets are now available in the IMS and may be requested from the any of the DAAC's via the IMS.

2.   Overview of the IMS

The IMS is a distributed client-server application, which accesses the metadata stored at each of the DAAC's in response to search criteria entered by the user into a common user interface. Both graphical and character user interfaces are provided by the system. The graphical user interface is based on the X-windows standard and runs on many variants of UNIX.

The IMS acts as an overlay to the native data base systems at each of the DAAC's. In response to user-defined criteria, the IMS generates queries internally and converts them using a translation layer into a form that is compatible with the native data base system. The response(s) to the query(s) are then translated back for display by the IMS user interface. Graphical coverage map representations generated by the IMS and browse images, where available, can be displayed.

3.   Operational Scenario

To use the IMS, a user logs onto the system via TELNET or MOSAIC. The system supports registration to allow a user to save search criteria and results and preference profiles. The first screen that appears is the user registration screen (fig. 1). If previously registered, a user signs on using a password, otherwise guest access is provided or a new user can register. A registered user can save preferences and searches, whereas guest access only allows runtime access to the IMS.
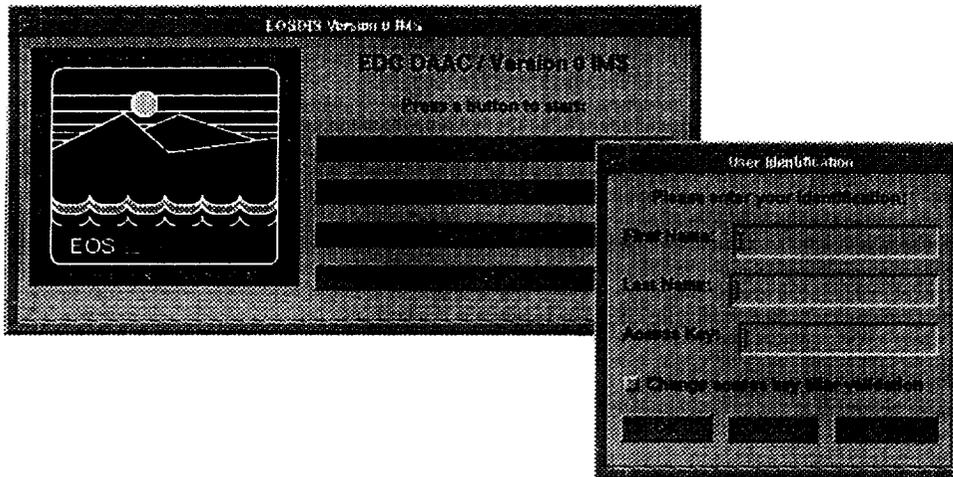
Figure 1. Welcome and Registration Screens.

After logging onto the system, a welcome screen describes the system and displays any recent updates or changes to the system. A user can then move to the search screen seen (fig. 2). The search screen lets a user define criteria for queries on DAAC data bases. Multiple data bases at multiple DAAC's can be searched simultaneously to locate coincident data sets. Geographic search criteria can be defined by entering coordinates or via polygon definition on a map.
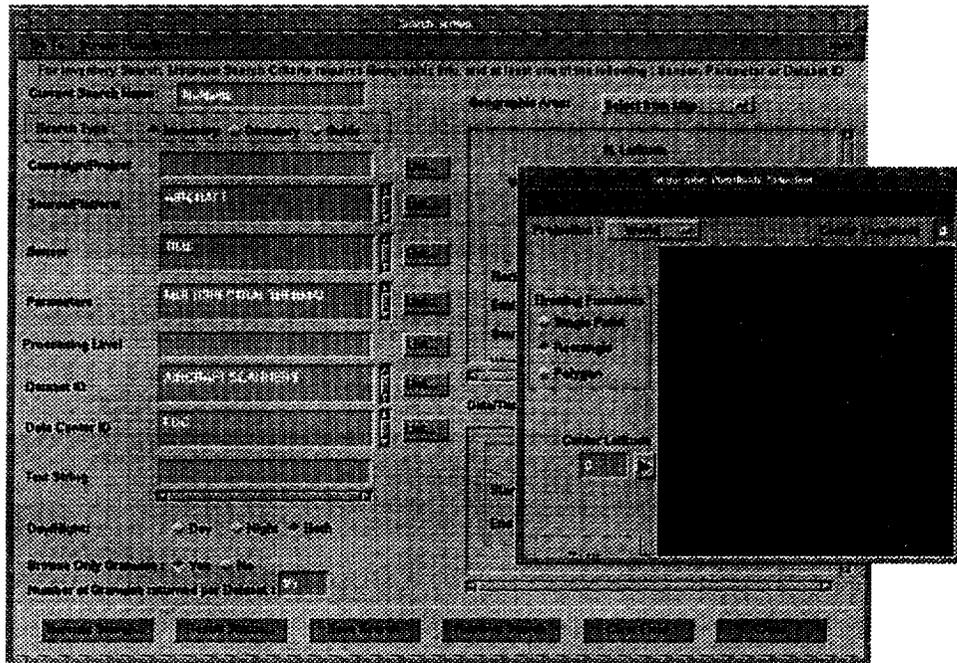
Figure 2. Search Screen showing Graphical Coordinate Selection.

When a search criteria is defined, the system searches the DAAC's specified and returns any results matching the search criteria. A communications screen is displayed whenever the IMS accesses a remote data base. The results are displayed in the results screen (fig. 3). Further detail is available in the form of more detailed metadata, a coverage map, or a browse image. Examples of a coverage map and a browse image are shown in figure 4.

118
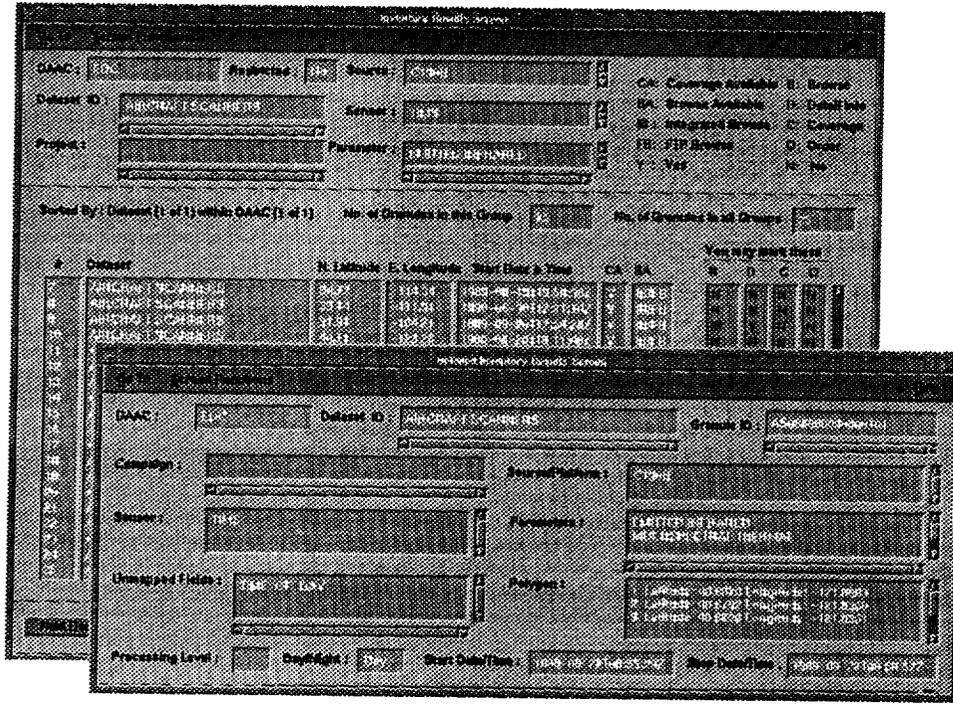
Figure 3. Results Screen.
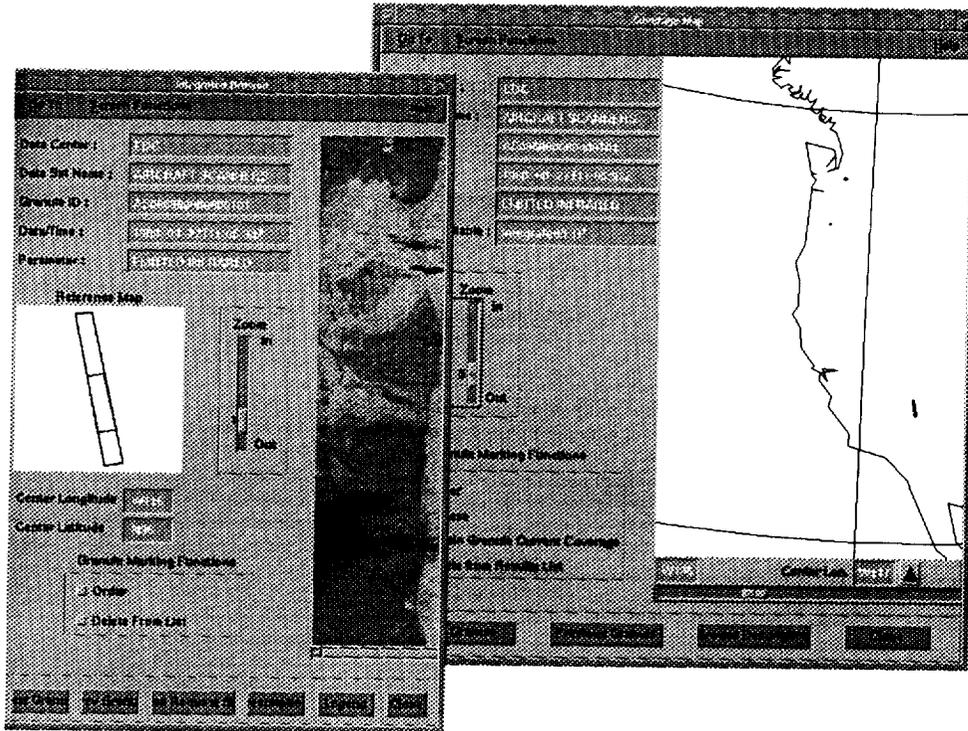
Figure 4. Browse and Coverage Map.
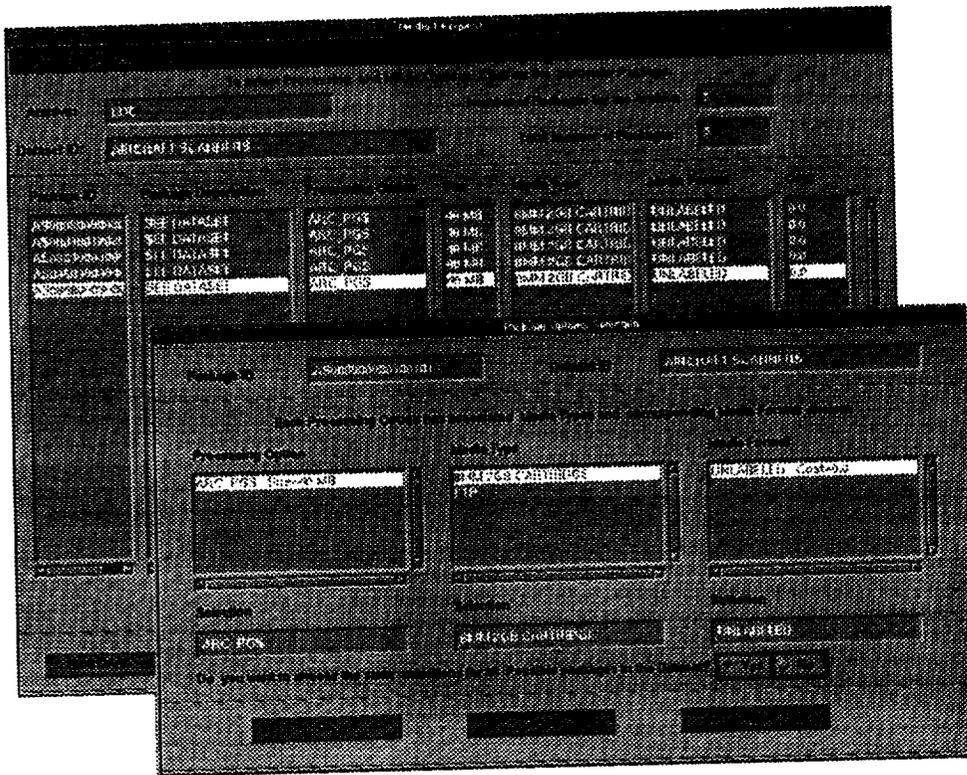
Figure 5. Order Screen.

When a user determines which of the data granules to obtain, the user flags the data in the results screen and moves to the order screen (fig. 5). The order screen asks a user to define the format and packaging of the data granule(s) and where to send the data. FTP or various tape media are available options. When a user submits a request, the IMS passes the order to user services personnel at the appropriate DAAC. The user services personnel will contact the user directly and make arrangements for data delivery.

4.   **Access to the IMS**

Local access to the IMS is available at each of the DAAC's. Remote access is also available via TELNET. The current version of the IMS uses local clients running at the DAAC's rather than on the local machines, so performance is somewhat reduced from a true client-server application. Future upgrades of the IMS will run the client locally, with access to the servers at the DAAC's for data base queries and searches, thus improving overall system performance. Access to the IMS is generally available from the MOSAIC home pages maintained by each DAAC or at the EDC DAAC via TELNET:

eosims.cr.usgs.gov 12345

or via MOSAIC at:

http://edcwww.cr.usgs.gov/landdaac/landdaac.html

5.   **Future Plans**

In fiscal year 1995, the EDC DAAC plans to ingest recent AVIRIS and ASAS data into the IMS. The inventories at the DAAC will be supported by appropriate product generation systems and each data set will have metadata and browse images similar to that of the TIMS or NS-001.

120

AN ALGORITHM FOR CHLOROPHYLL USING FIRST DIFFERENCE TRANSFORMATIONS OF AVIRIS REFLECTANCE SPECTRA

Evlyn Novo[1], Mary Gastil[2] and John Melack[2]

[1]Instituto Nacional de Pesquisas Espaciais
12 200 01 - Caixa Postal 515, São Jose' dos Campos, S.P., Brazil

[2]Marine Science Institute
University of California, Santa Barbara, CA 93106

1. INTRODUCTION

Experimental results have shown the existence of a strong relationship between chlorophyll a concentration and remote sensing reflectance measured at lake level with a high resolution spectroradiometer (Melack and Gastil, 1994). The objective of our study was to investigate the relationship between surface chlorophyll a concentration at Mono Lake and water reflectance retrieved from Airborne Visible - Infrared Imaging Spectrometer (AVIRIS) data obtained on October 7, 1992. AVIRIS data were atmospherically corrected as described by Green et al. (1993). A description of the lake-level sampling is found in Melack and Gastil (1994). The relationship between chlorophyll concentration and both the single band reflectance and the first difference transformation of the reflectance spectra for the first 40 AVIRIS spectral bands (400 nm to 740 nm) was examined. The relationship was then used to produce a map of the surface chlorophyll distribution.

2. METHODS

The data were obtained on October 7, 1992. Two chlorophyll measurements were obtained at each of 20 stations. The AVIRIS reflectance signal was improved by averaging a 10 by 10 pixel window around each sampling station. These water reflectance measurements derived from AVIRIS do not include the correction for the skylight reflectance.

A first difference transformation of the reflectance spectra was performed:

$$D\lambda_i = (R\lambda_{i-g} - R\lambda_{i+g}) / \Delta\lambda$$

where $D\lambda_i$ is the first difference transformation at band i, g is the gap, $R\lambda_{i-g}$ is the water reflectance at the i-g waveband, $R\lambda_{i+g}$ is the water reflectance at the i+g waveband and $\Delta\lambda$ is the center-to-center span in wavelength between the bands 2g apart. In this statistical analysis, two gaps were tested (gap=1 and gap=3). After the extraction of the reflectance spectra from the AVIRIS image cube and the computation of the first difference transformation with two different gaps, the three data sets were submitted to correlation analyses. The results of the correlation analyses were then used to select the best spectral bands for linear regression to measured chlorophyll.

3. RESULTS

The gap used in the computation of the first difference transformation strongly affected the results (Figure 1). The use of a three-band gap reduces the variance for all wavelengths and, as result, the correlation between the first derivative and the chlorophyll concentration. The highest r^2 between AVIRIS reflectance and chlorophyll are observed at 437 nm and 547 nm (Figure 2). These wavelengths correspond to the chlorophyll a absorption band in the blue region and to the minimum of the chlorophyll a absorption in the green band.

The correlation spectrum derived from the AVIRIS reflectance spectra differs from the correlation spectrum computed by Melack and Gastil (1994) using the field spectra measured on four different dates (44 samples) covering a chlorophyll range of 0.9 μg/l to 47.7 μg/l. The correlation spectrum in that case showed very low correlation between chlorophyll concentration and reflectance in the green region. The highest correlation ($r^2 > 0.80$) was located in the blue region and in the red/near-infrared region.

The AVIRIS reflectance is less correlated to chlorophyll concentration ($r^2 < 0.60$) than the first difference using either gap. The slope between adjacent bands of the reflectance spectrum better predicts chlorophyll than the reflectance brightness at a single band. The first difference transform with a gap of one band provided better results than a gap of three bands. The highest values are found from 540 to 580 nm. In the blue region no high correlation was observed. The improvement in the relationship between chlorophyll concentration and remotely sensed data by using the first difference of the reflectance spectra can be explained by the low water-leaving radiance that makes it difficult for AVIRIS to detect changes in the amount of reflected energy in single wavebands.

On the basis of the previous results, the first derivative at 557 nm was selected for computing the regression model to estimate the chlorophyll concentration (Figure 3). The statistical performance of the model is excellent, producing a standard error for the residuals equivalent to 2% of the average chlorophyll concentration (t=7.09, F=50.3, p<0.0001, r^2=0.74, rms=1.5 μg/l). The average difference between the measured and predicted surface chlorophyll concentration is 0.33 μg/l.

The regression model was used to derive a chlorophyll map of Mono Lake showing the spatial distribution of the surface chlorophyll concentration.

4. CONCLUSIONS

The results presented in this report show that first difference of AVIRIS spectral reflectance can be used to estimate chlorophyll concentration in eutrophic lakes. The best model performance for data collected at Mono Lake on October 7 1992 was obtained with the 557 nm band. This approach should be tested for different dates and for different ranges of concentration in order to assess how much the present model is affected by the optical conditions of the lake.

5. REFERENCES

Green, R.O., J.E. Conel, D.A. Roberts, "Estimation of aerosol optical depth, pressure elevation, water vapor, and calculation of apparent surface reflectance from radiance measured by the airborne visible/infrared imaging spectrometer (AVIRIS) using a radiative transfer code", **SPIE**, Imaging Spectrometry of the Terrestrial Environment, Vol 1937, p 2-11, 1993

Melack, J.M., M. Gastil, "Comparison of spectral feature algorithms for remote sensing of chlorophyll in eutrophic lakes", **IGARSS 94**, 1994.
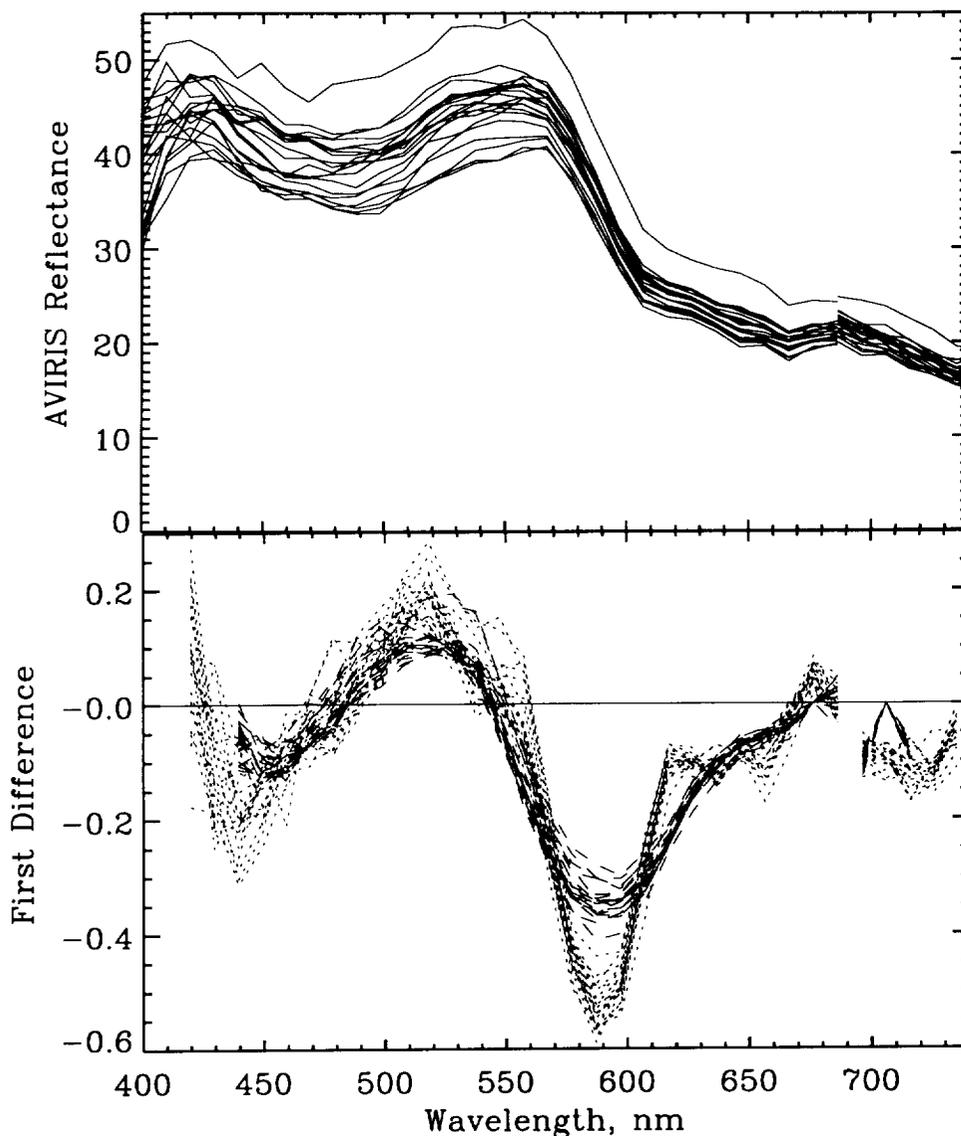
Figure 1. AVIRIS reflectance spectra at 20 stations in Mono Lake (top). First difference (gap=1 dotted and gap=3 dashed) of these AVIRIS reflectance spectra (bottom).
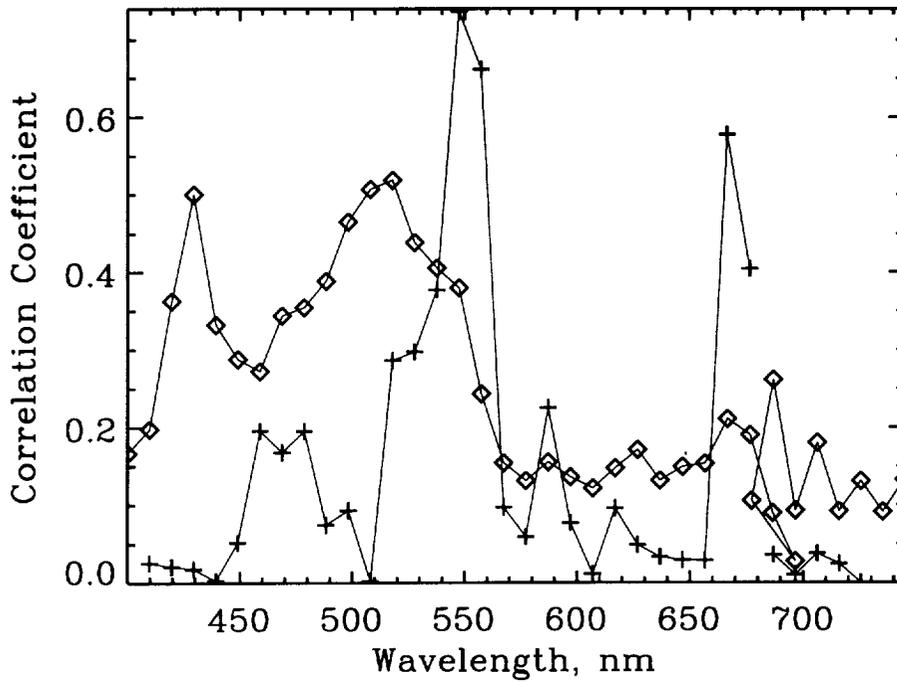
Figure 2. Spectral variation of the r^2 for the AVIRIS reflectance at single bands (◊) and first difference of the AVIRIS reflectance with gap 1 (+).
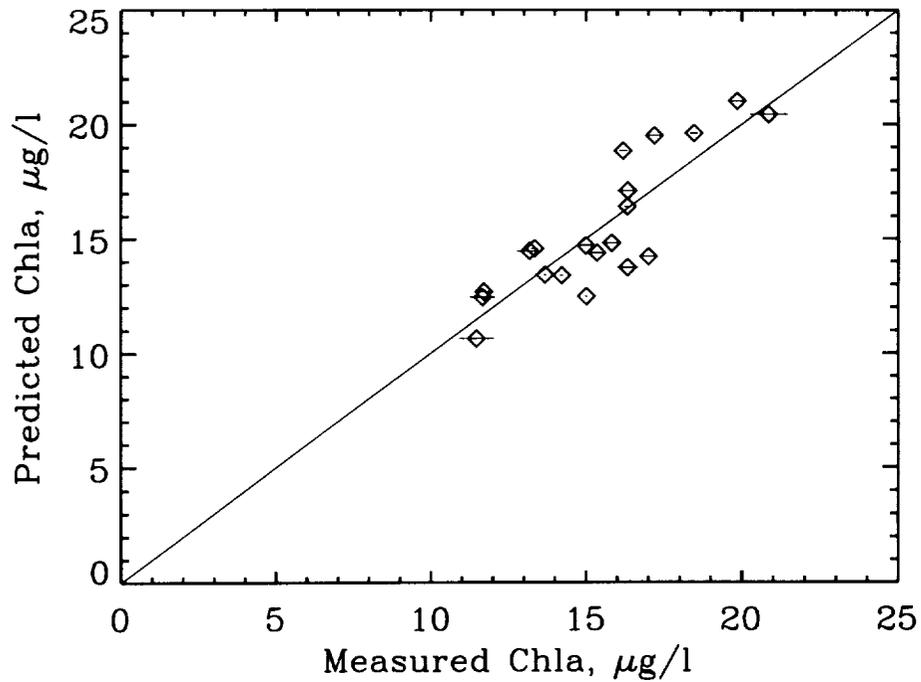
Figure 3. Predicted versus measured chlorophyll concentration. The horizontal bars show the range of two measurements at each of the 20 stations.

124

IMPROVING ALPINE-REGION SPECTRAL UNMIXING WITH OPTIMAL-FIT SNOW ENDMEMBERS

Thomas H. Painter[1], Dar A. Roberts[1], Robert O. Green[1,2] and Jeff Dozier[1]

[1]University of California, Santa Barbara 93106
[2]Jet Propulsion Laboratory, California Institute of Technology, Pasadena, CA 91109 USA

INTRODUCTION

Surface albedo and snow-covered-area (SCA) are crucial inputs to the hydrologic and climatologic modeling of alpine and seasonally snow-covered areas (Dozier, 1989). Because the spectral albedo and thermal regime of pure snow depend on grain size, areal distribution of snow grain size is required. Remote sensing has been shown to be an effective (and necessary) means of deriving maps of grain size distribution (Dozier and Marks, 1987; Nolin, 1993) and snow-covered-area (Dozier, 1989; Nolin, 1993; Rosenthal, 1993). Developed here is a technique whereby maps of grain size distribution improve estimates of SCA from spectral mixture analysis with AVIRIS data.

BACKGROUND

The spectral signature of snow is distinguished by very high reflectance in visible wavelengths and moderate reflectance in NIR wavelengths. While visible reflectance is strongly affected by absorbing impurities and nearly independent of grain size, NIR reflectance is primarily dependent on grain size with reflectance decreasing as grain size increases. Most sensitive to grain size is reflectance in the wavelength region from 1.0 - 1.3 microns which spans the diagnostic ice absorption features at 1.03 microns and 1.26 microns. These relationships are exploited in grain size mapping, most quantitatively by Nolin (Dozier and Marks, 1987; Nolin, 1993). When deposited on the surface, snow grains undergo a process called 'metamorphism' through which larger grains grow at the expense of smaller grains. Metamorphism is in most cases heightened with increased temperature, therefore snow covered regions exhibit grain size distributions inversely related to elevation.

Spectral mixture analysis has as an objective the definition of subpixel proportions of spectral endmembers which may be related to mappable surface constituents (Adams et al., 1993). The spectral mixture approach has been shown to be effective in mapping SCA in alpine regions with Thematic Mapper data (Rosenthal, 1993) and AVIRIS data (Nolin, 1993). These efforts have incorporated fixed endmember suites of snow, vegetation and rock (shade considered complementary). However, fixed suites of spectral endmembers are not necessarily optimal for image-wide endmember detectability (Sabol et al., 1992). It is theorized that the NIR-dependence of snow reflectance on grain size renders a single snow endmember inadequate for regions of significant grain size gradient. In this study we utilized multiple mixture models on a suite of snow endmembers (corresponding to the scene's grain size range) to optimize SCA estimates, pixel by pixel choosing the snow fraction estimated by the model with least mixing error (RMS).

DATA and METHODS

This theory was tested on an April 5, 1994 AVIRIS scene of Mammoth Mountain, CA. Calibrated radiance data was converted to apparent surface reflectance using the atmospheric transmittance model MODTRAN2 and a non-linear least-squares water vapor fitting routine (Green et al., 1993). A map of snow grain size was generated using the method of Nolin (1993). Spectral mixture analysis used the following mixing rules (Roberts et al., 1990):

$$Rc = \sum_{i=1}^{N} FiRi,c + Ec$$

R_c is the apparent surface reflectance in AVIRIS band c, F_i if the fraction of endmember i, $R_{i,c}$ is the reflectance of endmember i in AVIRIS band c. N is the number of spectral endmembers and E_c is the error in AVIRIS band c for the fit of the N endmembers. The average root mean squared (RMS) error is calculated as follows:

$$RMS = \left[M^{-1} \sum_{i=1}^{M} E_c^2 \right]^{1/2}$$

where M = number of AVIRIS bands in spectral mixture analysis.

The spectral mixture band-subset was chosen as per Nolin (1993). This consists of 4 VIS channels and 13 NIR channels spanning the diagnostic 1.03 micron ice absorption feature. Mixing models may be evaluated in three ways; RMSE analysis, fraction under/overflow analysis, and residuals analysis. In this work, RMSE analysis is emphasized while snow fraction under/overflow is used as a secondary qualitative tool.

Image endmembers were chosen for vegetation and rock. Guided by the grain size map for the scene, five image endmembers were chosen for snow of varying grain size, ~75 microns to ~500 microns. With vegetation and rock endmembers fixed, mixture models using the Modified Gram-Schmidt method were run with each snow endmember. RMSE and snow fraction images were produced for each. Optimization was then carried out by choosing for each pixel the lowest RMSE and its respective snow fraction estimate from among the five models to create a MIN RMS image (Figure 1) and accompanying snow fraction image.

RESULTS

Figure 1 shows RMS images for each mixing model and the RMS image for the minimum pixel by pixel RMS among the five models. As reference, Mammoth Mountain Ski Area lies just left of center in the lower half of each image and is the main above-timberline feature in the scene. The summit ridge runs from upper left to lower right. North is toward the upper right corner. Inspection of the model RMS images demonstrates that a single snow endmember is inadequate to model the entire domain. The SW SNOW endmember (~125 microns grain size) has very low RMSE in those regions of smaller grain sizes (high elevation), yet the RMSE increases to 2.5%+ where grain sizes approach 500 microns (lower elevation). The E SNOW endmember (~500 micron grain size) however gave near 0% RMSE in large grain domains and 2.5% RMSE in the smallest grain domains. A comparison of the N1 SNOW and S SNOW RMSE results gives preliminary indication that this technique may be insensitive to aspect: both endmembers are from regions of ~350 micron grain size but opposite aspects (different illumination). Nonetheless, spatial RMSE distribution and magnitude are very similar. Likewise, snow fraction estimates for this pair are nearly identical. The N2 SNOW endmember (extracted from north aspect with ~75 micron grain size) RMSE image poses an important question. Is the coincidence of its near 0% RMSE domain with high north aspects due to a sensitivity of image endmembers to aspect or the likely case that the smallest grains will be high on a northerly aspect? Most encouraging is the MINRMS image. The multiple snow endmember approach significantly bounds RMSE and serves to better characterize the spectral domain of this scene.

126

RMSE alone, however, is not sufficient to test the model results. Inspection of snow fraction images is also necessary. These images (not shown) showed in the individual models that where RMSE was lowest, snow fraction estimates were within reasonable bounds (0.0 - 1.0) and appropriate given location and spectral signature. Where RMSE increased, fraction overflow and/or inappropriate values dominated. All images showed underflow (snow fraction < 0.0) in regions of dense vegetation, indicating the vegetation endmember was contaminated by snow. The snow fraction image for MINRMS is well bounded (but for the vegetation) and spatially appropriate throughout.

DISCUSSION and FUTURE PLANS

Preliminary results indicate that multiple snow endmembers representing a range of grain sizes are necessary to spectrally characterize a scene containing significant snow grain size gradients. Further work will incorporate reference endmembers for vegetation and rock. Snow endmembers will be calculated for a range of grain sizes and illumination angles to more accurately determine grain size and aspect sensitivities. Tests will be run on temporally and spatially different AVIRIS cubes.

ACKNOWLEDGMENTS

REFERENCES

Adams, J.B., M.O. Smith, and A.R. Gillespie, 1993, Imaging Spectroscopy: Interpretation Based on Spectral Mixture Analysis, in Remote Geochemical Analysis: Elemental & Mineralogical Composition, Pieters and Englert, eds., pp 145-166, Cambridge Univ. Press.

Dozier, J., 1989, Remote Sensing of Snow in Visible and Near-infrared Wavelengths, in Theory and Applications of Optical Remote Sensing, G. Asrar, ed., pp 527-547, Wiley and Sons.

Dozier, J. and D. Marks, 1987, Snow Mapping and Classification from Landsat Thematic Mapper Data, Annals of Glaciology 9, 97-103.

Green, R.O., J.E. Conel, and D.A. Roberts, 1993, Estimation of Aerosol Optical Depth and Additional Atmospheric Parameters for the Calculation of Apparent Reflectance from Radiance Measured by the Airborne Visible/Infrared Imaging Spectrometer, Summaries of the Fourth Annual JPL Airborne Geoscience Workshop, JPL Publication 93-26, v 1, Jet Propulsion Laboratory, Pasadena, CA.

Nolin, A.W., 1993, Radiative Heating in an Alpine Snowpack, Ph.D. thesis, University of California, Santa Barbara.

Roberts, D.A., M.O. Smith, J.B. Adams, D.E. Sabol, A.R. Gillespie and S.C. Willis, 1990, Isolating Woody Plant Material and Senescent Vegetation from Green Vegetation in AVIRIS data, in Green, R.O., ed., JPL Pub 90-54, Proceedings of the Second AVIRIS Workshop, Jet Propulsion Laboratory, Pasadena, CA, pp 42-57.

Rosenthal, C.W., 1993, Mapping Montane Snow Cover at Subpixel Resolution from the Landsat Thematic Mapper, Master's thesis, University of California, Santa Barbara.

Sabol, D.E., J.B. Adams and M.O. Smith, 1992, Quantitative Sub-pixel Spectral Detection of Targets in Multispectral Images, J. Geophys. Res., 97, 2659-2672.
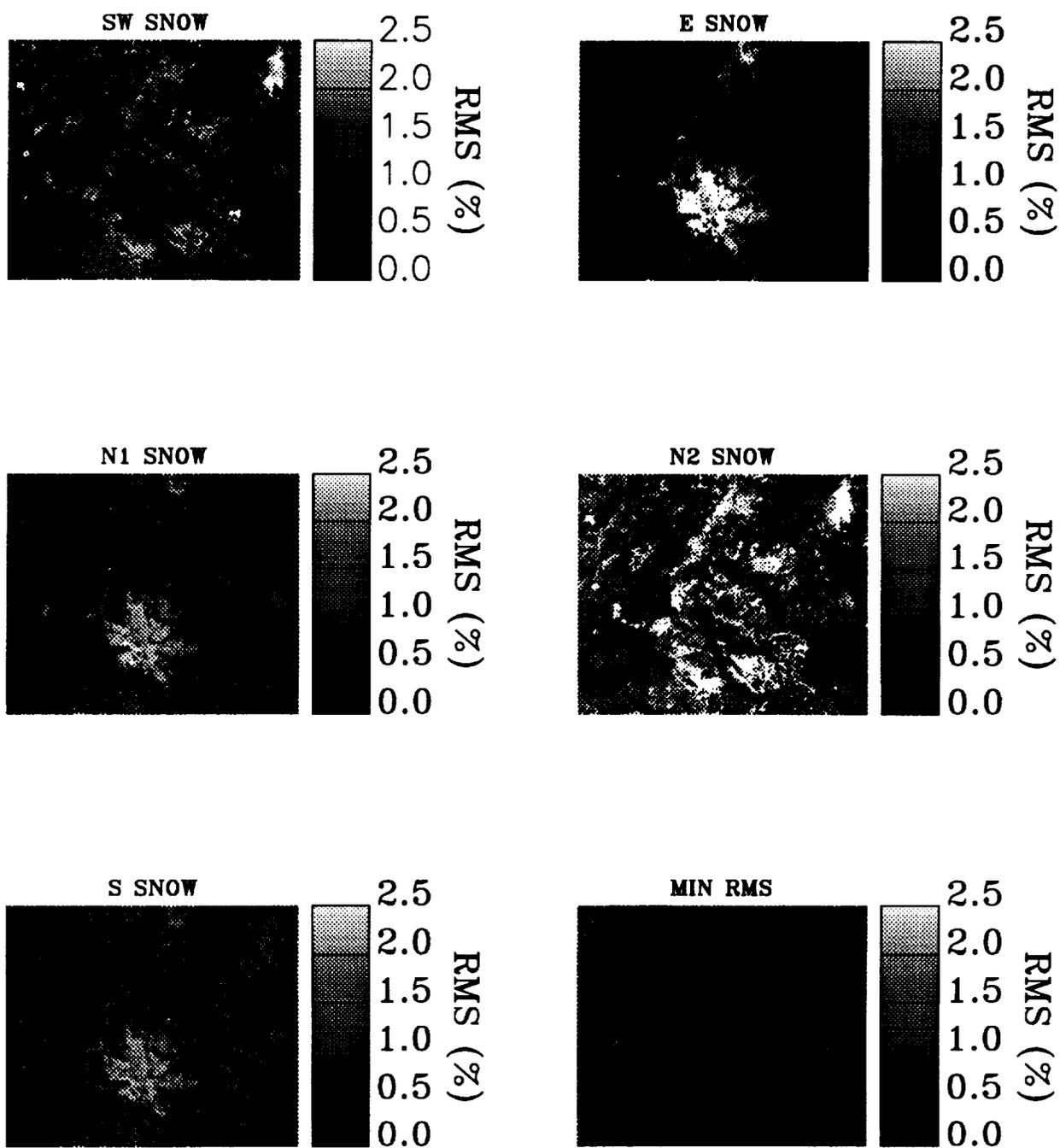
Figure 1. RMSE images for snow endmembers and minimum RMS image.

Using Foreground/Background Analysis to Determine Leaf and Canopy Chemistry

J.E. Pinzon[1], S.L. Ustin[1], Q.J. Hart[1], S. Jacquemoud[1], and M.O. Smith[2]

[1] Dept of Land, Air, and Water Resources, University of California, Davis, CA 95616
[2] Dept of Geological Sciences, University of Washington, Seattle, WA 94805

I. INTRODUCTION

Spectral Mixture Analysis (SMA) has become a well established procedure for analyzing imaging spectrometry data, however, the technique is relatively insensitive to minor sources of spectral variation (e.g., discriminating stressed from unstressed vegetation and variations in canopy chemistry). Other statistical approaches have been tried e.g., stepwise multiple linear regression analysis to predict canopy chemistry. Grossman et al. (1994) reported that SMLR is sensitive to measurement error and that the prediction of minor chemical components are not independent of patterns observed in more dominant spectral components like water. Further, they observed that the relationships were strongly dependent on the mode of expressing reflectance (R, –log R) and whether chemistry was expressed on a weight (g/g) or area basis (g/m^2). Thus, alternative multivariate techniques need to be examined. Smith et al. (1994) reported a revised SMA that they termed Foreground / Background Analysis (FBA) that permits directing the analysis along any axis of variance by identifying vectors through the n-dimensional spectral volume orthonormal to each other. Here, we report an application of the FBA technique for the detection of canopy chemistry using a modified form of the analysis.

II. DATA SETS AND METHODS

II.1. The leaf reflectance / chemistry data sets

The study used two datasets representing a wide range of species having divergent foliar adaptations and conditions. These datasets were the LOPEx (Leaf Optical Properties Experiment) obtained from the Joint Research Centre in (Jacquemoud et al., 1994), and a similar but smaller dataset from the Jasper Ridge Biological Preserve at Stanford University (Grossman et al., 1994). The range of variation – several orders of magnitude – depended on the dataset and the specific chemistry (Jacquemoud et al., 1995). Expressing reflectance as -log R or other transforms provides other characteristics of the variance structure that could be better exploited. The variance structure is especially critical for variables like nitrogen that are in low concentration and do not express a wide range of variance between species.

II.2. The analysis

The general form of the SMA equation for each band is expressed as:

$$DN_b = \sum_{em=1}^{Ne} F_{em}.DN_{em,b} + E_b$$

, where DN_b is the pixel radiance at band b, F_{em} is the fraction of each endmember DN_{em} weighting their radiance at band b, and E_b is an error term accounting for the unmodeled radiance in band b. Endmembers are chosen to explain the spectrally distinct materials that form the convex hull of the spectral volume. This approach can not minimize the spectral variation of endmembers whose characteristics are unrelated to chemistry detection. A methodology that could cluster this variation into a common point is desired. In response to this problem Smith et al. (1994) divide spectral measurements into groups called "foreground" and "background" spectra. Their FBA approach defines a w vector (with components w_b at each band b) such that all foreground DN spectral vectors are projected to 1 and all background DN vectors to 0. This property is set by the FBA system of equations:

$$\text{foreground} \sum_{b=1}^{N} w_b.DN_b + C = 1 \quad \text{and background} \sum_{b=1}^{N} w_b.DN_b + C = 0 \quad \text{material}$$

where C provides a translation. A singular value decomposition algorithm is used to determine the vector w and the real constant C that optimizes both foreground and background equations simultaneously. This analysis can be extend to a general system of equations in which the projections of each spectra along the vector w are its respective chemistry content. In such a way spectra are discriminated by their relation to chemistry variables. In the singular value decomposition we selected the seven highest eigenvalues and their respective orthonormal eigenvectors to account for the spectral variability.

III. RESULTS

III.1. At leaf level

The FBA was performed to define the best vector for discriminating each chemistry shown in Table 1. The analysis was performed both on the JRC and Jasper Ridge fresh leaf datasets, and on the JRC dry leaf dataset using R, −log R,and other non-standard transformations, like

FUNCTION	CHEMISTRY									
	NITROGEN			CELLULOSE			CARBON			WATER	
DATA	JRC fl	JRC dl	JR	JRC fl	JRC dl	JR	JRC fl	JRC dl	JR	JRC fl	JR
R2	0.69	0.60	0.33	0.38	0.29	0.81	0.40	0.27	0.63	0.94	0.91
R	0.68	0.54	0.31	0.31	0.27	0.79	0.40	0.39	0.71	0.94	0.89
Log(1/R)	0.60	0.34	0.30	0.20	0.22	0.64	0.42	0.39	0.82	0.94	0.87
Filter(R)	0.62	NO	0.32	0.50	NO	0.65	0.44	NO	0.83	0.92	0.90

the squared reflectance (R^2). We calculated the multiple correlation coefficient (r^2), to compare the predicted values to the measured chemical concentrations. The best fit overall (0.94) was found for predicting water content (g/g). These results show that the highest r^2 are found for spectra having high chemical variance (Fig. 1). Low r^2 values correspond to chemistry variables that have limited variance. For example, nitrogen has a wider range of variation in the JRC dataset than the Jasper Ridge dataset and the former has higher r^2. In contrast, cellulose has greater variance in the Jasper Ridge dataset and produces a higher r^2. The best-fit predicted and measured chemistry is shown in Figure 2. These results also show that spectra are dominated by the mean reflectance response (related to albedo) rather than variability due to minor absorptions. Clearly this is undesirable for detection of canopy chemistry. We can try to improve detection by considering additional transformations that reduce the effect of variance around the continuum reflectance and maximize shape differences. Such transformations might improve predictions and provide a better basis for predicting canopy biochemistry of minor constitutents.

The first operation was to normalize the spectra and remove albedo differences,

$$R = \frac{R}{\|R\|} \quad \text{where} \quad \|R\| = \sqrt{\sum_{i=1}^{N} R_i^2} \quad \text{denote the norm of the reflectance vector R.}$$

The next step uses the fact that high variance values in any signal (reflectance in our case) has frequency output in the Fourier domain that may be dominated by response to the dc (response at frequency zero). The dc problem can be alleviated in different ways in the Fourier domain. We applied a Discrete Fourier Transform (DFT) to the 211 band spectrum to remove high frequency response (typically related to noise) and a low frequency filter to alleviate the dc response. The effects of these operations are shown in Figure 3. Normalization of the reflectance spectrum does not affect the shape although it does affect the wavelength dependent variance structure. The DFT filtering step clearly changes the shape of the spectrum (mean reflectance information is lost), but enhances other desirable characteristics of the variance structure. The r^2s of the FBA analysis on the normalized DFT dataset are shown in

Table 2. The r^2s of the chemistry variables that have low sample variance (e.g., nitrogen and cellulose) are improved using the squared spectrum, while those with high concentration or having high intra-sample variability (like water) maintain an acceptable level of prediction

III.2. Application to AVIRIS data

The FBA chemistry vectors (water, nitrogen, lignin, and cellulose) derived from the JRC samples were applied to normalized and filtered AVIRIS images of agricultural fields near the city of Davis (CA) and to multitemporal images of Jasper Ridge (CA). These results showed distinct spatial patterns that were related to land cover and land use and with little evidence of random noise. The chemistry patterns were not identical and followed expected patterns for various land cover classes, e.g., high cellulose concentrations occurred in dry grasslands where water contents and nitrogen concentrations were low. Other patterns were generally consistent with ecological characteristics.

IV. CONCLUSIONS

The variance structure of the spectra is highly correlated with biochemical absorptions. Where large variance exists for absorption wavelengths, the relationship to chemistry can be demonstrated. Thus water, for instance, can be estimated by FBA with a high r^2 and a predicted relationship that is close to a 1:1 correlation. Relationships are less satisfactory for chemicals that do not show much intrasample variance or have poorly defined spectral features. However, the r^2 values are improved in datasets where variance has been maximized. These patterns are observed by comparing the nitrogen, cellulose and carbon r^2 between Jasper Ridge and JRC (Table 2). Nitrogen concentration at JRC is about 2 times that at Jasper Ridge while cellulose concentrations are reversed (Grossman et al., 1994). Chemistry predictions for low-variance datasets are improved by normalization and filtering before application of the FBA while these procedures do not significantly affect the prediction of chemistry for samples having a high range of variance.

When FBA vectors are applied to AVIRIS image datasets the results show distinct spatial patterns that follow ecological characteristics. Even biochemicals, like cellulose and carbon, that have low slopes and r^2 (~0.4–0.5) show spatially explicit patterns that follow expected landscape trends. Further, spatial patterns are somewhat independent for each biochemical. Thus, although we lack sufficient field data to adequately validate the image patterns, preliminary results support the possibility of developing direct detection of canopy chemistry using imaging spectrometry.

REFERENCES

Grossman, Y.L., S.L. Ustin, E. Sanderson, S. Jacquemoud, G. Schmuck, and J. Verdebout, 1994, "Examination of regression and correlation approaches for extraction of leaf biochemistry information from leaf reflectance data," *Remote Sens. Environ.* (Submitted).

Jacquemoud, S., J. Verdebout, G. Schmuck, G. Andreoli, and B. Hosgood, 1994, "Investigation of leaf biochemistry by statistics," *Remote Sens. Environ.* (Submitted)

Jacquemoud, S., S.L. Ustin, J. Verdebout, G. Schmuck, G. Andreoli, B. Hosgood, "PROSPECT Redux," (1995) Proceedings, 4th Airborne Imaging Spectrometry Workshop. Jet Propulsion Laboratory, Pasadena, CA (this volume).

Smith, M., D. Roberts, J. Hill, W. Mehl, B. Hosgood, J. Verdebout, G. Schmuck, C. Koechler, and J. Adams, 1994, "A new approach to quantifying abundances of materials in multispectral images," *Proc. Int. Geosci. Remote Sens. Symp. (IGARSS'94), Pasadena (CA).
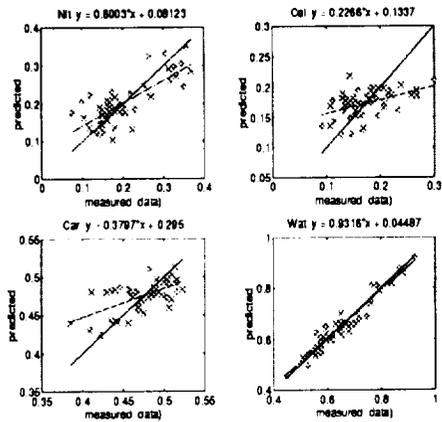
Fig. 1. Best fit by standard methods   Fig. 2. Best fit by filtering spectra
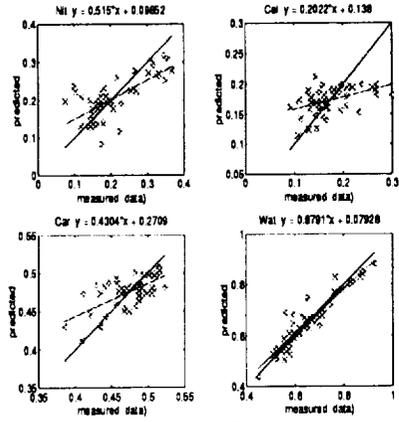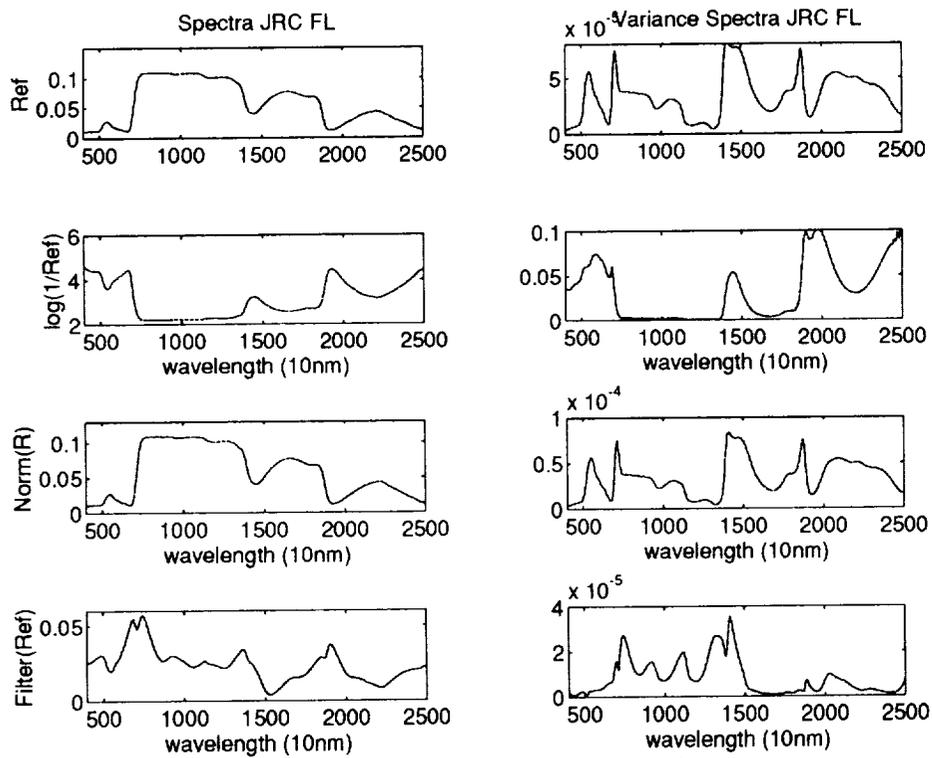
Fig. 3. Effects of the transformations for spectra and variance.

AVIRIS SPECTRAL TRAJECTORIES FOR FORESTED AREAS OF THE GIFFORD PINCHOT NATIONAL FOREST

[1]Donald E. Sabol Jr., [1]Milton O. Smith, [1]John B. Adams, [1]Janet H. Zukin,
[2]Compton J. Tucker, [3]Dar A. Roberts, and [1]Alan R. Gillespie

[1] Department of Geological Sciences, AJ-20, University of Washington,
Seattle, WA 98195
[2] Laboratory for Terrestrial Physics, NASA, Goddard Space Flight
Center, Greenbelt, MD 20771
[3] Department of Geography, University of California, Santa Barbara,
CA 93106

1. INTRODUCTION

In the Pacific Northwest, the practice of clear-cutting and replanting of "old-growth" (250+ year old) forest over the past 40 years has resulted in large areas of replanted trees in various stages of regrowth. How quickly a clear-cut area regrows is a function of many factors (e.g. soil condition, sun exposure, moisture availability, replanting history, elevation, etc.). Monitoring regrowth status is important for management decisions. Clearcutting has greatly decreased the amount of "old-growth" forests. For example, it was estimated that less than 28% of the major national forests of western Washington, Oregon, and northern California was old growth in 1990 (Morrison et al., 1991), raising questions of species diversity and overall forest "health." This estimate is very rough and hotly debated as it is difficult to separate mature forest from old-growth forest using remote sensing. Therefore, it is still uncertain how much "old growth" exists and where all of it is located.

In this study, we applied spectral mixture analysis to an AVIRIS image of a portion of the Gifford Pinchot National Forest, Washington to: 1) estimate forest regrowth stage and to provide a framework for monitoring the regrowth over time, and 2) present initial work on mapping old-growth forest as separate from other mature forest.

A simple mixing model using reference endmembers of green vegetation (GV), non-photosynthetic vegetation (NPV), soil, and shade was applied to a September 22, 1994 AVIRIS image of a portion of the Gifford Pinchot National Forest. Noisy bands were excluded leaving 180 of the 224 bands. The image data were calibrated to reflectance using spectral mixture analysis (Gillespie et. al, 1990). Results from the AVIRIS image were compared with a similar analysis of a 1992 Landsat TM image of the same area.

Fractions of endmembers were computed for each AVIRIS pixel and displayed as images. The shade-fraction image included the effects of topographic shading and shadow, as well as shade contributed by textural elements, such as forest canopy at the subpixel scale. In our analysis of the TM image topographic shade was "removed" by a digital elevation model (DEM), thereby enhancing the component of shade contributed by canopies. Registration of the DEM to the AVIRIS image is not completed: therefore, this report considers only a portion of the image that has moderate to low relief.

Means of fractions in the AVIRIS image were measured for variable sized blocks of pixels (3 by 7 and greater, depending on the size and shape of each site) at 90 sites known from field surveys (Fig.1). The sites included clearcuts of different ages, mature forest and old-growth forest. Field data were obtained from the US Forest Service and gathered by the authors in July and August of 1994. In the context of the field data, the simple mixing model provided a framework for understanding the main differences in

surface cover: however, it was not expected that four endmembers would model the full spectral complexity of the scene.

2. RESULTS

2.1 Forest Regrowth

Recent clearcuts were characterized by high fractions of NPV and low fractions of GV and shade. Burned clearcuts had enhanced fractions of apparent shade, caused by charcoal and dark ash mimicking the spectrum of shade. Clearcut areas with partial cover of ferns, grasses, forbs, and shrubs had low to moderate fractions of GV, without a significant component of shade.
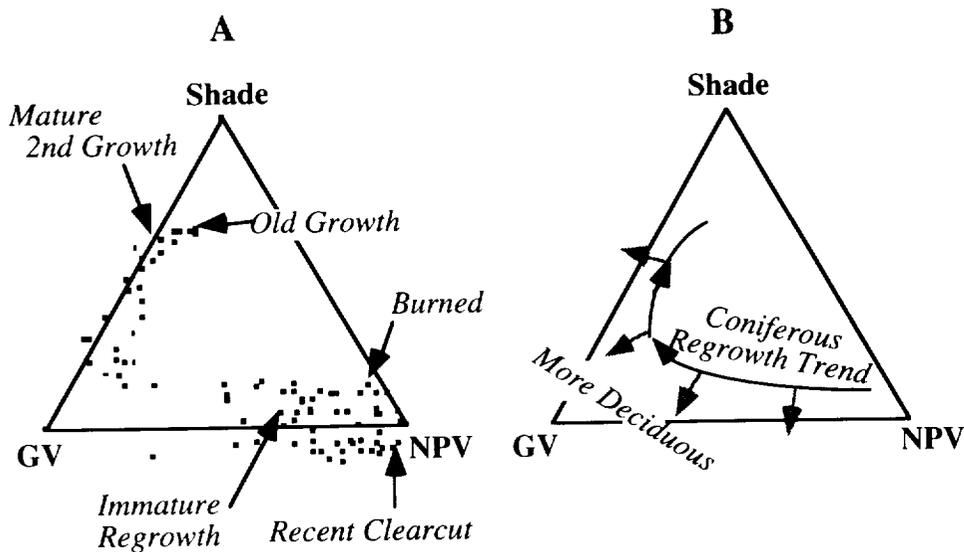
Figure 1. A) Ternary scatterplot of mean fractions for 90 sites (clearcuts of different ages, mature forest and old-growth forest). B) Generalized regrowth trends observed in the image data.

Typically, clearcuts were replanted with conifers within 1 to 3 years, most commonly with *Pseudotsuga menziesii* (Common Douglas Fir). With increasing cover, stands had correspondingly higher fractions of GV and shade, along with a decrease in the fraction of NPV. Closed-canopy stands had low (<0.1) fractions of NPV (contributed by exposed branches) and intermediate values of shade (Fig.1A). Older stands with increasingly complex canopies had higher fractions of shade. Pure stands of conifers of various ages defined a trajectory in the ternary fraction diagram (Fig 1B).

Although trees replanted in this part of Washington are exclusively coniferous, deciduous species such as *Alnus rubra* (Red Alder), *Acer circinatum* (Vine Maple), and various species of ferns occurred within many of the cut areas. Clearcuts containing deciduous species had higher fractions of GV than those with just conifers. Areas dominated by deciduous regrowth had the highest GV fractions, plotting farthest from the trend line (Fig. 1B) for pure coniferous regrowth.

For each of the 90 test areas on the AVIRIS image, ages of stands were determined from Forest Service records of date of planting. Stand age was compared with endmember fractions. The coniferous regrowth trend defined a general increase in age for the test areas on the image (Fig. 2). Fractions changed rapidly during the first decade as regrowth obscured the substrate. With further maturation of the stands, the rate of change of the fractions slowed, and the main effect was an increase in shade.

There was considerable scatter of ages along the coniferous regrowth trend. Although the general trend was clear, it was not possible to invert the AVIRIS spectral data to arrive at an unambiguous stand age for each test area. Various factors influenced rate of regrowth, including altitude, slope, aspect, soil conditions, disease, and management history. These factors would have to be known to use the spectral data to infer stand age; however, obvious departures from the main regrowth trend might be used to identify stands with retarded growth rates.

2.2 Old Growth

Mature forest and old-growth forest are spectrally similar in both TM and AVIRIS data. Both forests types have similar fractions of GV and relatively high fractions of shade. Separation can be complicated by the presence of topographic shade and shadow. It was possible to identify old growth in a TM image by high mean fractions of "textural shade" and high pixel-to-pixel variability in shade, after isolation of the main topographic effects with a cosine correction based on DEM data. No clear change in NPV was measurable in the TM data above the system noise, although field observations indicated exposure of woody material in the crowns of old-growth forests.

The AVIRIS image was used to test whether it was possible to detect a higher fraction of NPV in old growth relative to mature forest. Based on field observations we predicted that when the coniferous regrowth trend reached old growth it would hook back toward NPV (Fig. 2). The AVIRIS data showed the old growth to be higher in NPV than mature forest by 0.03 to 0.05. A 3 to 5% increase in NPV is detectable by AVIRIS, based on our experience with other test areas (Sabol et al., 1992). If this result is
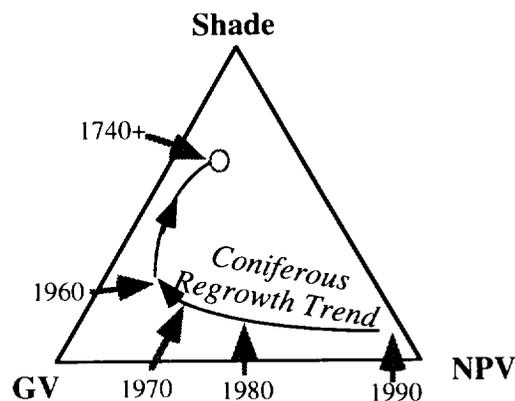
Figure 2. Mean date of replanting for 90 sites (clearcuts of different ages, mature forest, and old-growth forest).

confirmed by further analysis it provides a second spectral parameter by which to characterize old growth (the other being shade and shade variability). A more sensitive measure of NPV can be made using the new method of foreground-background analysis (Smith et al., 1994). This work is in progress.

The simple mixing model was used to locate old growth throughout the image. Within the image 13.6 % of the area was mapped as old growth. This result is in good agreement with the 11.2 % mapped by the Wilderness Society (Morrison et al., 1991). The comparison will be repeated after further analysis of the AVIRIS data to remove topographic shade and to increase the reliability of the NPV estimate.

3. CONCLUSION

A simple mixing model employing reference endmembers (green vegetation, non-photosynthetic vegetation, soil and shade), and using 180 AVIRIS bands, was used to established an interpretive framework for a forested area in the Pacific Northwest. A regrowth trend, based on changes in the endmember proportions, was defined for conifers that extends from clearcuts to mature forest, and by implication to old growth. Deciduous species within replanted forest plots caused the fractions to be displaced from the main coniferous regrowth trend and to move toward the green vegetation fraction. The results indicate that the spectral information in AVIRIS can be inverted to estimate approximate stand age and relative proportion of deciduous species in the context of the area studied.

Using AVIRIS we measured a 3 to 5% increase in woody material in old-growth forest, as distinct from other mature forest. This result is consistent with a predicted increase in NPV in old-growth forests, based on field observations. Previous application of the mixing analysis to a TM image of the same area separated old growth based solely on the shade fraction; however the approach required successful removal of shade introduced by topography. Our new results suggest that with the high spectral resolution and high signal-to-noise of AVIRIS images it may be possible to characterize and map old-growth forests in the Northwest using both the NPV fraction and shade.

4. REFERENCES

Gillespie, A.R.., Smith, M.O., Adams, J.B., Willis, S.C., Fischer, A.F., and Sabol, D.E., 1990, Interpretation of residual images: Spectral mixture analysis of AVIRIS images, Owens Valley, CA, *Proc. Second Visible/Infrared Imaging Spectrometer (AVIRIS) Workshop*, JPL Pub. 90-54, 243-270.

Morrison, P.H., Kloepfer, D., Leversee, D.A., Socha, C.M., and Ferber, D.L., 1991, Ancient forests in the Pacific Northwest: Analysis and maps of twelve national forests, *The Wilderness Society*, Allied Printers, Seattle, WA, 13pp.

Sabol, D.E., Adams, J.B., and Smith, M.O., 1992, Quantitative subpixel spectral detection of targets in multispectral images, *J. Geophys. Res.*, 97, 2659-2672.

Smith, M.O., Adams, J.B., and Sabol, D.E., 1994, Spectral mixture analysis - new strategies for the analysis of multispectral data, in J. Hill and J. Megier (eds.), *Imaging Spectrometry - a Tool for Environmental Observations*, Brussels and Luxembourg, 125 - 143.

SUB-PIXEL LOCALIZATION OF HIGHWAYS
IN AVIRIS IMAGES

Yehuda Salu

Department of Physics and CSTEA, Howard University, Washington DC, 20059

1. INTRODUCTION

Roads and highways show up clearly in many bands of AVIRIS images. A typical lane in the U.S. is 12 feet wide, and the total width of a four lane highway, including 18 feet of paved shoulders, is 19.8 m. Such a highway will cover only a portion of any 20x20 m AVIRIS pixel that it traverses. The other portion of these pixels will be usually covered by vegetation.

An interesting problem is to precisely determine the location of a highway within the AVIRIS pixels that it traverses. This information may be used for alignment and spatial calibration of AVIRIS images. Also, since the reflection properties of highway surfaces do not change with time, and they can be determined once and for all, such information can be of help in calculating and filtering out the atmospheric noise that contaminates AVIRIS measurements. The purpose of this report is to describe a method for sub-pixel localization of highways.

2. METHODS

2.1 General

Highways usually appear sharpest and clearest in only some of the bands. The ideal band to use for localizing a highway would have a high contrast between the highway's surface and its surrounding (vegetation). The ideal band should also be insensitive to the variations in the vegetation bordering the highway. The methodology presented here is based on first localizing the highway in each of the bands, and then making the final determination based upon the most consistent band. An extension of the basic correlator method (Hall, 1979) is presented here for localizing the highway within a one band scene.

2.2 Highway Localization

Figure 1 a. is a map in which a straight highway traverses a vegetated area. The width of the highway is known, but not its precise location. The observed intensities of the upwelling radiation from each pixel in the map are given too. To find the location of the highway, we first prepare templates of identical highways, that cross a grid at different locations and orientations. One such template is shown in Figure 1 b. Let H and V denote the intensity of the upwelling radiation from pixels completely covered by a highway, and by vegetation, respectively. The calculated intensity of the upwelling radiation from pixel i of a template is given by $H \cdot P_i + V \cdot Q_i$, where P_i is the portion of the pixel covered by the highway, and Q_i is the portion

covered by the vegetation. H and V are treated as unknowns. The P_i's and the Q_i's ($P_i + Q_i = 1$) are computed from the known geometry of each template.

1.a   1.b
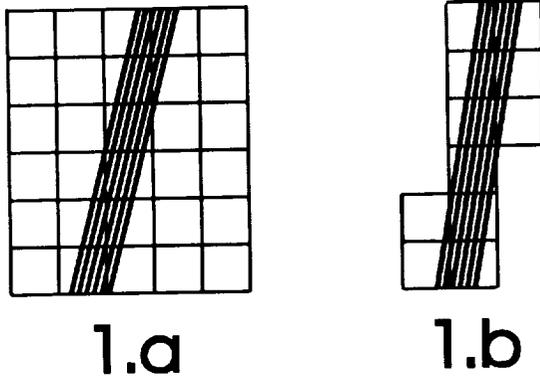
FIGURE 1. a. The pixels of a map of an area (vegetation), traversed by a highway. b. One of the templates that are used for finding the precise location of the highway.

To localize the highway, we shift each template over the given map, keeping the grids of the map and the template fitted. For each position r of template τ, we find H and V that minimize the Euclidean distance between the calculated intensities of the pixels of the template, and the observed intensities (Obs_i) of the corresponding map pixels that they cover:

$$D(r,\tau) = \min(\Sigma(Obs_i - (H \cdot P_i + V \cdot Q_i))^2 / \Sigma(Obs_i)^2) \qquad (1)$$

The summations in equation 1 are over all the pixels of the template.

The location of the highway in the template for which $D(r,\tau)$ is a minimum as a function of r and τ is the calculated location.

To reduce the effects of the noise caused by the atmosphere, and to increase the effectiveness of the least squares fit, it might be better to match the gradients of the radiation intensity instead of the radiation intensity itself. The use of the x component of the gradient for the least squares fit will accomplish these objectives. The x component can be approximated by the difference between the intensities of a pixel and that of its left neighbor. When this approach is taken, equation 1 becomes:

$$D(r,\tau) = \min(\Sigma(Dobs_i - B \cdot DP_i)^2 / \Sigma(Dobs_i)^2) \qquad (2)$$

Where $Dobs_i$ is the difference between the observed radiation of pixel i and its left neighbor, $B = H - V$, and DP_i is the difference between the portion of covered highway of pixel i and its left neighbor. The summations in equation 2 are over all the pixels of the template.

138

3. RESULTS

3.1 The Data

Two segments of Junipero Serra Freeway, that appear in the Jasper Ridge scene (Flight 920602A) were used in this study. Each segment was approximately 400 m long. Since the outcomes for these two segments were similar to each other, only one segment will be described here. The highway appears sharpest in the first 23 bands. In some of the other bands the highway could not be recognized at all. The analysis presented in the following was done on bands 1 through 99, excluding fuzzy bands.

3.2 Locating the Highway

Approximately two hundred templates of a highway 19.8 m wide were used. Each template was bounded within a 60x120m rectangle. The templates differed from each other by the orientation and location of the highway within the template's rectangle. The templates were shifted systematically over the portion of the map, that included the highway. Best matches, i.e. minima of $D(r,\tau)$ according to equation 2, were found and superimposed on the map. There were many local minima of $D(r,\tau)$, that did not correspond to a highway or to a road. However, most of these presumed highway segments were isolated. They were not linked with other segments in contiguous templates. Only two continuous roads were found in band 3 (figure 2.b), corresponding to the Northbound and Southbound lanes of the highway.

Band 4 gave similar results to those of band 3. The results of all the other bands were not as good; there were gaps in the two lanes, and in some cases the lanes crossed each other.

4. DISCUSSION

The results, as shown in figure 2.b, were compared with an aerial photograph of the area. The widths of the median in this portion of the road, as determined from the aerial photographs, were between one third to one quarter of the width of the road. These were also the results obtained from figure 2.b. Based on this, the accuracy of localizing the highway is estimated to be $\pm$ 2m.

It should be noted, that by looking at the raw data (figure 2.a), human observers could not detect the existence of two lanes in the scene.

References

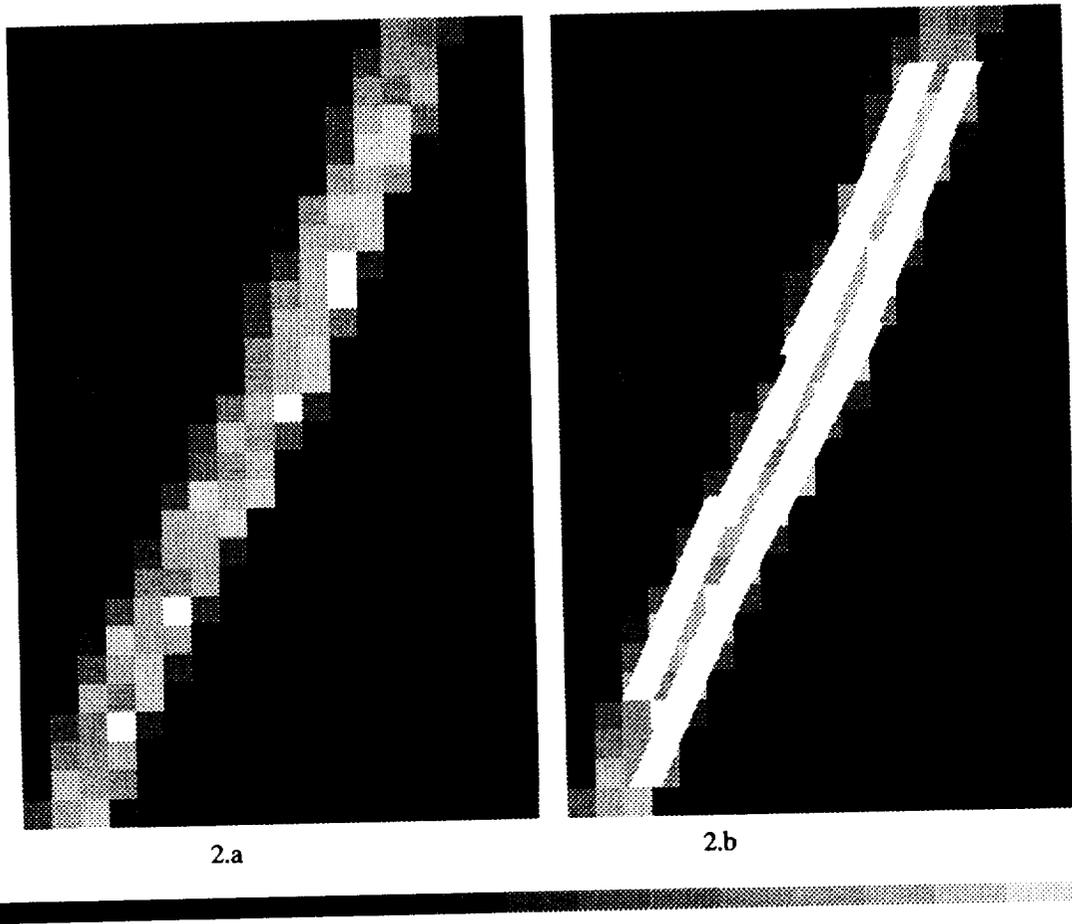Hall E.L., 1979, *Computer Image Processing and Recognition*, Academic Press, New York, pp. 480-484.

FIGURE 2. a. The highway as it appears in band 3.   b. The calculated location of
the highway superimposed on the original scene.

VALIDATING SPATIAL STRUCTURE IN CANOPY WATER CONTENT USING GEOSTATISTICS

E. W. Sanderson[1], M.H. Zhang[1], S.L. Ustin[1], E. Rejmankova[2], and R.S. Haxo[1],

[1]Dept. Land, Air, and Water Resources, University of California, Davis, CA 95616

[2]Division of Environmental Studies, University of California, Davis, CA 95616

Introduction

Heterogeneity in ecological phenomena are scale dependent and affect the hierarchical structure of image data (cf. Levin, 1992). AVIRIS pixels average reflectance produced by complex absorption and scattering interactions between biogeochemical composition, canopy architecture, view and illumination angles, species distributions, and plant cover as well as other factors. These scales affect validation of pixel reflectance, typically performed by relating pixel spectra to ground measurements acquired at scales of $1m^2$ or less (e.g., field spectra, foliage and soil samples, etc.). As image analysis becomes more sophisticated, such as those for detection of canopy chemistry, better validation becomes a critical problem. This paper presents a methodology for bridging between point measurements and pixels using geostatistics. Geostatistics have been extensively used in geological or hydrogeological studies but have received little application in ecological studies (Rossi et al, 1992). The key criteria for kriging estimation is that the phenomena varies in space and that an underlying controlling process produces spatial correlation between the measured data points. Ecological variation meets this requirement because communities vary along environmental gradients like soil moisture, nutrient availability, or topography.

Project Description: The overall goal of our AVIRIS project is to develop strategies for monitoring salt marsh conditions (species distributions, biomass, leaf area, water content, etc.) and identifying spectral signatures that can be used as diagnostic indicators of wetland functioning (chlorophyll, nitrogen, carbon, evapotranspiration and photosynthetic rates, etc.). The study site is located along the northern shore of San Pablo Bay, CA (northern extension of San Francisco Bay) and includes the Petaluma and Napa River estuaries and the Mare Island Naval Base. These systems experience large naturally occurring spatial and temporal gradients in salinity, nitrogen, redox potential and are subject to regional pollution and point sources of soil and groundwater contamination (toxics, heavy metals, and others). Mare Island, scheduled for decommissioning and transfer to the University of California, Davis, has multiple contaminated sites.

Methods

Study Area and Sampling Design: Three sites were studied along the Petaluma River estuary that are considered to be "healthy" but differ in species distributions, biomass, and in the magnitude and structure of their environmental gradients. This paper focuses on one site located approximately 8 km upriver. Sampling was coincident with AVIRIS overflights on May 21 and May 23, 1994. This site is threaded with a network of fine channels that bring nutrients and leach accumulated salts. Three salt tolerant species dominate. In the lower intertidal, *Spartina foliosa,* a grass is dominant. *Scirpus robustus,* a bulrush grows near mean high tide (10-20m above the low tide) and forms a patchy distribution at sites with low spring salinities. The most halophytic species and a succulent shrub, *Salicornia viriginica,* dominates the high marsh. Canopy and soil reflectance measurements, plant cover and height were measured at 196 locations on an evenly spaced 15m grid (see Figure 1, the schematic map in AVIRIS Workshop Slide 8) with the location determined by GPS. At 42 sites within the 200 point grid, aboveground biomass, soil salinity, redox potential, and soil nitrogen content, canopy carbon, nitrogen, and pigments' samples were obtained. Geostatistics were used to spatially interpolate these data to provide a basis for interpreting patterns in AVIRIS data.

Sample Collection and Water Content Analysis: Canopy spectra were measured using an ASD PSII for the 345-1072nm interval, with an 18° view restrictor on foreoptics suspended 1m above the canopy; spectra were calibrated to reflectance using a Spectralon panel. Spectra

were averaged to 10nm wavebands and normalized (defined as the $\sqrt{\Sigma(\text{reflectance}^2)}$) for comparison to AVIRIS spectra. Following Clark and Roush (1984), the continuum removal method was applied to a feature centered at 980nm to determine canopy equivalent water thickness. In this technique, a line is extended across an absorption feature and the depth is determined for each AVIRIS waveband, depths are summed over the 10nm intervals to estimate the area. Water depth features were calculated for all spectra and from the 40 spectra having corresponding biomass. Regression relationships were developed to predict water content (Figure 2). Aboveground biomass was harvested in 42 circular quadrats (0.126 m^2), the area corresponding to the FOV. Biomass was sorted by species into woody and green components (*Salicornia* and *Scirpus*) and green for *Spartina*. Fresh and dry weights were measured after drying for 2-3 days at 70°C. Water contents were determined by subtraction and relative water content as (fresh - dry weights)/(fresh weight). All water contents were normalized to an area of 1m^2 (kg water/ m^2). Descriptive statistics and histograms were compared among the datasets as described in the results section.

Geostatistical Methods: A contour map was prepared using the inverse distance squared method based on 196 site water contents predicted from the continuum removal (see Figure 3, AVIRIS Workshop Slide 8). Observed variograms were calculated and modeled and applied in kriging estimation using GEO-EAS (Englund and Sparks, 1988) and GEOPACK (Yates and Yates, 1989). A variety of lag distances and search neighborhoods were attempted to bring the best structure to the variogram. It was found that a lag of 15m, corresponding to the approximate spacing of the sample grid with an elliptical search neighborhood oriented roughly along the N-S axis gave the best results. The observed variogram was calculated from 0-100m in the E-W direction and 0-200m in the N-S direction. An exponential variogram model was fit for cokriging. Canopy water content was interpolated using cokriging estimation to a 5m by 5m grid of points over the sampling area. This denser network of interpolated points was combined with observed data for comparison to georeferenced AVIRIS pixels.

Results

Measured and Predicted Water Content : Water content varies between and within species. *Salicornia* dominated sites have the greatest water content, more than 86% water by weight. Preliminary evidence suggests that canopy water content increases closer to the channel network. *Spartina* foliage has less water content than *Salicornia*, and *Scirpus* has less still. Histograms of the predicted and measured water content show approximately normal distributions.

	Salicornia virginica		*Spartina foliosa*	*Scirpus robustus*		*Frankenia grandifolia*
	Green	Woody		Green	Woody	
Mean Water Content (kg/m^2)	1.034	0.750	0.718	0.145	0.057	0.061
Standard Deviation	0.854	0.561	0.415	0.260	0.039	0.041
Mean Relative Water Content (%)	86.5	52.5	78.3	65.4	32.7	60.9

Spatial Pattern of Water Content: Two distinct and important spatial structures are seen in the contour map. First, the patch size are differences between species distributions (~50m). In May, most of the *Scirpus* biomass was standing litter with little green biomass. In the northeast corner a large patch of *Scirpus* corresponds to the area of lower water content; similar patches occur along the eastern edge. The second spatial structure occurs near the center where the area is dissected by a network of fine drainage channels (~150m). As a result, conditions are apparently better for *Salicornia*, (indicated by the higher biomass and water content). Several elongated patches of high water content correspond to the channels. This interpretation will be further examined by more detailed comparison in the GIS currently

142

under construction. We expect other spatial features related to ecosystem functioning (e.g., biomass, chlorophyll and nitrogen) to be preserved in interpolation results.

Kriging Estimation of Spatial Pattern: Using the variogram model developed from the sampling points, kriging was used to estimate the water content at unsampled locations and over block areas (e.g., pixels). Interpolation techniques, like kriging, allow single measurements to be extended to area estimates and to make multiple point estimates within the block. We use the point estimates to describe probability density functions of the spectral components of the block reflectance. However unlike the block estimate, which is not directly interpreted from our grid measurements, we can spatially interpret the point estimates.

Conclusion

Spatial heterogeneity is large, even for a simple ecosystem like a salt marsh. Species distributions, biomass, and other characteristics vary over small distances, making it difficult to adequately test remote sensing models. Water content of point samples was shown to be related to the area of water absorption feature without a strong dependence on canopy architecture. It was possible to use geostatistics to interpolate spatial patterns within AVIRIS pixels to produce a more extensive network of points for generally realistic spatial patterns to be used for comparison to remote sensing imagery over block areas (pixels). To construct the relationships between the field observations and remote sensing data, variogram, contour line, and kriging were applied to simulated AVIRIS bands and TM band 3 and 4 (used for example) and water content. The semivariogram is frequently used because it describes the spatial autocorrelation structure. Kriging is a family of methods for data interpolation: we used cokriging and ordinary kriging to interpolate between points. Additionally, kriging allows extension of patterns defined within a sampling grid to adjacent unsampled areas. As a test to validate AVIRIS patterns, the relationship between water absorption and water content was determined and related to spatial patterns in interpolated field data.

Figure 2. Regression of Continuum Removed Area from Water Absorption Band at 980 nm Against Observed Canopy Water Content
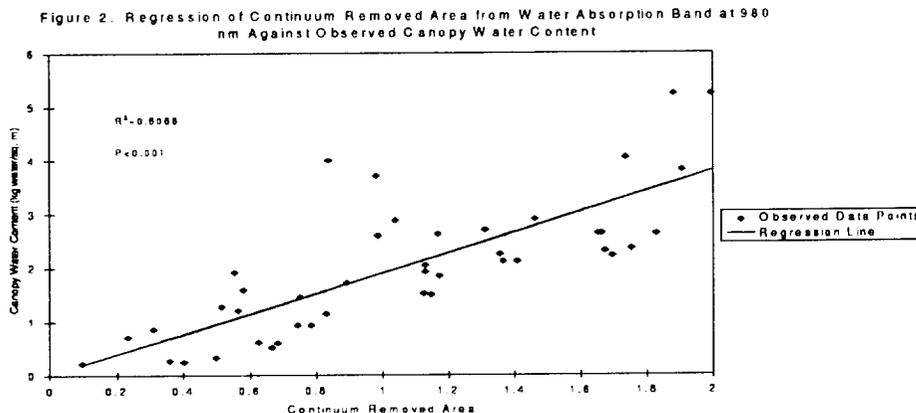
References

Clark, R.N. and T.L. Roush 1984, Reflectance spectroscopy: Quantitative analysis techniques for remote sensing applications. J. Geophys. Res. 89: 6329-6340.

Englund, E., and Sparks, A. 1988, GEO-EAS (Geostatistical Environmental Assessment Software) User's Guide. Environmental Monitoring Systems Laboratory, Las Vegas, NC. EPA600/4-88/033.

Levin, S. 1992, The Problem of Pattern and Scale in Ecology. Ecology 73:1943-1967.

Rossi, R., Mulla, D., Journel, A., and Franz, E. 1992, Geostatistical tools for modelling and interpreting ecological spatial dependence. Ecology 62: 277-314.

Yates, S.R., and Yates, M.V. 1989, Geostatistics for waste management: A User's manual for the GOEPACK Geostatistical Software System. USDA Salinity Lab, Riverside, CA.

AIRBORNE VISIBLE/INFRARED IMAGING SPECTROMETER (AVIRIS): SENSOR IMPROVEMENTS FOR 1994 AND 1995

C. M. Sarture, T. G. Chrien, R. O. Green, M. L. Eastwood,
J. J. Raney, and M. A. Hernandez

Jet Propulsion Laboratory, California Institute of Technology
Pasadena, CA 91109

1.0   INTRODUCTION

AVIRIS is a NASA-sponsored Earth-remote-sensing imaging spectrometer designed, built and operated by the Jet Propulsion Laboratory (JPL). While AVIRIS has been operational since 1989, major improvements have been completed in most of the sensor subsystems during the winter maintenance cycles. As a consequence of these efforts, the capabilities of AVIRIS to reliably acquire and deliver consistently high quality, calibrated imaging spectrometer data continue to improve annually (see Tables, Section 7.0), significantly over those in 1989. Improvements to AVIRIS prior to 1994 have been described previously (Porter et al., 1990, Chrien et al., 1991, Chrien, 1992, Chrien et al., 1993). This paper details recent and planned improvements to AVIRIS in the sensor task.

2.0   SENSOR IMPROVEMENTS

2.1   1994 Engineering and Maintenance Cycle

2.1.1 100 Lines of Post-Cal Dark Current

A 100-line sliding dark current average has been employed in the processed data since the 1993 flight season for noise reduction, but had a ramping-off artifact which would begin 100 lines before the end of each run. To compensate for this and also to provide an even more stable dark current value for the entire run, 100 scan lines of dark current are taken at the end of each run during the post-cal sequence.

2.1.2 Lyot Filters in and Temperature Telemetry from IFRS

The number of filter wheel positions in the in-flight reference source (IFRS) was increased from 4 to 8 to accommodate the additional four Lyot filters, one per spectrometer. Because of manufacturing delays, the first three Lyot filters (A, B, and C) were installed mid-way through the 1994 flight season during a two-week hiatus in July. The fourth Lyot filter (D) was installed at the end of the flight season. A temperature sensor was added for providing telemetry monitoring of the Lyot filters, which change spectral characteristics with temperature.

2.1.3 Spectrometer Thermal Testing and Additional Thermal Blanketing

All four spectrometers were tested in a thermal chamber to investigate operation at simulated mission temperatures, down to -10° C. Resulting data showed that a vertical thermal gradient existed even with the distributed, actively controlled spot heaters. Additional thermal blanketing applied to the lower part of the spectrometers was found to greatly ameliorate this condition, which was causing a spectral shift in the spectrometers.

2.1.4 Tape Recorder Thermal Testing

Both AVIRIS high-density digital recorders (HDDR) underwent testing in a thermal chamber to further refine the performance of the JPL developed thermal control. An adjustment to the thermal controller time constant improved the thermal tracking and enhanced the bit error rate performance at mission temperatures. One of the HDDR's was upgraded to the high-performance cross-cut scanner heads, bringing it current with the other AVIRIS unit.

2.1.5 High Resolution Scan Timer

A high resolution scan timer (HRST) was installed to measure the skew between the roll-compensated start of successive cross track scans. The scan timer is a 16 bit counter driven by a crystal stabilized 94.3 kHz clock, with a 10.6 μsec period. Nominally, the scan timer value rolls over every 8.33 scans (with no aircraft roll rate). One application for the HRST is temporally registering the cross track scan lines in an image so that an FFT can be used to remove coherent noise from a roll-compensated image.

2.1.6 Recovered Elements in Spectrometer B, C, and D Focal Plane Arrays (FPA's)

The first element of each of the four FPA's was previously saturating due to an artifact in the analog signal chain. A simple change in the timing generator was found to delay the ADC start pulse sufficiently to bring the B, C, and D spectrometer FPA's out of saturation and make them usable. In previous years (from 1989 on), these channels (33, 97, and 161) were present in data products as blank image planes.

2.1.7 Operational Features

To accommodate a request from Ames Research Center that AVIRIS operational indicators in the ER-2 cockpit be more like other ER-2 sensors, the AVIRIS cockpit control indicators now describe the operational state of AVIRIS. The operational states are: power-on-initiation; run-initiation, pre-cal/post-cal; and science data collection. This enhancement reduces the pilot workload, facilitating data gathering.

Another operational enhancement eliminates the requirement for a lead segment in a flight line following the completion of an ER-2 turn, resulting in greater flight efficiency while acquiring mosaic images. This was achieved by delaying the roll compensation gyro reset pulse until the last moment before commencing science (image) data collection.

2.1.8 Spares Program

The inventory of spare parts continues to grow with the addition of a spare gyro assembly. The need for spare parts is recognized especially for deployments outside the continental United States, when an unrecoverable AVIRIS breakdown in the field would mean the termination of a deployment.

Spare parts from the AVIRIS inventory during the 1993 flight season afforded a recovery within 5 hours from the damage caused by a power transient in the lab (which occurred less than 24 hours before the shipping date at the start of the flight season), and a 95% fix to the Freckles and Badspots problems midway through the 1993 season without impacting the flight schedule.

2.2 1995 Engineering and Maintenance Plans

2.2.1 New FPA's

Development and testing continue on candidate FPA designs toward the goals of 12-bit digitized data, lower noise, increased dynamic range, and snapshot mode readout. Several variations of buffered direct injection (BDI) and capacitive trans-impedance amplifier (CTIA) multiplexer designs are being investigated.

2.2.2 Dark Current Summing and 12 bit Data Path

An upgraded data formatter onboard AVIRIS will have 12-bit data paths and dark current summing on the flyback for lower noise dark current readings. The dark current summing will collect and add a fixed number of dark current samples for all 224 bands during the flyback period of the scan. Averaging of the sums will be done in the AVIRIS data facility. The number of samples collected will be selected after characterizing the foreoptics shutter to determine the maximum time available for collecting dark current samples during the flyback. A spare foreoptics shutter module is being built for characterization and will be added to the spares inventory.

2.2.3 Calibrator Lamp Stability

To improve the stability of the lamp in the IFRS, a photosensor has been added to the lamp regulator. In 1993 and 1994 a precision current regulator was used to control the lamp output, but it eventually became clear that changes in the filament over the life of the lamp and variations among lamps (if one failed between calibrations) would compromise the desired stability of the source.

2.2.4 IFRS Thermal Testing

Thermal chamber testing is planned for the IFRS to calibrate and measure the stability of the reference lamp and the Lyot filters down to -10° C. Results from this testing activity will expand the usefulness of the IFRS as an on-board spectral and radiometric calibration source during in-flight data runs.

146

2.3 Future Engineering and Maintenance Plans (C-130 Flight Demonstration Program)

Plans are under way to adapt AVIRIS to the C-130 and conduct 30 hours of demonstration flights in 1996. Special attention will be given to acoustic and vibration isolation in the C-130 airborne environment, which is more severe than the ER-2, reducing levels below those experienced in the ER-2. Data will be collected at altitudes as low as 5 km, increasing the AVIRIS spatial resolution by a factor of 16, or reducing the noise by a factor of 4.

3.0 CONCLUSION

Since AVIRIS first became operational in 1989, the AVIRIS system has been undergoing incremental improvements. A number of these improvements have occurred in the sensor component of the AVIRIS project. In all cases, the driver for these modifications and upgrades has been the quality of data provided to the science investigators. The important modifications in 1994 and 1995 have been described.

4.0 ACKNOWLEDGMENTS

5.0 REFERENCES

Chrien, T.G., "AVIRIS: Recent Instrument Maintenance, Modifications and 1992 Performance," *Summaries of the Third Annual JPL Airborne Geoscience Workshop*, JPL Pub. 92-14, Vol. 1, AVIRIS Workshop, 1992, Jet Propulsion Laboratory, Pasadena, CA, pp. 78-79.

Chrien, T.G., M.L. Eastwood, C.M. Sarture, R.O. Green, and W.M. Porter, "Current Instrument Status of the Airborne Visible/Infrared Imaging Spectrometer (AVIRIS)," *Proc. of the Third AVIRIS Workshop*, JPL Pub. 91-28, 1991, Jet Propulsion Laboratory, Pasadena, CA, pp. 302-313.

Chrien, T.G., R.O. Green, C.M. Sarture, C. Chovit, M.L. Eastwood, and B.T. Eng, "Airborne Visible/Infrared Imaging Spectrometer (AVIRIS): Recent Improvements to the Sensor," *Summaries of the Fourth Annual JPL Airborne Geoscience Workshop*, JPL Pub. 93-26, 1993, Vol. 1, AVIRIS Workshop, Jet Propulsion Laboratory, Pasadena, CA, pp. 27-30.

Porter, W.M., T.G. Chrien, E.G. Hansen, and C.M. Sarture, "Evolution of the Airborne Visible/Infrared Imaging Spectrometer (AVIRIS) Flight and Ground Data Processing System," *Proc. of the Second AVIRIS Workshop*, JPL Pub. 90-54, 1990, Jet Propulsion Laboratory, Pasadena, CA, pp. 271-277.

6.0 BIBLIOGRAPHY

Airborne Visible/Infrared Imaging Spectrometer (AVIRIS): A Description of the Sensor, Ground Data Processing Facility, Laboratory Calibration, and First Results, JPL Pub. 87-38, Jet Propulsion Laboratory, Pasadena, CA, 1987.

Proc. of the Second Airborne Visible/Infrared Imaging Spectrometer (AVIRIS) Workshop, JPL Pub. 90-54, Jet Propulsion Laboratory, Pasadena, CA, 1990.

Proc. of the Third Airborne Visible/Infrared Imaging Spectrometer (AVIRIS) Workshop, JPL Pub. 91-28, Jet Propulsion Laboratory, Pasadena, CA, 1991.

Remote Sensing of Environment, Vol. 44, Nos. 2/3, May/June 1993, Elsevier, ISSN 0034-4257.

Summaries of the Fifth Annual JPL Airborne Earth Science Workshop, Vol. 1, AVIRIS Workshop, JPL Pub. 95-1 (this document), Jet Propulsion Laboratory, Pasadena, CA, 1995.

Summaries of the Fourth Annual JPL Airborne Geoscience Workshop, Vol. 1, AVIRIS Workshop, JPL Pub. 93-26, Jet Propulsion Laboratory, Pasadena, CA, 1993.

Summaries of the Third Annual JPL Airborne Geoscience Workshop, Vol. 1, AVIRIS Workshop, JPL Pub. 92-14, Jet Propulsion Laboratory, Pasadena, CA, 1992.

7.0   TABLES

Table 1. AVIRIS Data Characteristics

SPECTRAL	Wavelength range	400 to 2500 nm
	Sampling	<= 10 nm
	Spectral response (fwhm)	10 nm nominal
	Calibration	<= 1 nm
RADIOMETRIC	Radiometric range	0 to maximum lambertian
	Sampling	~ 1 dn noise rms
	Absolute calibration	<= 7%
	Intraflight calibration	<= 2%
	Precision/noise	exceeding NEdL/SNR requirement
GEOMETRIC	Field of view (FOV)	30 degrees (11 km)
	Instantaneous FOV	1.0 mrad (20 m)
	Calibration	<= 0.2 mrad
	Flight line length	Up to ten 100 km flight lines

Table 2. AVIRIS Operational Characteristics

SENSOR	Imager type	Whisk-broom scanner
	Cross track samples	614 elements
	Scan rate	12 scans/second
	Dispersion	Four grating spectrometers (A,B,C,D)
	Detectors	224 detectors (32,64,64,64) Si & InSb
	Digitization	10 bits (12 bits planned for 1995)
	Data rate	2.125 Mwords/second
	Spectrum rate	7300 spectra/second
	Data capacity	>10 gigabytes (>10,000 km^2)
	Onboard calibration	Radiometric and spectral
	Position & pointing	Lat, lon, alt, and roll, pitch, yaw
	Launches	~30 per year
AVIRIS DATA FACILITY (ADF)	Performance monitoring	48 hours from acquisition
	Archiving	One week from acquisition
	Quick-look distribution	One week from acquisition via Internet (anon ftp)
	Calibration	Two weeks from request
	Quality monitoring	Prior to distribution
	Distribution	Two weeks from request
	Engineering analysis	Priority as high as required

Table 3. AVIRIS Data Acquisitions

	1992	1993	1994
Months of operations	8	7	8
Aircraft bases	4	4	4
Principal investigators supported	32	35	24
Investigator sites flown	172	211	382
Launches	34	38	53
Inflight calibration experiments	3	3	3
Square kilometers flown	114,300	138,400	250,000
Flight scenes	1143	1384	2500
Gigabytes processed	317	363	>600
Data scenes calibrated/distributed	1120	1212	2000
Approximate data turnaround (months)	2.5	1	1

EXTRACTION OF OZONE AND CHLOROPHYLL-A DISTRIBUTION FROM AVIRIS DATA

M. Schaepman[1], K.I. Itten[1], D. Schläpfer[1], U. Kurer[1], S. Veraguth[1] and J. Keller[2]

[1]Remote Sensing Laboratories, University of Zurich–Irchel, 8057 Zurich, Switzerland

[2]Paul Scherrer Institute, 5232 Villigen PSI, Switzerland

Data Basis and Preprocessing

The potential of airborne imaging spectrometry for assessing and monitoring natural resources is studied. Therefore, an AVIRIS scene of the NASA's MacEurope'91 campaign - acquired in Central Switzerland - is used. The test site consists of an urban area, the Lake Zug with its surrounding fields, the Rigi mountain in the center of the test site, and the Lake of Four Cantons. The region is covered by the AVIRIS flight #910705, run 6 and 7 of the NASA ER–2 aircraft resulting in an average nominal pixel size of about 18 m.

Simultaneous to the ER–2 overflight spectroradiometric measurements have been taken in various locations.Preselected reference targets were measured in the field with a GER Mark V spectroradiometer, and radiance measurements were taken on the lake using a Li–Cor LI 1800UW specroradiometer below and above the water surface [Itten et al., 1992].

A comprehensive meteorological data set was obtained by joining the POLLUMET experiment which carried out measurements to investigate the summer smog in Switzerland on the same day [Neininger, 1991].

The quality assessment for the actual data set can be found in detail in Meyer et al. [1993]. A parametric approach calculating the location of the airplane was used to simulate the observation geometry. This parametric preprocessing procedure, which takes care of effects of flight line and attitude variations as well as the pixel-by-pixel topographic corrections is described in Meyer, [1994].

Atmospheric Correction

The atmospheric correction is based on the radiative transfer code MODTRAN2. The correction itself is performed using a model proposed by Woodham [Woodham, 1985] and a pixel–by–pixel approach. The atmospheric profiles used, have been taken from radiosonde data. Where no data were available the standard midlatitude summer profile was used.

Another important factor was to estimate the visibility. The values obtained from the Swiss Meteorological network, and the estimations made in the field vary from 2–14 km for July 5th. Since small changes of the visibility have a siginficant impact on the output of the calculation in the radiative transfer code, a method to extract the visibility from AVIRIS data is tested. Two AVIRIS channels (53 / 71; 872 nm / 1045 nm) are selected. In these bands, the total attenuation of the radiance depends only on aerosol scattering. The meteorological visibility from this approach is estimated to be 5 km (eq. horizontal visibility of 3.85 km). The 5S code restricts however the horizontal visibility to 5 km, therefore this approach will have to be evaluated further also considering adjacency effects.

The pixel–by–pixel approach bases not on the reconstruction of the path through the atmosphere but relies on modelling the possible maximum and mininimum radiance at the sensor. Assuming that the objetct's reflectance is linear with the received radiance at the sensor, we did run the radiative transfer code twice for each pixel [Veraguth, 1994].

A comparison of two different corrections (visibilitiy decreasing with altitude and constant within the inversion layer) in a corrected AVIRIS scene using MODTRAN2 is shown in figure 1.

Extraction of Ozone

Ozone absorbs particulary in the ultraviolet and visible range of the spectrum. Hence, spectrometry is expected to be a promising tool to extract the ozone contents in a given air column by using the correlation between cumulative trace gas amount and absorption strength in the sensor channels located within the absorption bands. The following investigations were initiated to detect tropospheric ozone in the Chappuis-Band (500 - 700 nm), based on the POLLUMET data set, the AVIRIS specifications, and MODTRAN2 simulations.

Normally, the abundance of water vapor from imaging spectrometry data is usually determined by ratio methods [Frouin, 1990; Bruegge, 1990]. Two or more channels are combined to yield the total column water vapor abundance. The same method can be used to detect ozone.

First, the best channels within the Chappuis-Band have to be determined. It must be discriminated between 'Reference channels' which should not be affected by any absorbing gases including ozone and, on the other hand, 'Measurement channels' which should be sensitive to the change of ozone amount and not be disturbed by other absorbing gases. An empirical comparison of MODTRAN2 transmission calculations in the AVIRIS channels yielded a number of suitable AVIRIS ozone channels:

Measurement channel numbers: 22 (608nm), 23 (618 nm) ,17 (558 nm), 16 (549 nm)
Reference channel numbers: 1-12(< 515 nm), 28 (667 nm), 29 (677 nm), 40 (746 nm)

These selected channels could be combined both by three known splitting window techniques and by new approaches. To date, the following methods are used: Ratio of two channels [King, 1992], continuum interpolated band ratio (CIBR) using 2 reference channels [Bruegge, 1990] and the Narrow/Wide technique [Frouin, 1990] with two channels of different bandwith centered at the same wavelength. Two new approaches are introduced: The first is a quadratic interpolated band ratio (QIBR) which is analogous to the CIBR but which uses three reference channels. The second is a statistical approach (TOTAL) by ratioing several measurement channels by the same number of reference channels. Each of these five methods can be tested with different channel combinations, using the reference and measurement channels.

From radiosonde data and other POLLUMET in-situ measurements a reference atmosphere for July 5th (1991) was modelled, ending up in a complete profile of pressure, temperature, water vapor and ozone. The total ozone column in the different atmospheric layers was integrated with height and compared to standard atmospheric profiles. None of them represented the tropospheric ozone amounts in a satisfying manner; the ozone column was nearly twice as high as guessed by the tropical or the midlatidude summer model. This shows, that tropospheric ozone had a bigger influence on the total ozone signal than assumed.

In the evaluation of the methods, the influence of disturbing factors and the sensitivity to varying amounts of ozone were investigated. For this purpose the amount of the respective elements (aerosols, water vapor and ozone) were varied systematically in the atmospheric reference profiles. MODTRAN2 allows to simulate the corresponding radiance at the sensor channels and all the methods could be applied to the simulated radiance. A good sensitivity to ozone variations is obtained by the CIBR, the channel ratio and the TOTAL methods. The Narrow/Wide technique is only half as sensitive to ozone as the others. Changing visibility is proportional to the aerosol contents and affects especially the TOTAL and some of the CIBR-Methods. The Narrow/Wide and QIBR methods are not influenced that much. If tropospheric humidity is doubled, the influence on all investigated methods is only about one fifth of the change that is due to varying aerosol optical thickness. This evaluation step led to the elimination of most of the methods. The remaining ones were quantified using the ozone variation procedure described above. An absolute quantification was only possible for one CIBR (channels 10,28 and 22) and one Narrow/Wide ratio (channels 10, 28, 17 and 22). All the others yielded irrealistic high or low ozone contents. Finally the CIBR was selected because of the better sensitivity to ozone variations. However, the application to the AVIRIS scene (see figure 2) was only possible over water, which is due to the high sensitivity to changing ground response and the very low absorption in the Chappuis Band. The error which must be taken into account considering the disturbing factors is still about +/- 30% .

150

Extraction of Chlorophyll-a

During the overflight of the ER–2 aircraft, a wealth of limnologic measurements has been collected on the Lake Zug. For the results presented here, the measurements of chlorophyll concentrations using a two–filter method in various depths [Schanz, 1982] and the use of the Li–Cor 1800UW underwater spectroradiometer are of particular interest. Downwelling and upwelling irradiance measurements have been taken underwater as well as incident global radiation. The photosynthetically active radiation measurements of the solar irradiance are used to calculate the absorption coefficients.

The ER–2 overflight on July 5th 1991 was not during an algae bloom, hence very low chlorophyll concentrations were expected. In a first processing step, the AVIRIS radiance data are converted in upwelling irradiance data just below the water surface. Using MODTRAN2, the path scattered radiance was subtracted from the AVIRIS data and divided by the atmospheric transmission. Then the AVIRIS signal was transformed in upwelling radiance just unter the water surface. In the last step, the radiance had to be converted into irradiance data using a conversion proposed by Kirk [1983].

Different combinations of channels of the AVIRIS have been selected to extract chlorophyll-a. A CIBR method using the AVIRIS channels 26 / 29 / 31 (647 nm / 677 nm / 697 nm) shows promising results [Kurer, 1994] (see figure 3).

Conclusion

It is expected, that the presented applications to extract ozone and chlorophyll-a can be extended to many more environmentally sensitive parameters. Some efforts still have to be made in respect to adjacency effects and improvements of the atmospheric correction.

Acknowledgements

References

C.J. Bruegge, J.E. Conel, J.S. Margolis, R.O. Green, G. Toon, V. Carrère, R.G. Holm and G. Hoover, "In-situ Atmospheric Water-Vapor Retrieval in Support of AVIRIS Validation." SPIE Vol. 1298, Imaging Spectroscopy of the Terrestrial Environment, pp 150 - 163, 1990

R. Frouin, P.–Y. Deschamps and P. Lecomte, "Determination from Space of Atmospheric Total Water Vapor Amounts by Differential Absorption near 940 nm: Theory and Airborne Verification". Journal of Applied Meteorology, Vol. 29, American Meteorological Society, pp 448 - 459, 1990

K.I. Itten, P. Meyer, K. Staenz, T. Kellenberger, and M. Schaepman, "Evaluation of AVIRISwiss'91 Campaign Data", In Summaries of the Third Annual JPL Airborne Geoscience Workshop June 1–5, 1992, Vol. 1 AVIRIS Workshop, ed. R. Green, Pasadena, pp. 108–111, June 1–5, 1992

M.D. King, Y.J. Kaufmann, W.P. Menzel and D. Tanré, "Remote Sensing of Cloud, Aerosol, and Water Vapor Properties from the Moderate Resolution Imaging Spectrometer (MODIS)." IEEE Transactions on Geoscience and Remote Sensing, Vol. 30, No. 1, New York, pp 2 - 27, 1990

J.T.O. Kirk, "Light and photosynthesis in aquatic ecosystems", Cambridge University Press, Cambridge, GB, 1983

U. Kurer, "Bestimmung der Chlorophyllkonzentration im Zugersee anhand von AVIRIS–Bildspektrometriedaten", Masters Thesis, Department of Geography, University of Zurich, p. 122, Zurich, 1994

151

P. Meyer, "A Parametric Approach for the Geocoding of Airborne Visible/Infrared Imaging Spectrometer (AVIRIS) Data in Rugged Terrain", Remote Sens. Environ., Vol. 48, pp. 1–25, 1994

P. Meyer, R.O. Green, and T.G. Chrien, "Extraction of Auxiliary Data from AVIRIS Distribution Tape for Spectral, Radiometric, and Geometric Quality Assessment ", In Proc. of the Fourth Annual JPL Airborne Geoscience Workshop, ed. R. Green, Washington, 1993

B. Neininger, "Field Phase Report der POLLUMET-IOP's–91", Project–Report, POLLUMET, Federal Instiute of Technology, Zurich, Switzerland, 1991

F. Schanz, "A fluormetric method of determining chlorophyll a and phaeophytin a concentrations", Arch. Hydrobiol. Beih. Ergebn. Limnol., Vol. 16, Stuttgart, Germany, pp. 91–100, 1982

D. Schläpfer, "Bildspektrometrie atmosphärischer Spurengase", Masters Thesis, Department of Geography, University of Zurich, p. 116, Zurich, 1994

S. Veraguth, "Die atmosphärische Korrektur von AVIRIS–Daten", Masters Thesis, Department of Geography, University of Zurich, p. 117, Zurich, 1994

R.J. Woodham and T.K. Lee, "Photometric Method for Radiometric Correction of Multispectral Scanner Data", In Canadian Journal for Remote Sensing, Vol. 8, No. 2, Ottawa, Canada, 1985
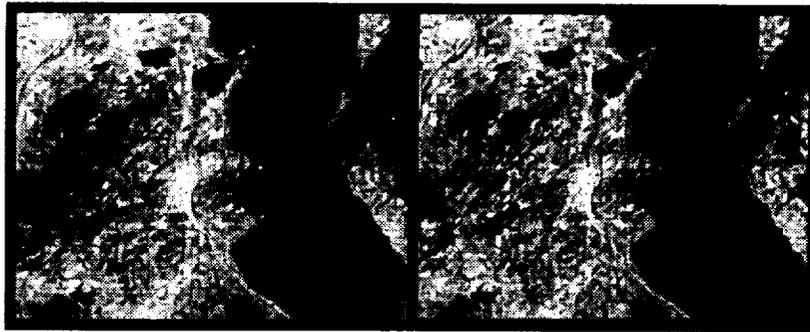
Figures

Figure 1: Atmospheric correction results by modelling the visibility decreasing with altitude (left), and constant within the inversion layer (right)
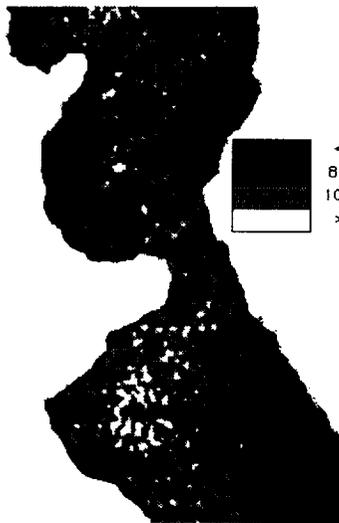

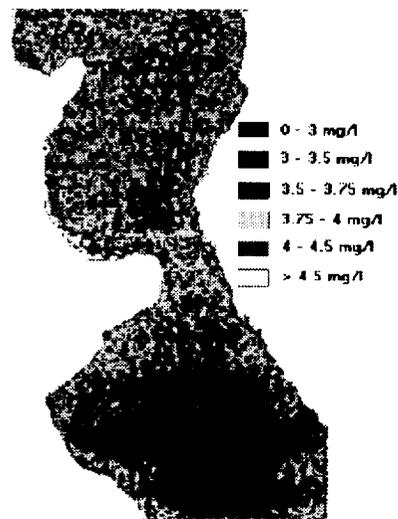Figure 2: Total column tropospheric ozone distribution over Lake Zug

Figure 3: Chlorophyll-a distribution in Lake Zug

152

IMPACT OF DIFFERENCES IN THE SOLAR IRRADIANCE SPECTRUM ON SURFACE REFLECTANCE RETRIEVAL WITH DIFFERENT RADIATIVE TRANSFER CODES

K. Staenz[1], D.J. Williams[2], G. Fedosejevs[1], and P.M. Teillet[1]

[1]Canada Centre for Remote Sensing
588 Booth Street, Ottawa, Ontario, Canada K1A 0Y7
[2]MacDonald Dettwiler and Associates Ltd.
13800 Commerce Parkway, Richmond, British Columbia, Canada V6V 2J3

1. INTRODUCTION

Surface reflectance retrieval from imaging spectrometer data as acquired with the Airborne Visible/Infrared Imaging Spectrometer (AVIRIS) has become important for quantitative analysis. In order to calculate surface reflectance from remotely measured radiance, radiative transfer codes such as 5S (Tanré et al., 1990) and MODTRAN2 (Berk et al., 1989) play an increasing role for removal of scattering and absorption effects of the atmosphere. Accurate knowledge of the exo-atmospheric solar irradiance (E_o) spectrum at the spectral resolution of the sensor is important for this purpose. The present study investigates the impact of differences in the solar irradiance function, as implemented in a modified version of 5S (M5S) (Teillet and Santer, 1991), 6S (Vermote et al., 1994), and MODTRAN2 (Berk et al., 1989), and as proposed by Green and Gao (1993), on the surface reflectance retrieved from AVIRIS data. Reflectance measured in situ is used as a basis of comparison.

2. DATA USED

An asphalt site within an AVIRIS scene acquired over the Greater Victoria Watershed near Victoria, British Columbia on August 29, 1993 was selected for this study. The extracted AVIRIS radiance spectrum was averaged over the target of 2 x 3 pixels, which excludes edge pixels. Corresponding ground-based reflectance data were acquired with a GER MARK V spectroradiometer and a Spectralon panel. These data are accurate to within ±5% reflectance. Solar attenuation measurements were collected on the ground at the time of the AVIRIS overflight with a SONOTEK sunphotometer for the calculation of atmospheric optical depths. In addition, estimated water vapour concentrations as reported by Staenz et al. (1994) for this particular AVIRIS dataset were used for atmospheric modelling.

Several E_o data sets were included in this study (Table 1). These E_o spectra are based on Iqbal (1983) for the M5S code, Neckel and Labs (1984) for 6S, and a combination of Neckel and Labs, Wehrli (1985), and Thekeakera (1974) for MODTRAN2. The proposed update of the E_o function in MODTRAN2 suggested by Green and Gao (1993) was also included. This E_o spectrum is based on Neckel and Labs (1984) and data provided by the ATMOS sensor onboard the Space Shuttle.

3. ANALYSIS AND RESULTS

Three radiative transfer codes, M5S, 6S and MODTRAN2, were used in combination with each of the four aforementiond E_o functions to generate a total of 12 computed surface reflectances for the asphalt site. The procedure was carried out in three steps. First, the radiative transfer codes were used to generate tables of simulated AVIRIS radiance spectra. Then, the tables were scaled by the spectral ratio of the E_o function under study to that which is implemented in the radiative transfer code (both convolved to the AVIRIS bandset). Finally, multiplicative and additive coefficients for atmospheric correction were computed

from the tables and applied to the airborne radiances (Williams et al., 1992).

The E_o functions are plotted for the AVIRIS bands in Figure 1. Variations of up to 20% occur between the different data sets, although the differences are generally within ±5%. The main differences are found in the 2100 - 2500 nm region and other notable discrepancies are apparent around 940 nm, 1300 nm, 1650 nm, and 1900 nm. The 6S E_o function follows the Green and Gao function very closely with the exception of the 1300 nm region. A similar trend can generally be seen for the M5S and the MODTRAN2 E_o spectra above 800 nm, although deviations from this tendency occur for some of the AVIRIS bands above 1800 nm.

These deviations between the E_o functions translated to similar relative differences in the retrieved surface reflectances for each of the radiative transfer codes used. Figure 2 shows the reflectances obtained with the MODTRAN2 code. Figure 3 is a blow-up of the 2050 - 2450 nm region of Figure 2. The reflectance spectra generated with the 6S and Green and Gao E_o functions are slightly smoother in this wavelength region than those produced with the original MODTRAN2 or M5S E_o datasets. However, none of the retrieved reflectances exactly matches the ground-based spectrum. This is also true for the 940 nm, 1300nm, and 1600 nm regions (Figure 2), although a closer match with ground-based reflectances is apparent in the last two regions for the reflectances generated with the 6S/Green and Gao E_o functions.

Changes in the overall shape of the surface reflectance spectra due to the different E_o functions (Figure 3) are less than those generated by the various radiative transfer codes using the same E_o dataset (Figure 4). Differences arising from the use of different radiative transfer codes occur especially in the wavelength regions affected by atmospheric gases. For example, Figure 4 shows major reflectance differences above 2250 nm between M5S and 6S/MODTRAN2 generated spectra, even though the E_o function used (Green and Gao) was the same in each case. This is mainly due to the different methods used for calculation of the atmospheric transmission in these codes (Staenz et al., 1994).

4.   CONCLUSIONS

Differences in the E_o spectra as implemented in M5S, 6S and MODTRAN2 radiative transfer codes and as proposed by Green and Gao can translate to relative differences in retrieved surface reflectance of up to 20%, although they are generally within ±5% at most wavelengths. The largest deviations are found above 2100 nm. In addition, notable differences occur in the 940 nm, 1300 nm, and 1650 nm regions. The overall shape of the retrieved reflectance spectrum is generally less affected by differences between E_o functions than by differences between the atmospheric radiative tansfer codes.

5.   ACKNOWLEDGEMENTS

The authors gratefully acknowledge the availability of the AVIRIS data from the Pacific Forestry Centre and the solar irradiance function proposed for MODTRAN2 from R.O. Green, Jet Propulsion Laboratory. Thanks are also due to P. Bouffard for technical assistance and to P. Geiger for wordprocessing.

6.   REFERENCES

Berk, A., L.S. Bernstein, and D.C. Roberston, 1989, "MODTRAN: A Moderate Resolution Model for LOWTRAN7", *Final Report GL-TR-0122*, AFGL, Hanscom AFB, Maryland, 42 pages.
Green, R.O., and B.-C. Gao, 1993, "A Proposed Update to the Solar Irradiance Spectrum Used

154

in LOWTRAN and MODTRAN", *Summaries of the Fourth Annual JPL Airborne Geoscience Workshop*, JPL Publication 93-26, Vol. I, Washington, D.C., pp.81-84.

Iqbal, M., 1983, *An Introduction to Solar Radiation*, Academic Press, New York, 390 pages.

Neckel, H., and D. Labs, 1984, "The Solar Radiation Between 3300 and 12500 Angstrom", *Solar Physics*, Vol. 90, pp.205-258.

Staenz, K., D.J. Williams, G. Fedosejevs, and P.M. Teillet, 1994, "Surface Reflectance Retrieval From Imaging Spectrometer Data Using Three Atmospheric Codes", *Proceedings of the European Symposium on Satellite Remote Sensing*, Rome Italy (in press).

Tanré, D., C. Deroo, P. Duhaut, M. Herman, J.J. Morcrette, J. Perbos, and P.Y. Deschamps, 1990, "Description of a Computer Code to Simulate the Satellite Signal in the Solar System: The 5S Code", *International Journal of Remote Sensing*, Vol. 11, No. 4, pp.659-668.

Teillet, P.M., and R. Santer, 1991, "Terrain Elevation and Sensor Altitude Dependence in a Semi-Analytical Atmospheric Code", *Canadian Journal of Remote Sensing*, Vol. 17, No. 1, pp.36-44.

Thekeakera, M.P. 1974, "Extra-terrestrial Solar Spectrum, 3000-6100Å at 1Å Intervals", *Applied Optics*, Vol. 13, pp.518-522.

Vermote, E., D. Tanré, J.L. Denzé, M. Herman, and J.J. Morcrette, 1994, "Second Simulation of the Satellite Signal in the Solar Spectrum (6S)", *6S User's Guide Version 0*, NASA-GSFC, Greenbelt, Maryland, 134 pages.

Wehrli, C.H., 1985, "Extra-terrestrial Solar Spectrum", *Publication No. 615*, Physikalisches-Meteorologisches Observatorium and World Radiation Center, Davos-Dorf, Switzerland, 8 pages.

Williams, D.J., A. Royer, N.T. O'Neill, S. Achal, and G. Weale, 1992, "Reflectance Extraction from CASI Spectra Using Radiative Transfer Simulations and a Rooftop Radiance Collector", *Canadian Journal of Remote Sensing*, Vol. 18, No. 4, pp.251-261.

Table 1: Exo-atmospheric solar irradiance functions (E_0) and their spectral resolution for the AVIRIS wavelength coverage (400-2500 nm) with respect to different radiative transfer codes.

Source	Radiative Transfer Code (spectral resolution)	Spectral Resolution of E_0 Function	
		original	as implemented in radiative transfer code
Iqbal	M5S (5 nm, 20 cm⁻¹)	5-100 nm[1]	5 nm
Neckel and Labs	6S (2.5 nm)	1-5 nm[2]	5 nm
Neckel and Labs, Wehrli, Thekeakera	MODTRAN2 (variable, finest = 1 cm⁻¹)	1-5 nm[2] 1-10 nm[3] 5- 100 nm[1]	20 cm⁻¹
Green and Gao	proposed for MODTRAN	2.5 nm	--------

[1] 5nm (400-610nm), 10 nm (610-1000 nm), 50 nm (1000-2000 nm), 100 nm (2000-2500 nm)
[2] 1 nm (400-630nm), 2 nm (630-869 nm), 5 nm (869-1248 nm)
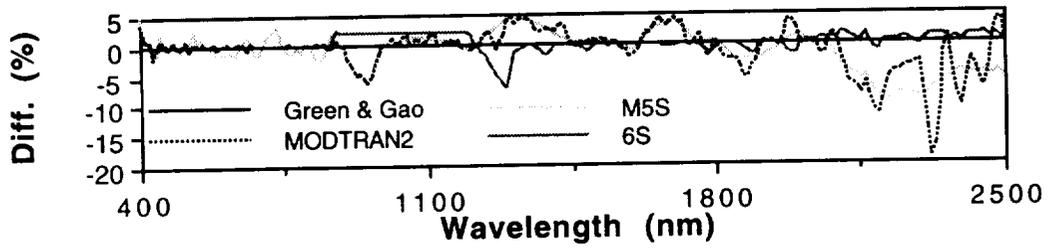[3] 1 nm (400-630nm), 2 nm (630-999 nm), 5 nm (999-2002 nm), 10 nm (2002-2500 nm)

155

Figure 1:   Percent differences between the exo-astmospheric solar irradiance (E_0) spectra with respect to the Green and Gao E_0 spectrum. The irradiance data sets were convolved to the AVIRIS bands.
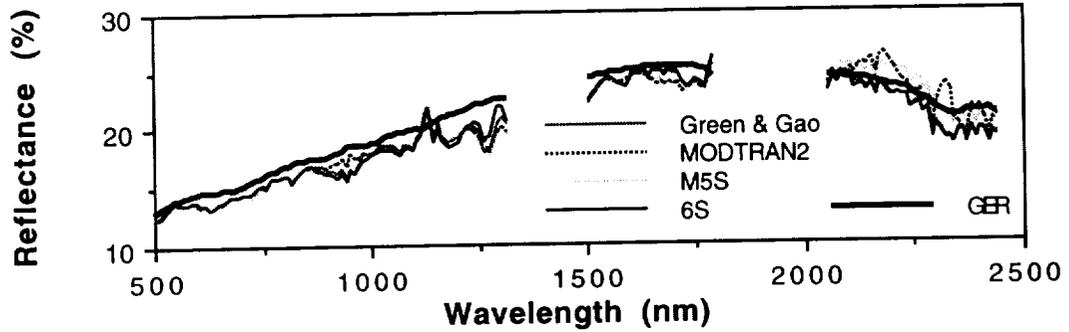

Figure 2:   Surface reflectances of asphalt retrieved from AVIRIS data with MODTRAN2 using different solar irradiance functions, and the corresponding ground-based reflectance (GER). The atmospheric conditions used in the retrieval were: water vapour = 1.5 g/cm^2; aerosol optical depth at 550 nm = 0.121.

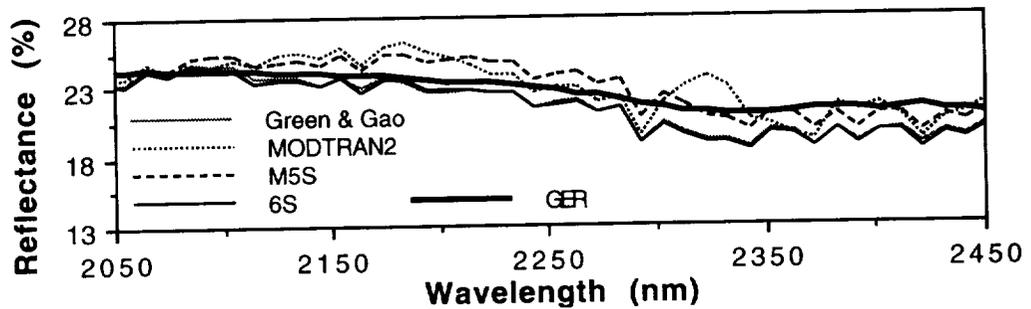Figure 3:   Surface reflectances of asphalt in the 2050-2450 nm region (Blow-up of Figure 2).
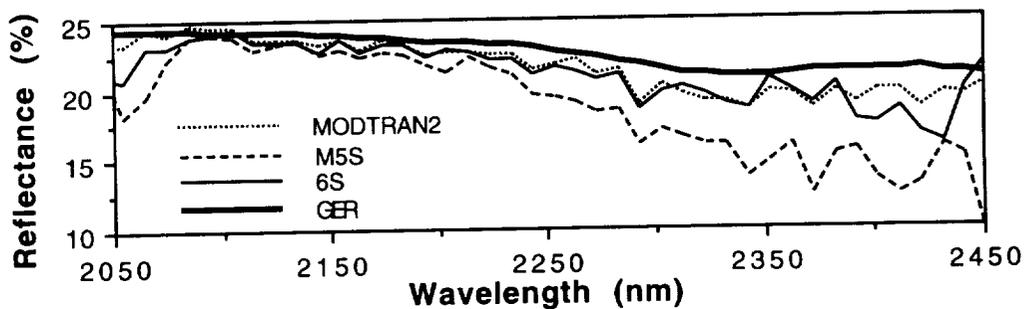

Figure 4:   Surface reflectances of asphalt retrieved from the AVIRIS data with the different radiative transfer codes using the solar irradiance function proposed by Green and Gao as well as the corresponding ground-based reflectance (GER). The models were run with the same atmospheric conditions as those noted in Figure 2.

156

Spectral Identification of Minerals using Imaging Spectrometry Data: Evaluating the Effects of Signal to Noise and Spectral Resolution using the Tricorder Algorithm

Gregg A. Swayze and Roger N. Clark

U.S. Geological Survey
Box 25046 MS964 Federal Center
Denver, CO 80225

INTRODUCTION

The rapid development of sophisticated imaging spectrometers and resulting flood of imaging spectrometry data has prompted a rapid parallel development of spectral-information extraction technology. Even though these extraction techniques have evolved along different lines (band-shape fitting, endmember unmixing, near-infrared analysis, neural-network fitting, and expert systems to name a few), all are limited by the spectrometer's signal to noise (S/N) and spectral resolution in producing useful information. This study grew from a need to quantitatively determine what effects these parameters have on our ability to differentiate between mineral absorption features using a band-shape fitting algorithm. We chose to evaluate the AVIRIS, HYDICE, MIVIS, GERIS, VIMS, NIMS, and ASTER instruments because they collect data over wide S/N and spectral-resolution ranges. The study evaluates the performance of the Tricorder algorithm (Clark and Swayze, this volume) in differentiating between mineral spectra in the 0.4-2.5 μm spectral region. The strength of the Tricorder algorithm is in its ability to produce an easily understood comparison of band shape that can concentrate on small relevant portions of the spectra, giving it an advantage over most unmixing schemes, and in that it need not spend large amounts of time reoptimizing each time a new mineral component is added to its reference library, as is the case with neural-network schemes. We believe the flexibility of the Tricorder algorithm is unparalleled among spectral-extraction techniques and that the results from this study, although dealing with minerals, will have direct applications to spectral identification in other disciplines.

METHOD

We decided to model only single-component mineral spectra because they allow us to establish the absolute minimum S/N and spectral resolution necessary to distinguish between mineral species. This type of simplified model was adopted with the understanding that multicomponent spectra will require even higher S/N and resolution because of overlapping absorptions and weaker band strengths due to dilution by the other mixture components. Minerals from seven mineral groups (alunite, calcite, chlorite, hematite, kaolinite, montmorillonite, and muscovite) were chosen for evaluation based on the presence of easily detected spectral features and common occurrence at the ground surface. All of these minerals have either Fe charge-transfer and crystal field bands in the VIS/NIR region or OH^-, Metal-OH, H_2O, CO_3^{2-}, and SO_4^{2-} vibrational features in the NIR region. Some of the minerals have features in both regions.

A bidirectional-reflectance spectrum of each mineral was first deconvolved to the spectral resolution of each imaging instrument, and then scaled random noise was added. Signal to noise is defined here as 50 percent reflectance divided by the standard deviation of the gaussian-noise spectrum, with standard deviation uniform at all wavelengths. To make our determinations statistically accurate, we generated over 20,000 noisy spectra for each convolved mineral spectrum. The S/N levels varied from 1 to 500 as did the number of noisy spectra at each level: 400 for the high S/N levels and up to two thousand at the low S/N levels. These spectra were then analyzed by the Tricorder algorithm and the best matching library mineral spectra chosen for each noisy-spectrum. Tricorder fits the noisy spectra to over 120 library mineral spectra (convolved to the noisy spectrum resolution) by first removing the continuum from diagnostic spectral regions of both the noisy spectrum and library spectra, and then least-squares scaling each library spectral absorption to the corresponding continuum-removed region in the noisy spectrum. During the process of scaling, a linear correlation coefficient, which we

call the "fit," is generated for each library mineral comparison. The mineral with the highest fit is chosen as the best spectral match. Tricorder determines the fit of each library mineral spectrum by individually fitting all the diagnostic absorptions in the library spectrum to the noisy spectrum and then calculating an overall fit by weighting each individual fit by its absorption-feature's area.

Because random noise can make a mineral's spectral features resemble those of other minerals and because this effect is magnified as S/N decreases, we expected Tricorder to choose several different mineral matches, especially at the low S/N levels. We also expected Tricorder to make correct identifications at high S/N levels. Tricorder gave the results that we expected at these S/N extremes. Of particular interest is the S/N region where Tricorder first starts to make incorrect identifications. By plotting the percentage of correct identifications versus S/N level, we can determine precise S/N levels at which the algorithm has a given percent accuracy in identifying this mineral at a given spectral resolution. By plotting the individual incorrect mineral identifications versus S/N we can determine which minerals are most likely to start spectrally resembling the noisy spectrum as S/N decreases. For example, calcite is misidentified 1 out of 9 times at a S/N of 13 at AVIRIS resolution. Stated another way, with Tricorder, we are able to spectrally recognize calcite 90 percent of the time at a S/N of 13 at AVIRIS resolution. The other 10 percent of the time we would either identify calcite as epidote, nontronite, hectorite, dolomite (each of which have strong 2.3-μm absorptions) or classify the noisy spectrum as having NO MATCH in the spectral library. As spectral resolution decreases this 90 percent identification level occurs at progressively higher S/N levels.

By compiling the S/N levels for each imaging spectrometer at which 90 percent of the identifications of a mineral are correct, we can quantitatively assess the effects of S/N and spectral resolution for each imaging spectrometer. Preliminary work shows that Tricorder's ability to correctly identify a mineral increases with increasing S/N and spectral resolution.

PRELIMINARY STUDY OF KELSO DUNES USING AVIRIS, TM, AND AIRSAR

Pung Xu, Dan G. Blumberg, and Ronald Greeley

Department of Geology
Arizona State University
Box 871404
Tempe, Arizona 85287-1404

1.   INTRODUCTION

Remote sensing of sand dunes helps in the understanding of aeolian process and provides important information about the regional geologic history, environmental change, and desertification. Remotely sensed data combined with field studies are valuable in studying dune morphology (Breed et al., 1979), regional aeolian dynamics (Mainguet, 1984), and aeolian depositional history (Blount and Lancaster, 1990). In particular, active and inactive sands of the Kelso Dunes have been studied using Landsat TM (Paisley et al., 1991) and AIRSAR (Lancaster et al., 1992). In this report, we describe the use of AVIRIS data to study the Kelso Dunes and to compare the AVIRIS information with that from TM and AIRSAR.

2.   STUDY SITE AND DATA

The Kelso Dunes, Mojave Desert, California, cover about 100 km^2 and range in elevation between 500 m to 900 m. The area of active dunes includes three large linear ridges (up to 170 m high) superimposed by 5-10 m high crescentic and reversing dunes and surrounded by 3-15 m high stabilized transverse and linear dunes (Paisley et al., 1991; Lancaster et al., 1992). Under present conditions, the prevailing westerly winds are counter-balanced by strong orographically controlled winds from the north, east, and south (Smith, 1984). This wind pattern accounts for the position of the dunes and the observation that there is little net change in dune location, even though there is active sand movement (Sharp, 1966). Smith (1967) suggested that the dunes formed under more arid conditions with stronger winds, and have since been modified due to climatic changes. The vegetation cover is less than 5% on the active dunes and 10-15% on the stabilized dunes (Lancaster et al., 1992).

3.   METHODS

AVIRIS data (PG02031) used in this study were flown on May 21, 1994. The AVIRIS image data were radiometrically calibrated and were reduced to "scaled surface reflectances" using an atmospheric and solar model, ATREM (Gao and Goetz, 1993). The AVIRIS data were then compared with a Landsat composite image (Paisley et al., 1991) and AIRSAR data collected during the Mojave Field Experiment campaign (Arvidson et al., 1991).

A color composite AVIRIS image is used in this preliminary study. The bands were selected using a laboratory spectra plot of major minerals from the dune area so that the spectra are most separated at these bands (Figure. 1). Point counting of field samples show that most of the Kelso sands are composed of 29-49% quartz, 22-39% plagioclase, 18-29% K-feldspar, 5-15% other minerals including dark minerals. Some sites have highly concentrated magnetite (28%; Paisley et al., 1991). Finally, band #10, #89, and #184, centered at 0.46029 μm, 1.2028 μm, and 2.1073 μm respectively, were assigned red, green, and blue in the image analyzed.
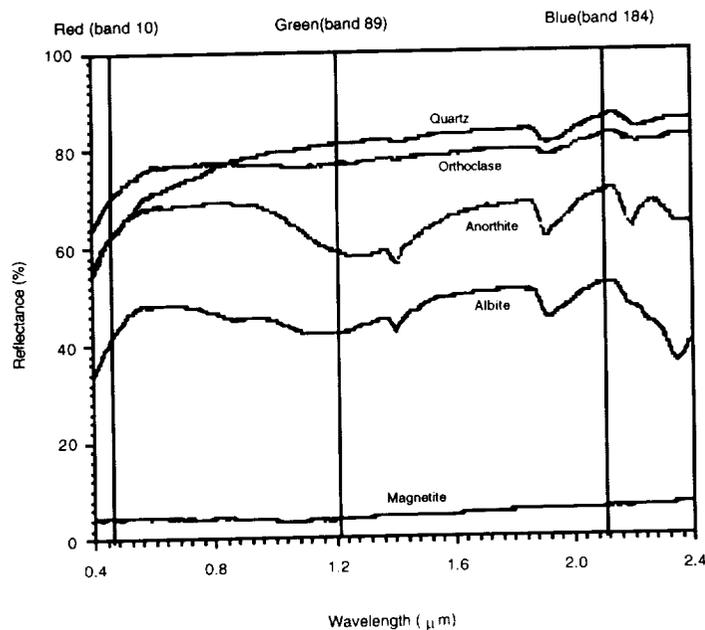
Figure 1. Band selection based on laboratory Spectra from SPAM spectral library (Mazer et al., 1988).

4. RESULTS

The composite AVIRIS image shows more color variation than the corresponding TM scene. The image shows not only the active and inactive units seen on TM and AIRSAR, but also an interesting feature which is not observed: the area to the west of Kelso Dunes is reddish in color and fades away toward the dunes. The same color can be traced to Granite Mountain, which is to the south of Kelso Dunes, through Devils Playground Wash. It has the same signature that is scattered on the large and small ridge of active dunes. This reddish color is on the north and south sides of the ridges which excludes the possibility of solar shadow affects. This signature is not observed on the more vegetated, stabilized dunes, thus excluding the possibility of vegetation. We suggest that certain mineral grains were eroded from rocks in the Granite Mountain, carried by the wash to the area west of Kelso Dunes, and transported to the active dunes by the prevailing westerly winds.

The widespread nature of the reddish color on active dunes on the image can be accounted for by major mineral components, i.e. quartz, plagioclase, K-feldspar, magnetite. The reason for a pixel to appear red is that the DN of the pixel at red band is higher than the DNs at green and blue bands. From the field sample point-counts and laboratory spectra plot, they may be plagioclase, K-feldspar, and/or magnetite. The reason for K-feldspar is that K-feldspar may have higher reflectance at 0.46029 μm, the red band, than other minerals. The reason for plagioclase or magnetite is that their reflectances at 0.46029 μm are closer to that of quartz and K-feldspar than at the other two bands. When the red band is stretched to compose with the other two bands, the red color appears for a pixel with high plagioclase or magnetite concentration. Yeend et al. (1984) noted the presence of areas rich in magnetite derived from local mountains. However, we cannot exclude other possibilities at this point. Further field work and use of mixing model analysis of AVIRIS data may confirm the hypothesis and narrow the possible minerals causing the reddish color.

160

5. CONCLUSIONS

In this study, AVIRIS data show promising results for analyzing sand dunes. AVIRIS provides higher spatial resolution and more spectral information than TM data. Future field work and unmixing analysis of AVIRIS data may lead to better explanations of material distributions around Kelso Dunes.

When comparing the AVIRIS, TM, and AIRSAR data, we find that AVIRIS data provide more information on mineralogy of the dunes and, thus, on the transport routes. The AIRSAR data provide information on the roughness of the dunes and on the vegetation. The TM data are useful mainly in obtaining a regional view.

6. REFERENCES

Arvidson R.E., S.B. Petroy, J.J. Plaut et al., 1991, "Mojave Remote Sensing Field Experiment", *EOS 72*, pp. 175.

Blount, G., and N. Lancaster, 1990, "Development of the Gran Desierto Sand Sea", *Geology 18,* pp.8183-8204.

Breed, C. S., Grolier, M. J., and J. F. McCauley, 1979, "Morphology and distribution of common 'sand' dunes on Mars: comparison with the Earth", *J. Geophys. Res. 84*, pp.8183-8204.

Breed, C. S., Grolier, M. J., and J. F. McCauley, 1979, "Morphology and distribution of common 'sand' dunes on Mars: comparison with the Earth", *J. Geophys. Res. 84*, pp.8183-8204.

Gao, B-C, K. B. Heidebrecht and A. F. H. Goetz, 1993, "Derivation of Scaled Surface Reflectances from AVIRIS data", *Remote Sensing of Environment*, Vol. 44, No. 2, pp. 165-178.

Lancater, N., L. R. Gaddis, and Ronald Greeley, 1992, "New Airborne Imaging Radar Observations of Sand Dunes: Kelso Dunes, California", *Remote Sens. Environ. 39*, pp.233-238.

Mazer, A.S., A. Martin, M. Lee, and J.E. Solomon, 1988, "Image processing software for imaging spectrometry data analysis," *Remote Sensing of Environ., 24*, 201-210.

Paisley, E. C. I., N. Lancater, L. R. Gaddis, and Ronald Greeley, 1991, "Discrimination of Active and Inactive Sand from Remote Sensing: Kelso Dunes, Mojave Desert, California", *Remote Sens. Environ. 37*, pp.153-166.

Sharp, R. P., 1966, "Kelso Dunes, Mojave Desert, California", *Geol. Soc. Am. Bull. 77*, pp.1045-1074.

Smith H. T. U., 1967, "Past versus present wind action in the Mojave Desert Region, California", In *U.S. Air Force Cambridge Research Laboratories Publication AFCRL-67-0683*, New Bedford, MA, 34pp.

Smith R. S. U., 1984, "Eolian geomorphology of the Devils Playground, Kelso Dunes and Silurian Valley, California", In *Surficial Geology of the Eastern Mojave Desert, California Field Trip 14* (J. c. Dohrenwend, Ed.), Geological Society of American, pp.162-174.

Yeend, W., J.C. Dohrenwend, R.S.U. Smith, R. Goldfarb, R.W. Simpson Jr., and S.R. Munts, 1984, "Mineral resources and mineral resource potential of Kelso Dunes Wilderness Study Area (CDCA-250), San Bernadino County, California", Washington, D. C., U.S. Geological Survey, Open-File Report 84-647.